DEVELOPMENT OF A PRACTICAL SYSTEM FOR SIMULATING EARTHQUAKE GROUND MOTIONS PAYING ATTENTION TO VOLCANIC ZONE AND ASPERITY ON A FAULT

張, 龍

https://doi.org/10.15017/1928631

出版情報：九州大学, 2017, 博士（工学）, 課程博士
バージョン：
権利関係：

DEVELOPMENT OF A PRACTICAL SYSTEM FOR SIMULATING EARTHQUAKE GROUND MOTIONS PAYING ATTENTION TO VOLCANIC ZONE AND ASPERITY ON A FAULT

Long Zhang

2017

DEVELOPMENT OF A PRACTICAL SYSTEM FOR SIMULATING EARTHQUAKE GROUND MOTIONS PAYING ATTENTION TO VOLCANIC ZONE AND ASPERITY ON A FAULT

A Thesis Submitted
In Partial Fulfillment of the Requirements
For the Degree of
Doctor of Engineering

By
Long Zhang

九州大学

to the
DEPARTMENT OF CIVIL AND STRUCTURAL ENGINEERING
GRADUATE SCHOOL OF ENGINEERING
KYUSHU UNIVERSITY
Fukuoka, Japan
September, 2017

DEPARTMENT OF CIVIL AND STRUCTURAL ENGINEERING
GRADUATE SCHOOL OF ENGINEERING
KYUSHU UNIVERSITY
Fukuoka, Japan

CERTIFICATE

The undersigned hereby certify that they have read and recommended to the Graduate School of Engineering for the acceptance of this thesis entitled, "***Development of a practical system for simulating earthquake ground motions paying attention to volcanic zone and asperity on a fault***" by **Long Zhang** in partial fulfillment of the requirements for the degree of **Doctor of Engineering**.

Dated: September, 2017

Thesis Supervisor:

Prof. Guangqi CHEN, Dr. Sci.

Examining Committee

Prof. Taiji MAZDA, Dr. Eng.

Prof. Takayuki SHIMAOKA, Dr. Eng.

ABSTRACT

Earthquake ground motions measures, such as acceleration time series and peak ground acceleration (PGA), are important and necessary in earthquake engineering. Although these measures can be obtained from seismic observations, they need to be simulated for the regions where records were not available during a past earthquake or for a future potential earthquake. For example, acceleration time series and PGA are necessary in hazard assessment of landslides induced by a potential earthquake on a specific active fault. However, there is no practical simulation system established for this purpose.

The key issues in simulating earthquake ground motion are how to consider the source effect, path effect and site effect. Up to now, the effect of asperity, one of the important factors in estimating source parameters, and the effect of volcanic zone on estimating path parameters have not been well investigated. Also, how to estimate the site effect for the location without seismic sensors remains a not well solved problem although site amplification can be estimated by the seismic observations from both the surface and borehole sensors at the same station. For these reasons, this study aims at developing a practical system for simulating earthquake ground motions based on the so-called stochastic finite-fault method (SFFM), especially, paying attention to volcanic zone and asperity. The system consists of four modules: (1) a module for estimating the site amplification based on a method developed even for the location without strong ground-motion observations; (2) a module for estimating shear-wave attenuation based on a new analysis approach which can distinguish non-volcanic zone from volcanic zone; (3) a module for estimating slip distribution field by considering the characteristics of the asperity on a fault; (4) the SFFM module for calculating ground motions. Also, the system is applied to simulate the PGA distribution for landslide hazard assessment in Aso-bridge region, Kumamoto, Japan. It is shown that the assessment accuracy is improved using the simulated PGA than the conventional assumed PGA by comparing with the landslides induced by the 2016 Kumamoto earthquake.

This thesis consists of the following chapters.

Chapter 1 introduces the background and objectives of the thesis. The needs and applications of ground-motion measures in earthquake engineering are introduced. Two popular methods for the generation of simulated acceleration time series are reviewed and their strengths and limitations are briefly summarized. The organization of the thesis is shown at the end of this chapter.

Chapter 2 reviews the stochastic finite-fault method in detail. The principle of the stochastic finite-fault method is introduced. Three key issues mentioned above are clearly addressed.

Chapter 3 develops a method for estimating the site amplification in considering site effects. Seismic site effects are related to the amplification of seismic waves in surficial geological layers. Firstly, a module is made for calculating site amplifications based on the spectral ratios between acceleration waves recorded by surface and borehole sensors in the same station. The site amplifications of 53 KiK-net stations in Kyushu region are calculated. And then, in order to estimate the site amplification for the location without strong motion records, an empirical relationship between site amplification and V_{S30} (a parameter of time-averaged shear-wave velocity to 30 m) is established. Since V_{S30} is one of the widely-used measures and can be accessed in a regional scale, it is possible to estimate the site amplification just based on V_{S30}. By comparing the estimated results with those directly calculated from the records of both surface and borehole sensors, the good agreement shows the developed method is reasonable and adaptable.

Chapter 4 proposes a method for determining the path parameter Q_s (the *S*-wave attenuation) by considering the volcanic effect. Q_s values are usually estimated without distinguishing non-volcanic zone from volcano zone. In fact, it has been reported that there is a higher Q_s in the non-volcanic area of a region with active volcanoes relative to the normal values. Therefore, how to clarify the lateral Q_s heterogeneities effect on the ground motions and how to estimate Q_s in such regions are important issues. In this chapter, a method for calculating Q_s by considering volcanic effect is presented and validated by simulating ground motions of 9 non-volcanic records from the 2016 Kumamoto earthquake. It has been shown that the accuracy of simulated ground motions is improved by using the proposed method. A module for estimating Q_s is developed based on the proposed method.

Chapter 5 discusses the accuracy of the PGA simulated by using the slip distributions inversed from different kinds of data. The slip distribution field is one of the critical source parameters and it is related to the pattern, dimension and location of the asperity. Since the asperity of an earthquake can be inversed from the following three kinds of data: regional strong ground-motion data, teleseismic body-wave data, and geodetic GPS data, it is not clear which one can provide better results. By a lot of practical comparisons, it is found that the accuracy of simulated PGA based on anyone of the three kinds of slip distribution field is not good enough. Thus, a combination of the three results is proposed. It has been shown that the accuracy of the simulated PGA based on the combination analysis is much improved by practical simulations.

Chapter 6 improves an approach for estimating the slip distribution field of a potential earthquake on a specific fault. Many earthquake engineering problems need to estimate seismic waves from an expected future earthquake. Since the slip distribution field before an earthquake occurs is unknown, the method proposed above cannot be applied. For this reason, an approach is improved for estimating the asperity on a specific fault for an expected magnitude of the potential earthquake. The slip distribution field is then obtained by using the assumed probability distribution in the asperity and rupture area. By analyzing 17 shallow crustal earthquakes in Japan from 1995 to 2016, it is found that a rectangle-ellipse asperity can be assumed. The scaling relations of asperity versus seismic moment are investigated, and empirical formulas are statistically obtained for estimating the dimension and location of the asperity. This approach is validated by the ground-motion simulations of the 2016 Kumamoto earthquake. A module for estimating asperity and slip distribution field is developed based on the improved approach.

Chapter 7 develops a system by combining the SFFM module for calculating ground motions with the other three modules and presents an application of the developed practical system to the hazard assessment of landslides induced by a potential earthquake on a specific fault. In conventional landslide hazard mapping, an approximate PGA value for an area is used, which makes the accuracy very low. In this study, the PGA for each mesh is calculated based on the slip distribution field of the target earthquake on a specific fault by using the developed system. Slope stability analysis is carried out using the PGA of each mesh in landslide hazard mapping. Thus, a landslide hazard map related to a potential earthquake on a specific fault can be made. A landslide hazard map induced by an assumed M7.0 earthquake on the Futagawa fault is made. It is shown that the assessment accuracy is improved using the simulated PGA than the conventional assumed PGA by comparing with the landslides induced by the 2016 Kumamoto earthquake.

Chapter 8 summarizes the conclusions of the thesis, and makes recommendations for future work.

ACKNOWLEDGMENTS

The last few days have been full of emotion for me! Accomplishing one of my biggest study career goals and being recognized for what I believe is achieving my Ph.D. degree in Kyushu University. I would like to show my hearty thanks to the following people. Without their help, it is impossible to complete this thesis.

I would like to express profound gratitude to my supervisor, Prof. Guangqi Chen, for his continuous support, encouragement and suggestions throughout my doctoral course. I am grateful he provided me the opportunity to be a member of his group and trusting in me. During the past three years at Kyushu University, I benefit a lot from his patient guidance, rich knowledge, great dedication and boundless enthusiasm. Besides, he is a perfect model of being a scientific researcher and professor. Great thanks goes to him for spending the time to advise many good ways to improve and revising this work thoroughly. His suggestions make this thesis fruitful.

I would like to express my gratitude to the committee members and examiners of this thesis, Prof. Taiji Mazda and Prof. Takayuki Shimaoka, for carefully revising and providing great comments on the manuscript, and for their encouragement and support.

A special thanks goes to all the faculty and staff in the department of civil and structural engineering, Kyushu University, and also to the education section of Consulate-general of the People's Republic of China in Fukuoka. Their great help aids me to adapt the life in Japan. This thesis was supported financially by the China Scholarship Council (CSC). This financial support is gratefully acknowledged.

My thanks are owed to assist. prof. Haruko Seikiguchi, Yukitoshi Fukahata from Kyoto University and Reiji Kobayashi from Kagoshima University, for providing me with the slip distributions they inversed. Dr. Hadi Ghofrani from UWO and Olga-Joan Ktenidou from University of Greenwich, for kind explanations about the details of their work. I express my thanks to Dr. Adrien Oth from ECGS for sharing the GIT code with me.

I was lucky enough to get to know some special and great persons, who have encouraged me, listened to my complaints, shared my happiness and pain, and helped me to insist on my life: Zhiyi Zhang, Muye Yang. My fellow students and colleagues at the lab of geo-disaster prevention, including Yingbin Zhang, Yange Li, Hong Zhang, Zheng Han, Fusong Fan, Peideng Jing, Suhua Zhou, Wei Wang, Chenwen Cai, Hui Niu, Zhujun Li and Ahmad Qasim Akbar. They have supported me beyond anything I could have imagined. I will always have great pride and love for the chance to be a part of you.

Finally, I would owe my greatest thanks to my parents, my sister and my wife. Their constant support, encouragement and love throughout everyday support me continue to pursue my life goal without any hesitation. I have grinded and hustled for THANK YOU from the bottom of my heart.

TABLE OF CONTENTS

LIST OF FIGURES

LIST OF TABLES

CHAPTER 1

INTRODUCTION

1.1 BACKGROUND

Earthquake is a sudden and quick shaking of the ground surface caused by rupture and movement of the rock in the crust and mantle (Varazanashvili et al. 2012; Walker et al. 2013; Han et al. 2015; Badawy et al. 2017; Villar-Vega and Silva 2017). There are three major seismic belts around the world, the circum-Pacific belt, the Alpine-Himalayan orogenic belt and the Mid-Ocean Ridge seismic zone. Among them, about 90% of the global earthquakes and 81% of the world largest earthquakes occurred in the circum-Pacific belt.

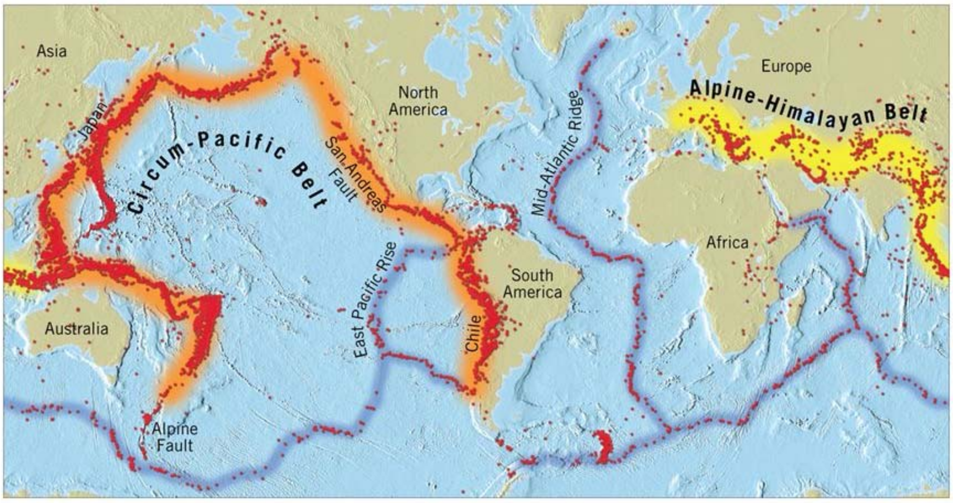

Figure 1-1 Global seismic belts (access from internet)

The earthquake ground motions, as the direct triggering force of geo-disasters and seismic load of collapsed engineered structures (Khazai and Sitar 2004; Baker and Cornell 2006; Meunier et al. 2008; Bose et al. 2016; Han et al. 2016), are the most interesting targets of seismologists and earthquake engineers. With the rapid development of economy, geo-disaster prevention and earthquake-resistant design play more and more important roles in the earthquake-induced hazard mitigation and reduction of fatalities and economic loss caused by catastrophic earthquakes. Therefore, the researches on earthquake ground motions attract more attention of geotechnical engineering scientists. Among such studies, the development of ground-motion simulation method is the most important and necessary.

Most of large earthquakes let people suffer huge loss, however, seismologists and engineers have never given up and proceeded to have research on ground motions. Fortunately, the past earthquakes provide us very rich information and encourage us to explore the mechanism of earthquakes.

1.1.1 EARTHQUAKE DAMAGES

A large earthquake usually causes so much loss, not only for fatalities but economic loss. In the past 5 centuries, over 8 million people have died due to earthquakes and their related geo-disasters, especially for the megathrust earthquakes. For example, the 2008 Wenchuan, China earthquake, and 2010 Haiti earthquake, caused about 87,000 and 220,000 fatalities, respectively (Hubbard and Shaw 2009; Gorum et al. 2013; Holzer and Savage 2013). Figure 1-1 lists the major catastrophic earthquakes occurred in the past two decades around the world.

Table 1-1 Catastrophic earthquakes in past two decades

Event	Date /County	fatalities	Economic loss	Reference
Haiti Earthquake	2010/1/12 Haiti	220,000	$14 billion	www.wikipedia.org
Christchurch Earthquake	2011/02/22 NewZealand	185	$40 billion	www.wikipedia.org
Wenchuan Earthquake	2008/05/12 China	87,587	$148 billion	www.wikipedia.org
Indonesian Earthquake	2004/12/26 Indonesia	230,000	$29 billion	www.wikipedia.ord
Tohoku Earthquake	2011/03/11 Japan	15894	$300 billion	Cabinet office of Japanese Government, 2011
Kumamoto Earthquake	2016/04/15 Japan	110	$22 billion	Cabinet office of Japanese Government, 2016

Only a small part of fatalities died from the earthquake itself, that is, the strong ground shaking and the rift of the surface. Most of the fatalities and economic loss, on the one hand, are caused by the subsequent geo-hazards, such as landslides, liquefaction, and tsunami, etc. (Guzzetti 2000; Lay et al. 2005; Nadim et al. 2006; Marano et al. 2010; Mori et al. 2011). Figure 1-2 shows the New Beichuan Middle School landslide, which is induced by the 2008 Wenchuan earthquake. It is reported that 1600 people were killed by this severe landslide, and the economic loss reached up to 35.5 million U.S. dollar (Huang et al. 2009; Sato and Harp 2009; Yin et al. 2009). Therefore, it is important and urgent to perform landslide hazard mitigations, e.g. landslide susceptibility assessment. The landslide hazard assessment provides an evaluation for landslide susceptibility regions where landslides are prone to be triggered by a potential earthquake occurs on a specific fault, which is effective to help government make decisions for mitigating landslide hazards.

On the other hand, the collapsed and damaged buildings and infrastructures are not too “strong” enough to resist the ground shaking. For some developing countries and regions, poor construction levels and inadequate seismic design codes caused numerous fatalities who died from the collapsed or damaged houses (Glass et al. 1977; Bird and Bommer 2004; Martin et al. 2015). For example, it is reported that more than 5 million people lost their houses during the 2008 Wenchuan earthquake (Ye et al. 2008; Cui et al. 2011). Figure 1-3 shows the collapsed buildings caused by 2008 Wenchuan earthquake. To avoid these devastating accidents, structural engineers should estimate the seismic effect under given levels of intensity measures using dynamic or static methods.

Figure 1-2 Image of the New Beichuan Middle School landslide induced by the 2008 Wenchuan Earthquake, China. Source from NASA.

Figure 1-3 Image of collapsed buildings during 2008 Wenchuan China earthquake. (access from internet)

1.1.2 APPLICATIONS OF SIMULATED GROUND MOTIONS TO EARTHQUAKE ENGINEERING

In order to mitigate geo-hazards and collapsed buildings induced by large earthquakes, earthquake ground motions should be utilized to perform geo-hazard assessment and engineered structure stability evaluation (Wilson and Keefer 1983; Shou and Wang 2003; Wright and Rathje 2003; Idriss and Boulanger 2006; Jibson 2011; Takatani and Nishikawa 2017; Wang et al. 2017a).

One of the most important applications of acceleration time series is the geo-hazard prevention. Generally speaking, in classical mechanics, the movement of bodies is controlled by the force applied on them (Strogatz 2014). The motion of geological unit is also without exception. Since complicated reasons of the occurrence of geo-hazards, it is very difficult to describe the movement of rock using analytical equations accurately (McDougall and Hungr 2004; Yoshimatsu and Abe 2006; Wu 2010). With the rapid development of computer science, numerical methods grow to be the major techniques to analyze the stability of geological unit. Among these geo-hazards, landslide and liquefaction are the two of most devastating disasters (Quigley et al. 2013; Rajendran et al. 2016; Tuttle et al. 2017). More attention is paid for them to mitigate the fatalities and economic loss during the recent years.

During a devastating earthquake, the strong ground shaking makes the soil subject to the high strain level, which is the major reason of the occurrence of liquefaction (Papathanassiou et al. 2015; Bastin et al. 2016; Carey et al. 2017). Ground failure induced by liquefaction is one of the most important reasons of structural damage during a severe earthquake (King et al. 2014; Towhata et al. 2014; Baziar and Rostami 2017). Numerous structures, such as nuclear plants, bridges, and residential buildings are threatened by liquefaction as strong ground shaking happens (Van Ballegooy et al. 2014; Villamor et al. 2016).The most widely-used method to assess the liquefaction susceptibility is the simplified method (Seed and Idriss 1971; Seed 1979; Seed and Idriss 1982). In this method, the factor of safety against liquefaction (F_L) is defined by the equation as follows,

$$F_L = \frac{CRR}{CSR / MSF}, \tag{1.1}$$

where CRR is cyclic shear resistance ratio, CSR is the cyclic shear stress ratio, and MSF is magnitude scaling factor. The expression of CSR is defined as follows,

$$CSR = 0.65\frac{a_{\max}}{g}\left(\frac{\sigma_{v0}}{\sigma'_{v0}}\right)\times r_d, \tag{1.2}$$

where $a_{\max}$ is the horizontal peak ground acceleration (PGA), g is the acceleration of gravity, σ_{v0} is the total overburden pressure, σ'_{v0} is the effective overburden pressure at the same depth, and r_d is the stress reduction coefficient. Figure 1-4 shows the liquefaction hazard map of Vijayawada city, India. As one of the most important variables, $a_{\max}$ is critical for evaluating liquefaction susceptibility. Therefore, the earthquake ground motion, which is specified as PGA in this case, should be estimated as accurate as possible for a future potential earthquake.

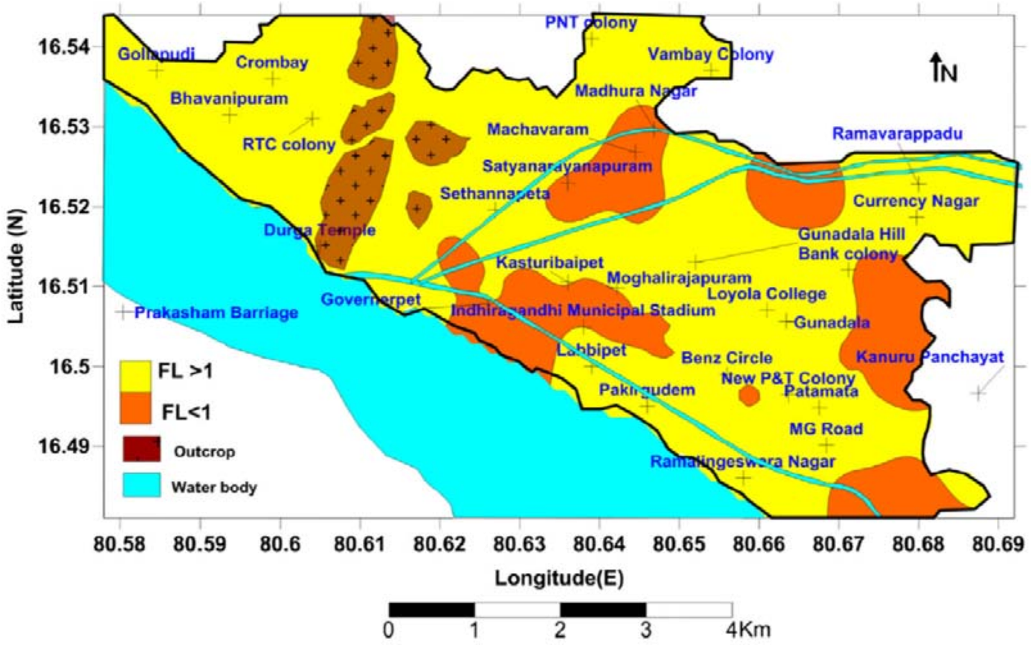

Figure 1-4 Liquefaction hazard map of Vijayawada city, India (after Satyam and Towhata (2016))

The other important application of earthquake ground motions to geo-hazard prevention is to evaluate the slope stability. Evaluating the stability of a slope and estimating the landslide run-out distance under the consideration of a seismic load are crucial for landslide hazard assessment and mitigation (Zhang et al. 2015; Sepúlveda et al. 2016; Cui et al. 2017). However, for a single slope, it is not easy to describe the displacement by an analytical function (Yang and Long 2015; Zhou et al. 2015; Zhang 2017). Therefore, as one of the most popular numerical methods, the discontinuous deformation analysis (DDA) method has been used to model the dynamic process for single slope (Zhang et al. 2016a; Jing et al. 2017; Wang et al. 2017c; Zhang et al. 2017). For example, Jing (2016) develops a practical 3D DDA program considering the seismic loading for landslide hazard assessment (Figure 1-5). To evaluate the slope stability under the consideration of a potential earthquake, a simulated acceleration time series should be provided.

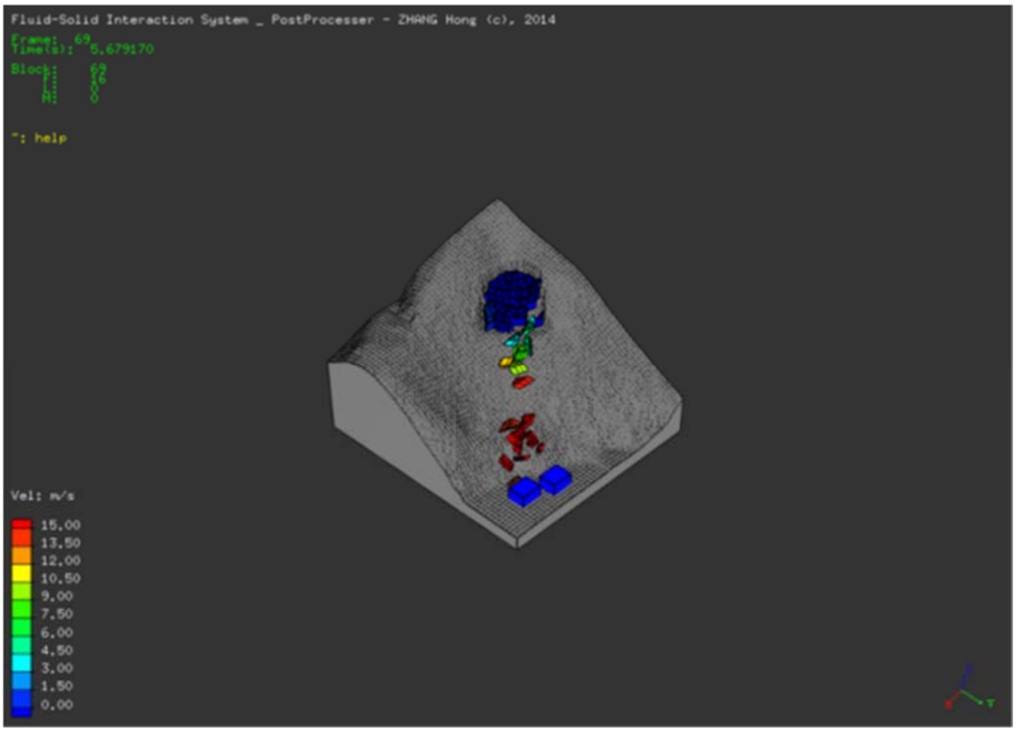

Figure 1-5 The final image of failure process of Daiganji slope under a seismic loading (after Jing (2016))

The other target of landslide hazard assessment is to evaluate the landslide susceptibility for a region. A large earthquake will induce thousands, even tens of thousands landslides in mountainous region (McPhillips et al. 2014; Xu et al. 2014; Liu et al. 2016). GIS-based landslide hazard mapping technique has been widely-used for identifying landslide susceptibility zones where landslides are prone to happen in a future earthquake (Chousianitis et al. 2016; Gaprindashvili and Van Westen 2016; Zhou et al. 2016a; Zhou et al. 2016b). A physically-based model to evaluate regional landslide susceptibility which using the PGA to represent the seismic loading is proposed and illustrated in Figure 1-6 (Zhou 2016). In the model, the factor of safety against landslide is defined in the following form,

$$F_s = \frac{c' + \left[(\gamma - n\gamma_w) H \cos\alpha - k_s \gamma H \sin\beta / g \right] \tan\varphi'}{\gamma H \sin\alpha + k_s \gamma H \cos\beta / g} \tag{1.3}$$

where c' is the soil cohesion, γ and γ_w are unit weight of sliding mass and groundwater, respectively, n is the percentage of saturated failure thickness, H is the slope normal thickness of the failure surface, α is the slope gradient, β is the angle between the ground surface and the incident direction of the seismic force, φ' is the friction angel of soil, k_s is the seismic coefficient, g is the acceleration of gravity. For equation (1.3), the numerator represents the resisting force while the denominator is the driving force. It is easy to identify the landslide prone region, of which the F_s is lower than 1, and vice versa.

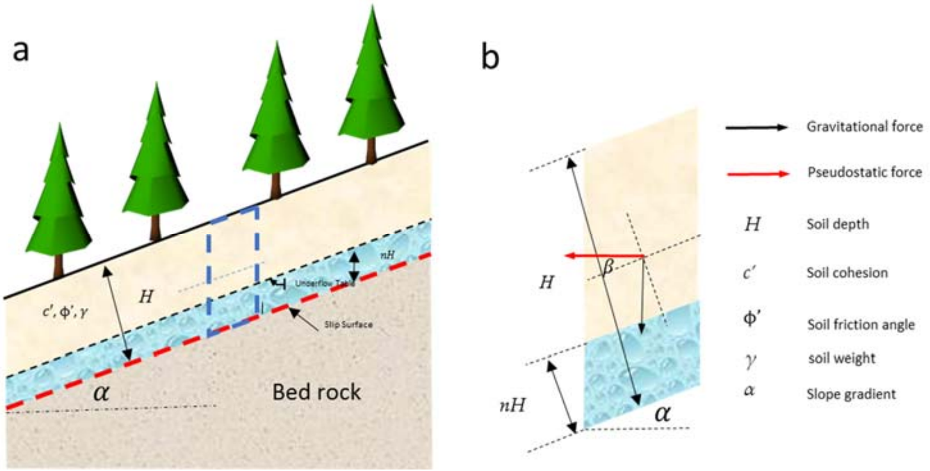

Figure 1-6 (a) Limit equilibrium analysis method for infinite slope considering a seismic force; (b) Force analysis of unit soil slice (dash rectangle in the panel (a)) (after Zhou (2016))

On the other hand, structural engineers usually use earthquake ground motions (e.g. acceleration time series or response spectra) as the intensity measures for analysis of structural response (Chen et al. 2016; Chopra and McKenna 2016; Seifried and Baker 2016; Sonmez et al. 2016). For example, Rossetto (2006) performs complicated dynamic inelastic time history finite element analyses of important buildings (Figure 1-7).

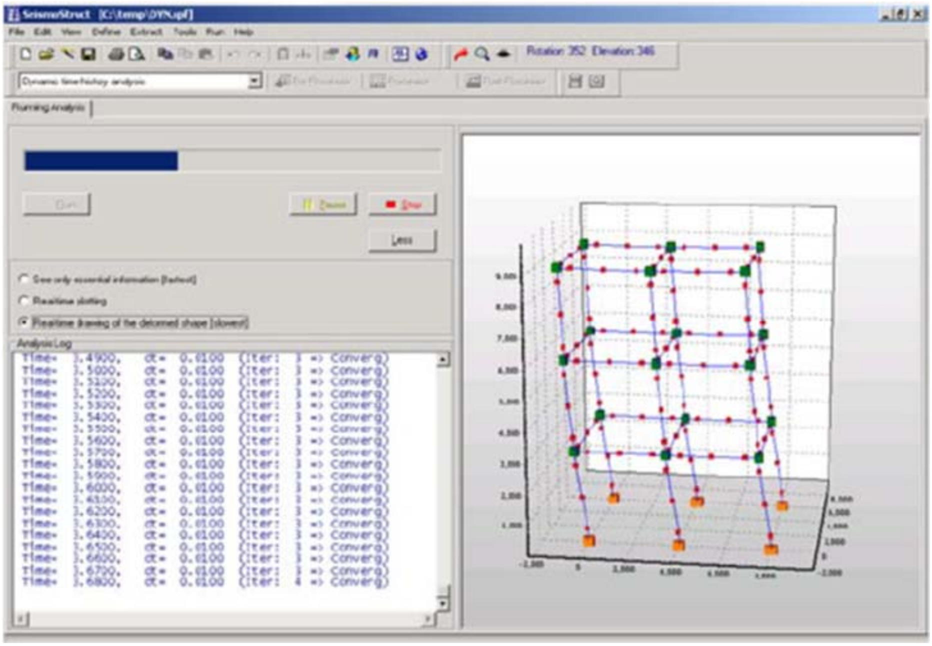

○ See only essential information [fastest]
○ Realtime plotting
● Realtime drawing of the deformed shape [slowest]

```
Time= 3.4900,   dt= 0.0100  (Iter: 3 => Converg)
Time= 3.5000,   dt= 0.0100  (Iter: 3 => Converg)
Time= 3.5100,   dt= 0.0100  (Iter: 3 => Converg)
Time= 3.5200,   dt= 0.0100  (Iter: 3 => Converg)
Time= 3.5300,   dt= 0.0100  (Iter: 3 => Converg)
Time= 3.5400,   dt= 0.0100  (Iter: 3 => Converg)
Time= 3.5500,   dt= 0.0100  (Iter: 3 => Converg)
Time= 3.5600,   dt= 0.0100  (Iter: 3 => Converg)
Time= 3.5700,   dt= 0.0100  (Iter: 3 => Converg)
Time= 3.5800,   dt= 0.0100  (Iter: 3 => Converg)
Time= 3.5900,   dt= 0.0100  (Iter: 3 => Converg)
Time= 3.6000,   dt= 0.0100  (Iter: 3 => Converg)
Time= 3.6100,   dt= 0.0100  (Iter: 3 => Converg)
Time= 3.6200,   dt= 0.0100  (Iter: 3 => Converg)
Time= 3.6300,   dt= 0.0100  (Iter: 3 => Converg)
Time= 3.6400,   dt= 0.0100  (Iter: 3 => Converg)
Time= 3.6500,   dt= 0.0100  (Iter: 3 => Converg)
Time= 3.6600,   dt= 0.0100  (Iter: 3 => Converg)
Time= 3.6700,   dt= 0.0100  (Iter: 3 => Converg)
Time= 3.6800,   dt= 0.0100  (Iter: 4 => Converg)
```

Figure 1-7 Complicated dynamic inelastic time history finite element analysis of a structure (after Rossetto (2006))

In a word, earthquake ground motions measures, such as acceleration time series and peak ground acceleration (PGA), are important and necessary in earthquake engineering and geo-disaster prevention engineering. Although these measures can be obtained from seismic observations, they need to be simulated for the regions where records were not available during a past earthquake or for a future potential earthquake. For example, acceleration time series and PGA are necessary in hazard assessment of landslides induced by a potential earthquake on a specific active fault. With the development of economy and the boost of population, earthquake ground motion simulations are growing to be more and more important and necessary.

1.2 METHODOLOGIES OF SIMULATING ACCELERATION TIME SERIES

With the rapid development of seismology during the past few decades, several ground-motion simulation methods boost. They are grown to be the most powerful tools for theoretical studies of earthquake engineering, earthquake-resistant design and geo-disaster prevention. Many scientists contribute to this research field and achieve fruitful work. In general, such methods can be classified into two major kinds, one is the deterministic method, including theoretical and empirical Green's function methods (Hartzell 1978; Irikura 1983, 1986; Joyner and Boore 1986; Dan et al. 1989; Oth et al. 2007); the other is the stochastic method, including point-source and finite-fault methods (Boore 1983; Beresnev and Atkinson 1997, 1998; Boore 2003; Motazedian and Atkinson 2005; Boore 2009; Boore and Thompson 2014; Atkinson and Assatourians 2015; Boore and Thompson 2015). In the next two sections, the theory of both kinds of method and their strengths and limitations will be introduced and summarized.

1.2.1 THE DETERMINISTIC METHOD

The deterministic method is composed of theoretical and empirical Green's function methods. In the theoretical method, seismogram is calculated by representation theorem, which transfers this issue to determine the source-time function and the Green's function (Aki 1968; Haskell 1969). The source-time function is usually shown as a form of ramp or exponential function (Aki and Richards 2002). The prior of determining the response of the real earth material from a point-source dislocation, that is, the Green's function, is assuming the earth as a homogeneous layered elastic half-space model (Hisada and Bielak 2003; Hartzell et al. 2005). However, real earth does not always consist of horizontal layered materials (Woodhouse and Dziewonski 1984; Su et al. 1994). Therefore, the 3D heterogeneous structural Green's function should be determined. On the other hand, the second prior is the requirement of 3D seismic-wave velocity structure and the local site information (Ritsema et al. 1999; Shapiro et al. 2005; Sato et al. 2012). In general, it is difficult to clear these information, so as to hard to specify the path and site effects. Both limitations mentioned above restrict its development and applications (Hartzell et al. 1999; Miyake et al. 2003).

Since the seismic-wave velocity structure and local site information are not easy to obtain (Chiu et al. 1986; Quan and Harris 1997; Panning and Romanowicz 2006), is there any wave to represent both of them by observed ground motion records? Such idea stimulates Hartzell (1978) to propose the empirical Green's function method. Hartzell (1978) considers small-event records as the Green's function, and sums the records to synthesize the ground motions of large earthquakes. The advantage of this method is the usage of small-event records which cover almost all the complicated factors, such as the rupture process of the source, the heterogeneous geological structures and local site information (Baltay et al. 2014; Abercrombie 2015; Mourhatch and Krishnan 2015). It is not easy to estimate such factors in existing manner. Irikura (1983) extends the empirical Green's function method by considering the similarity of the observed small-event and simulated large earthquake. The schematic figure of this method is illustrated in Figure 1-8. The fault areas of the mainshock and aftershock are defined as $L \times W$ and $l \times w$, respectively, which meets $L/l = W/w = N$.

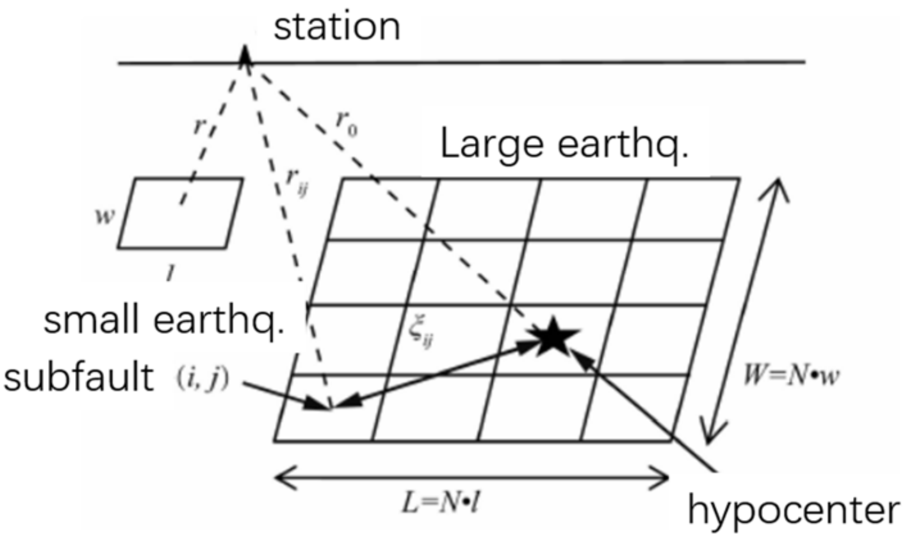

Figure 1-8 Schematic illustration of the empirical Green's function method

The basis of this method is assuming the ground motion from the large earthquake equals to the summation of ground motions from a suit of subsources. The small-event records, usually the aftershock or foreshock records, are regarded as the ground motions of each subsource. The equation of summation is shown as follows,

$$U(t)=\sum_{i=1}^{N}\sum_{j=1}^{N}\frac{r}{r_{ij}}F(t)[\mathrm{C}\cdot u(t)], \tag{1.4}$$

where $U(t)$ is the simulated large-event record, $u(t)$ is the observed small-event record, $F(t)$ is the correction function for adjusting the difference of source-time functions of small- and large-events, r and r_{ij} are the distance from source of small earthquake and ijth subsource of the large earthquake to the observation point, respectively.

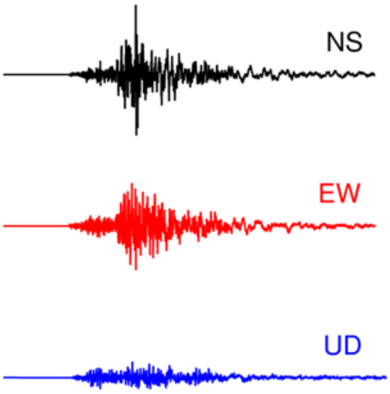

Figure 1-9 Three-component records

The empirical Green's function method has been used for the ground-motion simulations of some earthquakes (Kamae and Irikura 1998; Kamae et al. 2005; Suzuki et al. 2005; Kurahashi and Irikura 2011). The merit of the empirical Green's function method is three-component records can be simulated for each station (Figure 1-9). Since three-component records can be observed for a small earthquake, the acceleration time series in three components of the large earthquake can be simulated by adjusting and summing the corresponding component record of the small earthquake. The directivity effect of the seismic wave can be investigated by this method, because three-component records can be simulated.

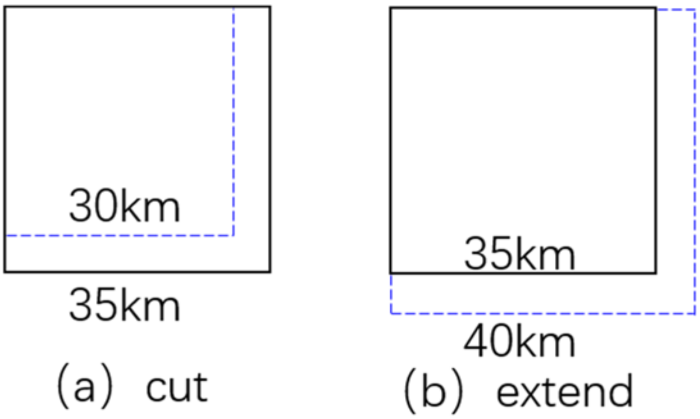

Figure 1-10 Different strategies to adjust the length of the mainshock fault

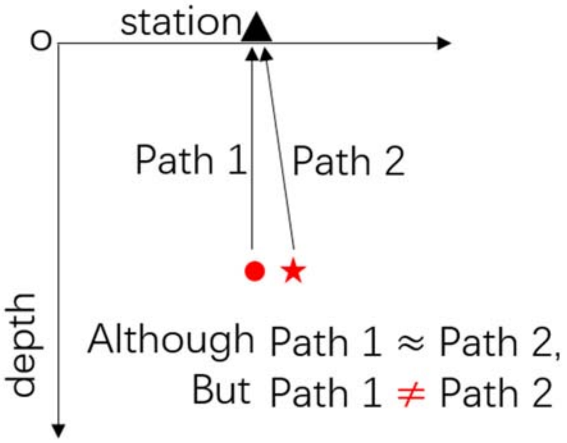

Figure 1-11 The different path effects of the large and small earthquakes. Star and circle represent the sources of the large and small earthquakes, respectively

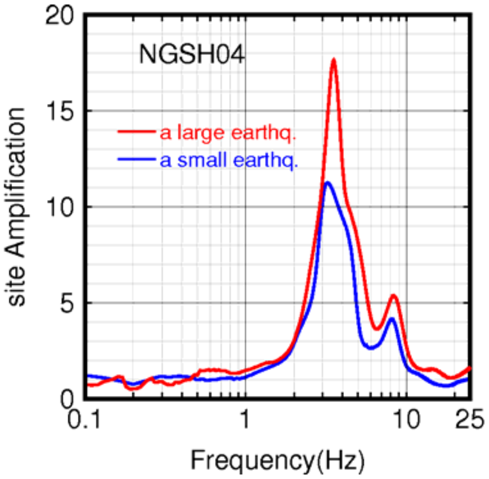

Figure 1-12 The different site effects of the large and small earthquakes

However, the empirical Green's function method also has some demerits. Firstly, the path and site effects of the large and small earthquakes are assumed to be the same, but they are not (Dreger 1994; Ordaz et al. 1995; Courboulex et al. 1996; Pavic et al. 2000). The hypocentre of the selected small earthquake should be close to that of the large earthquake, which ensures the path effects of them are the same (Aki 1972; Kanamori and Anderson 1975). Although in simulation the path and the mainshock are assumed to be the same with those of the selected small earthquake, they have some differences (Figure 1-11). For the site effect, the responses of a target site to the large and small earthquakes are generally different (Figure 1-12). For a soft soil site, the site amplification calculated from a large-earthquake record is larger than that of a small earthquake. Secondly, the times of summation for the small earthquake records are dependent of the researcher's experience, which cause the differences in the simulation results (Hutchings and Wu 1990; Mori and Frankel 1990; Hough et al. 1991; Irikura and Kamae 1994). The fault length ratio of the large and small earthquakes are required to be an integer in the method. Some empirical modifications of the fault geometry, such as extension or clip, should be done, which depends on the researcher's experience (Figure 1-10) (Pacheco et al. 1992; Dalguer et al. 2008). For example, in Figure 1-10, the lengths of fault of the large and small earthquake are assumed to be 35 km and 10 km, respectively. The ratio of them doesn't equal to an integer. Different researcher's will select different strategies, such as cutting or extending the fault plane, which are dependent of their own experiences. These empirical operation will result in different simulation results. Therefore, the assumptions of the empirical Green's function method are still controversial.

1.2.2 THE STOCHASTIC METHOD

The stochastic method can be classified into point-source method and finite fault method (Atkinson et al. 2009). For the far-field ground-motion simulations, both methods perform similarly. While for the near-field ground-motion simulations, the finite-fault method performs better since the fault surface cannot be regarded as a point source (Wang et al. 2015). The major objective of this thesis is to develop a practical system of simulating ground motions for landslide hazard assessment. In general, a slope under a seismic loading with the PGA value larger than 300 cm/s^2 is prone to be unstable (Miles and Ho 1999; Dai et al. 2002; Van Westen et al. 2008; Xu et al. 2012). This threshold corresponds to a distance range of 0-20 km which is usually considered as near field (Reasenberg and Simpson 1992; Bozorgnia et al. 1995; Larson et al. 2003). Therefore, the stochastic finite-fault method is selected as the tool to perform the ground-motion simulations.

Compare to the deterministic method, the stochastic method shows more merits. Firstly, it is originated from the theoretical derivation for the dislocation of a point source, which has a strong theoretical basis. Secondly, The source, path, and site effects are separately defined to describe the seismic-wave propagation clearly. (Motazedian and Atkinson 2002; Motazedian and Moinfar 2006; Poggi et al. 2011). Thirdly, in this method, the source, path and site processes of the seismic-wave propagation are specified using several meaningful geophysical parameters, such as site amplification, shear-wave (S-wave) attenuation and slip distribution, etc. These parameters can be extracted from the strong ground-motion records. The advantages of the observation data can be shown as much as possible. (Hartzell et al. 1999). The specific theory and equations of finite-fault method for synthetizing acceleration time series will be introduced in next chapter in detail.

In the stochastic finite-fault method, the source, path, and site effects should be considered to establish the Fourier spectrum and then to determine the acceleration time series. If the methods to determine the high-accuracy parameters are not established, it is hard to say that a practical simulation technique is developed. Until now, the effect of asperity, one of the important factors in estimating source parameters, and the effect of volcanic zone on estimating path parameters have not been well investigated when performing the ground-motion simulation (Somerville et al. 1999; Murotani et al. 2008). Also, how to estimate the site effect for the location without seismic sensors remains a not well solved problem although site amplification can be estimated by the seismic observations from both the surface and borehole sensors at the same station.

For the site effect, the site amplification should be considered in the ground motion simulation. On the one hand, for the area with strong ground-motion stations, the site amplification can be determined based on the records of the seismic sensors on the surface and in the borehole. There are two commonly used method to estimate the site amplification, the S/B and H/V spectral ratios techniques (Satoh et al. 1995; Boore 2004; D'Amico and Mucciarelli 2002; Nath et al. 2008). Which is more suitable for the Kyushu region? On the other hand, for the area without strong ground motion stations, how to estimate site amplification is an important issue (Figure 1-13).

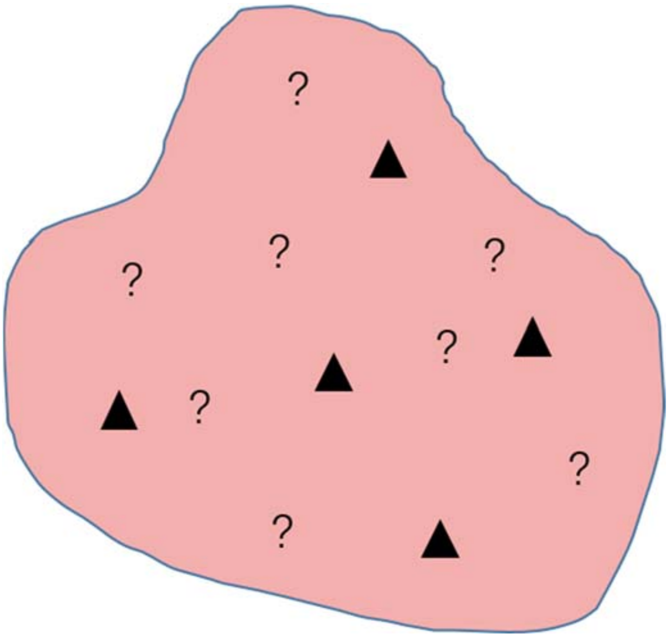

Figure 1-13 Schematic illustration of the estimation of site amplification in the region without strong ground-motion stations. Triangles represent the strong ground motion stations; question marks represent the region without stations.

For the path effect, the influence of volcano on the estimation of shear-wave attenuation (Q_s) has not been considered in the stochastic ground motion simulations. Many studies report that the Low-Q anomalies are observed beneath these volcanoes in the crust and the uppermost mantle, whereas the High-Q anomalies exist in the subduction of the Philippine Sea plate (Figure 1-14) (Yoshimoto et al. 2006; Arpa et al. 2013; Prudencio et al. 2015). For the volcanic zone, how does the Q_s heterogeneities influence on the ground motion simulations is an important issue.

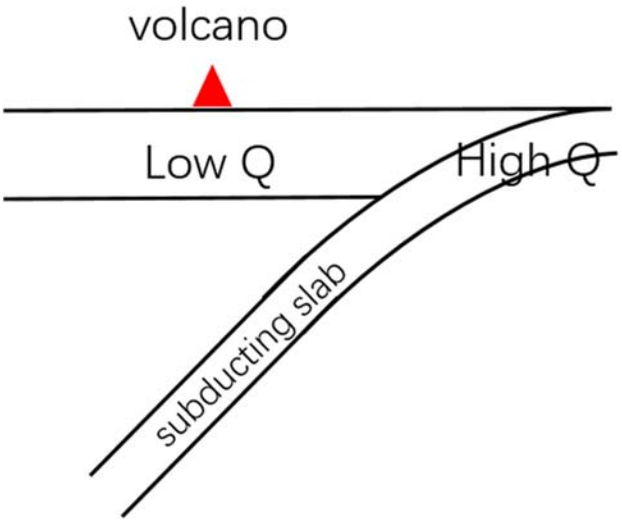

Figure 1-14 Schematic illustration of Q_s structure of the Kyushu region (refer from Pei et al, (2009))

For the source effect, the slip distribution field should be specified to simulate ground motions. On the one hand, for a past earthquake, three kinds of geophysical data are usually used for slip distribution field inversion (Yamanaka and Kikuchi 2003; Schmidt and Bürgmann 2006; Ji et al. 2015). Since the inversed asperities, the area with large slip amount on a fault plane, are not the same based on different data, the issue that which one will result in the most accurate simulation results should be clarified. On the other hand, for a future potential earthquake, the slip distribution field is unknown. The issue that how to establish the slip distribution field for a potential earthquake has not been well solved (Somerville et al. 1999; Murotani et al. 2008). For example, if a M7.0 earthquake occurs on the Futagawa fault (Figure 1-15), how will be the slip distribution field? Therefore, how to establish a slip distribution field for a potential earthquake occurs on a specific fault with an assumed magnitude is an important issue.

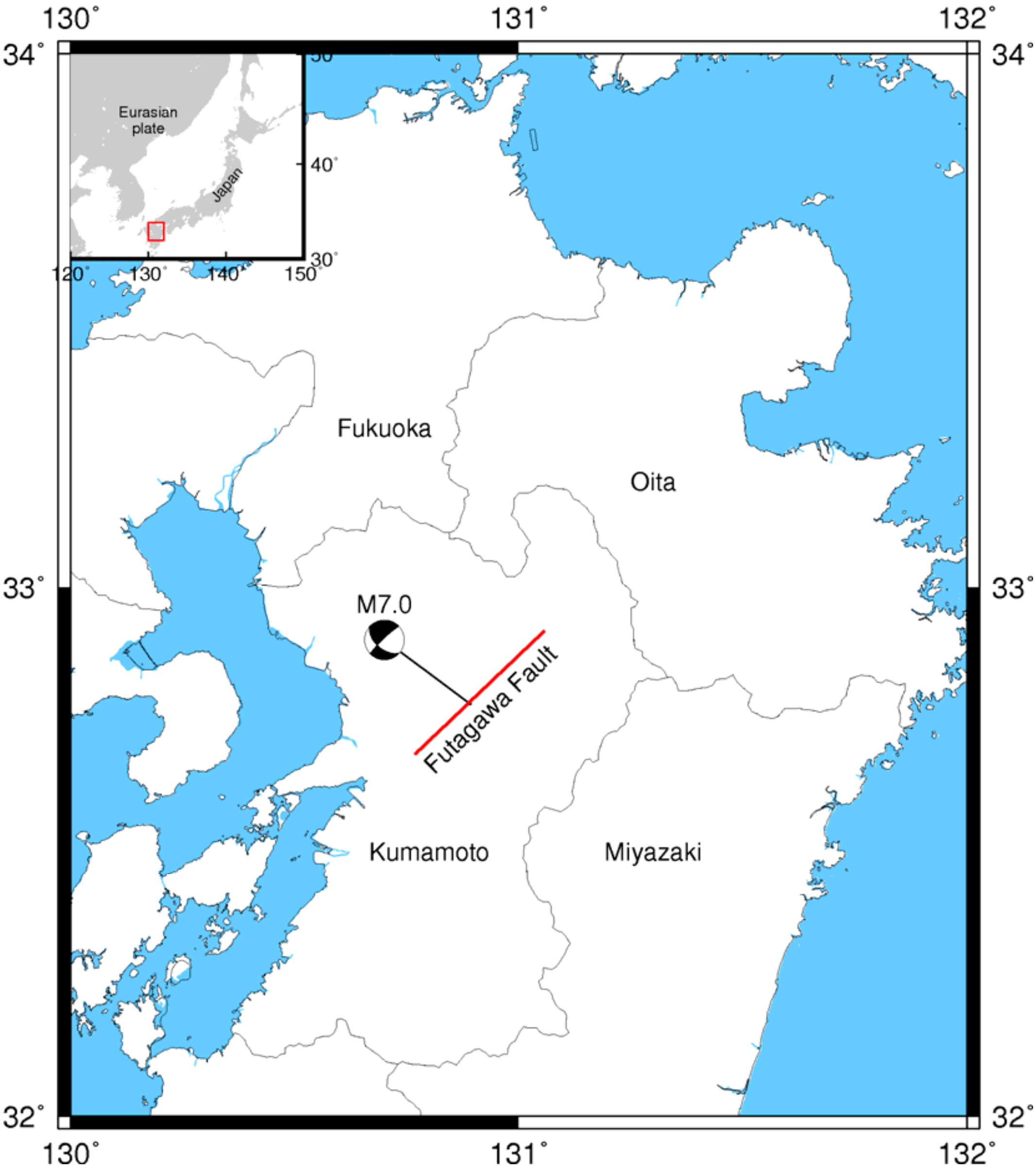

Figure 1-15 The locations of Futagawa fault and a potential earthquake with an assumed magnitude M7.0

1.3 SCOPE AND OBJECTIVES

This study aims at (1) developing a practical system for simulating earthquake ground motions based on the so-called stochastic finite-fault method, especially, paying attention to volcanic zone and asperity; (2) applying the new system to earthquake-induced landslide hazard assessment based on GIS-based hazard mapping. The following three key issues to be solved in the estimation of source, path and site parameters of the stochastic finite-fault method:

(i) how to estimate site amplification in the region without strong ground motion stations;

(ii) How to determine the S-wave attenuation Q_s considering the volcanic effect;

(iii) How to establish the slip distribution field for a potential earthquake occurs on a specific fault considering the effect of asperity.

In this thesis, these key issues are solved by using the developed methods, which are also made as three modules. A practical system is developed by combining the developed modules with the SFFM module to simulate ground motions paying attention to the volcanic zone and asperity on a fault. The flowchart of this system is shown as follows.

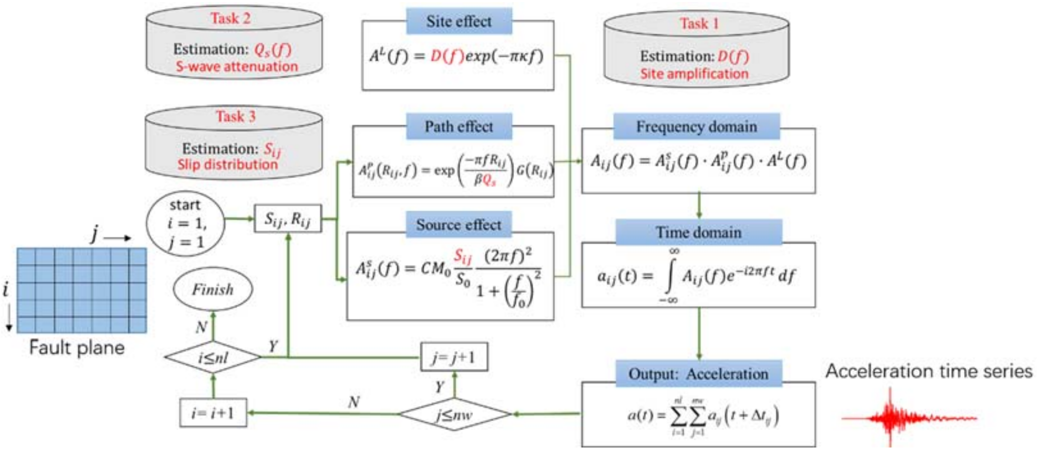

Figure 1-16 The flowchart of the developed practical system for simulating earthquake ground motions paying attention to volcanic zone and asperity on a fault

1.4 FRAMEWORK OF THE THESIS

This thesis consists of the 8 chapters. The framework of this thesis is shown in Figure 1-17 and introduced in detail as follows.

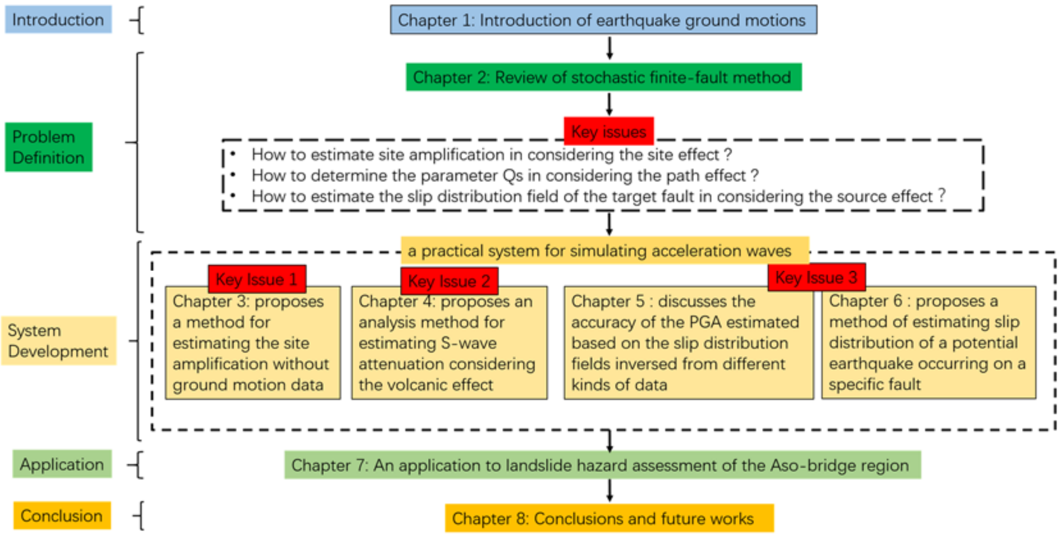

Figure 1-17 Framework of the thesis.

The thesis consists of the following chapters:

Chapter 1 introduces the background and objectives of the thesis. The needs and applications of ground-motion measures in earthquake engineering are introduced. Two popular methods for the generation of simulated acceleration time series are reviewed and their strengths and limitations are briefly summarized. The organization of the thesis is shown at the end of this chapter.

Chapter 2 reviews the stochastic finite-fault method in detail. The principle of the stochastic finite-fault method is introduced. Three key issues mentioned above are clearly addressed.

Chapter 3 develops a method for estimating the site amplification in considering site effects. Seismic site effects are related to the amplification of seismic waves in surficial geological layers. Firstly, a module is made for calculating site amplifications based on the spectral ratios between acceleration waves recorded by surface and borehole sensors in the same station. The site amplifications of 53 KiK-net stations in Kyushu region are calculated. And then, in order to estimate the site amplification for the location without strong motion records, an empirical relationship between site amplification and V_{S30} (a parameter of time-averaged shear-wave velocity to 30 m) is established. Since V_{S30} is one of the widely-used measures and can be accessed in a regional scale, it is possible to estimate the site amplification just based on V_{S30}. By comparing the estimated results with those directly calculated from the records of both surface and borehole sensors, the good agreement shows the developed method is reasonable and adaptable.

Chapter 4 proposes a method for determining the path parameter Q_s (the *S*-wave attenuation) by considering the volcanic effect. Q_s values are usually estimated without distinguishing non-volcanic zone from volcano zone. In fact, it has been reported that there is a lower Q_s in the region with active volcanoes relative to the normal values. Therefore, how to clarify the lateral Q_s heterogeneities effect on the ground motions and how to estimate Q_s in such regions are important issues. In this chapter, a method for calculating Q_s by considering volcanic effect is presented and validated by simulating ground motions of the 2016 Kumamoto earthquake. It has been shown that the accuracy of simulated ground motions is improved by using the proposed method. A module for estimating Q_s is developed based on the proposed method.

Chapter 5 discusses the accuracy of the PGA simulated by using the slip distributions inversed from different kinds of data. The slip distribution field is one of the critical source parameters and it is related to the pattern, dimension and location of the asperity. Since the asperity of an earthquake can be inversed from the following three kinds of data: regional strong ground-motion data, teleseismic body-wave data, and geodetic GPS data, it is not clear which one can provide better results. By a lot of practical comparisons, it is found that the accuracy of simulated PGA based on anyone of the three kinds of slip distribution field is not good enough. Thus, a combination of the three results is proposed. It has been shown that the accuracy of the simulated PGA based on the combination analysis is much improved by practical simulations.

Chapter 6 improves an approach for estimating the slip distribution field of a potential earthquake on a specific fault. Many earthquake engineering problems need to estimate seismic waves from an expected future earthquake. Since the slip distribution field before an earthquake occurs is unknown, the method proposed above cannot be applied. For this reason, an approach is improved for estimating the asperity on a specific fault for an expected magnitude of the potential earthquake. The slip distribution field is then obtained by using the assumed probability distribution in the asperity and rupture area. By analyzing 17 shallow crustal earthquakes in Japan from 1995 to 2016, it is found that a rectangle-ellipse asperity can be assumed. The scaling relations of asperity versus seismic moment are investigated, and empirical formulas are statistically obtained for estimating the dimension and location of the asperity. This approach is validated by the ground-motion simulations of the 2016 Kumamoto earthquake. A module for estimating asperity and slip distribution field is developed based on the improved approach.

Chapter 7 develops a system by combining the SFFM module for calculating ground motions with the other three modules and presents an application of the developed practical system to the hazard assessment of landslides induced by a potential earthquake on a specific fault. In conventional landslide hazard mapping, an approximate PGA value for an area is used, which makes the accuracy very low. In this study, the PGA for each mesh is calculated based on the slip distribution field of the target earthquake on a specific fault by using the developed system. Slope stability analysis is carried out using the PGA of each mesh in landslide hazard mapping. Thus, a landslide hazard map related to a potential earthquake on a specific fault can be made. A landslide hazard map induced by an assumed M7.0 earthquake on the Futagawa fault is made. It is shown that the assessment accuracy is improved using the simulated PGA than the conventional assumed PGA by comparing with the landslides induced by the 2016 Kumamoto earthquake.

Chapter 8 summarizes the conclusions of the thesis, and makes recommendations for future work.

REFERENCE

Abercrombie RE (2015) Investigating uncertainties in empirical Green's function analysis of earthquake source parameters. J Geophys Res 120, 4263-4277

Aki K (1968) Seismic displacements near a fault. J Geophys Res 73, 5359-5376

Aki K (1972) Scaling law of earthquake source time‐function. Geophys J Int 31, 3-25

Aki K, Richards PG, 2002. Quantitative seismology.

Atkinson GM, Assatourians K (2015) Implementation and validation of EXSIM (a stochastic finite‐fault ground‐motion simulation algorithm) on the SCEC broadband platform. Seismol Res Lett 86, 48-60

Atkinson GM, Assatourians K, Boore DM, Campbell K, Motazedian D (2009) A guide to differences between stochastic point-source and stochastic finite-fault simulations. Bull Seismol Soc Am 99, 3192-3201.doi:10.1785/0120090058

Badawy A, Korrat I, El-Hadidy M, Gaber H (2017) Update earthquake risk assessment in Cairo, Egypt. J Seismol 21, 571-589

Baltay AS, Beroza GC, Ide S (2014) Radiated energy of great earthquakes from teleseismic empirical Green's function deconvolution. Pure Appl Geophys 171, 2841-2862

Bastin SH, Bassett K, Quigley MC, Maurer B, Green RA, Bradley B, Jacobson D (2016) Late Holocene liquefaction at sites of contemporary liquefaction during the 2010–2011 Canterbury earthquake sequence, New Zealand. Bull Seismol Soc Am 106, 881-903

Baziar MH, Rostami H (2017) Earthquake Demand Energy Attenuation Model for Liquefaction Potential Assessment. Earthq Spectra 33, 757-780

Beresnev IA, Atkinson GM (1997) Modeling finite-fault radiation from the ωn spectrum. Bull Seismol Soc Am 87, 67-84

Beresnev IA, Atkinson GM (1998) FINSIM--a FORTRAN program for simulating stochastic acceleration time histories from finite faults. Seismol Res Lett 69, 27-32

Bird JF, Bommer JJ (2004) Earthquake losses due to ground failure. Eng geology 75, 147-179

Boore DM (1983) Stochastic simulation of high-frequency ground motions based on seismological models of the radiated spectra. Bull Seismol Soc Am 73, 1865-1894

Boore DM (2003) Simulation of ground motion using the stochastic method. Pure

Appl Geophys 160, 635-676

Boore DM (2009) Comparing stochastic point-source and finite-source ground-motion simulations: SMSIM and EXSIM. Bull Seismol Soc Am 99, 3202-3216

Boore DM, Thompson EM (2014) Path durations for use in the stochastic ‐ method simulation of ground motions. Bull Seismol Soc Am 104, 2541-2552

Boore DM, Thompson EM (2015) Revisions to some parameters used in stochastic-method simulations of ground motion. Bull Seismol Soc Am 105, 1029-1041

Bose S, Nozari A, Mohammadi ME, Stavridis A, Babak M, Wood R, Gillins D, Barbosa A, 2016. Structural assessment of a school building in Sankhu, Nepal damaged due to torsional response during the 2015 Gorkha earthquake, Dyn Civil Struct. Springer, pp. 31-41

Bozorgnia Y, Niazi M, Campbell KW (1995) Characteristics of free-field vertical ground motion during the Northridge earthquake. Earthq spectra 11, 515-525

Carey J, McSaveney M, Petley D (2017) Dynamic liquefaction of shear zones in intact loess during simulated earthquake loading. Landslides 14, 789-804

Chen MC, Pantoli E, Wang X, Astroza R, Ebrahimian H, Hutchinson TC, Conte JP, Restrepo JI, Marin C, Walsh KD (2016) Full-Scale Structural and Nonstructural Building System Performance during Earthquakes: Part I–Specimen Description, Test Protocol, and Structural Response. Earthq Spectra 32, 737-770

Chiu S, Kanasewich E, Phadke S (1986) Three-dimensional determination of structure and velocity by seismic tomography. Geophysics 51, 1559-1571

Chopra AK, McKenna F (2016) Modeling viscous damping in nonlinear response history analysis of buildings for earthquake excitation. Earthq Eng Struct Dyn 45, 193-211

Chousianitis K, Del Gaudio V, Sabatakakis N, Kavoura K, Drakatos G, Bathrellos GD, Skilodimou HD (2016) Assessment of earthquake ‐ induced landslide hazard in Greece: From Arias intensity to spatial distribution of slope resistance demand. Bull Seismol Soc Am 106, 174-188

Courboulex F, Virieux J, Deschamps A, Gibert D, Zollo A (1996) Source investigation of a small event using empirical Green's functions and simulated annealing. Geophys J Int 125, 768-780

Cui P, Chen X-Q, Zhu Y-Y, Su F-H, Wei F-Q, Han Y-S, Liu H-J, Zhuang J-Q (2011) The Wenchuan earthquake (May 12, 2008), Sichuan province, China, and resulting geohazards. Nat Hazards 56, 19-36

Cui S, Wang G, Pei X, Huang R, Kamai T (2017) On the initiation and movement mechanisms of a catastrophic landslide triggered by the 2008 Wenchuan (Ms 8.0) earthquake in the epicenter area. Landslides 14, 805-819

Dai F, Lee C, Ngai YY (2002) Landslide risk assessment and management: an overview. Eng geology 64, 65-87

Dalguer LA, Miyake H, Day SM, Irikura K (2008) Surface rupturing and buried dynamic-rupture models calibrated with statistical observations of past earthquakes. Bull Seismol Soc Am 98, 1147-1161

Dan K, Watanabe T, Tanaka T (1989) A Semi-empirical method to synthesize earthquake ground motions based on approximate source spectrum for far-field shear wave. J Struct Constr Eng (Transactions of AIJ) 396, 27-36

Dreger D (1994) Empirical Green's function study of the January 17, 1994 Northridge, California earthquake. Geophys Res Lett 21, 2633-2636

Gaprindashvili G, Van Westen CJ (2016) Generation of a national landslide hazard and risk map for the country of Georgia. Nat Hazards 80, 69-101

Glass RI, Urrutia JJ, Sibony S, Smith H, Garcia B, Rizzo L (1977) Earthquake injuries related to housing in a Guatemalan village. Science 197, 638-643

Gorum T, van Westen CJ, Korup O, van der Meijde M, Fan X, van der Meer FD (2013) Complex rupture mechanism and topography control symmetry of mass-wasting pattern, 2010 Haiti earthquake. Geomorphology 184, 127-138

Guzzetti F (2000) Landslide fatalities and the evaluation of landslide risk in Italy. Eng Geology 58, 89-107

Han Z, Chen G, Li Y, Tang C, Xu L, He Y, Huang X, Wang W (2015) Numerical simulation of debris-flow behavior incorporating a dynamic method for estimating the entrainment. Eng Geology 190, 52-64

Han Z, Li Y, Huang J, Chen G, Xu L, Tang C, Zhang H, Shang Y (2016) Numerical simulation for run-out extent of debris flows using an improved cellular automaton model. Bull Eng Geol Environ, 1-14

Hartzell S, Guatteri M, Mai PM, Liu P-C, Fisk M (2005) Calculation of broadband time histories of ground motion, Part II: Kinematic and dynamic modeling using theoretical Green’s functions and comparison with the 1994 Northridge earthquake. Bull Seismol Soc Am 95, 614-645

Hartzell S, Harmsen S, Frankel A, Larsen S (1999) Calculation of broadband time histories of ground motion: Comparison of methods and validation using strong-ground motion from the 1994 Northridge earthquake. Bull Seismol Soc Am 89, 1484-1504

Hartzell SH (1978) Earthquake aftershocks as Green's functions. Geophys Res Lett 5, 1-4

Haskell NA (1969) Elastic displacements in the near-field of a propagating fault. Bull Seismol Soc Am 59, 865-908

Hisada Y, Bielak J (2003) A theoretical method for computing near-fault ground motions in layered half-spaces considering static offset due to surface faulting, with a physical interpretation of fling step and rupture directivity. Bull Seismol Soc Am 93, 1154-1168

Holzer TL, Savage JC (2013) Global earthquake fatalities and population. Earthq Spectra 29, 155-175

Hough S, Seeber L, Lerner-Lam A, Armbruster J, Guo H (1991) Empirical Green's function analysis of Loma Prieta aftershocks. Bull Seismol Soc Am 81, 1737-1753

Huang R, Li, WL (2009) Analysis of the geo-hazards triggered by the 12 May 2008 Wenchuan Earthquake, China. Bull Eng Geol Environ 68, 363-371

Hubbard J, Shaw JH (2009) Uplift of the Longmen Shan and Tibetan plateau, and the 2008 Wenchuan (M= 7.9) earthquake. Nature 458, 194

Hutchings L, Wu F (1990) Empirical Green's functions from small earthquakes: a waveform study of locally recorded aftershocks of the 1971 San Fernando earthquake. J Geophys Res 95, 1187-1214

Idriss I, Boulanger R (2006) Semi-empirical procedures for evaluating liquefaction potential during earthquakes. Soil Dyn Earthq Eng 26, 115-130

Irikura K (1983) Semi-empirical estimation of strong ground motions during large earthquakes. Bull Disast Prev Res Inst Kyoto Univ 33, 63-104

Irikura K (1986) Prediction of strong acceleration motion using empirical Green’s function, Proc. 7th Japan Earthq. Eng. Symp, pp. 151-156

Irikura K, Kamae K (1994) Estimation of strong ground motion in broad-frequency band based on a seismic source scaling model and an empirical Green's function technique. Annals of Geophysics 37

Jibson RW (2011) Methods for assessing the stability of slopes during earthquakes—A retrospective. Eng Geology 122, 43-50

Jing P, 2016. Development of a practical 3D DDA program for hazard assessment of earthquake induced landslides, Department of civil and structural engineering. Kyushu University.

Jing P, Chen G, Zhang H, Wang W, 2017. Application of Three-Dimensional Discontinuous Deformation Analysis to Simulate Characteristics of Planar Translational Slope Failure, Geotechnical Hazards from Large Earthquakes and Heavy Rainfalls. Springer, pp. 339-345.

Joyner WB, Boore DM, 1986. On Simulating Large Earthquakes by Green's–Function Addition of Smaller Earthquakes, in: Monograph, A.G.U. (Ed.), Earthquake source mechanics, Washigto, DC, pp. 269-274.

Kamae K, Ikeda T, Miwa S (2005) Source model composed of asperities for the 2004 Mid Niigata Prefecture, Japan, earthquake (MJMA= 6.8) by the forward modeling using the empirical Green's function method. Earth Planets Space 57, 533-538

Kamae K, Irikura K (1998) Source model of the 1995 Hyogo-ken Nanbu earthquake and simulation of near-source ground motion. Bull Seismol Soc Am 88, 400-412

Kanamori H, Anderson DL (1975) Theoretical basis of some empirical relations in seismology. Bull Seismol Soc Am 65, 1073-1095

Khazai B, Sitar N (2004) Evaluation of factors controlling earthquake-induced landslides caused by Chi-Chi earthquake and comparison with the Northridge and Loma Prieta events. Eng Geology 71, 79-95

King A, Middleton D, Brown C, Johnston D, Johal S (2014) Insurance: its role in recovery from the 2010–2011 Canterbury earthquake sequence. Earthq Spectra 30, 475-491

Kurahashi S, Irikura K (2011) Source model for generating strong ground motions during the 2011 off the Pacific coast of Tohoku Earthquake. Earth Planets Space 63, 11

Larson KM, Bodin P, Gomberg J (2003) Using 1-Hz GPS data to measure deformations caused by the Denali fault earthquake. Science 300, 1421-1424

Lay T, Kanamori H, Ammon CJ, Nettles M, Ward SN, Aster RC, Beck SL, Bilek SL, Brudzinski MR, Butler R (2005) The great Sumatra-Andaman earthquake of 26 december 2004. Science 308, 1127-1133

Liu J, Mengtan G, Shuren W, Tao W, Jian W (2016) A Hazard Assessment Method for Potential Earthquake ‐ Induced Landslides ‐ A Case Study in Huaxian County, Shaanxi Province. Acta Geologica Sinica (English Edition) 90, 590-603

Marano KD, Wald DJ, Allen TI (2010) Global earthquake casualties due to secondary effects: a quantitative analysis for improving rapid loss analyses. Nat Hazards 52, 319-328

Martin SS, Hough SE, Hung C (2015) Ground motions from the 2015 M w 7.8 Gorkha, Nepal, earthquake constrained by a detailed assessment of macroseismic data. Seismol Res Lett 86, 1524-1532

McDougall S, Hungr O (2004) A model for the analysis of rapid landslide motion across three-dimensional terrain. Can Geotech J 41, 1084-1097

McPhillips D, Bierman PR, Rood DH (2014) Millennial-scale record of landslides in the Andes consistent with earthquake trigger. Nat Geosci 7, 925

Meunier P, Hovius N, Haines JA (2008) Topographic site effects and the location of earthquake induced landslides. Earth Planet Sci Lett 275, 221-232

Miles S, Ho C (1999) Rigorous landslide hazard zonation using Newmark's method and stochastic ground motion simulation. Soil Dyn Earthq Eng 18, 305-323

Miyake H, Iwata T, Irikura K (2003) Source characterization for broadband ground-motion simulation: Kinematic heterogeneous source model and strong motion generation area. Bull Seismol Soc Am 93, 2531-2545

Mori J, Frankel A (1990) Source parameters for small events associated with the 1986 North Palm Springs, California, earthquake determined using empirical Green functions. Bull Seismol Soc Am 80, 278-295

Mori N, Takahashi T, Yasuda T, Yanagisawa H (2011) Survey of 2011 Tohoku earthquake tsunami inundation and run‐up. Geophys Res Lett 38

Motazedian D, Atkinson G, 2002. Dynamic corner frequency: a new concept in stochastic finite fault modeling, Seismol Soc Am Meeting, pp. 17-19.

Motazedian D, Atkinson GM (2005) Stochastic finite-fault modeling based on a dynamic corner frequency. Bull Seismol Soc Am 95, 995-1010

Motazedian D, Moinfar A (2006) Hybrid stochastic finite fault modeling of 2003, M6. 5, Bam earthquake (Iran). J Seismol 10, 91-103

Mourhatch R, Krishnan S (2015) Simulation of broadband ground motion by superposing high-frequency empirical green’s function synthetics on low-frequency spectralelement synthetics. Bull Seismol Soc Am

Nadim F, Kjekstad O, Peduzzi P, Herold C, Jaedicke C (2006) Global landslide and avalanche hotspots. Landslides 3, 159-173

Ordaz M, Arboleda J, Singh SK (1995) A scheme of random summation of an empirical Green's function to estimate ground motions from future large earthquakes. Bull Seismol Soc Am 85, 1635-1647

Oth A, Wenzel F, Radulian M (2007) Source parameters of intermediate-depth Vrancea (Romania) earthquakes from empirical Green's functions modeling. Tectonophysics 438, 33-56

Pacheco JF, Scholz CH, Sykes LR (1992) Changes in frequency–size relationship from small to large earthquakes. Nature 355, 71-73

Panning M, Romanowicz B (2006) A three-dimensional radially anisotropic model of shear velocity in the whole mantle. Geophys J Int 167, 361-379

Papathanassiou G, Mantovani A, Tarabusi G, Rapti D, Caputo R (2015) Assessment of liquefaction potential for two liquefaction prone areas considering the May 20, 2012 Emilia (Italy) earthquake. Eng Geology 189, 1-16

Pavic R, Koller MG, Bard P-Y, Lacave-Lachet C (2000) Ground motion prediction with the empirical Green's function technique: an assessment of uncertainties and confidence level. J Seismol 4, 59-77

Poggi V, Edwards B, Fäh D (2011) Derivation of a reference shear-wave velocity model from empirical site amplification. Bull Seismol Soc Am 101, 258-274

Quan Y, Harris JM (1997) Seismic attenuation tomography using the frequency shift method. Geophysics 62, 895-905

Quigley MC, Bastin S, Bradley BA (2013) Recurrent liquefaction in Christchurch, New Zealand, during the Canterbury earthquake sequence. Geology 41, 419-422

Rajendran C, John B, Rajendran K, Sanwal J (2016) Liquefaction record of the great 1934 earthquake predecessors from the north Bihar alluvial plains of India. J Seismol 20, 733-745

Reasenberg PA, Simpson RW (1992) Response of regional seismicity to the static stress change produced by the Loma Prieta earthquake. Science 255, 1687

Ritsema J, van Heijst HJ, Woodhouse JH (1999) Complex shear wave velocity structure imaged beneath Africa and Iceland. Science 286, 1925-1928

Rossetto T, 2006. Earthquake engineering. University College London.

Sato H, Harp E (2009) Interpretation of earthquake-induced landslides triggered by the 12 May 2008, M7. 9 Wenchuan earthquake in the Beichuan area, Sichuan Province, China using satellite imagery and Google Earth. Landslides 6, 153-159

Sato H, Fehler MC, Maeda T, 2012. Seismic wave propagation and scattering in the heterogeneous earth. Springer.

Satyam ND, Towhata I (2016) Site-specific ground response analysis and liquefaction assessment of Vijayawada city (India). Nat Hazards 81, 705-724

Seed HB, Idriss IM (1971) Simplified procedure for evaluating soil liquefaction potential. J Soil Mech Found Div

Seed B (1979) Soil Liquefaction and cyclic mobility evalution for level ground during earthquakes. J Geotech Geoenv Eng 105

Seed HB, Idriss IM, 1982. Ground motions and soil liquefaction during earthquakes.

Earthq Eng Res Ins.

Seifried A, Baker J (2016) Spectral variability and its relationship to structural response estimated from scaled and spectrum-matched ground motions. Earthq Spectra 32, 2191-2205

Sepúlveda SA, Petley DN, Brain MJ, Tunstall N (2016) The effect of dynamic loading on the shear strength of pyroclastic Ash Deposits and implications for landslide hazard: The case of Pudahuel Ignimbrite, Chile. Eng Geology 205, 54-61

Shapiro NM, Campillo M, Stehly L, Ritzwoller MH (2005) High-resolution surface-wave tomography from ambient seismic noise. Science 307, 1615-1618

Shou K-J, Wang C-F (2003) Analysis of the Chiufengershan landslide triggered by the 1999 Chi-Chi earthquake in Taiwan. Eng Geology 68, 237-250

Sonmez E, Nagarajaiah S, Sun C, Basu B (2016) A study on semi-active tuned liquid column dampers (sTLCDs) for structural response reduction under random excitations. J Sound Vibration 362, 1-15

Strogatz SH, 2014. Nonlinear dynamics and chaos: with applications to physics, biology, chemistry, and engineering. Westview press.

Su Wj, Woodward RL, Dziewonski AM (1994) Degree 12 model of shear velocity heterogeneity in the mantle. J Geophys Res 99, 6945-6980

Suzuki W, Iwata T, Asano K, Yamada N (2005) Estimation of the source model for the foreshock of the 2004 off the Kii peninsula earthquakes and strong ground motion simulation of the hypothetical Tonankai earthquake using the empirical Green’s function method. Earth Planets Space 57, 345-350

Takatani T, Nishikawa H (2017) Seismic Performance of One-storey Thatched Roof Wooden Structure Against a Strong Earthquake Ground Motion. J Civil Eng Const 6, 1

Towhata I, Maruyama S, Kasuda K-i, Koseki J, Wakamatsu K, Kiku H, Kiyota T, Yasuda S, Taguchi Y, Aoyama S (2014) Liquefaction in the Kanto region during the 2011 off the pacific coast of Tohoku earthquake. Soils Found 54, 859-873

Tuttle MP, Villamor P, Almond P, Bastin S, Bucci MG, Langdridge R, Clark K, Hardwick CM (2017) Liquefaction Induced during the 2010–2011 Canterbury, New Zealand, Earthquake Sequence and Lessons Learned for the Study of Paleoliquefaction Features. Seismol Res Lett

Van Ballegooy S, Malan P, Lacrosse V, Jacka M, Cubrinovski M, Bray J, O'Rourke T, Crawford S, Cowan H (2014) Assessment of liquefaction-induced land damage for residential Christchurch. Earthq Spectra 30, 31-55

Van Westen CJ, Castellanos E, Kuriakose SL (2008) Spatial data for landslide susceptibility, hazard, and vulnerability assessment: an overview. Eng Geology 102, 112-131

Varazanashvili O, Tsereteli N, Amiranashvili A, Tsereteli E, Elizbarashvili E, Dolidze J, Qaldani L, Saluqvadze M, Adamia S, Arevadze N (2012) Vulnerability, hazards and multiple risk assessment for Georgia. Nat Hazards 64, 2021-2056

Villamor P, Almond P, Tuttle M, Giona‐Bucci M, Langridge R, Clark K, Ries W, Bastin S, Eger A, Vandergoes M (2016) Liquefaction Features Produced by the 2010–2011 Canterbury Earthquake Sequence in Southwest Christchurch, New Zealand, and Preliminary Assessment of Paleoliquefaction Features. Bull Seismol Soc Am 106, 1747-1771

Villar-Vega M, Silva V (2017) Assessment of earthquake damage considering the characteristics of past events in South America. Soil Dyn Earthq Eng 99, 86-96

Walker KT, Pichon AL, Kim TS, Groot‐Hedlin C, Che IY, Garcés M (2013) An analysis of ground shaking and transmission loss from infrasound generated by the 2011 Tohoku earthquake. J Geophys Res 118

Wang G, Ding Y, Borcherdt R (2015) Simulation of acceleration field of the Lushan earthquake (Ms7. 0, April 20, 2013, China). Engineering Geology 189, 84-97.doi:10.1006/j.enggeo.2015.02.003

Wang H-f, Lou M-l, Zhang R-l (2017) Influence of presence of adjacent surface structure on seismic response of underground structure. Soil Dyn Earthq Eng 100, 131-143

Wang W, Zhang H, Zheng L, Zhang Y-b, Wu Y-q, Liu S-g (2017b) A new approach for modeling landslide movement over 3D topography using 3D discontinuous deformation analysis. Computers and Geotechnics 81, 87-97

Wilson RC, Keefer DK (1983) Dynamic analysis of a slope failure from the 6 August 1979 Coyote Lake, California, earthquake. Bull Seismol Soc Am 73, 863-877

Woodhouse JH, Dziewonski AM (1984) Mapping the upper mantle: Three‐dimensional modeling of Earth structure by inversion of seismic waveforms. J Geophys Res 89, 5953-5986

Wright S, Rathje E, 2003. Triggering mechanisms of slope instability and their relationship to earthquakes and tsunamis, Landslide Tsunamis: Recent Findings and Research Directions. Springer, pp. 1865-1877.

Wu J-H (2010) Seismic landslide simulations in discontinuous deformation analysis. Comp Geotech 37, 594-601

Xu C, Xu X, Lee YH, Tan X, Yu G, Dai F (2012) The 2010 Yushu earthquake triggered landslide hazard mapping using GIS and weight of evidence modeling. Environ Earth Sci 66, 1603-1616

Xu C, Xu X, Yao X, Dai F (2014) Three (nearly) complete inventories of landslides triggered by the May 12, 2008 Wenchuan Mw 7.9 earthquake of China and their spatial distribution statistical analysis. Landslides 11, 441-461

Yang X-L, Long Z-X (2015) Seismic and static 3D stability of two-stage rock slope based on Hoek–Brown failure criterion. Can Geotech J 53, 551-558

Yin Y, Wang F, Sun P (2009) Landslide hazards triggered by the 2008 Wenchuan earthquake, Sichuan, China. Landslides 6, 139-152

Yoshimatsu H, Abe S (2006) A review of landslide hazards in Japan and assessment of their susceptibility using an analytical hierarchic process (AHP) method. Landslides 3, 149-158

Zhang H, Liu S-g, Chen G-q, Zheng L, Zhang Y-b, Wu Y-q, Jing P-d, Wang W, Han Z, Zhong G-h (2016a) Extension of three-dimensional discontinuous deformation analysis to frictional-cohesive materials. Int J Rock Mech Min Sci 86, 65-79

Zhang H, Chen G, Liu S, Jing P, Han Z, 2017. An Extension to Weiler–Atherton Clipping Algorithm for the Face-to-Face Contact in Three-Dimensional Discrete Element Method, Geotechnical Hazards from Large Earthquakes and Heavy Rainfalls. Springer, pp. 333-338

Zhang Y, 2017. Earthquake-Induced Landslides: Initiation and run-out analysis by considering vertical seismic loading, tension failure and the trampoline effect. Springer.

Zhang Y, Xing H, Chen G, Zheng L, 2015. A New Movement Mechanism of Earthquake-Induced Landslides by Considering the Trampoline Effect of Vertical Seismic Loading, Eng Geol Soc Terr Vol 2. Springer, pp. 753-757

Zhou S, 2016. Development of a GIS-based integrated landslide hazard mapping system and its applications, Department of civil and structural engineering. Kyushu University.

Zhou S, Chen G, Fang L (2016) Distribution pattern of landslides triggered by the 2014 Ludian earthquake of China: Implications for regional threshold topography and the seismogenic fault identification. ISPRS International Journal of Geo-Information 5, 46

Zhou S, Wei W, Guangqi C, Baochen L, Ligang F (2016b) A Combined Weight of Evidence and Logistic Regression Method for Susceptibility Mapping of Earthquake‐induced Landslides: A Case Study of the April 20, 2013 Lushan Earthquake, China. Acta Geologica Sinica (English Edition) 90, 511-524

Zhou X, Qian Q, Cheng H, Zhang H (2015) Stability analysis of two-dimensional landslides subjected to seismic loads. Acta Mechanica Solida Sinica 28, 262-27

CHAPTER 2

REVIEW OF STOCHASTIC METHOD FOR STRONG GROUND-MOTION SIMULATION

2.1 INTRODUCTION

The stochastic finite-fault method has been widely used in the near-field ground-motion simulations during the past two decades (Ghasemi et al. 2010; Ugurhan and Askan 2010; Ghofrani et al. 2013; Safarshahi et al. 2013; Azarbakht et al. 2014; Zengin and Cakti 2014; Mittal and Kumar 2015; Holden and Kaiser 2016; Zhang et al. 2016; Chen et al. 2017). All the ground-motion intensity measures, including acceleration time series, PGA, Fourier amplitude spectrum (FAS) and pseudo-acceleration response spectra (PSA), can be predicted for both the past and future earthquakes (Beresnev and Atkinson 1998; Boore 2003). It has been one of the most powerful tools to model strong ground motions near the epicenter at frequency range of engineering interest (Boore 1973; Toro et al. 1997; Atkinson and Boore 2003; Atkinson 2004; Rathje et al. 2004; Baker 2007; Atkinson et al. 2009). However, the effect of asperity, one of the important factors in estimating source parameters, and the effect of volcanic zone on estimating path parameters have not been well investigated when performing the ground-motion simulation (Somerville et al. 1999; Murotani et al. 2008). Also, how to estimate the site effect for the location without seismic sensors remains a not well solved problem although site amplification can be estimated by the seismic observations from both the surface and borehole sensors at the same station. These key issues are introduced in this chapter in details.

2.2 EVOLUTION OF STOCHASTIC FINITE-FAULT METHOD

Stochastic simulation technique of strong ground motion originated from the point-source model (Boore 1983), which regards the source as a propagating array of Brune point sources (Aki 1967; Brune 1970, 1971) regardless of the fault geometry during the simulation. Stochastic finite-fault model was then developed by Beresnev and Atkinson (1998), who took fault geometry and slip heterogeneity into calculation to overcome the limitations of point-source model. Motazedian and Atkinson (2005) developed it by introducing the concept of dynamic corner frequency (code EXSIM) to conserve the total radiated energy and to make the

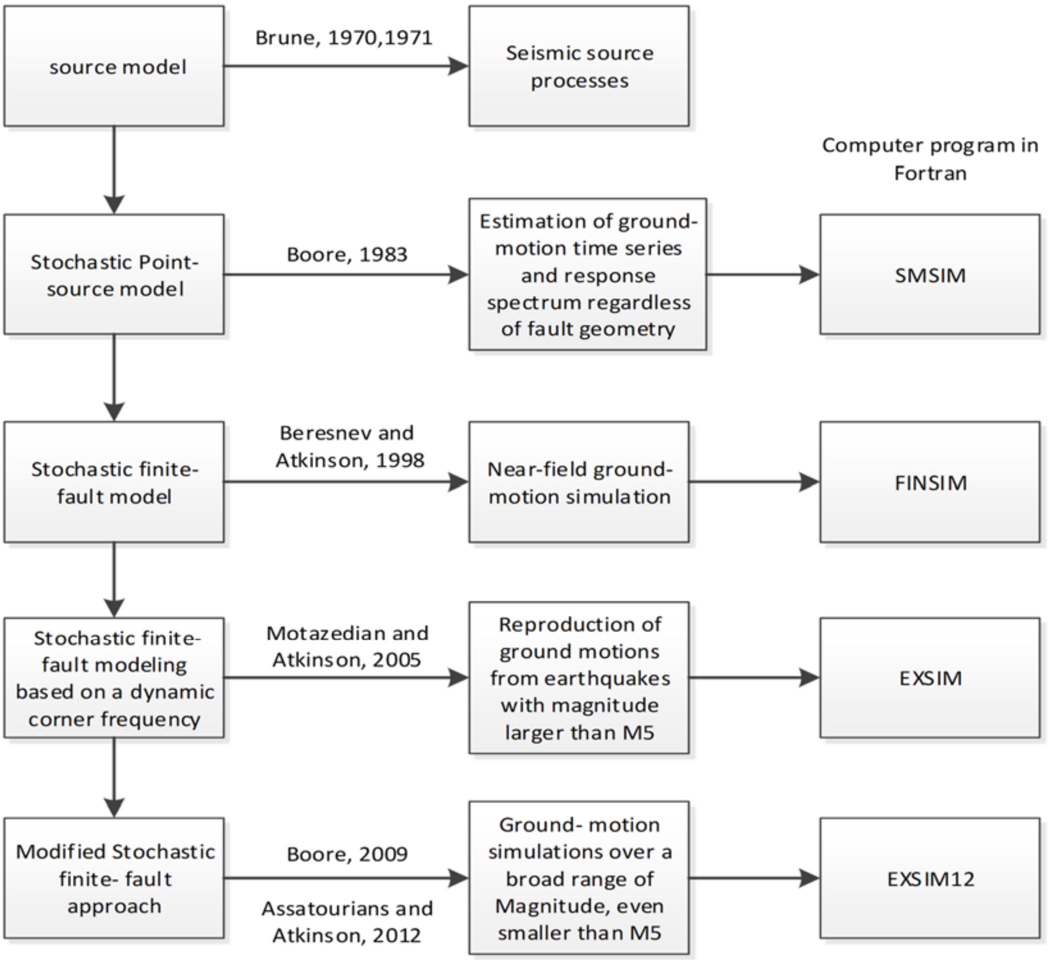

Figure 2-1 The evolution process of the stochastic finite-fault method

spectral shape and spectral level of the synthetic accelerograms relatively independent of subfault size. Further modifications and improvements to the EXSIM algorithm suggested by Boore (2009) include the scaling of high-frequency ground motions on the basis of the squared FAS rather than the velocity spectrum and no truncation applied to the time series from each subfault. Furthermore, the inverse of the subfault corner frequency for the duration of motions and a filter function to boost spectral amplitudes at frequencies near and less than the subfault corner frequencies are both used (Assatourians and Atkinson 2012). Figure 2-1 shows the evolution process of the stochastic finite-fault method.

2.3 METHODOLOGY

The seismic-wave propagation consists of three processes, including the source rupture (source effect)(Hanks 1979; Somerville et al. 1997; Campbell and Bozorgnia 2003), the past attenuation through the earth (path effect) (Mele et al. 1997; Faul et al. 2004; Jackson et al. 2004) and the site response on the surface (site effect), as shown in Figure 2-2 (Campillo et al. 1989; Chin and Aki 1991; Schneider et al. 1993). These three kinds of influences are all taken into the synthetization of acceleration wave using stochastic finite-fault method (Laba 2011; Shen et al. 2014; Carvalho et al. 2016; Heidari 2016).

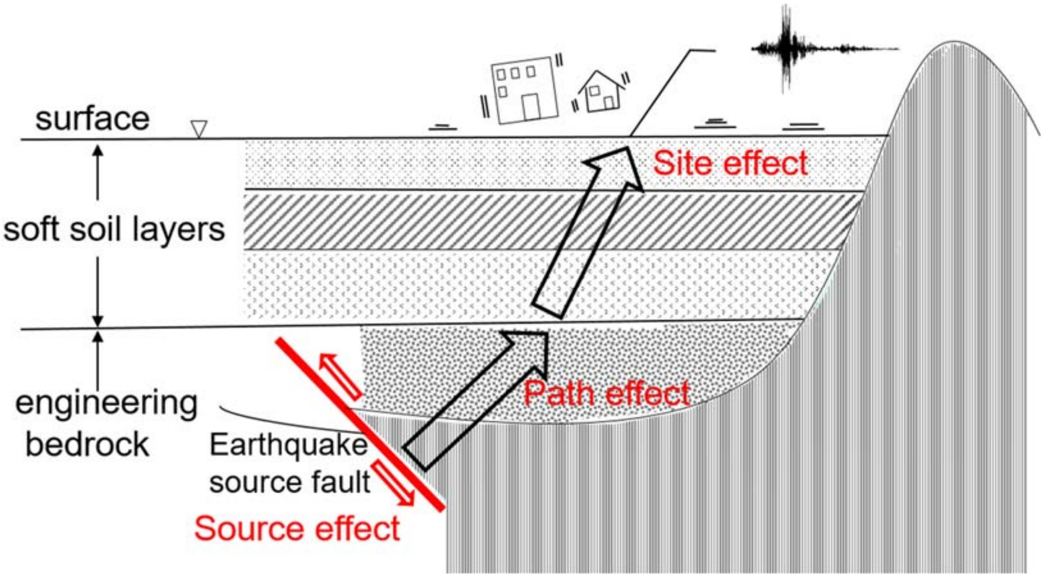

Figure 2-2 Schematic illustration of seismic wave propagation

The stochastic method originated from the point source model, which assumes that the source is a point (McGuire and Hanks 1980; Hanks and McGuire 1981; Atkinson and Boore 1997; Liu and Hong 2013). The acceleration time series are generated at an observation point considering both the deterministic and random parts of earthquake ground motions (Housner 1947; Saragoni and Hart 1974; Park et al. 1986). Since it is difficult to consider the source, path and site effects together in the time domain, the synthetization of the ground motion is performed in the frequency domain. The point-source spectrum at the observation point is derived by multiplication of source, path, and site spectra and shown as follows,

$$A(M,R,f)=Source(M,f)Path(R,f)Site(f). \tag{2.1}$$

The synthesized spectrum is multiplied by a normalized random-signal complex spectrum to obtain the Fourier amplitude spectrum (FAS) of ground motion at the site. Then the simulated acceleration time series is calculated by the inverse Fourier transform of FAS as follows,

$$a(t)=\int_{0}^{+\infty}A(f)e^{-i2\pi ft}df \tag{2.2}$$

The assumption of regarding the source as a point is only reasonable in the case of the source-to-site distance is much larger than the size of source (Spudich and Frazer 1984; Sabetta and Pugliese 1996; Halldórsson et al. 2010). On the one hand, if the seismogenic fault is so large, such as the Longmenshan fault on which the 2008 Wenchuan M8 earthquake occurred, the length of which is more than 300 km, the source is cannot considered as a point (Lei and Zhao 2009; Xu et al. 2009; Zhang et al. 2009; Ran et al. 2010; Ran et al. 2013). On the other hand, if the target site is located at the near field, that is, the source-to-site distance is comparable to the fault size, such as the station KMMH16 of the 2016 Kumamoto earthquake with the epicentral distance of 2 km, the source also cannot be regarded as a point (Ohno et al. 1993; Sun and Okubo 1998; Yamazaki et al. 2013).

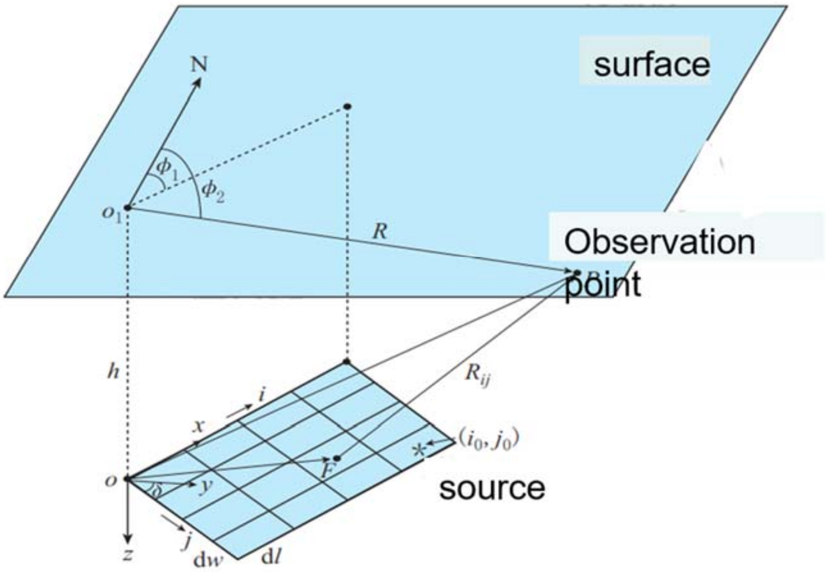

Figure 2-3 The sketch of stochastic finite-fault model

Many significant factors which affect the ground motions from large earthquakes are neglected by the stochastic point-source model, such as the effects of faulting geometry, distributed slip, and slip heterogeneity (Aki 1984; Oglesby and Day 2002; Guatteri et al. 2003). In order to overcome such limitations and take the source process of the fault into the generation of ground motions, Hartzell (1978) suggested to divide a large seismic fault plane into N subfaults, and each one is considered as a small point source (Figure 2-3). Beresnev and Atkinson (1998) implemented this idea and developed the point-source model to the finite-fault model. In the stochastic finite-fault method, the ground motions of subfaults are summed with a proper time delay to obtain the ground-motion acceleration at the observation, $a(t)$, from the entire fault using the follow equation,

$$a(t) = \sum_{i=1}^{nl} \sum_{j=1}^{nw} a_{ij}\left(t + \Delta t_{ij}\right) \tag{2.3}$$

where n_l and n_w are the number of subfaults along the length and width of the main fault, a_{ij} is the acceleration time series at recording site generated by ijth subfault, Δt_{ij} is the relative delay time for the radiation wave from the ijth subfault to the observation point. The specific form of the source, path and site terms of FAS is introduced in the following sections.

2.2.1 SOURCE PARAMETERS

From the observation of many earthquake displacement spectra (e.g. Figure 2-4), and from the scaling of moment with earthquake size, Aki (1967) and Brune (1970) propose a simple ω^{-2} model to describe the displacement spectrum decay at high frequencies,

$$\Omega(\omega) = \frac{\Omega_0}{1 + (\omega/\omega_0)^2} \tag{2.4}$$

where, ω is the angular frequency, given by $2\pi f$, ω_0 is the so-called angular corner frequency, Ω_0 is the zero-frequency limit of spectrum, given by CM_0. Although this source model is so simple, it can represent the shape of spectra (Snoke 1987; Miyake et al. 2003; Drouet et al. 2008). For example, the displacement spectrum of NS component of station KMMH16 and the best-fit ω^{-2} model is shown in Figure 2-5. It is easy to get the acceleration spectrum by twice differentiation for equation (2.4),

$$A(\omega) = \frac{\omega^2 CM_0}{1 + (\omega/\omega_0)^2}. \tag{2.5}$$

Then if ω is replaced by $2\pi f$, the source spectrum is shown as

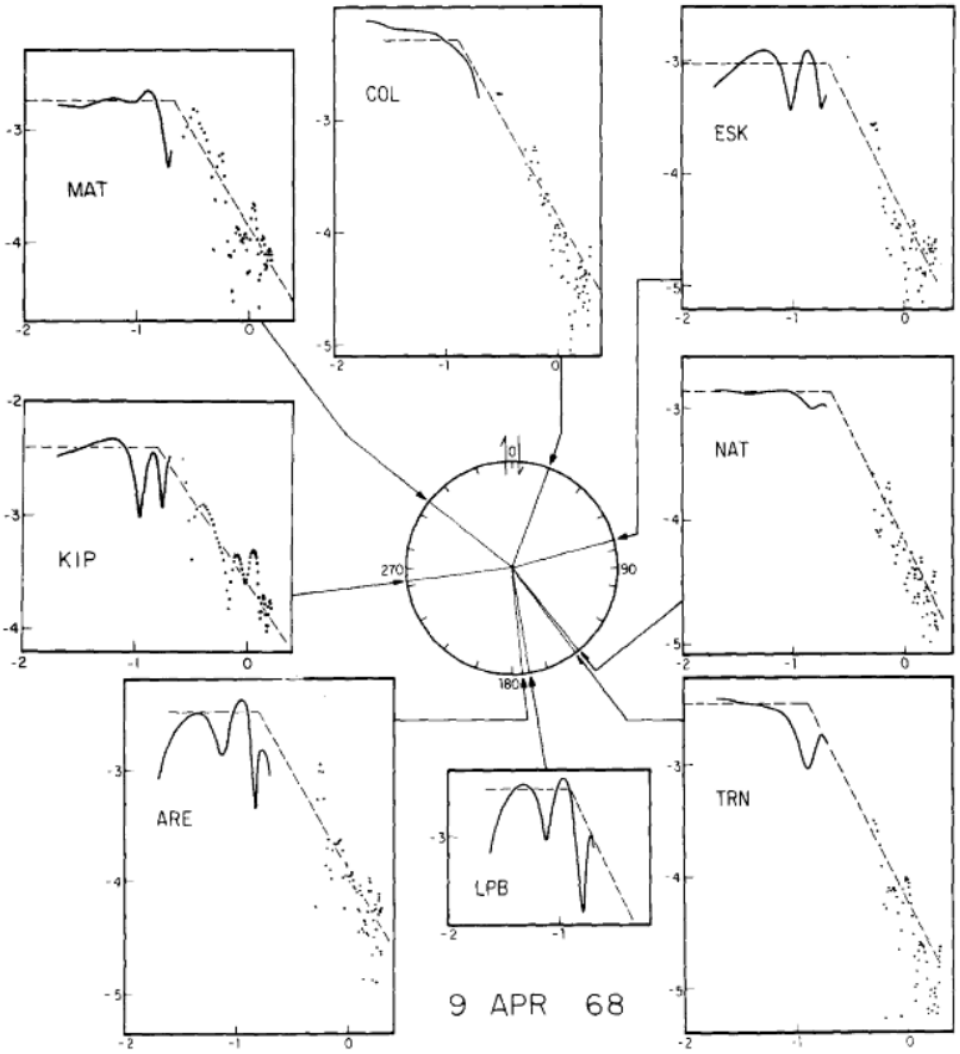

Figure 2-4 Displacement spectra, California earthquake, presented with respect to azimuth of fault trace. Solid lines are spectral data from long-period instrument; points are spectral data from short-period instrument. Vertical scales are $\log_{10}$ amplitude, horizontal scales are $\log_{10}$ frequency (after Hanks and Wyss (1972)).

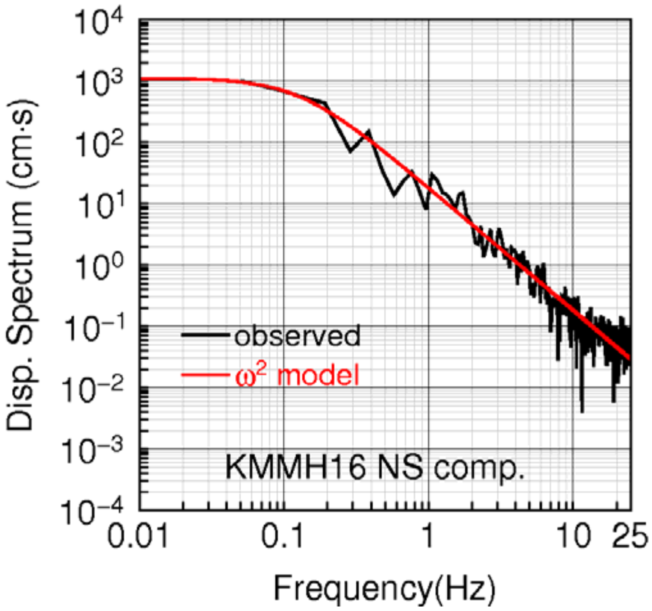

Figure 2-5 The observed displacement spectrum of the NS component of the station KMMH16 from the 2016 Kumamoto earthquake

$$A^s(f) = CM_{0ij}(2\pi f)^2 \Big/ \left[1 + (f/f_0)^2\right] \tag{2.6}$$

where the constant C is given by $C = R_{\theta\phi}FV/4\pi\rho\beta^3$, $R_{\theta\phi}$ is the radiation pattern (0.55 for shear waves), F is free surface amplification (2.0), V is the partition factor into two horizontal components (0.71), ρ is density in $g \cdot cm^{-3}$, β is shear-wave velocity in kilometres per second, f is the frequency in Hertz, f_0 is the corner frequency, given by $f_0 = 4.9 \times 10^6 \beta(\Delta\sigma/M_0)$, in which the $\Delta\sigma$ is the stress drop in bars (Boore 1983; Beresnev and Atkinson 1998), M_{0ij} is the seismic moment of ijth subfault in dyne centimetres, which is defined by

$$M_{0ij} = \frac{M_0 S_{ij}}{S_0} \tag{2.7}$$

where M_0 and S_0 are the total seismic moment and slip amount of the entire fault plane, S_{ij} is the relative slip weight of the ijth subfault (Motazedian and Atkinson 2005). For each subfault, the radiated elastic energy or the seismic moment is dependent of the slip amount on it.

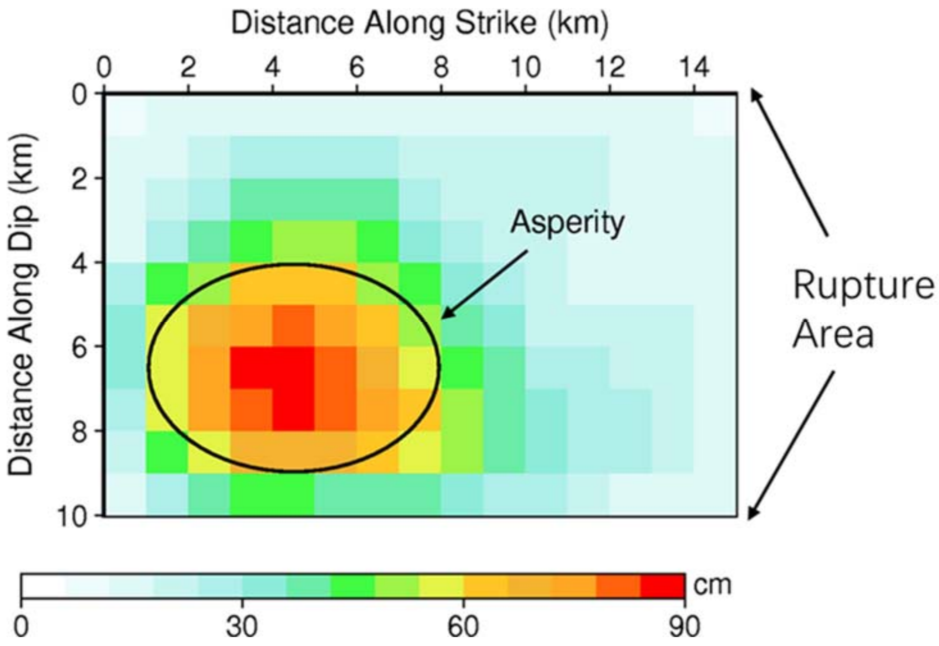

Figure 2-6 The slip distribution field of 1997 M6.1 Kagoshima earthquake (after Horikawa (2001), refigured)

Asperity, the area with large slip amount on a fault plane, plays an important role in generating the slip distribution field. For example, the slip distribution inversion of the 1997 Kagoshima earthquake shows that the asperity only occupies 20% of the rupture area, but it makes up 40% of the total seismic energy (Figure 2-6). However, the effect of asperity on the ground motion simulations has not been well investigated. On the one hand, for a past earthquake, three kinds of geophysical data are usually used for slip distribution field inversion (Yamanaka and Kikuchi 2003; Schmidt and Bürgmann 2006; Ji et al. 2015). Since the inversed asperity is not the same based on different data, the issue that which one will result in the most accurate simulation results should be clarified. On the other hand, for a future potential earthquake, the slip distribution field is unknown. Therefore, how to establish a slip distribution field for a potential earthquake occurs on a specific fault with an assumed magnitude is an important issue.

2.2.2 PATH PARAMETERS

The amplitude decay of seismic wave as it propagates from the source, including two components, the geometrical spreading and inelastic absorption (Boore and Atkinson 1987; Sharma et al. 2015). One of basic assumptions of geophysics is the seismic wave radiates from the source in the form of spherical wave (Blackstock 2000; Sato 2007; Ben-Menahem and Singh 2012). In physics, from the solution of wave functions, the amplitude of a spherical wave is inversely proportional to the travel distance. The decay rate is defined as the geometrical spreading, $G(R) = R^{-1}$ for body wave in the elastic whole space (Atkinson 1989; Atkinson and Mereu 1992; Zhao 2010). Besides, the seismic energy is also absorbed by the medium the wave travelled and turns to heat (Aki 1969; Aki and Chouet 1975; Aki 1980; Bugeja 2011). To characterize this influence, the S-wave attenuation (Q_s) is defined as

$$\frac{2\pi}{Q_s} = \frac{-\Delta E}{E} \tag{2.8}$$

where E is the energy of *S* wave, and ΔE is the change in energy per cycle (Knopoff 1964; Nigam 2004; Shearer 2009). The equation above indicates the fraction of energy dissipated per cycle of *S*-wave over total energy. It is well known that the energy is proportional to the squared amplitude A. Hence,

$$\frac{1}{Q_s} = -\frac{\Delta A}{\pi A} \tag{2.9}$$

In one cycle,

$$\frac{dA}{dr} = \frac{\Delta A}{\lambda} \tag{2.10}$$

where λ is the wave length, given by β / f, r is the S-wave propagation direction in spherical coordinates. Then take equation (2.9) into (2.10), giving

$$\frac{1}{A} dA = -\frac{\pi f}{\beta Q_s} dr \tag{2.11}$$

Finally, do the integration and calculate the natural logarithm, we have

$$A(f) = C \exp\left(\frac{-\pi fR}{\beta Q_s} \right) \tag{2.12}$$

where C is a constant when do the integration, R is the distance.

Both the geometrical spreading and inelastic absorption (S-wave attenuation) are considered to modify the amplitude spectra to represent the path effect in the stochastic finite-fault method (Boore 1983; Beresnev and Atkinson 1998; Boore 2003) in the form of

$$A^{p}\left(R, f\right) = \exp\left(\frac{-\pi fR}{\beta Q_{s}}\right) G\left(R\right) \tag{2.13}$$

where R is source-to-site distance in km, Q_s is the quality factor which shows the Shear-wave (S-wave) attenuation, $\mathrm{G}\left(R\right)$ is the geometrical spreading. For the region with heterogeneity of geological structures, such as the volcanoes, the Q_s shows the lateral variations.

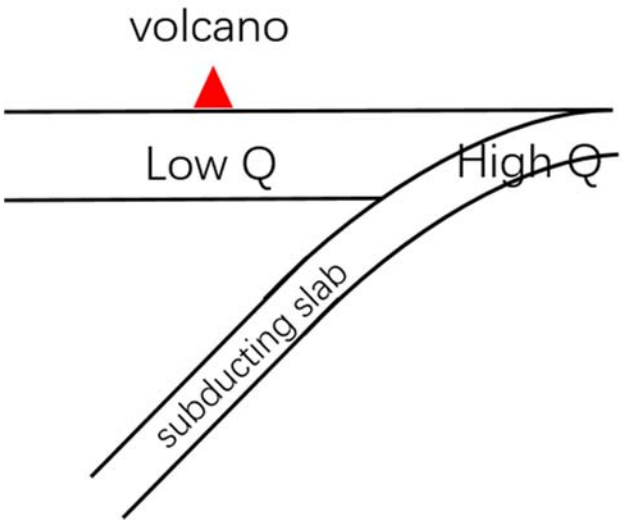

Figure 2-7 Schematic illustration of Q_s structure of the Kyushu region (refer from Pei et al, (2009))

For the path effect, the influence of volcano on the estimation of shear-wave attenuation (Q_s) has not been considered in the stochastic finite-fault modelling. Many studies report that the Low-Q anomalies are observed beneath these volcanoes in the crust and the uppermost mantle, whereas the High-Q anomalies exist in the subduction of the Philippine Sea plate (Figure 2-7) (Yoshimoto et al. 2006; Arpa et al. 2013; Prudencio et al. 2015). For the volcanic zone, the Q_s

determination is conventionally performed without distinguishing the non-volcanic area from the volcanic area. However, some large cities, such as Fukuoka city, are located in the non-volcanic area with a higher Q_s values compared to the normal Q_s. Since the Q_s is an critical parameter to represent the path effect, how to estimate the Q_s for volcanic zone accurately is an important and necessary issue for earthquake ground-motion simulations.

2.2.3 SITE PARAMETERS

The site response in the stochastic model includes two parts, the site amplification and kappa effect (Boore 1983; Atkinson et al. 2009; Atkinson and Assatourians 2015), which is specified as the form of

$$A^{l} = \exp\left(-\pi f \kappa\right) D\left(f\right) \tag{2.14}$$

where κ is a high-cut filter to model commonly-observed near-surface rapid spectral decay at high frequencies, $D\left(f\right)$ is the site amplification which is the increase in amplitudes of seismic waves as they traverse soft soil layers near the surface.

The theoretical acceleration source spectrum (equation (2.6)) based on the ω^{-2} model is plotted in Figure 2-8. There is an obvious problem: it predicts a flat acceleration at high frequencies, which is unmatched with the observed spectrum in practice (Figure 2-9). The decay of FAS can be considered as an approximately linear trend observed in log-linear space (Hough et al. 1988; Singh et al. 1989; Anderson and Humphrey 1991; Lay and Wallace 1995; Cotton et al. 2006; Van Houtte et al. 2011; Ktenidou et al. 2013; Laurendeau et al. 2013; Ktenidou et al. 2014) . The slope of this linear trend is controlled by a spectral decay rate. Anderson and Hough (1984) propose the kappa model, $\exp\left(-\pi f \kappa\right)$, for the prediction of the shape of FAS at high frequencies (Figure 2-10).

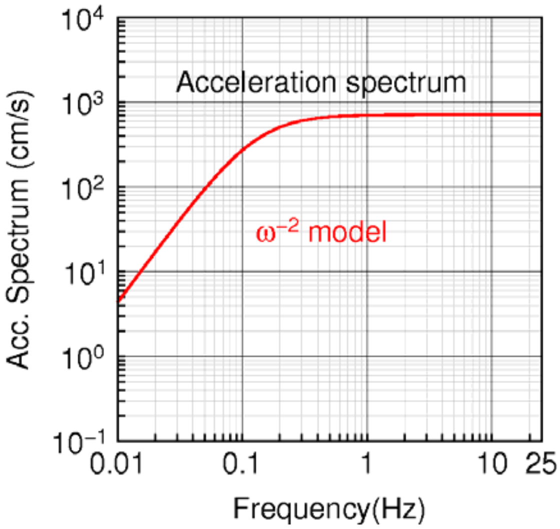

Figure 2-8 Acceleration source spectrum using ω^{-2} model

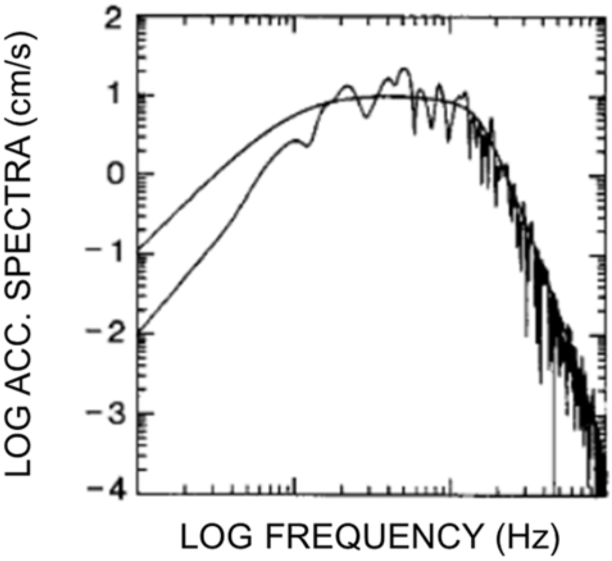

Figure 2-9 Observed acceleration source spectrum (after Brune (1970))

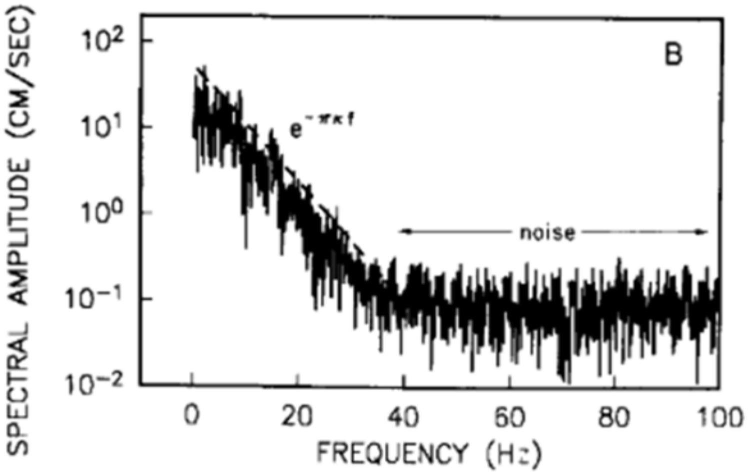

Figure 2-10 FAS of record at Cucapah during the Maxicali Valley earthquake of 9 June 1980 (after Anderson and Hough (1984))

Site amplification refers to the increase in amplitude of seismic waves as they travel through soft-soil layers (Figure 2-11) (Nakamura 1989; Cadet et al. 2010; Cadet et al. 2012; Boore 2013). The amplified waves usually lead to significant damages to engineered structures at the surface (Borcherdt 1970; Lermo and Chávez-García 1994; Mahin 1998; Assimaki and Jeong 2013). One of the most widely-used techniques is the surface-to-borehole (S/B) spectral ratios method, which takes the in situ borehole recordings as reference data (Abercrombie 1997; Stephenson et al. 2005; Oth et al. 2011; Garofalo et al. 2016). Specifically, site amplification of each station is determined by the ratio of smoothed FAS recorded at the ground surface to those recorded at the bottom of a borehole (Alharbi et al. 2015; Ogiso et al. 2016; Tallett-Williams et al. 2016). The KiK-net offers an appropriate opportunity to compute S/B spectral ratios due to having boreholes of 100 m-200 m in depth (Fujiwara et al. 2004).

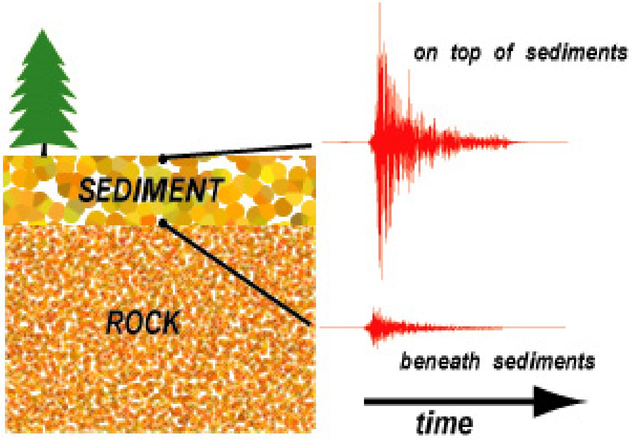

Figure 2-11 Schematic illustration of site amplification (accessed from http://pubs.usgs.gov/fs/fs-131-02/fs-131-02-p4.html)

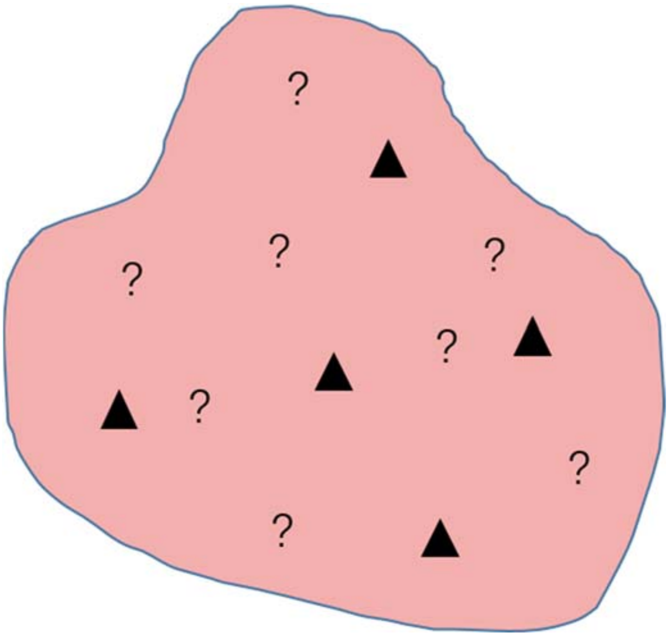

Figure 2-12 Schematic illustration of the estimation of site amplification in the region without strong ground-motion stations. Triangles represent the strong ground motion stations; question marks represent the region without stations.

Although site amplification can be estimated based on the seismic observations from both the surface and borehole sensors at the same station, how to estimate the site effect for the location without seismic sensors remains an unsolved problem (Figure 2-12). It is important for the ground motion simulation in the region where the records were unavailable during a past earthquake and for a future earthquake. To solve this problem, some relations between the accurate site amplification and regional site response measures, such as the V_{S30}, should be established. The site amplification in the region without stations can be estimated by inputting the regional measures into the relations established. Therefore, how to estimate the site amplification for the region without seismic sensors is an important and necessary issue.

2.4 CONCLUSIONS

In this chapter, the stochastic finite-fault method is reviewed in detail. As one of the most powerful tools to simulate ground motions for earthquake engineering, it has been applied to some large and important earthquakes, such as the 2008 M7.9 Wenchuan earthquake, 2011 M9.0 Tohoku earthquake, and 2016 M7.1 Kumamoto earthquake. The evolution process of the stochastic finite-fault method, includes some major improvement and modification, has been reviewed and summarized.

In the existing stochastic finite-fault modelling, the effects of volcano and asperity have not been considered in the estimation of S-wave attenuation and the slip distribution field, respectively. Three processes of seismic-wave radiation and propagation, that is, the source, path and site effects are taken into consideration of the stochastic finite-fault simulations. They are characterized by some geophysical parameters, such as the slip distribution field on the fault plane, the *S*-wave attenuation, and site amplification, etc. However, how to estimate (1) the site amplification in the region without seismic sensors, (2) the *S*-wave attenuation considering the volcanic effect, and (3) the slip distribution field for a potential earthquake are still important and not well solved issues. Besides, there is no a practical system for simulating earthquake ground motions paying attention to the volcanic zone and asperity on a fault. In the following chapters, they will be discussed in detail and solved.

REFERENCE

Abercrombie RE (1997) Near-surface attenuation and site effects from comparison of surface and deep borehole recordings. Bull Seismol Soc Am 87, 731-744

Aki K (1967) Scaling law of seismic spectrum. J Geophys Res 72, 1217-1231

Aki K (1969) Analysis of the seismic coda of local earthquakes as scattered waves. J Geophys Res 74, 615-631

Aki K (1980) Scattering and attenuation of shear waves in the lithosphere. J Geophys Res 85, 6496-6504

Aki K (1984) Asperities, barriers, characteristic earthquakes and strong motion prediction. J Geophys Res 89, 5867-5872

Aki K, Chouet B (1975) Origin of coda waves: source, attenuation, and scattering effects. J Geophys Res 80, 3322-3342

Alharbi M, Fnais M, Al-Amri A, Abdelrahman K, Andreae MO, Al-Dabbagh M (2015) Site response assessment at the city of Al Khobar, eastern Saudi Arabia, from microtremor and borehole data. Arab J Geosci 8, 10015-10030

Anderson JG, Hough SE (1984) A model for the shape of the Fourier amplitude spectrum of acceleration at high frequencies. Bull Seismol Soc Am 74, 1969-1993

Anderson JG, Humphrey JR (1991) A least squares method for objective determination of earthquake source parameters. Seismol Res Lett 62, 201-209

Assatourians K, Atkinson GM (2012) EXSIM12: a stochastic finite fault computer program in FORTRAN, http://www.seismotoolbox.ca (last accessed May 2015)

Assimaki D, Jeong S (2013) Ground-motion observations at Hotel Montana during the M 7.0 2010 Haiti earthquake: Topography or soil amplification? Bull Seismol Soc Am 103, 2577-2590

Atkinson GM (1989) Attenuation of the Lg phase and site response for the Eastern Canada Telemetered Network. Seismol Res Lett 60, 59-69

Atkinson GM (2004) Empirical attenuation of ground-motion spectral amplitudes in southeastern Canada and the northeastern United States. Bull Seismol Soc Am 94, 1079-1095

Atkinson GM, Assatourians K, Boore DM, Campbell K, Motazedian D (2009) A guide to differences between stochastic point-source and stochastic finite-fault simulations. Bull Seismol Soc Am 99, 3192-3201.doi:10.1785/0120090058

Atkinson GM, Assatourians K (2015) Implementation and validation of EXSIM (a stochastic finite‐fault ground‐motion simulation algorithm) on the SCEC broadband platform. Seismol Res Lett 86, 48-60

Atkinson GM, Boore DM (1997) Stochastic point-source modeling of ground motions in the Cascadia region. Seismol Res Lett 68, 74-85

Atkinson GM, Boore DM (2003) Empirical ground-motion relations for subduction-zone earthquakes and their application to Cascadia and other regions. Bull Seismol Soc Am 93, 1703-1729

Azarbakht A, Sadeghi M, Mousavi M (2014) Ground motion record simulation for structural analysis by consideration of spectral acceleration autocorrelation pattern. Earthq Eng Eng Vibrat 13, 195-202

Baker JW (2007) Quantitative classification of near-fault ground motions using wavelet analysis. Bull Seismol Soc Am 97, 1486-1501

Ben-Menahem A, Singh SJ, 2012. Seismic waves and sources. Springer Science & Business Media.

Beresnev IA, Atkinson GM (1998) FINSIM--a FORTRAN program for simulating stochastic acceleration time histories from finite faults. Seismol Res Lett 69, 27-32

Blackstock DT, 2000. Fundamentals of physical acoustics. John Wiley & Sons

Boore DM (1973) The effect of simple topography on seismic waves: implications for the accelerations recorded at Pacoima Dam, San Fernando Valley, California. Bull Seismol Soc Am 63, 1603-1609.

Boore DM (1983) Stochastic simulation of high-frequency ground motions based on seismological models of the radiated spectra. Bull Seismol Soc Am 73, 1865-1894

Boore DM (2013) The uses and limitations of the square‐root‐impedance method for computing site amplification. Bull Seismol Soc Am 103, 2356-2368

Boore DM, Atkinson GM (1987) Stochastic prediction of ground motion and spectral response parameters at hard-rock sites in eastern North America. Bull

Seismol Soc Am 77, 440-467

Borcherdt RD (1970) Effects of local geology on ground motion near San Francisco Bay. Bull Seismol Soc Am 60, 29-61

Brune JN (1970) Tectonic stress and the spectra of seismic shear waves from earthquakes. J Geophys Res 75, 4997-5009

Brune JN (1971) Correction. J geophys Res 76, 5002

Bugeja R, 2011. Crustal Attenuation in the region of the Maltese Islands using Coda Wave Decay, Deparment of Physics. University of Malta.

Cadet H, Bard P-Y, Rodriguez-Marek A (2010) Defining a standard rock site: Propositions based on the KiK-net database. Bull Seismol Soc Am 100, 172-195

Cadet H, Bard PY, Adrian RM (2012) Site effect assessment using KiK-net data: Part 1. A simple correction procedure for surface/downhole spectral ratios. Bull Earthq Eng 10, 421-448.doi:10.1007/s10518-011-9283-1

Campbell KW, Bozorgnia Y (2003) Updated near-source ground-motion (attenuation) relations for the horizontal and vertical components of peak ground acceleration and acceleration response spectra. Bull Seismol Soc Am 93, 314-331

Campillo M, Gariel J, Aki K, Sanchez-Sesma F (1989) Destructive strong ground motion in Mexico city: Source, path, and site effects during great 1985 Michoacan earthquake. Bull Seismol Soc Am 79, 1718-1735

Carvalho A, Reis C, Vales D (2016) Source and high-frequency decay parameters for the Azores region for stochastic finite-fault ground motion simulations. Bull Earthq Eng 14, 1885-1902

Chen C-T, Chang S-C, Wen K-L (2017) Stochastic ground motion simulation of the 2016 Meinong, Taiwan earthquake. Earth Planets Space 69, 62.doi:10.1186/s40623-017-0645-z

Chin B-H, Aki K (1991) Simultaneous study of the source, path, and site effects on strong ground motion during the 1989 Loma Prieta earthquake: a preliminary result on pervasive nonlinear site effects. Bull Seismol Soc Am 81, 1859-1884

Cotton F, Scherbaum F, Bommer JJ, Bungum H (2006) Criteria for selecting and adjusting ground-motion models for specific target regions: Application to central Europe and rock sites. J Seismol 10, 137-156

Drouet S, Chevrot S, Cotton F, Souriau A (2008) Simultaneous inversion of source spectra, attenuation parameters, and site responses: application to the data of the French accelerometric network. Bull Seismol Soc Am 98, 198-219

Faul UH, Gerald F, John D, Jackson I (2004) Shear wave attenuation and dispersion in melt-bearing olivine polycrystals: 2. Microstructural interpretation and seismological implications. J Geophys Res 109.doi:10.1029/2003JB002407

Fujiwara H, Aoi S, Kunugi T, Adachi S (2004) Strong-motion Observation Networks of NIED: K-NET and KiK-net. Cosmos Report

Garofalo F, Foti S, Hollender F, Bard P, Cornou C, Cox B, Dechamp A, Ohrnberger M, Perron V, Sicilia D (2016) InterPACIFIC project: Comparison of invasive and non-invasive methods for seismic site characterization. Part II: Inter-comparison between surface-wave and borehole methods. Soil Dyn Earthq Eng 82, 241-254

Ghasemi H, Fukushima Y, Koketsu K, Miyake H, Wang Z, Anderson JG (2010) Ground-motion simulation for the 2008 Wenchuan, China, earthquake using the stochastic finite-fault method. Bull Seismol Soc Am 100, 2476-2490

Ghofrani H, Atkinson GM, Goda K, Assatourians K (2013) Stochastic finite-fault simulations of the 2011 Tohoku, Japan, earthquake. Bull Seismol Soc Am 103, 1307-1320

Guatteri M, Mai PM, Beroza GC, Boatwright J (2003) Strong ground-motion prediction from stochastic-dynamic source models. Bull Seismol Soc Am 93, 301-313

Halldórsson B, Mavroeidis GP, Papageorgiou AS (2010) Near-fault and far-field strong ground-motion simulation for earthquake engineering applications using the specific barrier model. J Struct Eng 137, 433-444

Hanks TC (1979) b values and $\omega - \gamma$ seismic source models: Implications for tectonic stress variations along active crustal fault zones and the estimation of high-frequency strong ground motion. J Geophys Res 84, 2235-2242

Hanks TC, McGuire RK (1981) The character of high-frequency strong ground motion. Bull Seismol Soc Am 71, 2071-2095

Hartzell SH (1978) Earthquake aftershocks as Green's functions. Geophys Res Lett 5, 1-4

Heidari R (2016) Stochastic finite-fault simulation of ground motion from the August 11, 2012, Mw 6.4 Ahar earthquake, northwestern Iran. J Seismol 20, 463-473

Holden C, Kaiser A (2016) Stochastic ground motion modelling of the largest M w 5.9+ aftershocks of the Canterbury 2010–2011 earthquake sequence. New Zeal J Geol Geophys 59, 187-201.doi:10.1080/00288306.2015.1133664

Hough S, Anderson J, Brune J, Vernon F, Berger J, Fletcher J, Haar L, Hanks L, Baker L (1988) Attenuation near Anza, California. Bull Seismol Soc Am 78, 672-691

Housner GW (1947) Characteristics of strong-motion earthquakes. Bull Seismol Soc Am 37, 19-31

Jackson I, Faul UH, Gerald F, John D, Tan BH (2004) Shear wave attenuation and dispersion in melt-bearing olivine polycrystals: 1. Specimen fabrication and mechanical testing. J Geophys Res 109.doi:10.1029/2003JB002406

Ktenidou OJ, Cotton F, Abrahamson NA, Anderson JG (2014) Taxonomy of κ: A review of definitions and estimation approaches targeted to applications. Seismol Res Lett 85, 135-146

Knopoff L (1964) Q. Rev Geophys 2, 625-660

Ktenidou OJ, Gélis C, Bonilla LF (2013) A study on the variability of kappa (κ) in a borehole: Implications of the computation process. Bull Seismol Soc Am 103, 1048-1068

Laba C, 2011. Seismo-tectonics around Lhasa, Tibet, Institute of Earth Science. The University of Bergen

Laurendeau A, Cotton F, Ktenidou OJ, Bonilla LF, Hollender F (2013) Rock and stiff-soil site amplification: Dependency on VS30 and kappa (κ0). Bull Seismol Soc Am 103, 3131-3148

Lay T, Wallace TC, 1995. Modern global seismology. Academic press.

Lei J, Zhao D (2009) Structural heterogeneity of the Longmenshan fault zone and the mechanism of the 2008 Wenchuan earthquake (Ms 8.0). Geochem Geophys Geosyst 10, Q10010.doi:10.1029/2009GC002590

Lermo J, Chávez-García FJ (1994) Are microtremors useful in site response evaluation? Bull Seismol Soc Am 84, 1350-1364

Liu T, Hong H (2013) Simulation of Multiple-Station Ground Motions Using Stochastic Point-Source Method with Spatial Coherency and Correlation Characteristics. Bull Seismol Soc Am 103, 1912-1921

Madariaga R, 2007. Seismic Source Theory-4.02.

Mahin SA (1998) Lessons from damage to steel buildings during the Northridge earthquake. Eng Struct 20, 261-270

McGuire RK, Hanks TC (1980) RMS accelerations and spectral amplitudes of strong ground motion during the San Fernando, California earthquake. Bull Seismol Soc Am 70, 1907-1919

Mele G, Rovelli A, Seber D, Barazangi M (1997) Shear wave attenuation in the lithosphere beneath Italy and surrounding regions: tectonic implications. J Geophys Res 102, 11863-11875

Mittal H, Kumar A (2015) Stochastic finite-fault modeling of Mw 5.4 earthquake along Uttarakhand–Nepal border. Nat Hazards 75, 1145-1166.doi:10.1007/s11069-014-1367-1

Miyake H, Iwata T, Irikura K (2003) Source characterization for broadband ground-motion simulation: Kinematic heterogeneous source model and strong motion generation area. Bull Seismol Soc Am 93, 2531-2545

Motazedian D, Atkinson GM (2005) Stochastic finite-fault modeling based on a dynamic corner frequency. Bull Seismol Soc Am 95, 995-1010

Nakamura Y (1989) A method for dynamic characteristics estimation of subsurface using microtremor on the ground surface. Railway Technical Research Institute, Quarterly Reports 30, 25-33

Nigam N, 2004. Chapter 4: Seismic attenuation problem, Proceedings of the Eighth PIMS-MITACS Industrial Problem Solving Workshop. McGill University, pp. 53-67.

Ogiso M, Aoki S, Hoshiba M (2016) Real-time seismic intensity prediction using frequency-dependent site amplification factors. Earth Planets Space 68, 83

Oglesby DD, Day SM (2002) Stochastic fault stress: Implications for fault dynamics and ground motion. Bull Seismol Soc Am 92, 3006-3021

Ohno S, Ohta T, Ikeura T, Takemura M (1993) Revision of attenuation formula considering the effect of fault size to evaluate strong motion spectra in near field. Tectonophysics 218, 69-81

Oth A, Bindi D, Parolai S, Di Giacomo D (2011) Spectral analysis of K-NET and KiK-net data in Japan, Part II: On attenuation characteristics, source spectra, and site response of borehole and surface stations. Bull Seismol Soc Am 101, 667-687

Park Y, Wen Y, Ang A (1986) Random vibration of hysteretic systems under bi‑directional ground motions. Earthq Eng Struct Dynam 14, 543-557

Ran Y-K, Chen W-S, Xu X-W, Chen L-C, Wang H, Yang C-C, Dong S-P (2013) Paleoseismic events and recurrence interval along the Beichuan–Yingxiu fault of Longmenshan fault zone, Yingxiu, Sichuan, China. Tectonophysics 584, 81-90

Ran Y, Chen L, Chen J, Wang H, Chen G, Yin J, Shi X, Li C, Xu X (2010) Paleoseismic evidence and repeat time of large earthquakes at three sites along the Longmenshan fault zone. Tectonophysics 491, 141-153

Rathje EM, Faraj F, Russell S, Bray JD (2004) Empirical relationships for frequency content parameters of earthquake ground motions. Earthq Spectra 20, 119-144

Sabetta F, Pugliese A (1996) Estimation of response spectra and simulation of nonstationary earthquake ground motions. Bull Seismol Soc Am 86, 337-352

Safarshahi M, Rezapour M, Hamzehloo H (2013) Stochastic Finite-Fault Modeling of Ground Motion for the 2010 Rigan Earthquake, Southeastern Iran. Bull Seismol Soc Am 103, 223-235.doi:10.1785/0120120027

Saragoni G, Hart G (1974) Simulation of artificial earthquakes. Int J Earthq Eng Struct Dynam 2, 249-267

Sato H (2007) Synthesis of vector wave envelopes in three-dimensional random elastic media characterized by a Gaussian autocorrelation function based on the Markov approximation: Spherical wave case. J Geophys Res 112, B1. doi: 10.1029/2006JB004437

Schneider JF, Silva WJ, Stark C (1993) Ground motion model for the 1989 M 6.9 Loma Prieta earthquake including effects of source, path, and site. Earthq Spectra 9, 251-287

Sharma B, Mittal H, Kumar A (2015) A reappraisal of Attenuation of Seismic Waves and its relevance towards Seismic Hazard. Int J Advan Res 3, 296-305

Shearer PM, 2009. Introduction to seismology. Cambridge University Press.

Shen W, Zhong Q, Shi B (2014) Strong ground motion simulation for the 2013 Lushan M W6. 6 earthquake, Sichuan, China, based on the inversed and synthetic slip models. Earthq Sci 27, 377-389

Singh S, Ordaz M, Anderson J, Rodriguez M, Quaas R, Mena E, Ottaviani M, Almora D (1989) Analysis of near-source strong-motion recordings along the Mexican subduction zone. Bull Seismol Soc Am 79, 1697-1717

Snoke J (1987) Stable determination of (Brune) stress drops. Bull Seismol Soc Am 77, 530-538

Somerville PG, Smith NF, Graves RW, Abrahamson NA (1997) Modification of empirical strong ground motion attenuation relations to include the amplitude and duration effects of rupture directivity. Seismol Res Lett 68, 199-222

Spudich P, Frazer LN (1984) Use of ray theory to calculate high-frequency radiation from earthquake sources having spatially variable rupture velocity and stress drop. Bull Seismol Soc Am 74, 2061-2082

Stephenson WJ, Louie JN, Pullammanappallil S, Williams R, Odum JK (2005) Blind shear-wave velocity comparison of ReMi and MASW results with boreholes to 200 m in Santa Clara Valley: Implications for earthquake ground-motion assessment. Bull Seismol Soc Am 95, 2506-2516

Sun W, Okubo S (1998) Surface potential and gravity changes due to internal dislocations in a spherical Earth—II. Application to a finite fault. Geophys J Int 132, 79-88

Tallett-Williams S, Gosh B, Wilkinson S, Fenton C, Burton P, Whitworth M, Datla S, Franco G, Trieu A, Dejong M (2016) Site amplification in the Kathmandu

Valley during the 2015 M7. 6 Gorkha, Nepal earthquake. Bull Earthq Eng 14, 3301-3315

Toro GR, Abrahamson NA, Schneider JF (1997) Model of strong ground motions from earthquakes in central and eastern North America: best estimates and uncertainties. Seismol Res Lett 68, 41-57

Ugurhan B, Askan A (2010) Stochastic strong ground motion simulation of the 12 November 1999 Düzce (Turkey) earthquake using a dynamic corner frequency approach. Bull Seismol Soc Am 100, 1498-1512.doi:10.1785/0120090358

Van Houtte C, Drouet S, Cotton F (2011) Analysis of the origins of κ (kappa) to compute hard rock to rock adjustment factors for GMPEs. Bull Seismol Soc Am 101, 2926-2941

Xu X, Wen X, Yu G, Chen G, Klinger Y, Hubbard J, Shaw J (2009) Coseismic reverse-and oblique-slip surface faulting generated by the 2008 Mw 7.9 Wenchuan earthquake, China. Geology 37, 515-518

Yamazaki Y, Cheung KF, Lay T (2013) Modeling of the 2011 Tohoku Near-Field Tsunami from Finite-Fault Inversion of Seismic Waves. Bull Seismol Soc Am 103, 1444-1455

Zengin E, Cakti E (2014) Ground motion simulations for the 23 October 2011 Van, Eastern Turkey earthquake using stochastic finite fault approach. Bull Earthq Eng 12, 627-646

Zhang L, Chen G, Wu Y, Jiang H (2016) Stochastic ground-motion simulations for the 2016 Kumamoto, Japan, earthquake. Earth Planets Space 68, 1-13.doi:10.1186/s40623-016-0565-3

Zhang Z, Wang Y, Chen Y, Houseman GA, Tian X, Wang E, Teng J (2009) Crustal structure across Longmenshan fault belt from passive source seismic profiling. Geophys Res Lett 36, L17310.doi:10.1029/2009GL039580

Zhao JX (2010) Geometric spreading functions and modeling of volcanic zones for strong-motion attenuation models derived from records in Japan. Bull Seismol Soc Am 100, 712-732

CHAPTER 3

DEVELOPMENT OF A METHOD FOR ESTIMATING SITE AMPLIFICATION IN CONSIDERING THE SITE EFFECTS

3.1 INTRODUCTION

Let's start with the definition of site amplification. Site amplification indicates the amplitude of seismic wave is increased as it propagates through the soft soil layers near the surface (Borcherdt 1970; Field and Jacob 1995; Seekins et al. 1996; Bonilla et al. 1997; Olsen 2000). A significant site amplification can induce severe damages to engineered structures, especially for the case that megathrust earthquakes occur (Lermo and Chávez-García 1994; Mucciarelli and Monachesi 1999; Bakir et al. 2002; Boore et al. 2003; Dolce et al. 2003; Maruyama et al. 2010). Therefore, how to estimate site amplification accurately and evaluate the site response to large earthquakes is important in earthquake engineering. Besides, in the stochastic finite-fault method for simulating acceleration time series, site effect is one of three key factors which are considered to synthesize the amplitude spectrum (Ghasemi et al. 2010; Safarshahi et al. 2013; Zengin and Cakti 2014; Zhang et al. 2016b; Chen et al. 2017). Therefore, selecting the best method for estimating site amplification is important for the generation of acceleration time series.

For the site effect, two issues should be discussed and solved. (1) For the area with strong ground-motion stations, the site amplification can be determined based on the records of the seismic sensors on the surface and in the borehole. For two commonly used method mentioned above, the S/B and H/V spectral ratios techniques, which is more accurate? (2) For the area without strong ground motion stations, how to estimate site amplification?

In this chapter, a module is made for calculating site amplification based on spectral ratios between acceleration waves recorded by surface and borehole sensors in the same station. The site amplifications of 53 stations in Kyushu area are calculated. Also, whether the site amplification can be estimated by using the H/V spectral ratios technique is investigated based on the same strong ground-motion records. Before the estimation, the commonly used smoothing techniques are compared and the Konno-Ohmachi smoother is selected. And then, in order to estimate the site amplification for the location without strong motion records, an empirical relationship between site amplification and V_{S30} is established.

3.2 SURFACE-TO-BOREHOLE SPECTRAL RATIOS TECHNIQUE

The most important step of estimating site amplification is the selection of a proper reference site. In the surface-to-borehole ratios technique, a borehole record in situ is considered as the reference site (Liu et al. 1992; Satoh et al. 1995; Boore 2004; Satoh 2006; Kokusho and Sato 2008; Holt et al. 2017). In general, the observed acceleration time series on the surface and in the borehole are different in amplitude. For example, in Figure 3-1, the PGA of surface EW component of the station MYZH15 is more than ten times of that of borehole record. This difference rises from the site amplification of the soft soil layers.

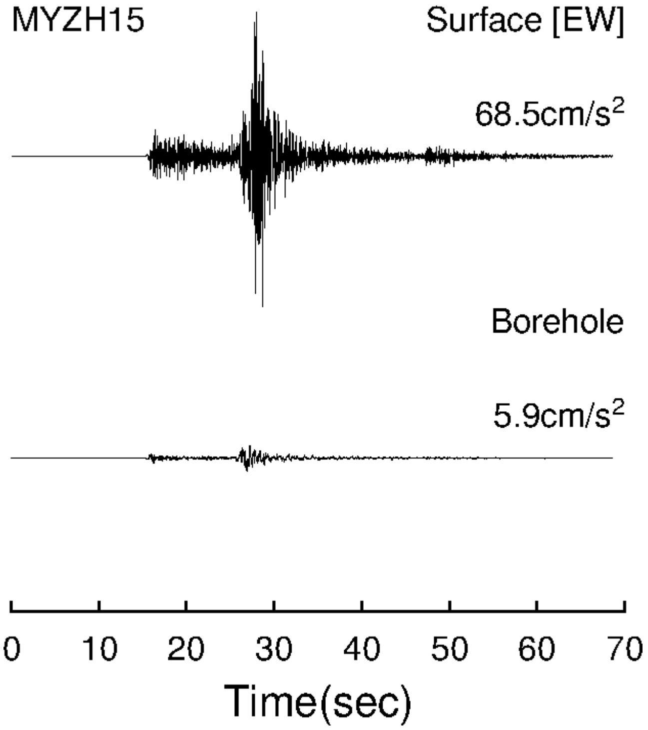

Figure 3-1 The surface and borehole acceleration time series of station MYZH15 EW component from the 13 July 2015 M5.7 Southern Oita earthquake

As one important division of standard spectral ratio approach, the surface-to-borehole ratios technique is more effective to determine the site amplification. The original standard spectral ratios technique takes the nearby rock site as the reference (Hartzell 1992; Kato et al. 1995; Hartzell et al. 1996; Su et al. 1996; Bard 1999). There are two problems in it. One is that it is hard to find a true reference rock site since the widespread weathered layer near the surface. The other is that the incidence wave field of the reference rock site may not be as same as that of the target soil site, if distance between them is not very close. Considering such limitations, the surface-to-borehole ratios technique is proposed to estimated site amplification. In the surface-to-borehole ratios technique, the reference rock site is at the bottom of a borehole, directly below the target soil site (Field and Jacob 1993; Steidl et al. 1996; Satoh et al. 1997; Margheriti et al. 2000; Bonilla et al. 2002; Rubinstein and Beroza 2005; Parolai et al. 2007; Oth et al. 2011). The depth effect in this thesis is also considered and corrected using the power spectral density ratios.

The borehole recordings have been obtained in many countries and regions, such as Japan, USA, and European counties (Trampert et al. 1993; Abercrombie 1995, 1998; Ide et al. 2003; Stork and Ito 2004; Langbein 2015). Take Japan as an example. The 1995 M6.9 Kobe, Japan earthquake killed more than 6400 people. After this devastating earthquake, a strong-motion observation network consisting of nearly 700 stations grows to be established, the so-called Kiban-Kyoshin network (KiK-net). For each station of this network, the strong-motion instruments are installed on the surface and at the bottom of borehole (Figure 3-2). The borehole of each station is at the depth of 100-200 m, which is usually considered as the engineering bedrock depth (Kawase and Matsuo 2004; Sawada et al. 2004; Kinoshita 2005; Petukhin et al. 2008; Okada 2013). With the enough electricity supplement and high techniques (Figure 3-3), the collected strong-motion records by KiK-net stations can be stored and provided to publics for free (Aoi et al. 2004; Fujiwara et al. 2004).

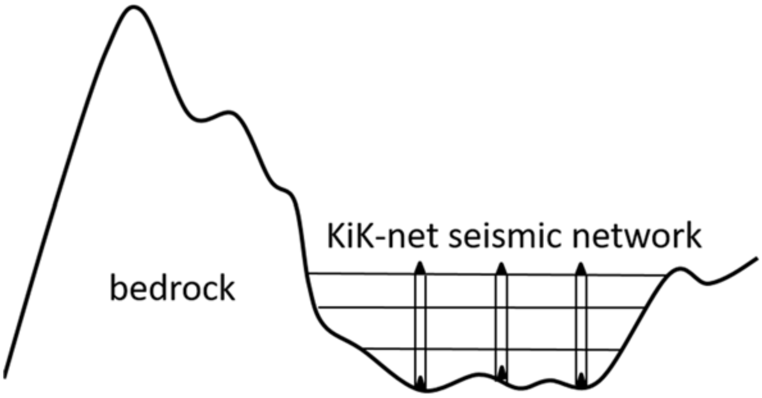

Figure 3-2 Sketch of KiK-net strong-motion network

It should be noted that in this thesis, the strong-motion data are all accessed from the KiK-net, which is operated by National Research Institute for Earth Science and Disaster Prevention (NIED).

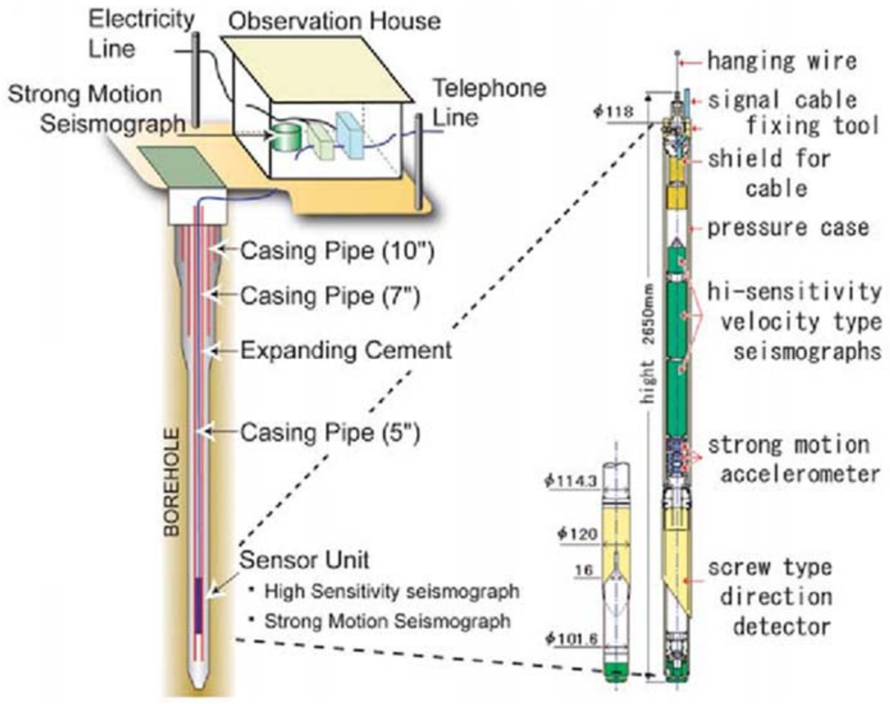

Figure 3-3 Observation facility for KiK-net. (after Aoi et al. (2004))

3.2.1 THEORETICAL BASIS

The surface-to-borehole technique has its physical foundation. In theory, the seismic-wave propagation consists of three critical processes, including source, path, and site effects. In the frequency domain, they are multiplied to synthesize the Fourier amplitude spectrum,

$$A(f)=A^{s}(f)A^{p}(f)A^{l}(f) \tag{3.1}$$

where, $A(f)$ is the synthesized Fourier amplitude spectrum, the variable on the right side of the equation (3.1) with superscript s, p, and l indicates the source, path, and site spectra, respectively. In the surface-to-borehole ratios technique, the site amplification in one station, $D(f)$, is determined using the equation

$$D(f)=A^{surface}(f)/A^{borehole}(f) \tag{3.2}$$

where the variable on the right side of equation above with superscript surface and borehole indications the Fourier amplitude spectra of recordings on the surface and in the borehole.

For equation (3.2), the source and path effects are all corrected by performing the division. There is no doubt that the source effect can be dismissed since both recordings are same for one earthquake. As for the path effect, maybe someone will doubt that the distances of source-to-surface and source-to-borehole are different. However, compare to the tens of kilometers hypocentral distance, the effect of 100-200 m borehole length can be neglected. For the site spectrum, in the stochastic method, it is composed of the kappa effect and site amplification. The specified kappa effect, $\exp(-\pi f \kappa)$, is also removed by division. Therefore, the site amplification can be represented by the ratios of Fourier amplitude spectrum of surface and borehole recordings at the same site. The so-called depth effect (Cadet et al, 2012) is also corrected by the following equations

$$S/B' = \frac{|S_{12}(f)|^2}{S_{11}(f)S_{22}(f)}(S/B) \tag{3.3}$$

Where $S_{11}(f)$ and $S_{22}(f)$ are the power spectral densities of the surface and borehole ground motions, respectively; $S_{12}(f)$ is the cross-power-spectral density function; S/B is the ratios determined by equation (3.2).

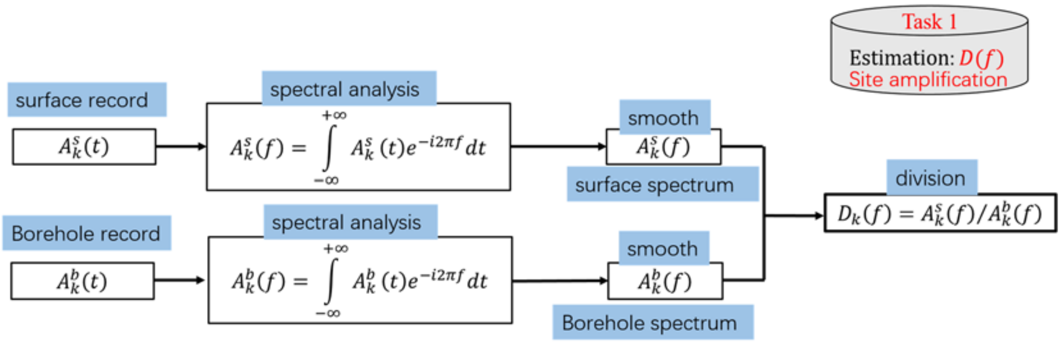

Figure 3-4 The procedure of estimating site amplification using S/B method

The procedure of determining the site amplification is illustrated in Figure 3-4 and introduced as follows

(1) Access the surface and borehole records in the same station;

(2) Based on the spectral analysis, perform the Fourier transform for the S-wave

windows extracted from the acceleration time series;

(3) Smooth the surface and borehole spectra; Since there are some noises, or the rapid random variations, in the raw S-wave amplitude spectrum, the smoothing operation guarantees the accuracy of estimating site amplification.

(4) Calculate the site amplification by dividing the surface spectra over the borehole ones.

For the spectral analysis, the Fourier transform is applied to the acceleration time series using the equation as follows,

$$A(f)=\int_{-\infty}^{+\infty} a(t)e^{-i2\pi f}dt \tag{3.4}$$

where $a(t)$ is the acceleration time series, $A(f)$ is the Fourier acceleration spectrum. It should be noted that the baseline of the record should be corrected first. Since the purpose of estimating site amplification is to simulate ground motions using the stochastic finite fault method which is based on the shear dislocation of a point source, the shear-wave window needs to be extracted from the record. The extracted shear-wave window is taped with a 10% of Hanning window at both ends to avoid the leaky of frequency.

An example of estimating site amplification based on the S/B spectral ratios technique is given as follows. The surface and borehole records in the NS component of station KGSH04 from the 2016 Kumamoto earthquake are selected to illustrate the process of estimating site amplification by S/B spectral ratios technique. (1) Extract the S-wave windows from the surface and borehole records (Figure 3-5); (2) Perform the spectral analysis for the surface and borehole records to determine the Fourier amplitude spectra (Figure 3-6); (3) Smooth the surface and borehole spectra using the Konno-Ohmachi smoother (Figure 3-7); (4) Calculate the surface-to-borehole spectral ratios (Figure 3-8).

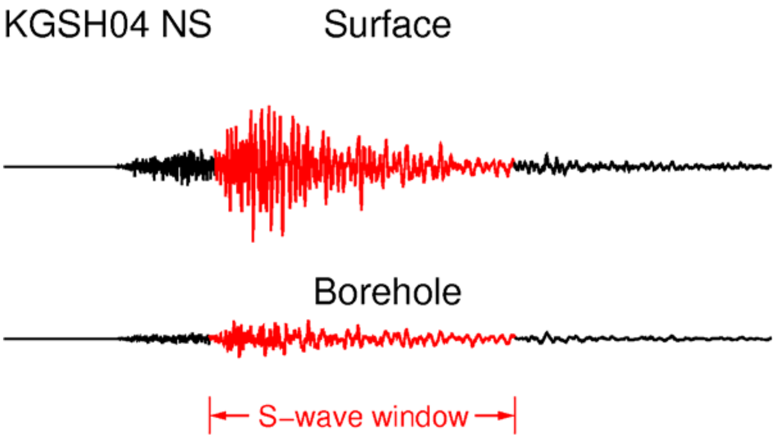

Figure 3-5 Surface and borehole records at station KGSH04 in the NS component

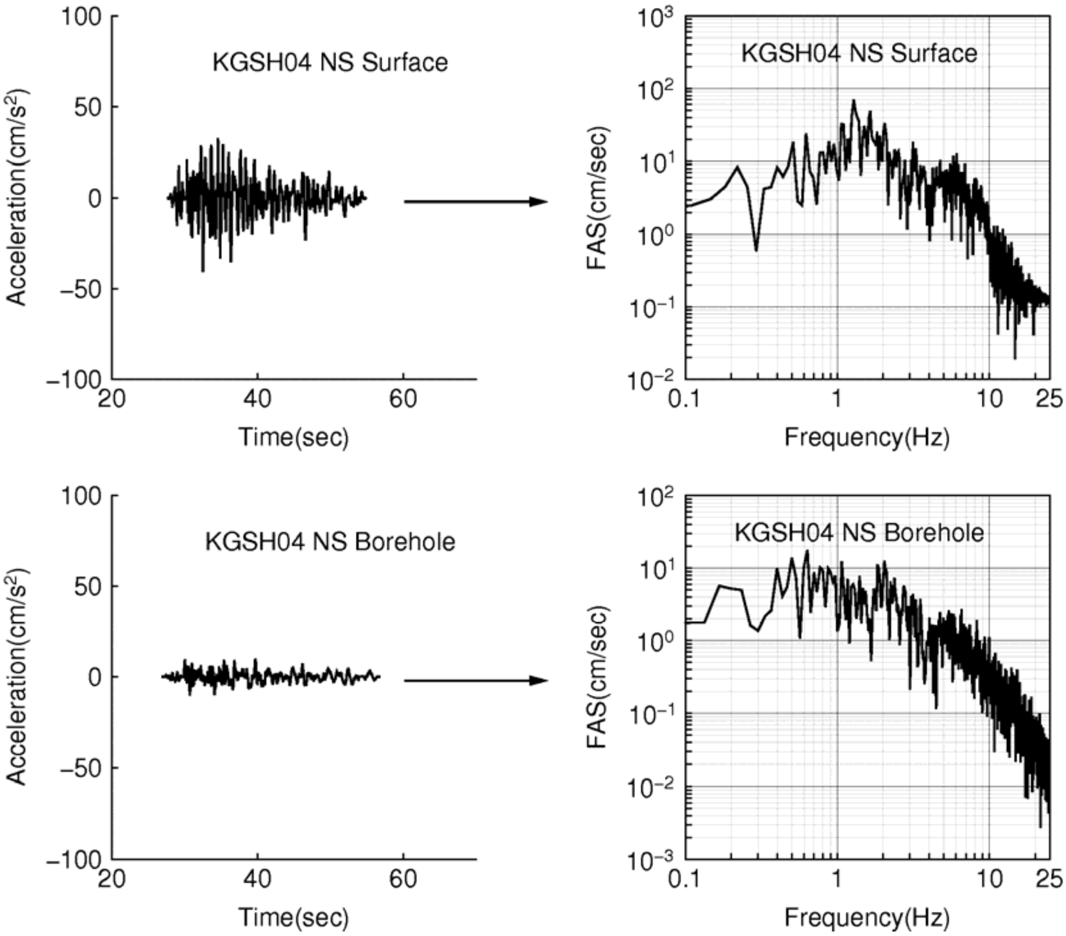

Figure 3-6 Spectral analysis of the S-wave windows of surface and borehole

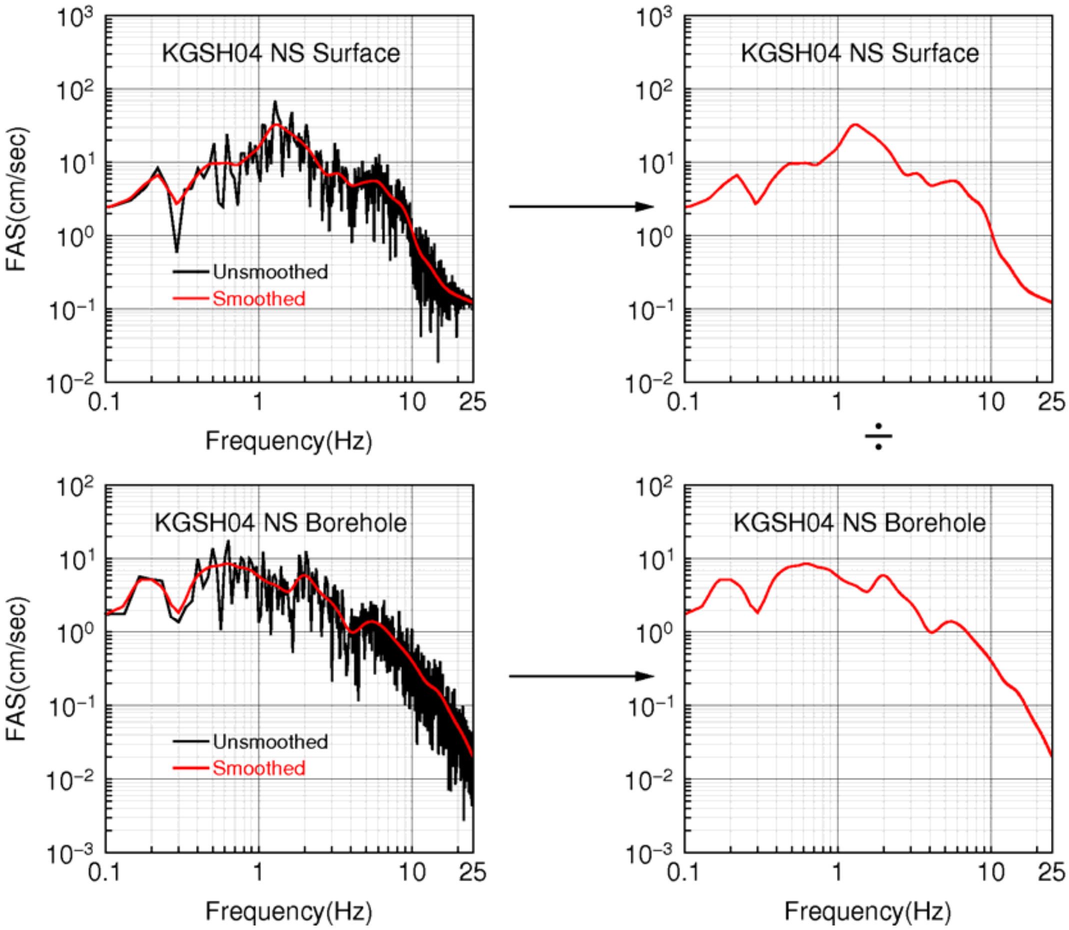

Figure 3-7 Illustration of smoothing the surface and borehole spectra at station KGSH04

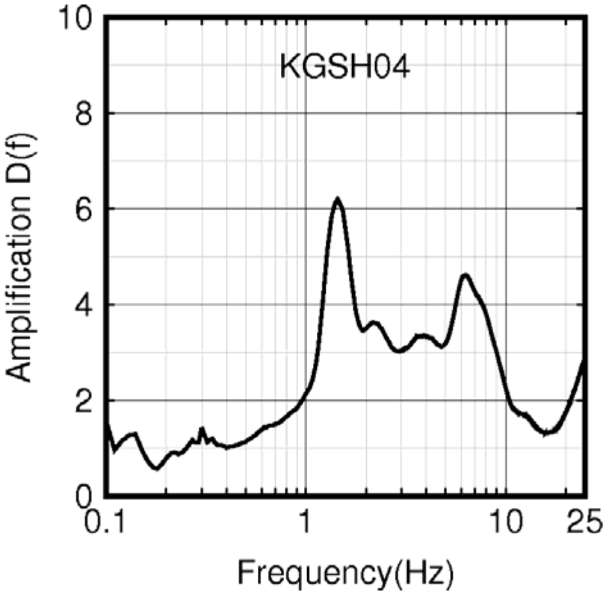

Figure 3-8 Site amplification of the station KGSH04 from the 2016 Kumamoto earthquake

3.2.2 SMOOTHING TECHNIQUE

As mentioned above, the smoothing operation should be done before the determination of spectral ratios to reduce the noise and evaluate the quality of signal (Bindi et al. 2006; Gueguen et al. 2011; Abdel-Rahman et al. 2012; Sivaram et al. 2012; Akkaya 2015; Layadi et al. 2016). Here the commonly used triangular and the Konno-Ohmachi smoothing techniques are introduced and compared.

3.2.2.1 COMMONLY USED SMOOTHING TECHNIQUES

Smoothing techniques include weighted and unweighted sliding-average smooth (Savitzky and Golay 1964; Robin et al. 1991; Sun et al. 1994; Holt 2004; Heitler 2009; Deak et al. 2010; Harris et al. 2010). For the unweighted smoothing technique, the original spectrum at the central frequency is alternated by the average of m adjacent frequencies, where is the so-called smooth width. For instance, for the case of $m = 5$,

$$A_i^s = \frac{A_{i-2}^u + A_{i-1}^u + A_i^u + A_{i+1}^u + A_{i+2}^u}{5} \tag{3.5}$$

where A_i^s and A_i^u are the ith frequency in the smoothed and unsmoothed amplitude spectra, respectively, for $i = 3$ to n-1, and n is the total number of frequencies in the spectra. Since the unweighted smoothing technique is so simple, it can be just used for some case without significant variation.

The other kind of smoothing approaches is the weighted one. One of the most popular weighted smoothing techniques is the so-called triangular smooth. For the case of $m = 5$,

$$A_i^s = \frac{A_{i-2}^u + 2A_{i-1}^u + 3A_i^u + 2A_{i+1}^u + A_{i+2}^u}{9}. \tag{3.6}$$

In the triangular smoothing, the assigned weight for each frequency decays from the central frequencies, and they are symmetrically balanced around the central frequencies, which looks like a triangle. Figure 3-9 shows the unsmoothed and unsmoothed Fourier amplitude spectrum of the station KMMH09 NS component from the 2016 Kumamoto, Japan earthquake. The smoothing width for this case are 0.2 Hz, 0.3 Hz, 0.5 Hz, 1 Hz, and 2 Hz, respectively. A wider smoothing width (e.g. 2 Hz) cannot provide an enough smooth at low frequencies, whereas a thinner smoothing width (e.g. 0.2 Hz) provide too much smooth at high frequencies. Therefore, many trials should be done to test which one is reasonable.

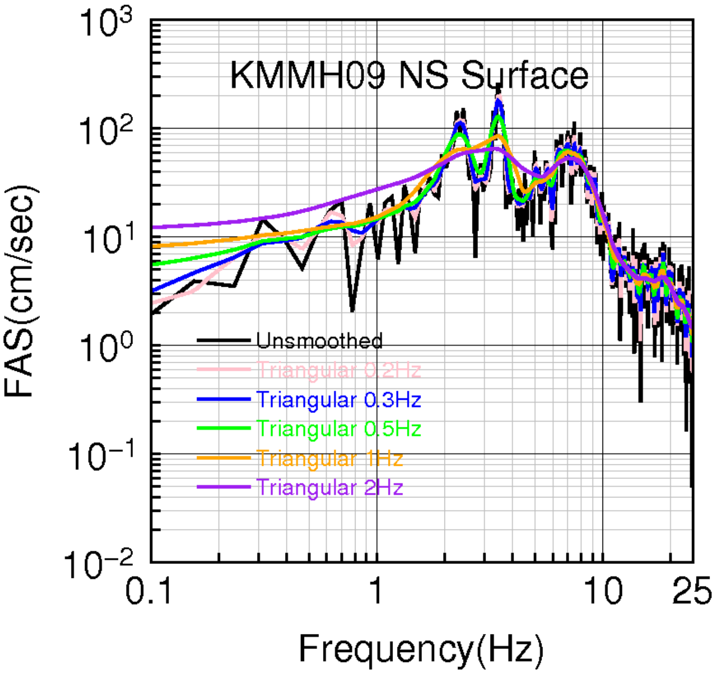

Figure 3-9 The smoothed Fourier amplitude spectra of station KMMH09 NS component from the 2016 Kumamoto earthquake using traditional smoothing techniques

3.2.2.2 KONNO-OHMACHI SMOOTHER

Based on the analysis above, the so-called Konno-Ohmachi weighted smoothing function is employed in the practical system for estimating site amplification more accurately (Konno and Ohmachi 1998). The specific form of this weighted smoothing function is shown as follows,

$$w(f, f_c) = \left[\sin\left(\log_{10}(f/f_c)^b\right) \Big/ \log_{10}(f/f_c)^b \right]^4 \tag{3.7}$$

where, b is an variable coefficient, f is the frequency, f_c is the central frequency. Figure 3-10 shows the smoothed Fourier amplitude spectrum of the station KMMH09 NS component using Konno-Ohmachi smoothing technique with the $b = 40$. It is suggested to use this smoothing parameter ($b = 40$) for all the spectra since it can provide an appropriate smoothing at both low and high frequencies.

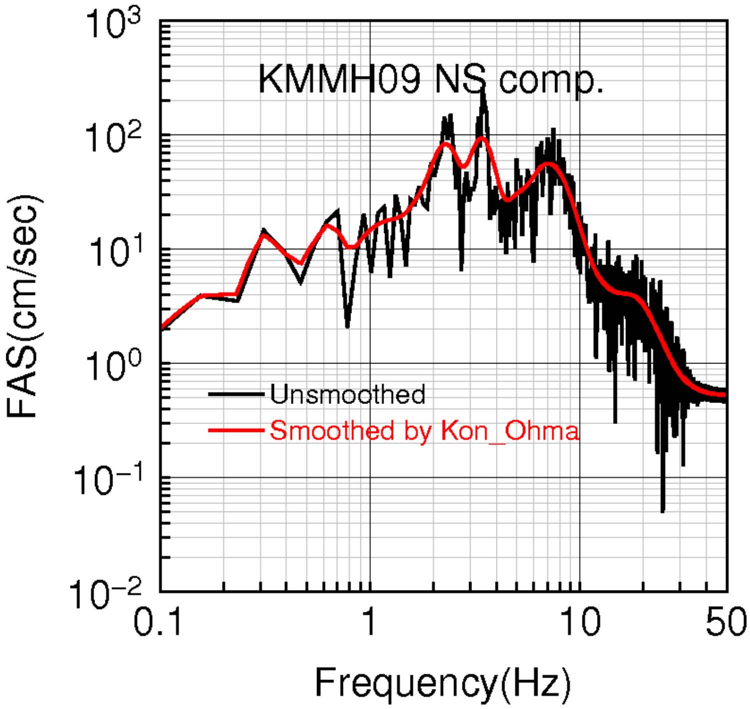

Figure 3-10 The smoothed Fourier amplitude spectra of station KMMH09 NS component from the 2016 Kumamoto earthquake using Konno-Ohmachi smoothing techniques

3.2.2.3 COMPARISON OF DIFFERENT SMOOTHING TECHNIQUES

The comparison of smoothed Fourier amplitude spectra using different techniques shows significant difference. How does this difference influence on the estimation of site amplification, and even on the simulated spectra? To solve this issue, we calculate the site amplification using smoothed Fourier amplitude spectra based on Konno-Ohmachi and triangular smoothers. Besides, the simulated Fourier amplitude spectra are also compared to validate the accuracy of Konno-Ohmachi smoother at both low and high frequencies.

Figure 3-11 and Figure 3-12 show the unsmoothed and smoothed Fourier amplitude spectra for station KMMH09 NS component using the surface and borehole recordings from the 2016 Kumamoto earthquake. The low- and high frequency characteristics of the Fourier amplitude spectra for both the surface and borehole recordings are well remained when using the Konno-Ohmachi smoother.

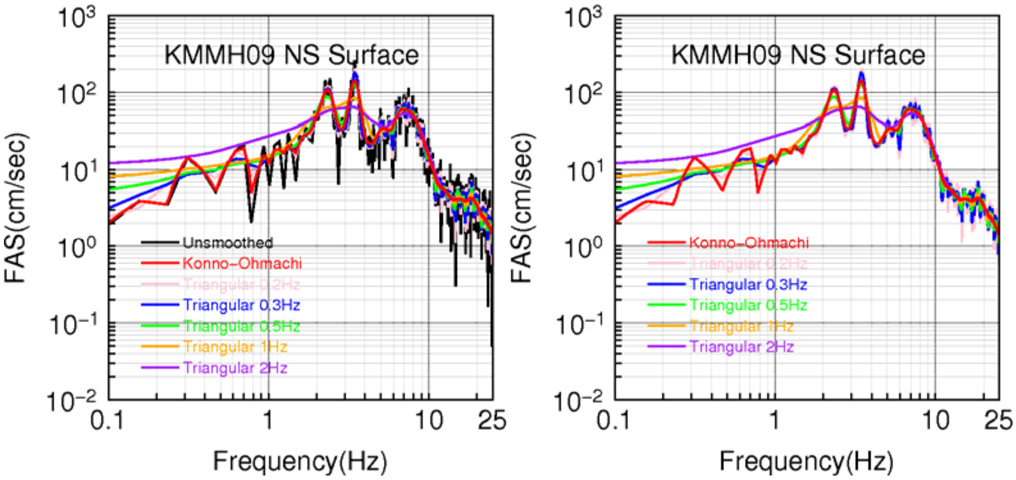

Figure 3-11 Smoothed and unsmoothed Fourier amplitude spectrum for station KMMH09 NS component using the surface recording

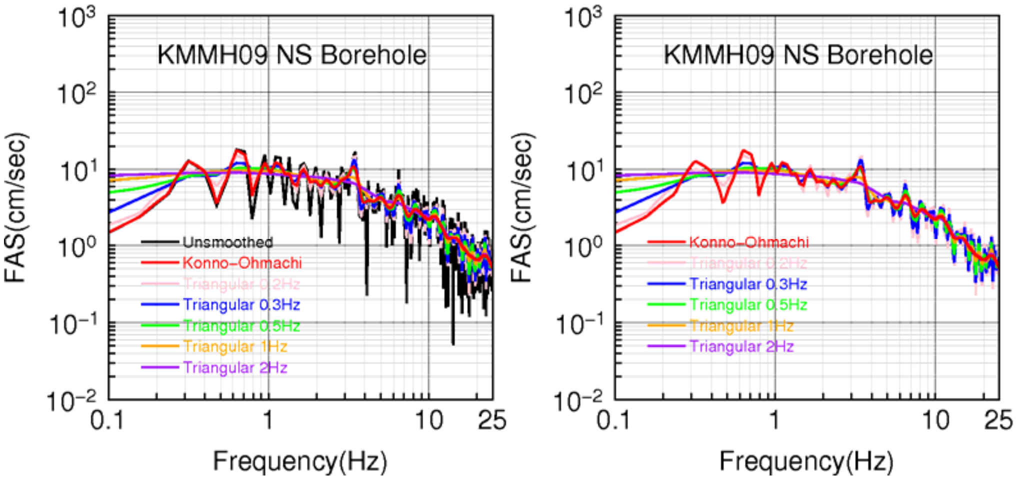

Figure 3-12 Smoothed and unsmoothed Fourier amplitude spectrum for station KMMH09 NS component using the borehole recording

Then the site amplification of station KMMH09 is determined using the surface-to-borehole ratios technique (Figure 3-13). At low-frequency part ($f < 2$ Hz in this case) , the site amplification shows significant differences. Compare to the commonly used techniques, the Konno-Ohmachi smoothing technique provides enough smoothing for the crest and trough of the spectrum.

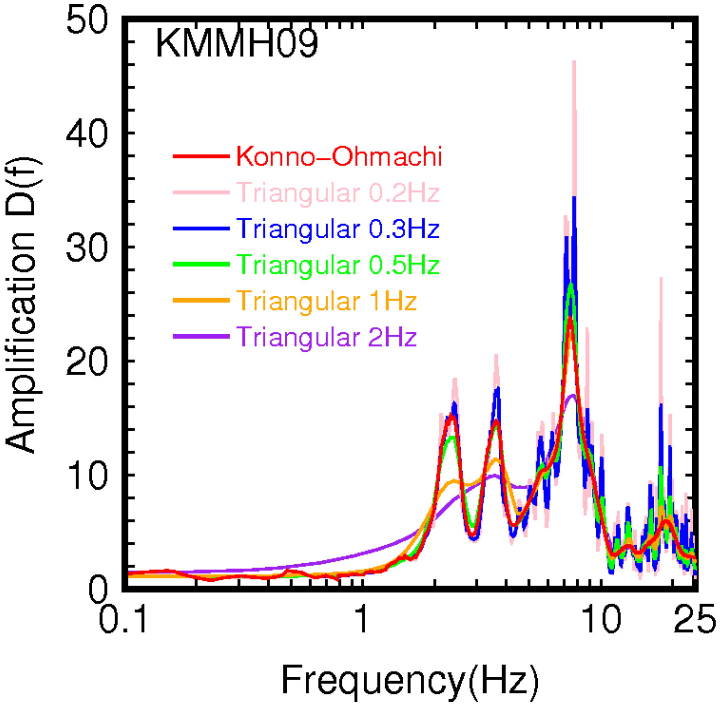

Figure 3-13 site amplification of station KMMH09 using different smoothing techniques without correcting the depth effect

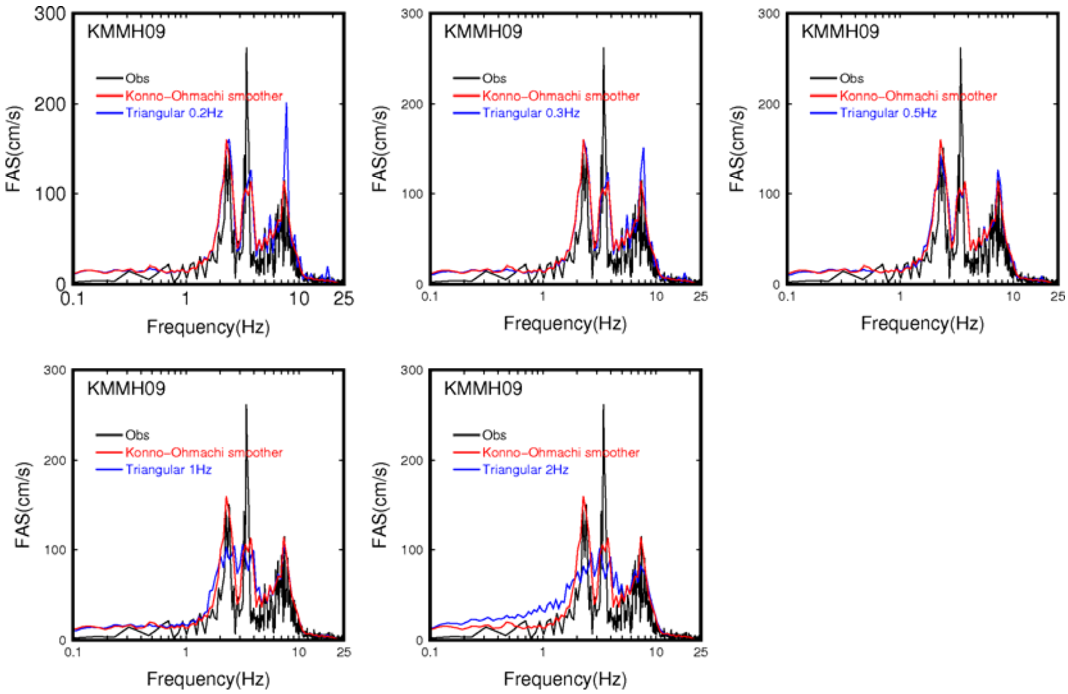

Figure 3-14 Comparison of observed and simulated spectra using different smoothing techniques.

To validate the practical smoothing technique furtherly, Fourier amplitude spectra are simulated using the site amplification in Figure 3-13 based on the stochastic finite-fault method (Figure 3-14). The simulated Fourier amplitude spectrum based on the Konno-Ohmachi smoothing technique matches the observed one better than those based on the triangular smoothing technique at low and high frequencies. For the triangular smoother, a thinner smooth width (e.g. 0.2 Hz) cannot matches the high-frequency part well, whereas a wider smooth width (e.g. 2 Hz) cannot matches the low-frequency part. Although the accuracy of 0.5 Hz- width is very close to that of Konno-Ohmachi, it is obtained after many trials. Therefore, the commonly used triangular smoother cannot provide a stable smoothing effect at both low and high frequencies. It is suggested to use the Konno-Ohmachi smoothing technique to smooth the Fourier spectra.

3.3 THE ESTIMATION OF SITE AMPLIFICATION IN THE REGION WITH SEISMIC SENSORS

Two commonly used techniques have been used to estimate the site amplification for the region with seismic sensors. The first method is the surface-to-borehole (S/B) spectral ratios technique. In this method, the surface and borehole recordings are selected to calculate the site amplification. It will be introduced in the following sections in detail. Another commonly used method to estimate the site amplification is the horizontal-to-borehole (H/V) spectral ratios technique (Chávez-García et al. 1996; Yamazaki and Ansary 1997; Albarello 2001; D'Amico and Mucciarelli 2002; Chavez-García et al. 2007; Gosar 2007; Nath et al. 2008). In this method, the vertical component is considered as the reference site to estimate the amplification. Since its simplicity and costly less, it is widely accepted. However, this method has some limitations. On the one hand, there is no physical basis to estimate the site amplifications. Specifically, there is no strong physical reason to take the vertical component as the reference (Paolucci 1999). On the other hand, in the H/V technique, the amplification in vertical component is neglected. In practical, although the vertical component of a record is considered as the reference site, strictly speaking, the vertical component is also amplified as seismic wave travels through the soft soil layers (Tucker and King 1984; Yang and Sato 2000; Ahmadizadeh and Shakib 2004; Elgamal and He 2004; Kunnath et al. 2008; Yamada et al. 2009; Buech et al. 2010; Fry et al. 2011). Therefore, the accuracy of this technique is dependent of the amplification extent of vertical component. For example, if the vertical component is larger than that of two horizontal components, this technique is invalid. In this case, the vertical component cannot be regarded as the reference as usual.

3.3.1 COMPARISON OF SITE AMPLIFICATION ESTIMATED BY USING S/B AND H/V SPECTRAL RATIOS TECHNIQUES

To select a good method for the estimation of site amplification, two most popular methods are compared using the 53 strong ground-motion stations in Kyushu Island. In earthquake engineering, two methods are commonly used for the estimation of site amplification. One is the surface-to-borehole (S/B) spectral ratios technique, the other is the horizontal-to-vertical (H/V) spectral ratios technique. Their strengths and limits have been introduced above. However, whether the H/V spectral ratios can be used for site amplification in Kyushu region should be investigated. 53 KiK-net records from the 2016 Kumamoto earthquake are used for this comparison. It is found that less than 30% stations support this assumption.

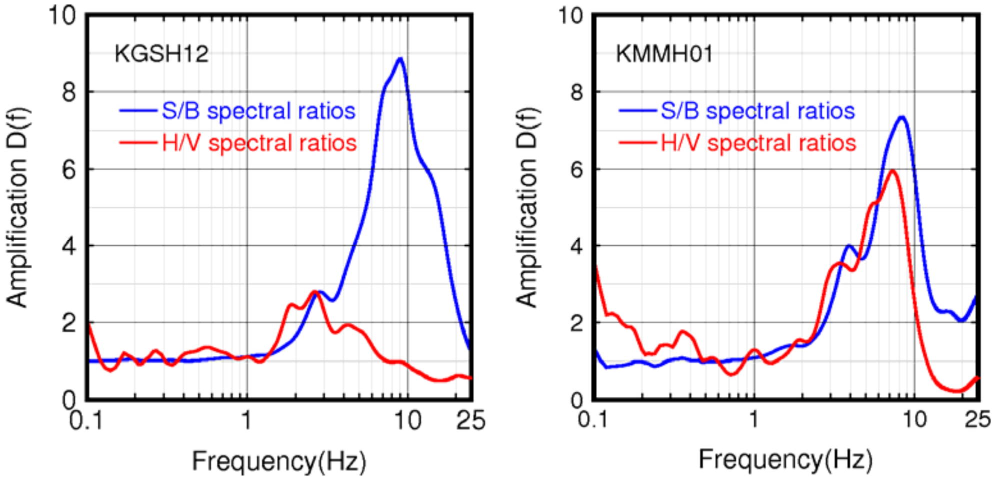

Figure 3-15 site amplification in two representative stations using S/B and H/V spectral ratios techniques

In Figure 3-15, the site amplification at two selected stations are shown. The left panel shows a bad agreement in both the amplification values and the fundamental frequency, which is the frequency corresponds to the peak amplification factors. There are more than 70% stations showing the bad agreement. The reason may come from the assumption that vertical component is considered does not amplify the seismic wave in the H/V method. However, in the real situation, the site amplification in the vertical component cannot be neglected. Therefore, in this thesis, we select the S/B spectral ratios technique to be the method for the estimation of site amplification.

3.3.2 SITE AMPLIFICATION IN KYUSHU REGION

According to the calculation and discussion above, the S/B spectral ratios technique is employed to determine the site amplification of the 53 KiK-net stations in Kyushu region (Figure 3-16).

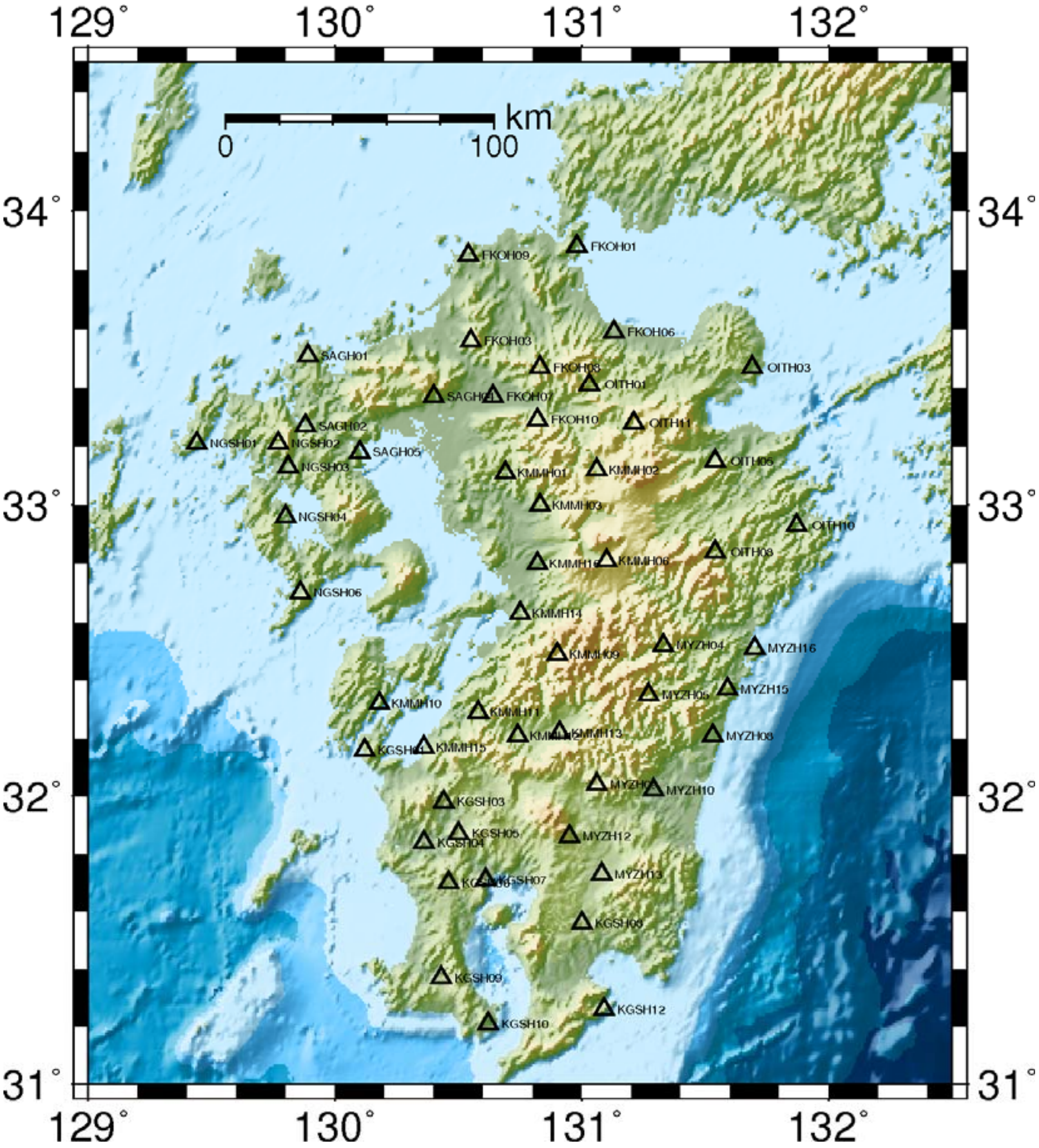

Figure 3-16 The location of KiK-net stations in the Kyushu region. Black open triangles are the stations.

The selected recordings should be the high-quality ones. Therefore, before the calculation of site amplification, signal-to-noise ratios of the records should be evaluated. In this thesis, we use the value of 3 as the cutoff threshold to pick the higher quality records. The signal-to-noise ratio is defined in this study as the ratio between the Fourier amplitude spectra of S-wave window and that of the pre-event noise window (Zaré and Bard 2002; Ktenidou et al. 2011). After the evaluation and selection of data source, the site amplification of KiK-net stations in Kyushu region are calculated and shown in Figure 3-17. Based on the calculated site amplification, the strong ground motion simulations of the 2016 Kumamoto earthquake can be performed.

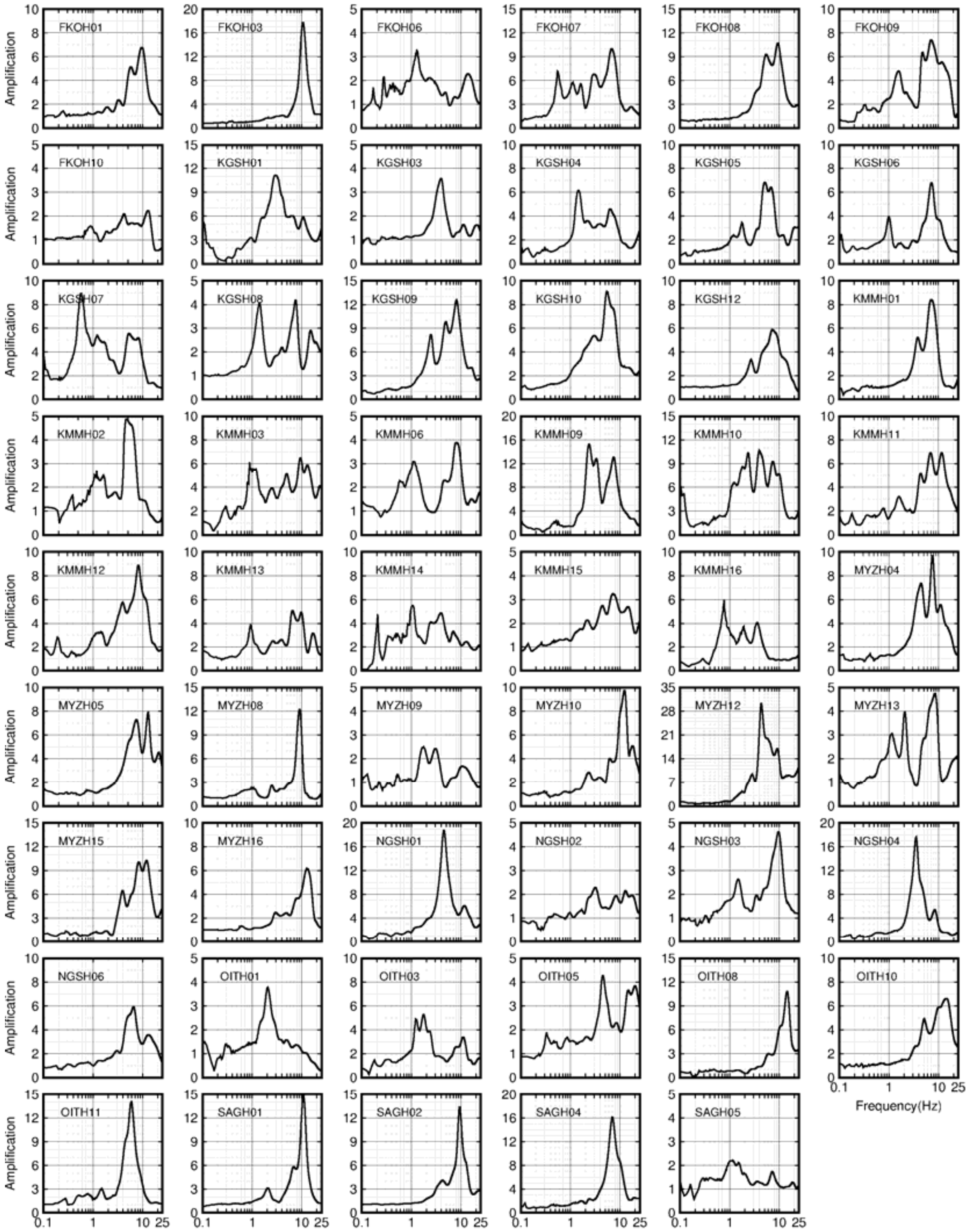

Figure 3-17 The site amplification of 53 KiK-net stations in Kyushu region

3.4 DEVELOPMENT OF A METHOD FOR ESTIMATING SITE AMPLIFICATION OF THE REGION WITHOUT STRONG-GROUND STATIONS

One of the most important purposes of earthquake engineering is to predict the ground motions for a region of most engineering interest. To achieve this goal, three kinds of information should be specified. That is, the source effect, path effect and the site response. Compare to the former two effects, the site response can be investigated before an earthquake in detail. Some necessary information, including thickness, depth, density and P- and S-wave velocity profile can be obtained from the logging database of strong ground-motion network. For example, the detailed soil condition data of Japan can be accessed from the KiK-net and K-NET logging profile. Figure 3-18 shows the soil condition image of the station FKOH09.

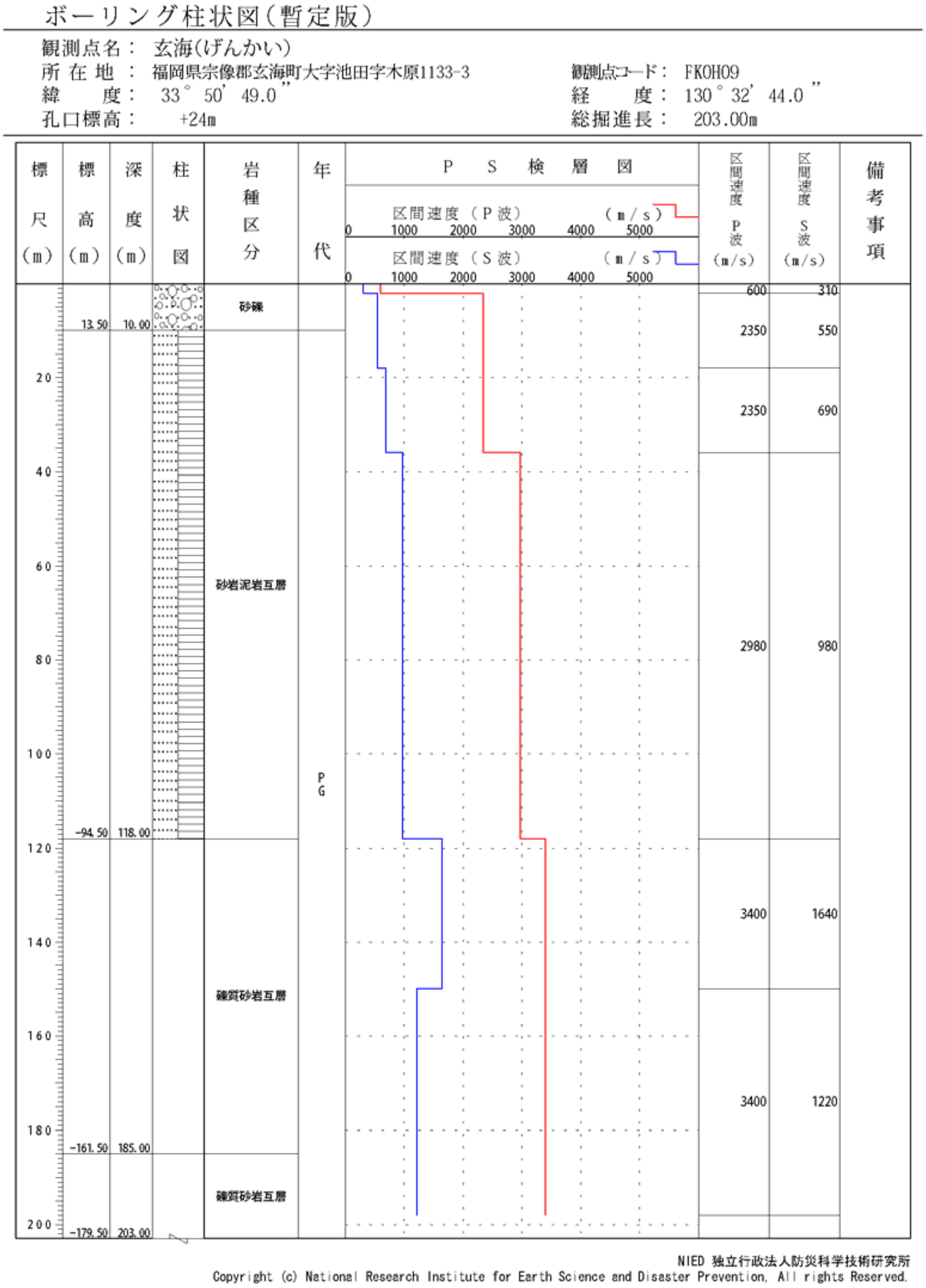

Figure 3-18 The soil condition image of the KiK-net station FKOH09. (Accessed from NIED)

For a specific site where a strong ground-motion station is installed, it is not difficult to determine the accurate site amplification using the surface-to-borehole spectral ratios technique. Rich data set is a strong support to the estimation of site amplification by considering the average response of the recorded events at one site. However, for the area without strong ground motion stations, how to estimate site amplification to meet the engineering demands is an important and urgent issue. The motivation for determining an empirical relation between the accurate site amplification and some other measures, which should relate to the geological conditions and are able to be accessed in a regional scale, rises from a practical demand to estimate the site amplification without strong ground motion stations. The so-called V_{S30} meets these criteria.

As the most widely used indicator for site classification, the V_{S30} represent the response of shallow soil layers. Borcherdt (1994) evaluates the influence of soil depth on the natural period of response spectra and PGA, and suggests to use the V_{S30}, the averaged shear-wave velocity to a depth of 30 m, to classify the site as 6 categories. And then this advice is selected by the NEHRP (BSSC, 2000) and the International Building Code (IBC) as a recommendation measure to classify the engineering site. The V_{S30} of 52 KiK-net stations in Kyuhsu region is determined and tabulated in Table 3-1. It should be noted that PS logging data of station KGSH08 is unavailable.

Table 3-1 V_{S30} of KiK-net stations in Kyushu region

Station code	Longitude ($^{\circ}E$)	Latitude ($^{\circ}N$)	V_{S30} (m/s)
FKOH01	130.9798	33.8849	588.5
FKOH03	130.5499	33.5608	497.0
FKOH06	131.1348	33.5925	1001.8
FKOH07	130.6354	33.3678	282.9
FKOH08	130.8285	33.4654	535.8
FKOH09	130.5432	33.8501	566.7
FKOH10	130.817	33.2891	921.3
KGSH01	130.1191	32.1554	603.0
KGSH03	130.4438	31.9812	1196.2

KGSH04	130.3602	31.8374	280.4
KGSH05	130.4958	31.8699	477.5
KGSH06	130.4594	31.6988	454.9
KGSH07	130.6149	31.714	260.0
KGSH09	130.4333	31.5618	409.1
KGSH10	130.6183	31.3741	254.9
KGSH12	131.0877	31.2066	451.6
KMMH01	130.6949	31.2583	574.6
KMMH02	131.0629	33.1089	576.7
KMMH03	130.8301	33.122	421.2
KMMH06	131.101	32.8114	567.8
KMMH09	130.9046	32.4901	399.7
KMMH10	130.1811	32.3151	176.9
KMMH11	130.5777	32.2918	1292.3
KMMH12	130.7371	32.2054	409.8
KMMH13	130.9096	32.2209	402.5
KMMH14	130.7521	32.6345	248.3
KMMH15	130.3647	32.1704	499.9
KMMH16	130.8199	32.7967	279.7
MYZH04	131.3349	32.5181	484.4
MYZH05	131.2668	32.347	1072.5
MYZH08	131.5309	32.2132	374.4
MYZH09	131.0618	32.0421	973.0
MYZH10	131.29	32.0215	494.7
MYZH12	130.9454	31.8643	319.5
MYZH13	131.0791	31.7301	251.2
MYZH15	131.5893	32.3654	445.7
MYZH16	131.6958	32.506	847.5
NGSH01	129.4353	33.2116	397.8
NGSH02	129.7652	33.2122	642.1
NGSH03	129.8102	33.1256	634.5

NGSH04	129.8026	32.9553	633.2
NGSH06	129.8625	32.6999	1421.1
OITH01	131.0326	33.4122	865.1
OITH03	131.6856	33.4736	486.0
OITH05	131.542	33.1525	1269.4
OITH08	131.5357	32.8392	657.4
OITH10	131.8695	32.9278	836.9
OITH11	131.2118	33.2844	458.0
SAGH01	129.8877	33.508	980.2
SAGH02	129.8798	33.2656	557.9
SAGH04	130.4046	33.3654	724.1
SAGH05	130.1046	33.1806	1000.0

And then, the relation between the V_{S30} and topography is established based on statistical analysis. Intuitively, the topography is a kind of indicators of rock type near the surface. The steep mountains usually indicate the existing hard rock, while the flat basin indicates the widely distributed soil layers. The strong correlations between the topography, such as the elevation and slope angle, and V_{S30} are revealed by some literatures (Matsuoka et al. 2005; Chiou and Youngs 2006; Wald and Allen 2007). To some extent, the slope or gradient can be used to judge the value range of V_{S30}, because most of the hard materials are more possible to combine as a steep slope, while the soft sediments are deposited mainly in the low gradient environments. Further, the fineness of the sedimentary materials should have a relationship with the slope. For instance, the steep and coarse mountain-front deposits generally grades to finer materials with the increasing distance and the decreasing slopes. Therefore, the empirical relation between the V_{S30} and topography is reasonable. In a regional scale, the V_{S30} can be estimated using these empirical relations. Figure 3-19 shows the V_{S30} distribution in Kyushu Island.

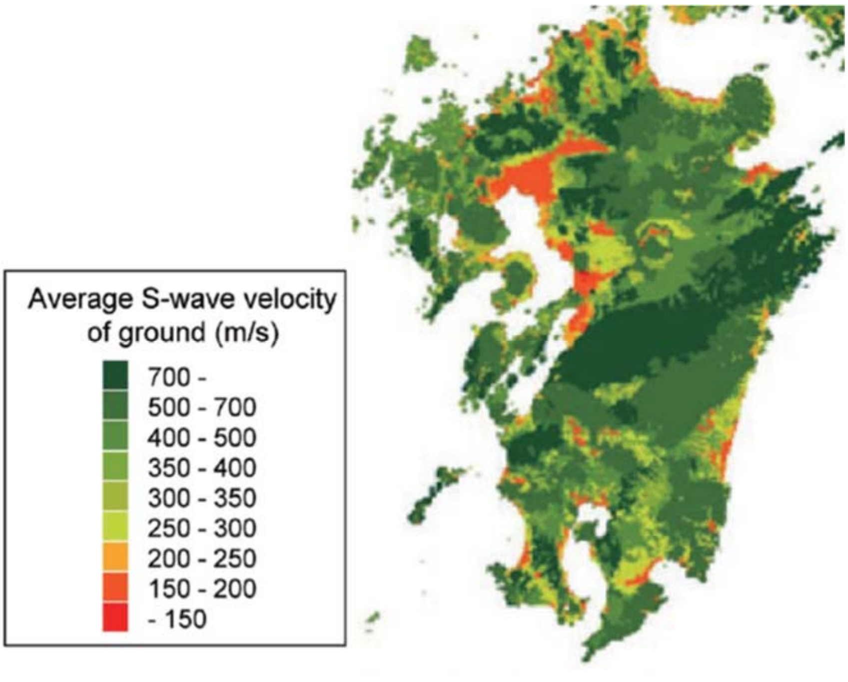

Figure 3-19 V_{S30} distribution of the Kyushu region (Matsuoka et al. (2005))

After obtaining the V_{S30} distribution, the site amplification of a region without strong ground-motion stations can be estimated by deriving the empirical relation between the site amplification and V_{S30}. In this chapter, four forms of empirical relations are developed as follows,

$$D(f) = a\left(V_{S30}/V_{ref}\right) + b \tag{3.8}$$

$$D(f) = a\log_{10}\left(V_{S30}/V_{ref}\right) + b \tag{3.9}$$

$$\log_{10} D(f) = a\log_{10}\left(V_{S30}/V_{ref}\right) + b \tag{3.10}$$

$$\log_{10} D(f) = a\left(V_{S30}/V_{ref}\right) + b \tag{3.11}$$

Here, the reference velocity, V_{ref}, referred as the value of 760 m/s, which is considered as the boundary of class A (hard rock) and B (firm to hard rock) sites in the NEHRP provisions (Table 3-2). The regression is performed in the frequency range of 0.1-25 Hz with a 0.05 Hz space. At each frequency, the linear-squares fit is used to obtain the regression coefficient of the V_{S30} and then to calculate site amplification of three components (NS, EW and UD), respectively. It should be noted that the site amplification in the regression are determined by equation (3.2). That is, the depth effect is neglected and not corrected. Figure 3-20 shows an example for the regression. It is clear that in log-linear space, the relation between site amplification and V_{S30} shows a linear trend.

Table 3-2 Site classification based on the V_{S30}

NEHRP Category	Description	V_{S30}
A	Hard rock	> 1500 m/s
B	Firm to hard rock	760-1500 m/s
C	Dense soil, soft rock	360-760 m/s
D	Stiff soil	180-360 m/s
E	Soft clays	< 180 m/s
F	Special study soils, e.g. liquefiable soils, sensitive clays, organic soils, soft clays > 36 m thick	

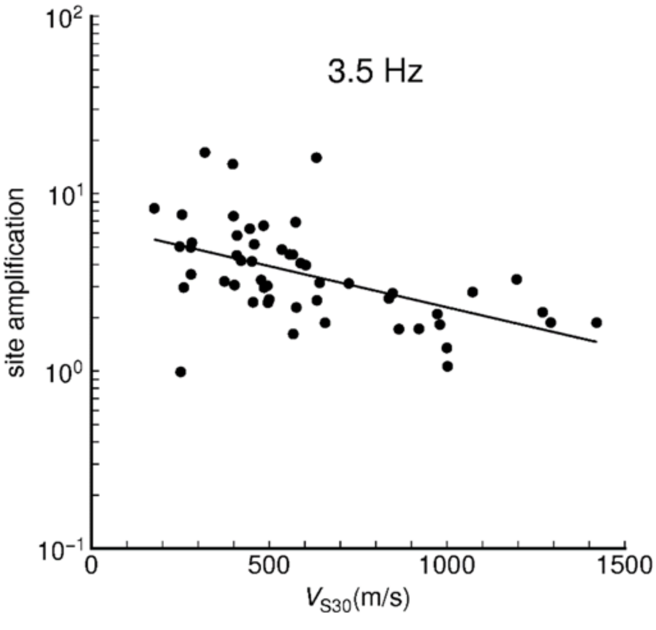

Figure 3-20 The relation between site amplification (EW) and V_{S30} at 3.5 Hz

The strong ground-motion recordings used for the determination of site amplification is accessed from the 2016 Kumamoto earthquake. The comparison of R-squares of these four empirical relations developed above shows that the forth one is the best due to its largest R-squares at most of the frequencies. Therefore, it is suggested to use the relation of $\log_{10} D\left(f\right)=a\left(V_{S30}/V_{ref}\right)+b$ to estimate the site amplification for a region without strong ground-motion records in Kyushu.

For simplicity, only a part of regression coefficients on the EW component is tabulated in Table 3-3. For a site of engineering interest, the V_{S30} should be identified first. And then, the site amplification can be estimated using the empirical relation (4) with the regression coefficients list in this form.

Table 3-3 Regression coefficients of equation (3.11) for site amplification, EW component

Frequency (Hz)	a	b	Frequency (Hz)	a	b
0.10	-0.0270	0.0713	3.45	-0.3519	0.8172
0.20	-0.0339	0.0393	3.95	-0.3317	0.8664
0.30	-0.1186	0.1608	4.55	-0.3018	0.8995
0.40	-0.1548	0.2119	5.50	-0.3355	0.9489
0.55	-0.1739	0.2503	6.00	-0.3395	0.9605
0.75	-0.2234	0.3698	7.00	-0.3103	0.9748
0.95	-0.2548	0.4259	8.05	-0.3148	0.9944
1.10	-0.2781	0.5093	9.25	-0.3258	0.9833
1.25	-0.2795	0.5388	10.70	-0.2200	0.8506
1.50	-0.2319	0.5294	12.30	-0.0713	0.6751
1.70	-0.2793	0.6052	14.20	-0.0083	0.5473
1.95	-0.3308	0.6607	16.35	-0.0196	0.4814
2.25	-0.3895	0.7275	18.85	-0.0486	0.4377
2.60	-0.4071	0.7930	21.70	-0.1022	0.4455
3.00	-0.3475	0.7836	25.00	-0.2296	0.5479

NEHRP: National Earthquake Hazard Reduction Program

Some stations which didn't record the 2016 Kumamoto earthquake are used for validation. There are 18 KiK-net station which meet this condition in Kyushu Island. However, they recorded other earthquake such as the 2005 Fukuoka earthquake. The site amplification of these stations are also calculated using the surface-to-borehole spectral ratios method using the records from the 2005 Fukuoka earthquake. To validate the method for the estimation of site amplification developed in this chapter, the site amplification at these stations are also determined by using their V_{S30}. These station can be classified into 5 categories based on the Table 3-2. For each class, one station is selected for validation.

Figure 3-21, Figure 3-22 and Figure 3-23 show the comparisons between the calculated and predicted site amplification for five-class sites on the NS, EW and UD components. By comparing the predicted results with those directly calculated from the records of both surface and borehole sensors, the good agreement in the frequency range of engineering interest shows the developed method is reasonable and adaptable.

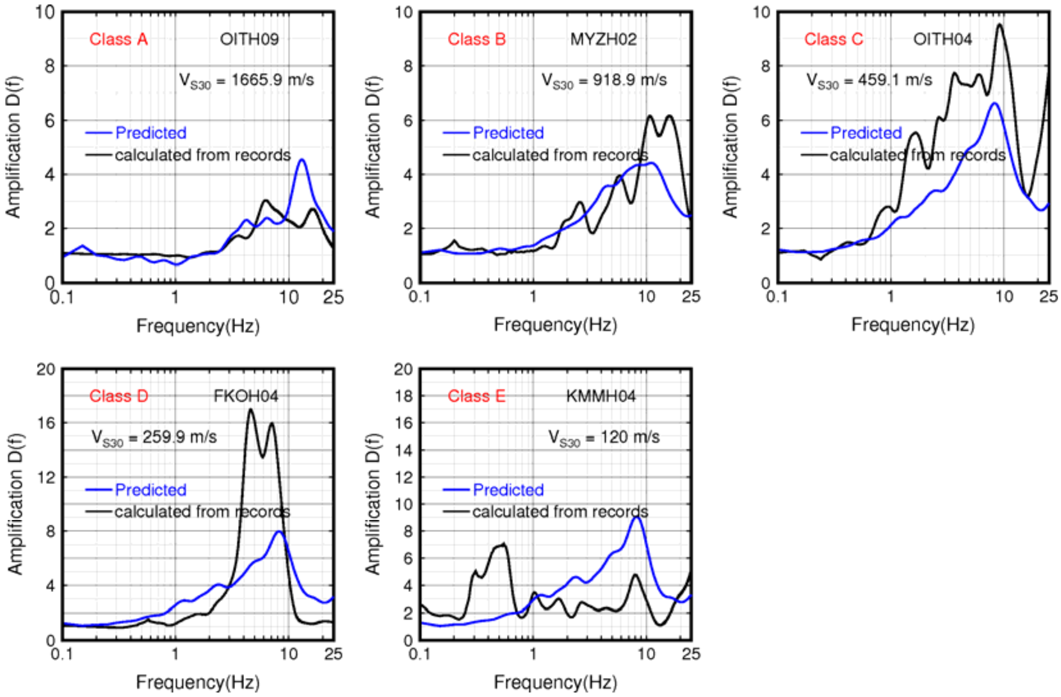

Figure 3-21 Comparison between calculated and predicted site amplification in the NS component of five-class sites

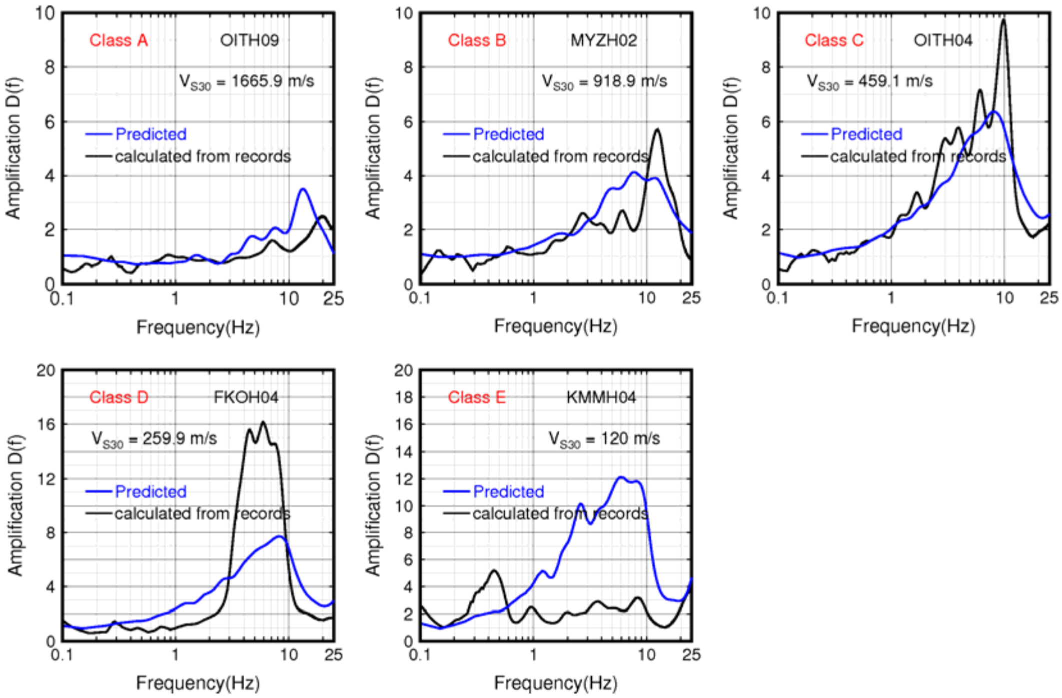

Figure 3-22 Comparison between calculated and predicted site amplification in the EW component of five-class sites

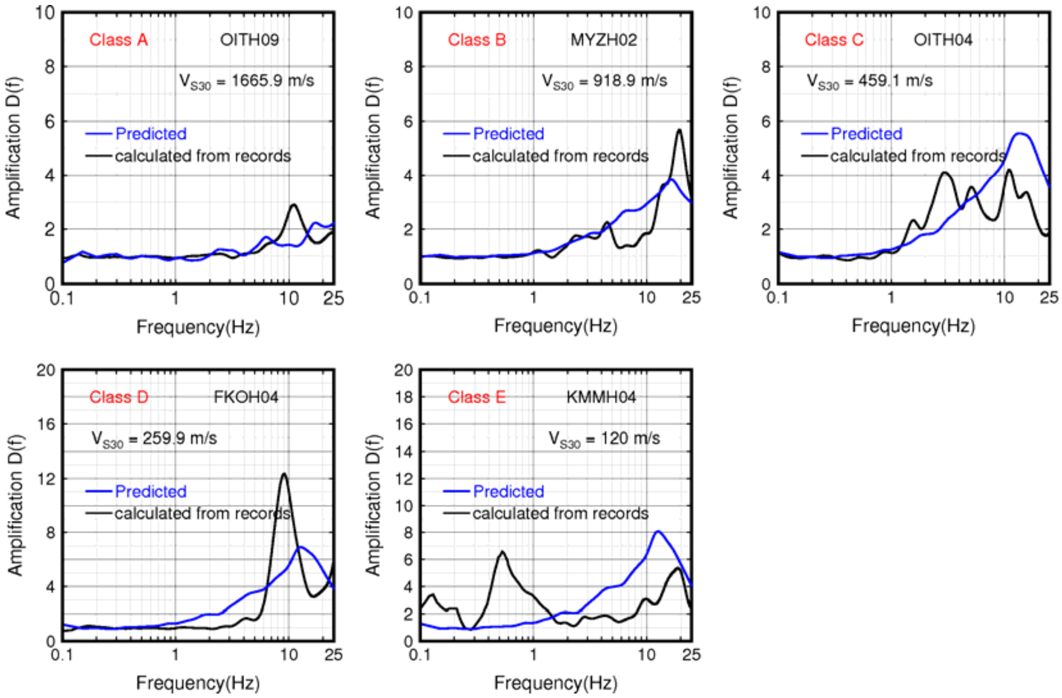

Figure 3-23 Comparison between calculated and predicted site amplification in the UD component of five-class sites

3.5 THE FLOWCHART OF ESTIMATION OF SITE AMPLIFICATION IN DEVELOPED PRACTICAL SYSTEM

In this thesis, a practical system for estimating ground motion is developed. As one of three important parts, the site amplification should be estimated first. Figure 3-24 shows the flowchart of the estimation of site amplification in developed system. The procedure for estimating site amplification is shown as follows.

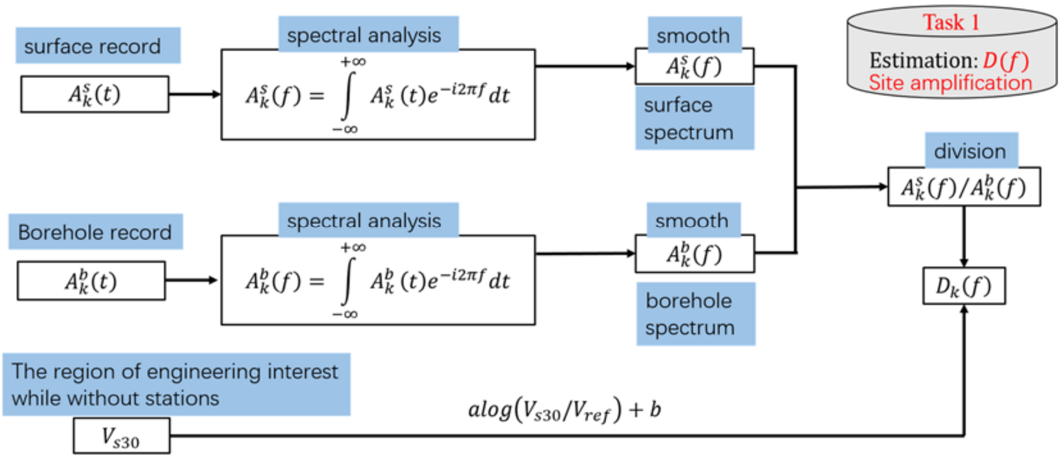

Figure 3-24 The flowchart of the estimation of site amplification

For the region with strong ground motion recordings, the procedures are

(1) Extract the S-wave window from the surface and borehole records in the same station;

(2) Based on the spectral analysis, perform the Fourier transform for the S-wave windows of surface and borehole;

(3) Smooth the Fourier amplitude spectra using Konno-Ohmachi smoothing technique;

(4) Calculate the site amplification by dividing the surface spectra over the borehole ones and correct the depth effect using equation (3.3).

For the region without strong ground motion recording, the site amplification is predicted by using the empirical relation of $\log_{10} D(f) = a\left(V_{S30}/V_{ref}\right) + b$.

Base on the procedure we designed, the site amplification will be prepared very well for the ground motion simulations.

3.6 CONCLUSIONS

The estimation of site amplification in the region without strong ground motion stations is an important issue for earthquake engineering. In this chapter, a method based on the surface-to-borehole spectral ratios technique and the V_{S30} is developed. The surface-to-borehole ratios technique is selected since it can represent the real site amplification in situ and solve the problem about the selection of a reference site. In this technique, both the surface and borehole recordings are required. One of the important steps is to smooth the Fourier amplitude spectra before the division of surface spectra over the borehole spectra. A practical Konno-Ohmachi smoothing technique is selected and incorporated into this module. The conclusions can be drawn as follows:

(1) A module of estimating the site amplification in the region with and without seismic sensors is made and incorporated in the developed practical system for earthquake ground-motion simulation. The specific procedure is introduced.

(2) The site amplification of the 53 KiK-net stations in the Kyushu region are calculated using the ground motion recordings from the 2016 Kumamoto earthquake based on the surface-to-borehole (S/B) and horizontal-to-vertical (H/V) spectral ratios techniques, respectively. It is found that less than 30% stations support the assumption of using the H/V methods to determine site amplification in the Kyushu region since the vertical amplification is obvious and cannot be neglected. Therefore, in this module, S/B spectral ratios technique is selected to determine the site amplification.

(3) The method for estimating site amplification in the region without strong ground-motion stations is developed, which is based on the empirical relation between the calculated site amplification and the so-called V_{S30}.

Four kinds of relations are selected to perform the least-squares fit to determine the regression coefficient. The relation in the form of $\log_{10} D(f) = a\left(V_{S30}/V_{ref}\right) + b$ is employed due to its larger R-squares. This method is validated by comparing the calculated and predicted site amplification in five-class sites.

(4) A practical smoothing technique, the Konno-Ohmachi smoother, is employed to smooth the surface and borehole Fourier spectra. Compare to the commonly used triangular smoothing techniques, this technique can provide a good smooth at both low- and high-frequency parts. This smoothing technique is incorporated in the module for the estimation of site amplification.

REFERENCE

Abdel-Rahman K, El AE-AKA, El-Hady S, Mohamed A, Abdel-Moniem E (2012) Fundamental site frequency estimation at New Domiat city, Egypt. Arab J Geosci 5, 653-661

Abercrombie RE (1995) Earthquake source scaling relationships from− 1 to 5 ML using seismograms recorded at 2.5-km depth. J Geophys Res 100, 24015-24036

Abercrombie RE (1998) A summary of attenuation measurements from borehole recordings of earthquakes: the 10 Hz transition problem. Pure Appl Geophys 153, 475-487

Ahmadizadeh M, Shakib H (2004) On the December 26, 2003, southeastern Iran earthquake in Bam region. Eng Struct 26, 1055-1070

Akkaya İ (2015) The application of HVSR microtremor survey method in Yüksekova (Hakkari) region, eastern Turkey. J African Earth Sci 109, 87-95

Albarello D (2001) Detection of spurious maxima in the site amplification characteristics estimated by the HVSR technique. Bull Seismol Soc Am 91, 718-724

Ambraseys N, Douglas J, Sarma S, Smit P (2005) Equations for the estimation of strong ground motions from shallow crustal earthquakes using data from Europe and the Middle East: horizontal peak ground acceleration and spectral acceleration. Bull Earthq Eng 3, 1-53

Aoi S, Kunugi T, Fujiwara H (2004) Strong-motion seismograph network operated by NIED: K-NET and KiK-net. Journal of Japan association for earthquake engineering 4, 65-74

Atkinson GM (2008) Ground-motion prediction equations for eastern north America from a referenced empirical approach: implications for epistemic uncertainty. Bull Seismol Soc Am 98, 1304-1318

Atkinson GM (2010) Ground-motion prediction equations for Hawaii from a referenced empirical approach. Bull Seismol Soc Am 100, 751-761

Atkinson GM (2015) Ground-motion prediction equation for small-to-moderate events at short hypocentral distances, with application to induced-seismicity hazards. Bull Seismol Soc Am 105.doi:10.1785/0120140142

Atkinson GM, Adams J (2013) Ground motion prediction equations for application to the 2015 Canadian national seismic hazard maps. Can J Civil Eng 40, 988-998

Atkinson GM, Boore DM (1995) Ground-motion relations for eastern North America. Bull Seismol Soc Am 85, 17-30

Atkinson GM, Boore DM (2006) Earthquake ground-motion prediction equations for eastern North America. Bull Seismol Soc Am 96, 2181-2205.doi:10.1785/0120050245

Bakir BS, Sucuoğlu H, Yilmaz T (2002) An overview of local site effects and the associated building damage in Adapazari during the 17 August 1999 Izmit earthquake. Bull Seismol Soc Am 92, 509-526

Bard P-Y (1999) Microtremor measurements: a tool for site effect estimation. The effects of surface geology on seismic motion 3, 1251-1279

Benjumea B, Hunter JA, Pullan SE, Brooks GR, Pyne M, Aylsworth JM (2008) VS 30 and fundamental site period estimates in soft sediments of the Ottawa Valley from near-surface geophysical measurements. J Environ Eng Geophys 13, 313-323

Bindi D, Massa M, Luzi L, Ameri G, Pacor F, Puglia R, Augliera P (2014) Pan-European ground-motion prediction equations for the average horizontal component of PGA, PGV, and 5%-damped PSA at spectral periods up to 3.0 s using the RESORCE dataset. Bull Earthq Eng 12, 391-430

Bindi D, Parolai S, Grosser H, Milkereit C, Karakisa S (2006) Crustal attenuation characteristics in northwestern Turkey in the range from 1 to 10 Hz. Bull Seismol Soc Am 96, 200-214

Bonilla LF, Steidl JH, Gariel J-C, Archuleta RJ (2002) Borehole response studies at the Garner Valley downhole array, southern California. Bull Seismol Soc Am 92, 3165-3179

Bonilla LF, Steidl JH, Lindley GT, Tumarkin AG, Archuleta RJ (1997) Site amplification in the San Fernando Valley, California: Variability of site-effect estimation using the S-wave, coda, and H/V methods. Bull Seismol Soc Am 87, 710-730

Boore DM (2004a) Can site response be predicted? J Earthq Eng 8, 1-41

Boore DM (2004b) Estimating Vs (30)(or NEHRP site classes) from shallow velocity models (depths< 30 m). Bull Seismol Soc Am 94, 591-597

Boore DM, Atkinson GM (2008) Ground-motion prediction equations for the average horizontal component of PGA, PGV, and 5%-damped PSA at spectral periods between 0.01 s and 10.0 s. Earthq Spectra 24, 99-138

Boore DM, Gibbs JF, Joyner WB, Tinsley JC, Ponti DJ (2003) Estimated ground motion from the 1994 Northridge, California, earthquake at the site of the Interstate 10 and La Cienega Boulevard bridge collapse, West Los Angeles, California. Bull Seismol Soc Am 93, 2737-2751

Boore DM, Stewart JP, Seyhan E, Atkinson GM (2014) NGA-West2 equations for predicting PGA, PGV, and 5% damped PSA for shallow crustal earthquakes. Earthq Spectra 30, 1057-1085

Boore DM, Thompson EM, Cadet H (2011) Regional correlations of VS30 and velocities averaged over depths less than and greater than 30 meters. Bull Seismol Soc Am 101, 3046-3059

Borcherdt RD (1970) Effects of local geology on ground motion near San Francisco

Bay. Bull Seismol Soc Am 60, 29-61

Borcherdt RD (1994) Estimates of site-dependent response spectra for design (methodology and justification). Earthq spectra 10, 617-653

Buech F, Davies T, Pettinga J (2010) The little red hill seismic experimental study: topographic effects on ground motion at a bedrock-dominated mountain edifice. Bull Seismol Soc Am 100, 2219-2229

Building Seismic Safety Council (BSSC) (2000). The 2000 NEHRP Recommended Provisions for New Buildings and Other Structures, Part I (Provisions) and Part II (Commentary), FEMA 368/369, Washington D.C.

Campbell KW, Bozorgnia Y (2008) NGA ground motion model for the geometric mean horizontal component of PGA, PGV, PGD and 5% damped linear elastic response spectra for periods ranging from 0.01 to 10 s. Earthq Spectra 24, 139-171

Castellaro S, Mulargia F (2009) VS30 estimates using constrained H/V measurements. Bull Seismol Soc Am 99, 761-773

Castellaro S, Mulargia F, Rossi PL (2008) VS30: Proxy for seismic amplification? Seismol Res Lett 79, 540-543

Chávez-García FJ, Sánchez LR, Hatzfeld D (1996) Topographic site effects and HVSR. A comparison between observations and theory. Bull Seismol Soc Am 86, 1559-1573

Chavez-García F, Dominguez T, Rodriguez M, Perez F (2007) Site effects in a volcanic environment: A comparison between HVSR and array techniques at Colima, Mexico. Bull Seismol Soc Am 97, 591-604

Chen C-T, Chang S-C, Wen K-L (2017) Stochastic ground motion simulation of the 2016 Meinong, Taiwan earthquake. Earth Planets Space 69, 62.doi:10.1186/s40623-017-0645-z

Chiou B, Darragh R, Gregor N, Silva W (2008) NGA project strong-motion database. Earthq Spectra 24, 23-44

Chiou BS-J, Youngs RR (2006) PEER-NGA empirical ground motion model for the average horizontal component of peak acceleration and pseudo-spectral acceleration for spectral periods of 0.01 to 10 seconds. PEER Report Draft, Pacific Earthquake Engineering Research Center, Berkeley, CA, 219-232

Choi Y, Stewart JP (2005) Nonlinear site amplification as function of 30 m shear wave velocity. Earthq Spectra 21, 1-30

D'Amico V, Mucciarelli M (2002) Validation through HVSR measurements of a method for the quick detection of site amplification effects from intensity data: an application to a seismic area in Northern Italy. Soil Dynam Earthq Eng 22, 475-483

Deak G, Curran K, Condell J, 2010. Wireless sensor networks-smoothing algorithms for RSSI-based device-free passive localisation, The Tenth International Conference on Information Technology and Telecommunications (IT&T 2010), pp. 99-107.

Dolce M, Masi A, Marino M, Vona M (2003) Earthquake damage scenarios of the building stock of Potenza (Southern Italy) including site effects. Bull Earthq Eng 1, 115-140

Elgamal A, He L (2004) Vertical earthquake ground motion records: an overview. J Earthq Eng 8, 663-697

Field E, Jacob K (1993) The theoretical response of sedimentary layers to ambient seismic noise. Geophys Res Lett 20, 2925-2928

Field EH, Jacob KH (1995) A comparison and test of various site-response estimation techniques, including three that are not reference-site dependent. Bull Seismol Soc Am 85, 1127-1143

Fry B, Benites R, Kaiser A (2011) The character of accelerations in the Mw 6.2 Christchurch earthquake. Seismol Res Lett 82, 846-852

Fujiwara H, Aoi S, Kunugi T, Adachi S (2004) Strong-motion Observation Networks of NIED: K-NET and KiK-net. Cosmos Report

Gallipoli M, Bianca M, Mucciarelli M, Parolai S, Picozzi M (2013) Topographic versus stratigraphic amplification: mismatch between code provisions and observations during the L’Aquila (Italy, 2009) sequence. Bull Earthq Eng 11, 1325-1336

Gallipoli MR, Mucciarelli M (2009) Comparison of site classification from VS30, VS10, and HVSR in Italy. Bull Seismol Soc Am 99, 340-351

Ghasemi H, Fukushima Y, Koketsu K, Miyake H, Wang Z, Anderson JG (2010) Ground-motion simulation for the 2008 Wenchuan, China, earthquake using the stochastic finite-fault method. Bull Seismol Soc Am 100, 2476-2490

Ghofrani H, Atkinson GM, Goda K, Assatourians K (2013) Stochastic finite-fault simulations of the 2011 Tohoku, Japan, earthquake. Bull Seismol Soc Am 103, 1307-1320

Gosar A (2007) Microtremor HVSR study for assessing site effects in the Bovec basin (NW Slovenia) related to 1998 M w 5.6 and 2004 M w 5.2 earthquakes. Eng Geology 91, 178-193

Gueguen P, Langlais M, Foray P, Rousseau C, Maury J (2011) A natural seismic isolating system: the buried mangrove effects. Bull Seismol Soc Am 101, 1073-1080

Héloïse C, Bard P-Y, Duval A-M, Bertrand E (2012) Site effect assessment using KiK-net data: part 2—site amplification prediction equation based on f 0 and Vsz. Bull Earthq Eng 10, 451-489

Harris P, Charlton M, Fotheringham AS (2010) Moving window kriging with geographically weighted variograms. Stochastic Environmental Research and Risk Assessment 24, 1193-1209

Hartzell S, Leeds A, Frankel A, Michael J (1996) Site response for urban Los Angeles using aftershocks of the Northridge earthquake. Bull Seismol Soc Am 86, S168-S192

Hartzell SH (1992) Site response estimation from earthquake data. Bull Seismol Soc Am 82, 2308-2327

Heitler W (2009) Practical tools for analysing rhythmic neural activity. Journal of neuroscience methods 185, 151-164

Holt CC (2004) Forecasting seasonals and trends by exponentially weighted moving averages. International journal of forecasting 20, 5-10

Holt J, Edwards B, Pilz M, Fäh D, Rietbrock A, 2017. Improving 1D Site Specific Velocity Profiles for the Kik-Net Network, EGU General Assembly Conference Abstracts, p. 3333.

Ide S, Beroza GC, Prejean SG, Ellsworth WL (2003) Apparent break in earthquake scaling due to path and site effects on deep borehole recordings. J Geophys Res 108

Kato K, Aki K, Takemura M (1995) Site amplification from coda waves: validation and application to S-wave site response. Bull Seismol Soc Am 85, 467-477

Kawase H, Matsuo H, 2004. Amplification characteristics of K-NET, KiK-net, and JMA Shindokei network sites based on the spectral inversion technique, 13th World Conference on Earthquake Engineering, Vancouver, Canada, pp. 1-6.

Kinoshita S (2005) Development of strong-motion observation network constructed by NIED. Directions in Strong Motion Instrumentation, 181-196

Kishida T, Boulanger RW, Abrahamson NA, Driller MW, Wehling TM (2009) Site effects for the Sacramento-San Joaquin Delta. Earthq Spectra 25, 301-322

Kokusho T, Sato K (2008) Surface-to-base amplification evaluated from KiK-net vertical array strong motion records. Soil Dynam Earthq Eng 28, 707-716

Konno K, Ohmachi T (1998) Ground-motion characteristics estimated from spectral ratio between horizontal and vertical components of microtremor. Bull Seismol Soc Am 88, 228-241

Ktenidou O-J, Chávez-García FJ, Pitilakis KD (2011) Variance reduction and signal-to-noise ratio: reducing uncertainty in spectral ratios. Bull Seismol Soc Am 101, 619-634

Kunnath SK, Erduran E, Chai Y, Yashinsky M (2008) Effect of near-fault vertical ground motions on seismic response of highway overcrossings. J Bridge Eng 13, 282-290

Langbein J (2015) Borehole strainmeter measurements spanning the 2014 Mw6. 0 South Napa Earthquake, California: The effect from instrument calibration. J Geophys Res 120, 7190-7202

Layadi K, Semmane F, Yelles-Chaouche A (2016) Site-Effects Investigation in the City of Chlef (Formerly El-Asnam), Algeria, Using Earthquake and Ambient Vibration Data. Bull Seismol Soc Am

Lermo J, Chávez-García FJ (1994) Are microtremors useful in site response evaluation? Bull Seismol Soc Am 84, 1350-1364

Liu H-P, Warrick RE, Westerlund RE, Sembera ED, Wennerberg L (1992)

Observation of local site effects at a downhole-and-surface station in the Marina District of San Francisco. Bull Seismol Soc Am 82, 1563-1591

Margheriti L, Azzara R, Cocco M, Delladio A, Nardi A (2000) Analysis of borehole broadband recordings: Test site in the Po basin, northern Italy. Bull Seismol Soc Am 90, 1454-1463

Maruyama Y, Yamazaki F, Mizuno K, Tsuchiya Y, Yogai H (2010) Fragility curves for expressway embankments based on damage datasets after recent earthquakes in Japan. Soil Dynam Earthq Eng 30, 1158-1167

Matsuoka M, Wakamatsu K, Fujimoto K, Midorikawa S, 2005. Nationwide site amplification zoning using GIS-based Japan engineering geomorphologic classification map, Proc. 9th int. conf. on struct. Safety and reliability, pp. 239-246.

Mucciarelli M, Monachesi G (1999) The bovec (Slovenia) earthquake, April 1998: preliminary quantitative association among damage, ground motion amplification and building frequencies. J Earthq Eng 3, 317-327

Nath S, Raj A, Sharma J, Thingbaijam K, Kumar A, Nandy D, Yadav M, Dasgupta S, Majumdar K, Kayal J (2008) Site Amplification, Qs, and Source Parameterization in Guwahati Region from Seismic and Geotechnical Analysis. Seismol Res Lett 79, 526-539

Okada Y, 2013. Recent progress of seismic observation networks in Japan, J Physics: Conference Series. IOP Publishing, p. 012039.

Olsen K (2000) Site amplification in the Los Angeles basin from three-dimensional modeling of ground motion. Bull Seismol Soc Am 90, S77-S94

Oth A, Bindi D, Parolai S, Di Giacomo D (2011) Spectral analysis of K-NET and KiK-net data in Japan, Part II: On attenuation characteristics, source spectra, and site response of borehole and surface stations. Bull Seismol Soc Am 101, 667-687

Paolucci R (1999) Numerical evaluation of the effect of cross-coupling of different components of ground motion in site response analyses. Bull Seismol Soc Am 89, 877-887

Parolai S, Mucciarelli M, Gallipoli M, Richwalski S, Strollo A (2007) Comparison of empirical and numerical site responses at the Tito test site, southern Italy. Bull Seismol Soc Am 97, 1413-1431

Petukhin A, Irikura K, Okazaki A, Hada K, Miyakoshi K, 2008. Estimation of the low-frequency Q-value (below 1Hz), 2003 Joint Meeting of Earth and Planetary Science, Chiba, Japan. CD-ROM, pp. S225-P001.

Pitilakis K, Riga E, Anastasiadis A (2012) Design spectra and amplification factors for Eurocode 8. Bull Earthq Eng, 1-24

Poovarodom N, Plalinyot N (2013) Site characterization in the Greater Bangkok area by microtremor observations. J Earthq Eng 17, 209-226

Pousse G, Berge-Thierry C, Bonilla LF, Bard P-Y (2005) Eurocode 8 design response spectra evaluation using the K-Net Japanese database. J Earthq Eng 9, 547-574

Pulido N, Matsuoka M, 2006. Broadband strong motion simulation of the 2004 Niigata-ken Chuetsu earthquake: Source and site effects, Third international symposium on the effects of surface geology on seismic motion, Grenoble, France, pp. 657-666.

Robin M, Sudicky E, Gillham R, Kachanoski R (1991) Spatial variability of strontium distribution coefficients and their correlation with hydraulic conductivity in the Canadian Forces Base Borden aquifer. Water Resources Research 27, 2619-2632

Rubinstein JL, Beroza GC (2005) Depth constraints on nonlinear strong ground motion from the 2004 Parkfield earthquake. Geophys Res Lett 32

Safarshahi M, Rezapour M, Hamzehloo H (2013) Stochastic Finite-Fault Modeling of Ground Motion for the 2010 Rigan Earthquake, Southeastern Iran. Bull Seismol Soc Am 103, 223-235.doi:10.1785/0120120027

Satoh T (2006) Inversion of Qs of deep sediments from surface-to-borehole spectral ratios considering obliquely incident SH and SV waves. Bull Seismol Soc Am 96, 943-956

Satoh T, Kawase H, Sato T (1995) Evaluation of local site effects and their removal from borehole records observed in the Sendai region, Japan. Bull Seismol Soc Am 85, 1770-1789

Satoh T, Kawase H, Sato T (1997) Statistical spectral model of earthquakes in the eastern Tohoku district, Japan, based on the surface and borehole records observed in Sendai. Bull Seismol Soc Am 87, 446-462

Savitzky A, Golay MJ (1964) Smoothing and differentiation of data by simplified least squares procedures. Analytical chemistry 36, 1627-1639

Sawada Y, Taga M, Watanabe M, Nakamoto T, Nagumo H, Kudo K, Horike M, Sakajiri N, Sasatani T (2004) Applicability of microtremor H/V method for KiK-net strong motion observation sites and Nobi plain. Proceedings of 13th WCEE, paper

Seekins LC, Wennerberg L, Margheriti L, Liu H-P (1996) Site amplification at five locations in San Francisco, California: A comparison of S waves, codas, and microtremors. Bull Seismol Soc Am 86, 627-635

Seyhan E, Stewart JP (2014) Semi-empirical nonlinear site amplification from NGA-West2 data and simulations. Earthq Spectra 30, 1241-1256

Sivaram K, Mahesh P, Rai S (2012) Stability assessment and quantitative evaluation of H/V spectral ratios for site response studies in Kumaon Himalaya, India using ambient noise recorded by a broadband seismograph network. Pure Appl Geophys 169, 1801-1820

Steidl JH, Tumarkin AG, Archuleta RJ (1996) What is a reference site? Bull Seismol Soc Am 86, 1733-1748

Stork A, Ito H (2004) Source parameter scaling for small earthquakes observed at the western Nagano 800-m-deep borehole, central Japan. Bull Seismol Soc Am 94, 1781-1794

Su F, Anderson JG, Brune JN, Zeng Y (1996) A comparison of direct S-wave and coda-wave site amplification determined from aftershocks of the Little Skull Mountain earthquake. Bull Seismol Soc Am 86, 1006-1018

Sun X-Y, Singh H, Millier B, Warren CH, Aue WA (1994) Noise, filters and detection limits. Journal of Chromatography A 687, 259-281

Trampert J, Cara M, Frogneux M (1993) SH propagator matrix and Qs estimates from borehole-and surface-recorded earthquake data. Geophys J Int 112, 290-299

Tucker B, King J (1984) Dependence of sediment-filled valley response on input amplitude and valley properties. Bull Seismol Soc Am 74, 153-165

Wald DJ, Allen TI (2007) Topographic slope as a proxy for seismic site conditions and amplification. Bull Seismol Soc Am 97, 1379-1395

Yamada M, Mori J, Heaton T (2009) The slapdown phase in high-acceleration records of large earthquakes. Seismol Res Lett 80, 559-564

Yamazaki F, Ansary MA (1997) Horizontal-to-vertical spectrum ratio of earthquake ground motion for site characterization. Earthq Eng Struct Dynam 26, 671-689

Yang J, Sato T (2000) Interpretation of seismic vertical amplification observed at an array site. Bull Seismol Soc Am 90, 275-285

Zaré M, Bard P-Y (2002) Strong motion dataset of Turkey: data processing and site classification. Soil Dyn Earthq Eng 22, 703-718

Zengin E, Cakti E (2014) Ground motion simulations for the 23 October 2011 Van, Eastern Turkey earthquake using stochastic finite fault approach. Bull Earthq Eng 12, 627-646

Zhang L, Chen G, Wu Y, Jiang H (2016) Stochastic ground-motion simulations for the 2016 Kumamoto, Japan, earthquake. Earth Planets Space 68, 1-13.doi:10.1186/s40623-016-0565-3

CHAPTER 4

DEVELOPMENT OF A PRACTICAL ANALYSIS METHOD FOR THE ESTIMATION OF SHEAR-WAVE ATTENUATION CONSIDERING VOLCANIC EFFECT

In the active tectonic regions, earthquakes usually occur with the severe magmatic activities (Wyss et al. 1997; Italiano et al. 1998; Ishizuka et al. 2015; Saita et al. 2015). Sometimes the active volcanoes play an important role in the nucleation of megathrust earthquakes due to the complex stress field, sometimes they stop the ruptures or dislocations propagating (Nakamura 1977; Giudice and Rasà 1992; Gudmundsson et al. 1997; Takada and Fukushima 2013). For example, in the 2016 Kumamoto, Japan, earthquakes, the surface ruptures on the Futagawa fault stopped in front of the Aso volcano, one of the 7 active volcanoes in Kyushu Island (Suleiman and Doser 1995; Davies et al. 2008; Lin et al. 2016; Lin et al. 2017). Besides, low-frequency micro-earthquakes with the magnitude of 0.5-4.5 are identified and located beneath the active volcanoes (Hasegawa and Yamamoto 1994; Nakamichi et al. 2003; Giampiccolo et al. 2007; Takahashi et al. 2007). It is ensured that the magmatic activities change the tectonic settings and homogeneity of earth medium, which caused by dehydration of the subducting slab and corner flow in the mantle wedge above the slab (Cavinato and De Celles 1999; Long and van der Hilst 2006; Wada et al. 2008; Zhao et al. 2011). The high temperature in the medium beneath the volcanoes prompts the process of the dehydration and changes the properties of overburden rock layers (Iwamori 2000; Van Keken et al. 2002; Hattori and Guillot 2003; Plank et al. 2009). Therefore, when seismic wave propagates through the volcanic area, the extent of decay loss of seismic wave is different from that in the non-volcanic area. Figure 4-1 shows the amplitude of seismic wave decays as it propagates from the source to the site. Since the seismic energy is proportional to the squared amplitude of the wave, this sketch also indicates the loss of seismic energy as it travel through the earth medium (Suyehrio et al. 1996; Haberland and Rietbrock 2001; Wong et al. 2001; Zhao et al. 2002; Schurr et al. 2003; Judenherc and Zollo 2004).

Since most of the seismic energy is contributed by shear wave (S wave), the major damages on the surface to engineering structures are also induced by the S wave (Kawase and Aki 1989; Tokimatsu et al. 1994; Kawase 1996; Tokimatsu et al. 1996; Bakir et al. 2002; Dong et al. 2004; Krishnan et al. 2006; Snieder and Şafak 2006; Zonno et al. 2010; Shiradhonkar and Shrikhande 2011). To characterize the loss of seismic energy with the increasing distance of the wave propagation, shear-wave attenuation (Q_s) is introduced into the path effect (Knopoff 1964). That is to say, the Q_s in the crust and the uppermost mantle beneath the volcanic area is different from that beneath non-volcanic area (Shelly et al. 2006; Snieder and Şafak 2006; Zhao et al. 2010; Liu et al. 2014; Liu and Zhao 2016b, a, 2017). When synthesizing the seismic acceleration wave using the stochastic finite-fault method, the Q_s should be specified in a function of frequency. The Q_s is commonly shown as a power law in the form of $Q_s = Q_0 f^n$, where Q_0 is the value of Q_s at 1 Hz and n is frequency parameter (Aki and Chouet 1975).

In the conventional method, the Q_s in volcanic zone is determined without distinguishing the non-volcanic area from the volcanic area (Rogers et al. 1987; Abercrombie 1998; Bindi et al. 2004; Nakamura et al. 2006). In the volcanic zone, the Q_s is usually estimated from one specific earthquake without considering the volcanic effect mentioned above (Oth et al. 2011; Safarshahi et al. 2013; Zengin and Cakti 2014). The lateral Q_s heterogeneities are not taken into the determination. In fact, some large cities are located in the non-volcanic area with a higher Q_s. Using a unique Q_s expression is not appropriate to simulate ground motions in the volcanic zone, especially for the ground motion simulations of non-volcanic area.

In this chapter, an analysis method for estimating Q_s considering the volcanic effect is developed. First, the effect of Q_s on ground motions is investigated. Then, the procedure of determining the Q_s is introduced. Finally, the developed method is integrated in the practical system for simulating acceleration waves and validated by the ground motion simulations of the 2016 Kumamoto earthquake.

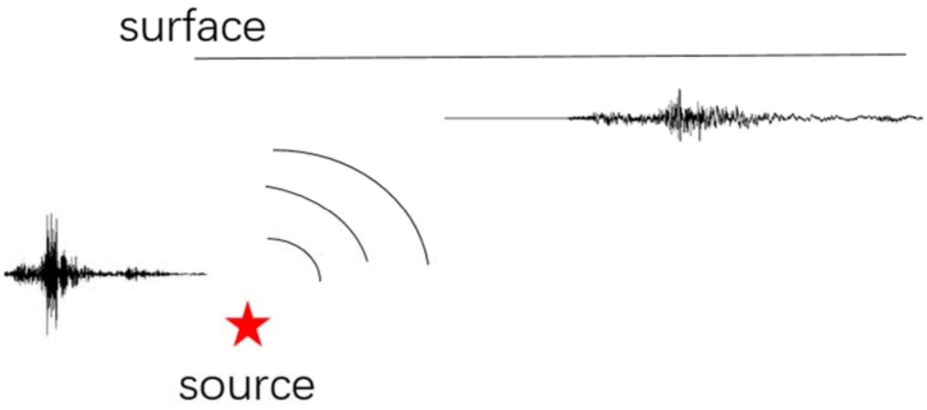

Figure 4-1 Schematic illustration of seismic wave attenuation

4.1 EFFECT OF S-WAVE ATTENUATION ON GROUND MOTIONS

The effect of S-wave attenuation (Q_s) on ground motions is investigated first. A numerical test is performed by varying the value of Q_s at 1 Hz, that is the value of Q_0, from 80 to 150 (Figure 4-2). Ghofrani et al. (2013) suggest to use the equation (4.1) to calculate the residual of simulated and observed Fourier amplitude spectra for the evaluation of simulation goodness.

$$res = \log_{10}\left(FAS_{obs}\right) - \log_{10}\left(FAS_{sim}\right) \tag{4.1}$$

where, obs and sim are the abbreviations of observed and simulated FAS. In this thesis, it is defined that if the absolute residual is smaller than 0.2, the simulated spectrum is rational. The strong ground-motion record of station KGSH10 from the 2016 Kumamoto earthquake is selected to make this test.

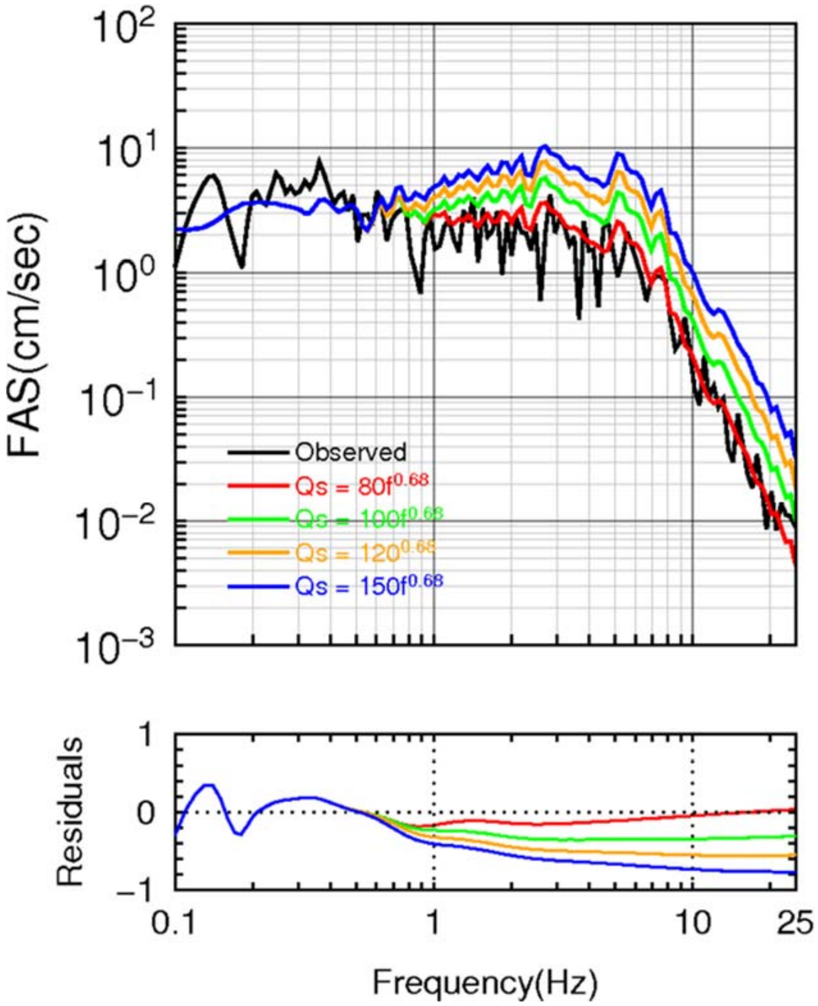

Figure 4-2 Effect of Q_s on the simulated FAS at station KGSH10

Figure 4-2 shows the simulated and observed Fourier amplitude spectra and their residuals in a function of frequency. The upper inset shows the comparison of observed and simulated spectra, while the lower inset shows their residuals determined from equation (4.1). At low frequencies (f < 0.5 Hz in this case), no matter which expression of Q_s is used, its performance is the same. However, the systematic differences are observed at high frequencies when using different Q_s to simulate the Fourier amplitude spectra. Specifically, the larger Q_0 are used, the higher spectral amplitude at high frequencies are simulated. The average residuals at the frequency range of 0.5-25 Hz are 0.05, 0.32, 0.53, 0.71 for $Q_s = 80 f^{0.68}$, $Q_s = 100 f^{0.68}$, $Q_s = 120 f^{0.68}$, $Q_s = 150 f^{0.68}$, respectively. Therefore, an accurate Q_s needs to employ in the ground motion simulations. The lateral Q_s heterogeneities caused by the volcanic effect should be considered into the determination of Q_s in the volcanic zone, especially for the non-volcanic area with a high Q_s.

4.2 THE CONVENTIONAL METHOD OF ESTIMATING SHEAR-WAVE ATTENUATION

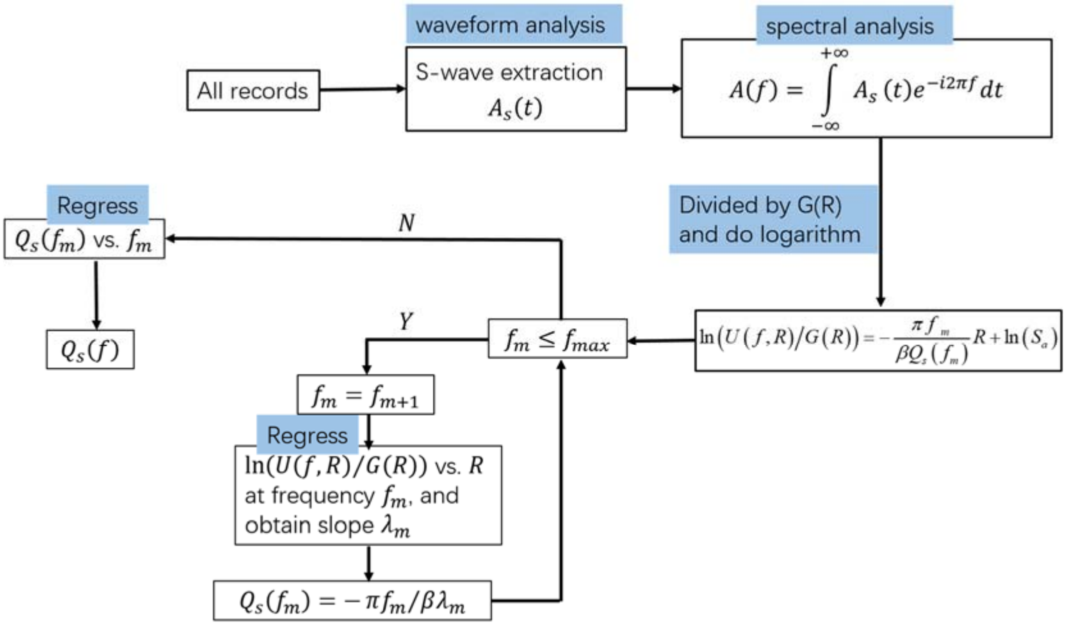

Figure 4-3 Flowchart of the conventional method of estimating Q_s

The most popular method to determine the Q_s based on the observations is the so-called spectral decay method (Anderson and Quaas 1988). The specific procedures of the calculation are illustrated in Figure 4-3 and introduced as follows. First, the S-wave window should be extracted from the records (Figure 4-4). The S-wave arrival is determined by using the P-wave arrival and their time difference, since the initial motion of the amplitude is usually considered as the P-wave arrival and is easier to be detected. The time difference between the P- and S-wave arrival is calculated from the epicentral distance and their average velocities. After finishing the extraction, the S-wave window is taped with a 10% of Hanning window at both ends to avoid the leaky of frequency. Finally, it is transformed to the Fourier amplitude spectrum.

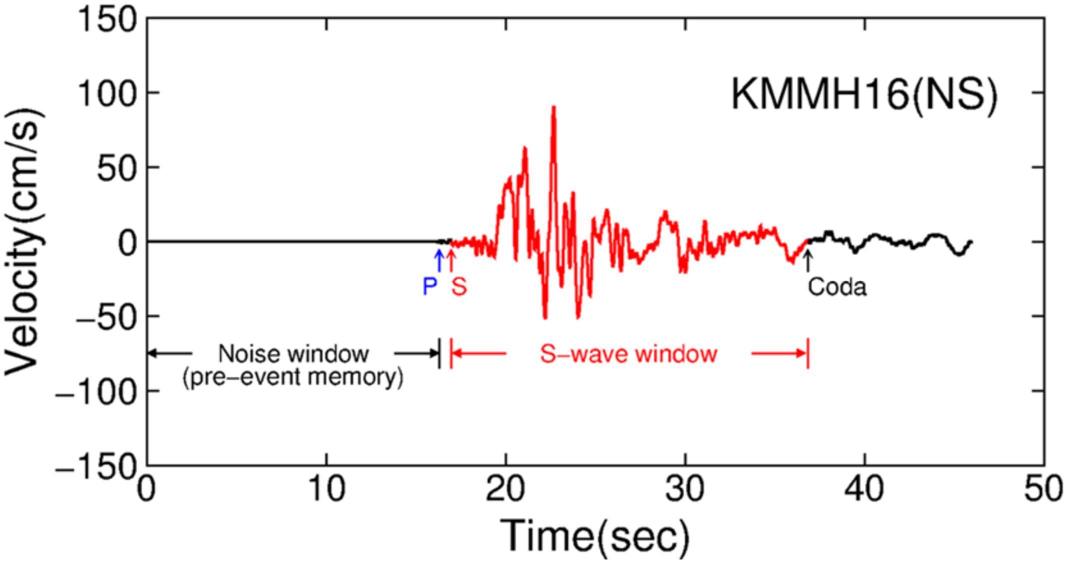

Figure 4-4 Schematic illustration of S-wave windows extraction. The acceleration time series is the surface record (NS component) at station KMMH16 from the 2016 Kumamoto earthquake

The observed spectra then are corrected by the geometrical spreading. In theory, the spectral amplitude of body wave decay as the it propagates only considering the elastic attenuation at the rate of R^{-1}. However, the complex geological structures will affect the geometrical spreading. Atkinson and Mereu (1992) investigate the attenuation characteristics of different wave phases in south eastern Canada and propose a trilinear model with the piecewise points of 70 km and 130 km. Zengin and Cakti (2014) use a bilinear model to fit the transition from the direct wave to Lg phase at approximately 100 km for Turkey. Here we select the bilinear model to correct the Fourier amplitude. That is, at distances less than 100 km, amplitudes decays at a rate of R^{-1}, whereas more than 100 km, spectral amplitude decay slightly at a rate of $R^{-0.5}$.

The next step is to determine the Q_s at some specific frequencies. The

Fourier amplitude spectrum, $U\left(f,R\right)$, recorded at hypocentral distance R, can be represented by the following form,

$$U\left(f,R\right)=S\cdot G\left(R\right)\exp\left(-\pi fR/\beta Q_s\right) \tag{4.2}$$

where S is the source and site term which is independent of distance R, $G\left(R\right)$ is the geometrical spreading, β is the S-wave velocity. A linear relationship derived from the equation (4.2) by taking natural logarithm is showed as

$$\ln(U\left(f,R\right)/G\left(R\right))=-\frac{\pi f}{\beta Q_s}R+\ln\left(S\right). \tag{4.3}$$

The left hand of this equation represents the spectral amplitude corrected by geometrical spreading function. For a given frequency, plot the corrected spectral amplitude of all stations versus their hypocentral distances (Figure 4-5). Then the Q_s at each frequency can be calculated from the slope of equation (4.3) under an assumption of the S-wave velocity. And then, plot the Q_s versus the corresponding frequencies in log-log scale and perform the least-squares fit. The frequency-dependent quality factor relation can be obtained (Figure 4-6) as the form of $Q_s=103.5f^{0.67}$ in Kyushu.

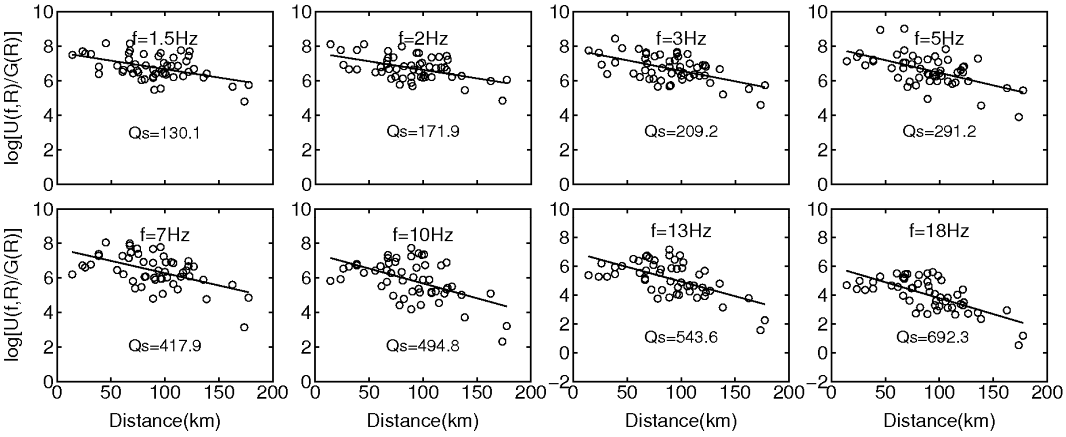

Figure 4-5 The Q_s results at some frequencies in conventional method

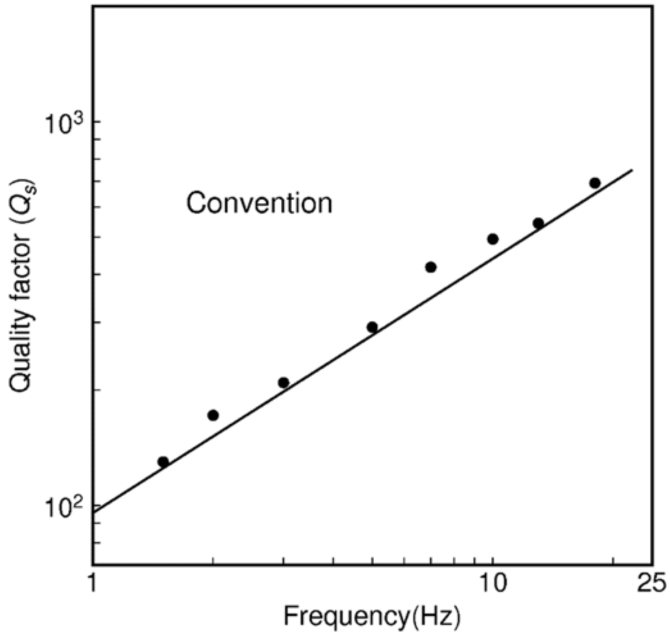

Figure 4-6 Q_s estimation in conventional method

4.3 LATER S-WAVE ATTENUATION HETEROGENEITIES IN KYUSHU ISLAND

There are many active volcanoes in Kyushu Island (Figure 4-9). Tsurumidake-Garandake, Kuju, Aso, Unzen, Kirishima, Sakurajima, and Ikeda-Yamagawa volcanoes locates as a sequence from the north to south (Zhao et al. 2000; Wang and Zhao 2006; Zhao et al. 2011). Many studies report that the Low-Q anomalies are observed beneath these volcanoes in the crust and the uppermost mantle, while the High-Q anomalies exists in the subduction of the Philippine Sea plate (Figure 4-7) (Patanè et al. 1994; Obara and Sato 1995; Whitman et al. 1996; Ben‐Zion 1998; Takanami et al. 2000; Tsumura et al. 2000; Kanno et al. 2006; Yoshimoto et al. 2006; Arpa et al. 2013; Prudencio et al. 2015). Zhao et al. (2011) suggest the widely-spread Q_s anomalies in the western Japan subduction zone are caused by dehydration of the Philippine Sea plate and the corner flow in the mantle. Such magmatic activities induced the eruption of active volcanoes and the occurrence of large earthquakes in the shallow crustal area.

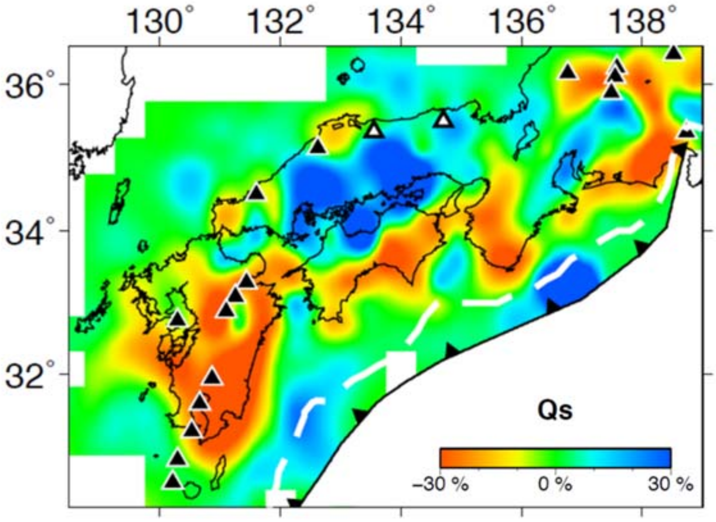

Figure 4-7 Q_s tomography results of the Kyushu region at the depth of 10 km (clipped from Liu and Zhao (2015)) Black solid triangles indicates the active volcanoes.

Figure 4-8 shows the schematic figure of the Q_s distribution in the Kyushu Island. Such lateral Q_s heterogeneities will affect the decay loss of seismic energy as the seismic wave travels through the magmatic and fluid regions. This effect should be considered into the ground motion simulations, since it would seriously affect the amplitude and frequency content of ground motions.

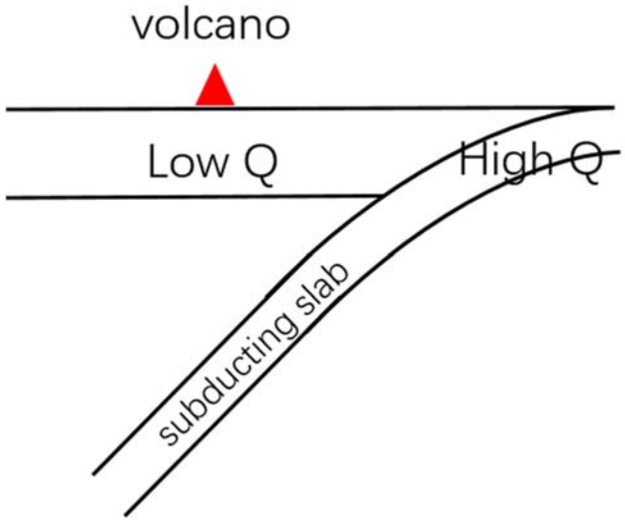

Figure 4-8 Schematic illustration of Q_s structure of the Kyushu region (refer from Pei et al. (2009))

Figure 4-9 shows the locations of active volcanoes in Kyushu Island. The comparison between Figure 4-7 and Figure 4-9 indicates most of the area of the Kyushu Island is in low-Q anomalies due to the volcanic effect. In the conventional method, the Q_s in Kyushu Island is determined using one unique formula or value for an entire region. The lateral Q_s heterogeneities are not taken into account. The effect of Q_s on ground motions has been proved in the last section and a suggestion of considering the volcanic effect is also given. Therefore, the conventional method should be modified for the determination of Q_s using the spectral decay method. Besides, some large cities, such as the Fukuoka city, the 5th largest cities of Japan, are usually located at the non-volcanic area. It is necessary and important to estimate the Q_s in such area, which can be used for earthquake ground motion simulations and then for the earthquake-resistant design.

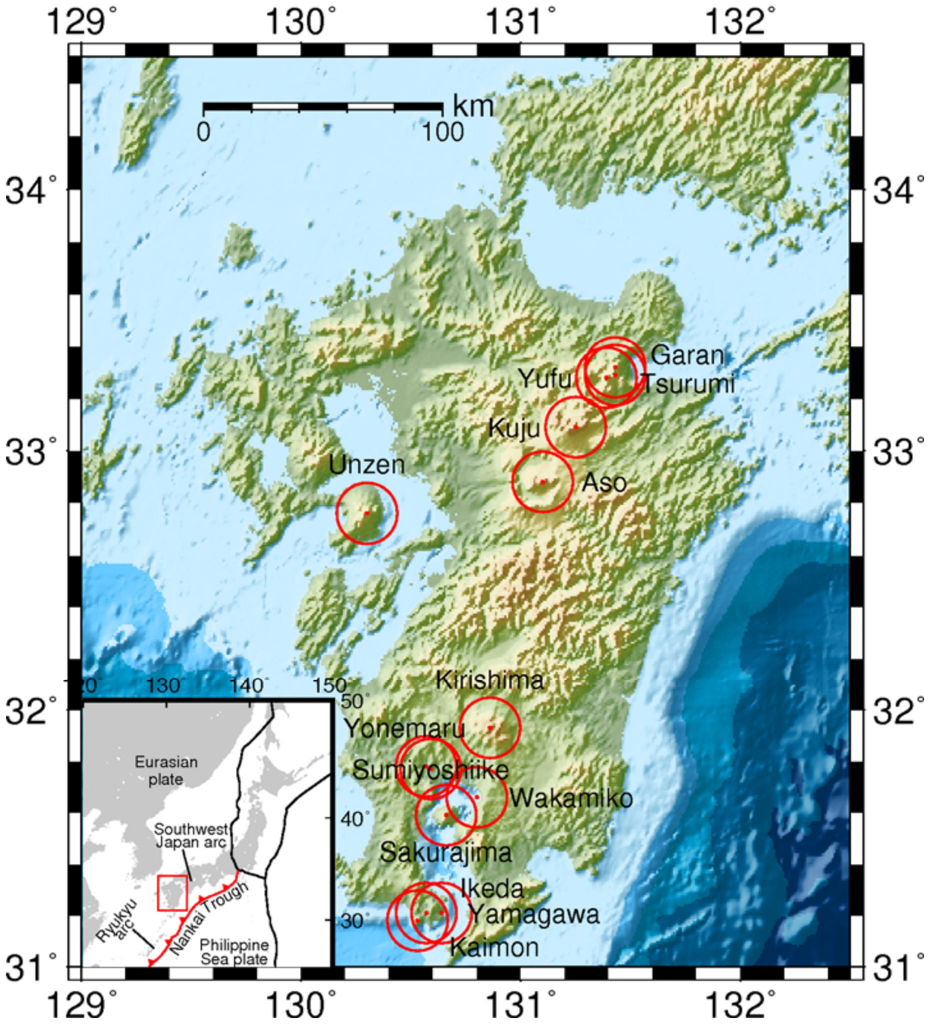

Figure 4-9 The active volcanoes in Kyushu Island. The red circles show the location and possible range of volcanoes.

4.3 DEVELOPMENT OF A PRACTICAL ANALYSIS METHOD CONSIDERING THE VOLCANIC EFFECT

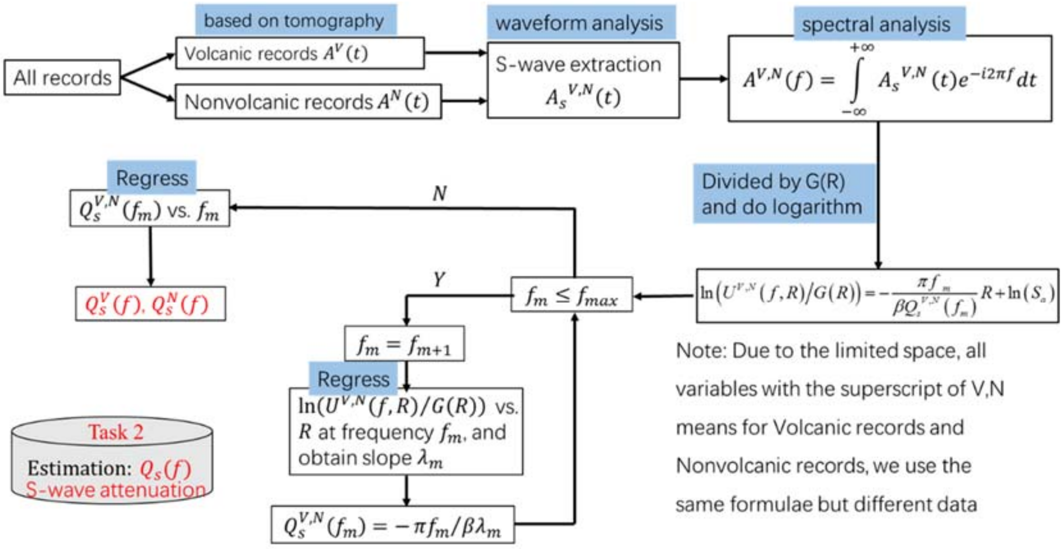

Figure 4-10 The flowchart of developed practical method for the estimation of Q_s

In this chapter, we propose a method considering the volcanic effect in estimating Q_s. Q_s values are usually estimated without distinguishing non-volcanic area from volcanic area in one region. In fact, it has been reported that there is a Low Q_s in the region with active volcanoes comparing to the normal values. Therefore, we propose to separate the strong ground-motion stations into volcanic and non-volcanic ones based on the tomographic results. The specific procedures are illustrated in Figure 4-10 and shown as follows,

1. Separate the stations, that is, the strong ground motion records as the volcanic and non-volcanic ones based on the published tomographic results
2. Calculate the Q_s using the spectral decay method for volcanic and non-volcanic region separately.

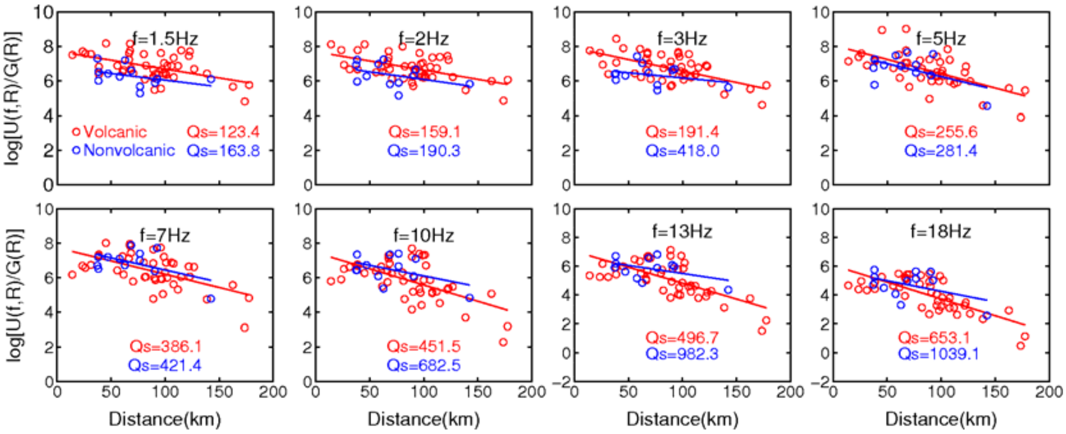

Figure 4-11 The Q_s results at some central frequencies for the Kyushu region. The red and blue circles are spectral amplitudes of the volcanic and non-volcanic records corrected by the geometrical spreading, $\ln(U(f,R)/G(R))$, respectively.

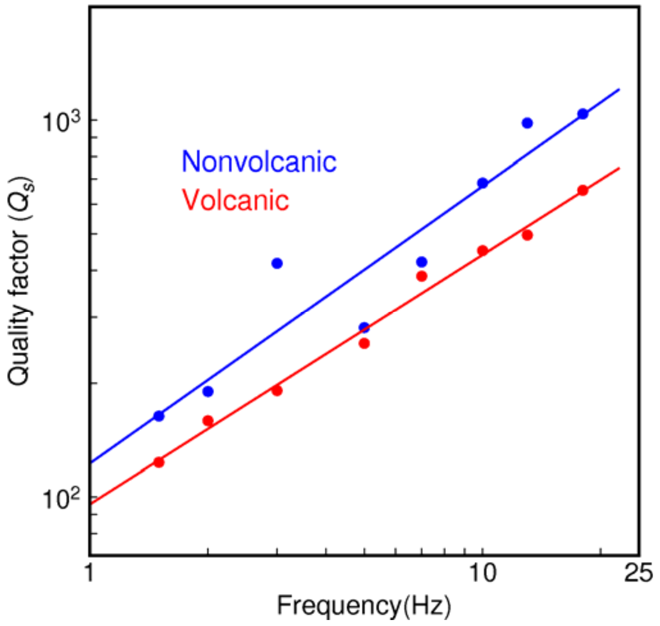

Figure 4-12 Q_s estimation in the Kyushu Island, Japan by using the least square linear fit

It should be noted that when calculate the Q_s in the volcanic area, the strong ground-motion records for calculating Q_s should be accessed from the earthquake which the hypocentre is located in the volcanic area. This criterion ensures the calculated Q_s only shows the volcanic effect on the S-wave attenuation. For the non-volcanic area, the criterion is vice versa. That is, to calculate the Q_s for the non-volcanic area, the earthquake should be selected as the one which the hypocentre should be surrounded by the non-volcanic stations, which ensures the direct S wave will reach the stations without travelling through the volcanic area and containing the information from the non-volcanic area only. The Q_s beneath the volcanic and non-volcanic area in Kyushu are expressed in the form of $Q_s = 95.7 f^{0.66}$ and $Q_s = 122.6 f^{0.74}$, respectively.

4.4 VALIDATION: THE CASE OF THE 2016 KUMAMOTO EARTHQUAKE

To validate the method proposed in this chapter, the Kyushu region is selected as an example due to its active magmatic activities. The tomography result shows the Q_s perturbations at different depths (Zhao 2015; Zhao et al. 2016; Wang et al. 2017d; Zhao 2017; Zhao et al. 2017). In earthquake engineering, such as the landslide hazard assessment, only the large PGA values in a site will be considered in the evaluation. As the focal depth increases, the hypocentral distance will also increase. The amplitudes of seismic wave on the surface will be smaller since a lot of seismic energy decays as the seismic wave travel through the longer distance. Therefore, in our calculation, only the Q_s tomography result at the depth of 10 km is considered, which is also the average focal depth of devastating earthquakes in Kyushu Island, such as the 2016 Kumamoto earthquake (Asano and Iwata 2016a; Hata et al. 2016; Mukunoki et al. 2016; Sano et al. 2016; Yagi et al. 2016; Yoshida et al. 2016; Dai et al. 2017; Kobayashi 2017; Setiawan et al. 2017; Wang et al. 2017e).

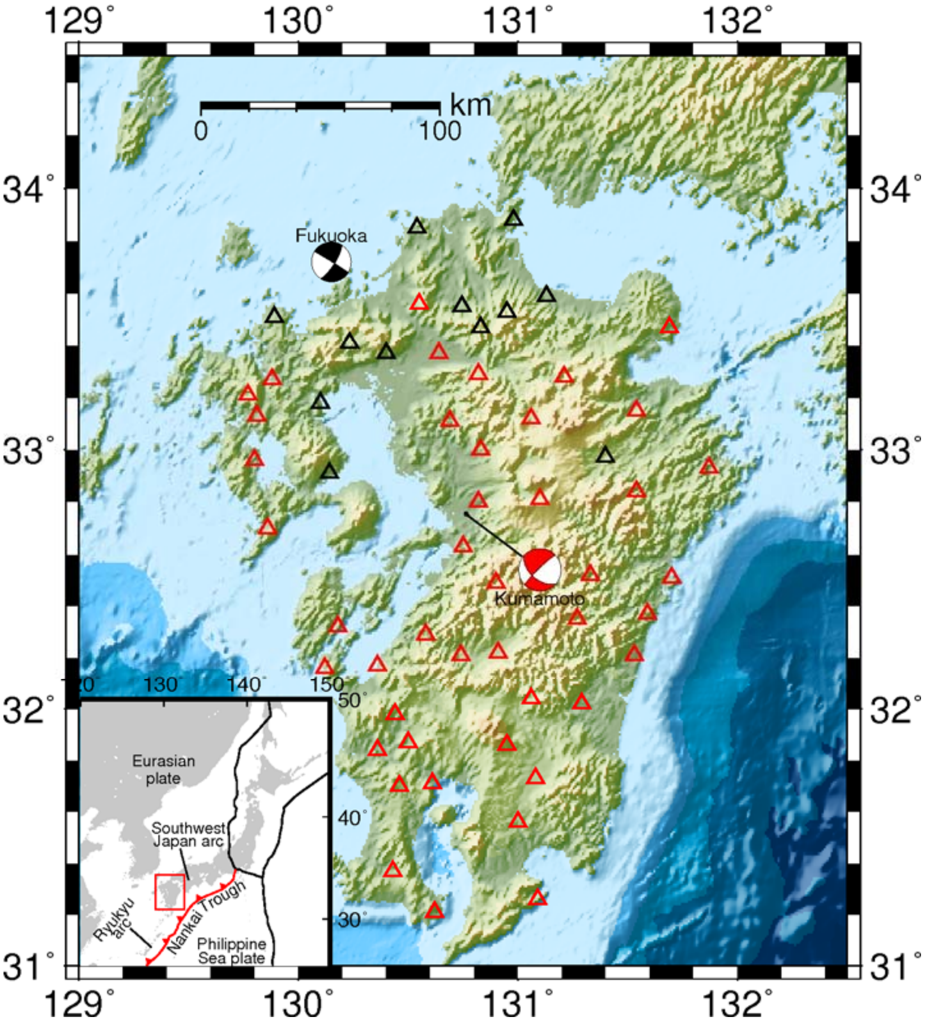

Figure 4-13 The KiK-net stations in the Kyushu region, Japan. Triangles are the KiK-net stations, the red and black ones are volcanic and non-volcanic stations, respectively.

At first, the separation of volcanic and non-volcanic stations should be done. According to the Q_s tomography results (Figure 4-7), the High-Q region should be considered as the non-volcanic area, while the Low-Q region should be regarded as the volcanic area based on the analysis and discussion from Liu and Zhao (2015). The separation results are shown in Figure 4-13.

Secondly, based on the separation of ground-motion stations, two earthquakes should be selected to estimate the Q_s for these two regions separately. Here the strong ground-motion records from the 2016 Kumamoto earthquake are employed to calculate the Q_s in the volcanic region, whereas those from the 2005 M6.6 Fukuoka earthquake are used for Q_s determination in the non-volcanic region (Asano and Iwata 2006; Horikawa 2006; Kobayashi et al. 2006b; Matsumoto et al. 2006; Sekiguchi et al. 2006b; Furumura 2016; Irikura et al. 2017; Nagasaka and Nozu 2017; Suzuki et al. 2017; Xie et al. 2017). Besides, to compare with the conventional method, the Q_s for the entire Kyushu Island is determined using the whole records from the 2016 Kumamoto earthquake due to the widely-spread active volcanoes. It should be noted that the calculation is performed by using the EW component of surface recordings. Then the Q_s at some central frequencies are calculated using the spectral decay method (Castro et al. 1997; Castro and Group 1998; Castro et al. 1999; Akyol et al. 2002; Castro et al. 2003; Polatidis et al. 2003; Kamalian et al. 2007; Castro et al. 2008; Padhy and Subhadra 2010; Vidales - Basurto et al. 2014). To obtain an accurate regression between the selected frequencies and the corresponding Q_s values, the space of frequency in log-log scale should be almost equal. Finally, the expressions of Q_s are determined by plotting the Q_s versus the corresponding frequencies in log-log scale. The Q_s beneath the volcanic and non-volcanic area are expressed in the form of $Q_s = 95.7 f^{0.66}$ and $Q_s = 122.6 f^{0.74}$, respectively.

To validate the method proposed in this chapter, the ground motion simulations are performed and compared with the observations for 9 non-volcanic stations. The Kyushu region is usually considered as a volcanic zone due to the widely-spread active volcanoes. The conventional way to determine the Q_s in such region is using as many as strong ground motion records without any separation. The Q_s without considering the volcanic effect, is determined and expressed as the form of $Q_s = 103.5 f^{0.67}$. This Q_s is totally determined using the recordings from the 2016 Kumamoto earthquake. The ground motions are simulated using the Q_s with and without considering the volcanic effect and compared with the observations separately.

Table 4-1 Comparison of simulated PGA using the conventional and proposed methods

Station code	Obs. PGA (in cm/s^2)	Sim. PGA conventional method (in cm/s^2)	Relative Error	Sim. PGA proposed method (in cm/s^2)	Relative Error
FKOH01	60	20.06	66.57%	30.65	48.92%
FKOH06	75	41.96	44.05%	56.65	24.47%
FKOH08	103	70.49	31.56%	94.68	8.08%
FKOH09	43	25.77	40.07%	39.63	7.84%
NGSH01	42	19.79	52.88%	33.31	20.69%
OITH01	70	69.38	0.89%	73.40	4.86%
SAGH01	37	23.02	37.78%	35.69	3.54%
SAGH04	149	76.97	48.34%	103.07	30.83%
SAGH05	32	47.16	47.38%	61.49	92.16%

The comparison shows that the accuracy of simulated PGA is improved when considering the volcanic effect. Compare to using the conventional method, the average relative error of simulated PGA in the non-volcanic area is reduced from 41% to 27% using the proposed method. Here the relative error is defined as

$$\text{Relative Error of PGA} = \frac{\left|PGA_{obs} - PGA_{sim}\right|}{PGA_{obs}}, \tag{4.4}$$

where the subscripts of obs and sim indicate the observed and simulated PGA, respectively. Then the differences are also compared in the frequency domain. To show the difference with and without considering the volcanic effect clearly, one representative station in the non-volcanic area is selected. In Figure 4-14, the average residual of station FKOH01 at the frequency range of 0.4 to 25 Hz are reduced from 0.33 to 0.1 when considering the lateral Q_s heterogeneities. It is concluded that ground-motion results are improved when considering the volcanic effect. The method proposed in this chapter is useful and acceptable in determining the path parameter, Q_s.

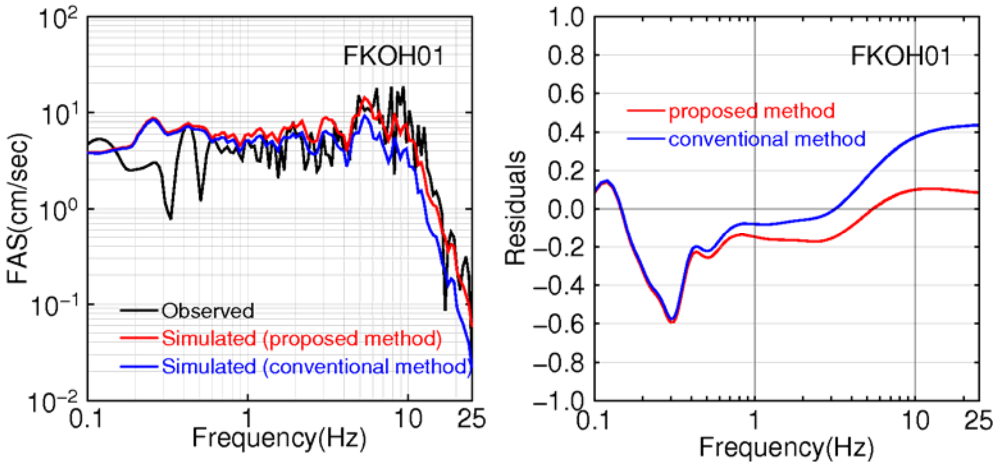

Figure 4-14 Comparison of simulated FAS and their residuals with and without considering the volcanic effect at station FKOH01.

4.5 CONCLUSIONS

In this chapter, an analysis method for estimating the S-wave attenuation (Q_s) considering the volcanic effect is proposed. The following conclusions can be drawn:

(1) The effect of S-wave attenuation on the ground motion is evaluated by varying the Q_s values. At high frequencies, the spectral amplitude level is systematically increased as a larger Q_s is used, whereas the low-frequency part of the Fourier amplitude spectra is not sensitive to the Q_s. It is in agreement with the definition of Q_s, which is an indicator of decay loss of seismic energy during the wave propagation. The larger Q_s indicates less decay of seismic energy. The influence of Q_s on the simulated Fourier amplitude spectra is quantified.

(2) An analysis method for estimating the Q_s considering the volcanic effect is developed and complied as a module. The detailed procedure for determining the Q_s of the region with active volcanoes is introduced. This module is also integrated in the practical system for simulating

earthquake ground motions.

(3) The proposed analysis method is validated by simulating the ground motions of 9 non-volcanic records from the 2016 Kumamoto earthquake. Compare to without distinguishing, the accuracy of simulated PGA is improved when considering the volcanic effect. The simulated Fourier amplitude spectra also match the observations better than the situation without considering the Q_s heterogeneities. The difference of simulated FAS with and without considering the lateral Q_s heterogeneities are also quantified. It is concluded that the developed method is useful and acceptable for the estimation of Q_s in the volcanic zone.

REFERENCE

Abercrombie RE (1998) A summary of attenuation measurements from borehole recordings of earthquakes: the 10 Hz transition problem. Pure Appl Geophys 153, 475-487

Aki K, Chouet B (1975) Origin of coda waves: source, attenuation, and scattering effects. J Geophys Res 80, 3322-3342

Akyol N, AKinci A, EYidogan H (2002) Separation of Source, Propagation and Site Effects from S Waves¶ of Local Earthquakes in Bursa Region, Northwestern Turkey. Pure Appl Geophys 159, 1253-1269

Anderson J, Quaas R (1988) The Mexico earthquake of September 19, 1985—Effect of magnitude on the character of strong ground motion: An example from the Guerrero, Mexico strong motion network. Earthq Spectra 4, 635-646

Andrews D (1986) Objective determination of source parameters and similarity of earthquakes of different size. Earthquake source mechanics, 259-267

Arpa MC, Hernández PA, Padrón E, Reniva P, Padilla GD, Bariso E, Melián GV, Barrancos J, Nolasco D, Calvo D (2013) Geochemical evidence of magma intrusion inferred from diffuse CO2 emissions and fumarole plume chemistry: the 2010–2011 volcanic unrest at Taal Volcano, Philippines. Bull Volcanol 75, 747

Asano K, Iwata T (2006) Source process and near-source ground motions of the 2005 West Off Fukuoka Prefecture earthquake. Earth Planets Space 58, 93-98

Asano K, Iwata T (2016) Source rupture processes of the foreshock and mainshock in the 2016 Kumamoto earthquake sequence estimated from the kinematic waveform inversion of strong motion data. Earth Planets Space 68, 147

Bakir BS, Sucuoğlu H, Yilmaz T (2002) An overview of local site effects and the associated building damage in Adapazari during the 17 August 1999 Izmit earthquake. Bull Seismol Soc Am 92, 509-526

Ben‐Zion Y (1998) Properties of seismic fault zone waves and their utility for imaging low‐velocity structures. J Geophys Res 103, 12567-12585

Bindi D, Castro R, Franceschina G, Luzi L, Pacor F (2004) The 1997–1998 Umbria‐Marche sequence (central Italy): Source, path, and site effects estimated from strong motion data recorded in the epicentral area. J Geophys Res 109

Castro R, Anderson J, Singh S (1990) Site response, attenuation and source spectra of S waves along the Guerrero, Mexico, subduction zone. Bull Seismol Soc Am 80, 1481-1503

Castro R, Group RW (1998) P-and S-wave site response of the seismic network RESNOM determined from earthquakes of northern Baja California, Mexico. Pure Appl Geophys 152, 125

Castro RR, Fabriol H, Bour M, Le Brun B (2003) Attenuation and site effects in the region of Guadeloupe, Lesser Antilles. Bull Seismol Soc Am 93, 612-626

Castro RR, Massa M, Augliera P, Pacor F (2008) Body-wave attenuation in the region of Garda, Italy. Pure Appl Geophys 165, 1351-1366

Castro RR, Monachesi G, Mucciarelli M, Trojani L, Pacor F (1999) P-and S-wave attenuation in the region of Marche, Italy. Tectonophysics 302, 123-132

Castro RR, Rebollar CJ, Inzunza L, Orozco L, Sánchez J, Gálvez O, Farfán F, Méndez I (1997) Direct body-wave Q estimates in northern Baja California, Mexico. Phys Earth Planetary Inter 103, 33-38

Cavinato G, De Celles P (1999) Extensional basins in the tectonically bimodal central Apennines fold-thrust belt, Italy: response to corner flow above a subducting slab in retrograde motion. Geology 27, 955-958

Dai Z, Wang F, Song K, Iio A (2017) A first look at a landslide triggered by the 2016 Kumamoto earthquake near the Aso Volcanological Laboratory. Quart J Eng Geol Hydrog 50, 111-116

Davies RJ, Brumm M, Manga M, Rubiandini R, Swarbrick R, Tingay M (2008) The East Java mud volcano (2006 to present): An earthquake or drilling trigger? Earth Planet Sci Lett 272, 627-638

Dong J, Wang C, Lee C, Liao J, Pan Y (2004) The influence of surface ruptures on building damage in the 1999 Chi-Chi earthquake: a case study in Fengyuan City. Eng Geology 71, 157-179

Furumura T (2016) Destructive near-fault strong ground motion from the 2016 Kumamoto prefecture, Japan, M7. 3 earthquake. Landslides 13, 1519-1524

Giampiccolo E, D’Amico S, Patanè D, Gresta S (2007) Attenuation and source parameters of shallow microearthquakes at Mt. Etna Volcano, Italy. Bull Seismol Soc Am 97, 184-197

Giudice EL, Rasà R (1992) Very shallow earthquakes and brittle deformation in active volcanic areas: The Eatnean region as an example. Tectonophysics 202, 257-268

Ghofrani H, Atkinson GM, Goda K, Assatourians K (2013) Stochastic finite‐fault simulations of the 2011 Tohoku, Japan, earthquake. Bull Seismol Soc Am 103, 1307-1320

Gudmundsson A, Marti J, Turon E (1997) Stress fields generating ring faults in volcanoes. Geophys Res Lett 24, 1559-1562

Haberland C, Rietbrock A (2001) Attenuation tomography in the western central Andes: A detailed insight into the structure of a magmatic arc. J Geophys Res 106, 11151-11167

Hasegawa A, Yamamoto A (1994) Deep, low-frequency microearthquakes in or around seismic low-velocity zones beneath active volcanoes in northeastern Japan. Tectonophysics 233, 233-252

Hata Y, Goto H, Yoshimi M (2016) Preliminary analysis of strong ground motions in the heavily damaged zone in Mashiki town, Kumamoto, Japan, during the mainshock of the 2016 Kumamoto earthquake (M w 7.0) observed by a dense seismic array. Seismol Res Lett 87, 1044-1049

Hattori KH, Guillot S (2003) Volcanic fronts form as a consequence of serpentinite dehydration in the forearc mantle wedge. Geology 31, 525-528

Horikawa H (2006) Rupture process of the 2005 west off Fukuoka prefecture, Japan, earthquake. Earth Planets Space 58, 87-92

Irikura K, Miyakoshi K, Kamae K, Yoshida K, Somei K, Kurahashi S, Miyake H (2017) Applicability of source scaling relations for crustal earthquakes to estimation of the ground motions of the 2016 Kumamoto earthquake. Earth Planets Space 69, 10

Ishizuka O, Taylor RN, Geshi N, Oikawa T, Kawanabe Y, Ogitsu I (2015) Progressive mixed-magma recharging of Izu-Oshima volcano, Japan: A guide to magma chamber volume. Earth Planet Sci Lett 430, 19-29

Italiano F, Pecoraino G, Nuccio P (1998) Steam output from fumaroles of an active volcano: Tectonic and magmatic ‐ hydrothermal controls on the degassing system at Vulcano (Aeolian arc). J Geophys Res 103, 29829-29842

Iwamori H (2000) Deep subduction of H2O and deflection of volcanic chain towards backarc near triple junction due to lower temperature. Earth Planet Sci Lett 181, 41-46

Judenherc S, Zollo A (2004) The Bay of Naples (southern Italy): Constraints on the volcanic structures inferred from a dense seismic survey. J Geophys Res 109

Kamalian N, Hamzehloo H, Ghasemi H (2007) S-wave attenuation and spectral decay parameter for the Avaj region, Iran. Iran J Sci Technol (Sci) 31, 63-71

Kanno T, Narita A, Morikawa N, Fujiwara H, Fukushima Y (2006) A new attenuation relation for strong ground motion in Japan based on recorded data. Bull Seismol Soc Am 96, 879-897

Kawase H (1996) The cause of the damage belt in Kobe:“The basin-edge effect,” constructive interference of the direct S-wave with the basin-induced diffracted/Rayleigh waves. Seismol Res Lett 67, 25-34

Kawase H, Aki K (1989) A study on the response of a soft basin for incident S, P, and Rayleigh waves with special reference to the long duration observed in Mexico City. Bull Seismol Soc Am 79, 1361-1382

Knopoff L (1964) Q. Rev Geophys 2, 625-660

Kobayashi R, Miyazaki Si, Koketsu K (2006) Source processes of the 2005 West Off Fukuoka Prefecture earthquake and its largest aftershock inferred from strong motion and 1-Hz GPS data. Earth Planets Space 58, 57-62

Kobayashi T (2017) Earthquake rupture properties of the 2016 Kumamoto earthquake foreshocks (M j 6.5 and M j 6.4) revealed by conventional and multiple-aperture InSAR. Earth Planets Space 69, 7

Krishnan S, Ji C, Komatitsch D, Tromp J (2006) Case studies of damage to tall steel moment-frame buildings in southern California during large San Andreas earthquakes. Bull Seismol Soc Am 96, 1523-1537

Lin A, Satsukawa T, Bian D, Sado K, Takahashi N, Hirata S (2017) Millennium recurrence interval of morphogenic earthquakes on the seismogenic fault zone that triggered the 2016 M w 7.1 Kumamoto earthquake, SW Japan. Bull Seismol Soc Am

Lin A, Satsukawa T, Wang M, Asl ZM, Fueta R, Nakajima F (2016) Coseismic rupturing stopped by Aso volcano during the 2016 Mw 7.1 Kumamoto earthquake, Japan. Science 354, 869-874

Liu X, Zhao D (2015) Seismic attenuation tomography of the Southwest Japan arc: new insight into subduction dynamics. Geophys J Int 201, 135-156

Liu X, Zhao D (2016a) Backarc spreading and mantle wedge flow beneath the Japan Sea: insight from Rayleigh-wave anisotropic tomography. Geophys J Int 207, 357-373

Liu X, Zhao D (2016b) P and S wave tomography of Japan subduction zone from joint inversions of local and teleseismic travel times and surface-wave data. Phys Earth Planet Inter 252, 1-22.doi:10.1016/j.pepi.2016.01.002

Liu X, Zhao D (2017) P-wave anisotropy, mantle wedge flow and olivine fabrics beneath Japan. Geophys J Int 210, 1410-1431

Liu X, Zhao D, Li S (2014) Seismic attenuation tomography of the Northeast Japan arc: insight into the 2011 Tohoku earthquake (Mw 9.0) and subduction dynamics. J Geophys Res 119, 1094-1118

Long MD, van der Hilst RD (2006) Shear wave splitting from local events beneath the Ryukyu arc: trench-parallel anisotropy in the mantle wedge. Phys Earth Planet Inter 155, 300-312

Matsumoto T, Ito Y, Matsubayashi H, Sekiguchi S (2006) Spatial distribution of F-net moment tensors for the 2005 West Off Fukuoka Prefecture Earthquake determined by the extended method of the NIED F-net routine. Earth Planets Space 58, 63-67

Mukunoki T, Kasama K, Murakami S, Ikemi H, Ishikura R, Fujikawa T, Yasufuku N, Kitazono Y (2016) Reconnaissance report on geotechnical damage caused by an earthquake with JMA seismic intensity 7 twice in 28h, Kumamoto, Japan. Soils and Foundations 56, 947-964

Nagasaka Y, Nozu A (2017) Strong ground motion simulation of the 2016 Kumamoto earthquake of April 16 using multiple point sources. Earth Planets Space 69, 25

Nakamichi H, Hamaguchi H, Tanaka S, Ueki S, Nishimura T, Hasegawa A (2003) Source mechanisms of deep and intermediate-depth low-frequency earthquakes beneath Iwate volcano, northeastern Japan. Geophys J Int 154, 811-828

Nakamura K (1977) Volcanoes as possible indicators of tectonic stress orientation—principle and proposal. J Volcanology Geothermal Res 2, 1-16

Nakamura R, Satake K, Toda S, Uetake T, Kamiya Si (2006) Three‐dimensional attenuation (Qs) structure beneath the Kanto district, Japan, as inferred from strong motion records. Geophys Res Lett 33

Obara K, Sato H (1995) Regional differences of random inhomogeneities around the volcanic front in the Kanto‐Tokai area, Japan, revealed from the broadening of S wave seismogram envelopes. J Geophys Res 100, 2103-2121

Oth A, Bindi D, Parolai S, Di Giacomo D (2011) Spectral analysis of K-NET and KiK-net data in Japan, Part II: On attenuation characteristics, source spectra, and site response of borehole and surface stations. Bull Seismol Soc Am 101, 667-687

Padhy S, Subhadra N (2010) Frequency-dependent attenuation of P and S waves in northeast India. Geophys J Int 183, 1052-1060

Patanè D, Ferrucci F, Gresta S (1994) Spectral features of microearthquakes in volcanic areas: Attenuation in the crust and amplitude response of the site at Mt. Etna, Italy. Bull Seismol Soc Am 84, 1842-1860

Plank T, Cooper LB, Manning CE (2009) Emerging geothermometers for estimating slab surface temperatures. Nat Geosci 2, 611

Polatidis A, Kiratzi A, Hatzidimitriou P, Margaris B (2003) Attenuation of shear-waves in the back-arc region of the Hellenic arc for frequencies from 0.6 to 16 Hz. Tectonophysics 367, 29-40

Prudencio J, Ibáñez J, Del Pezzo E, Martí J, García-Yeguas A, De Siena L (2015) 3D attenuation tomography of the volcanic island of Tenerife (Canary Islands). Surveys in Geophysics 36, 693-716

Rogers A, Harmsen S, Herrmann R, Meremonte M (1987) A study of ground motion attenuation in the Southern Great Basin, Nevada ‐ California, using several techniques for estimates of Qs, log A 0, and coda Q. J Geophys Res 92, 3527-3540

Safarshahi M, Rezapour M, Hamzehloo H (2013) Stochastic Finite ‐ Fault Modeling of Ground Motion for the 2010 Rigan Earthquake, Southeastern Iran. Bull Seismol Soc Am 103, 223-235.doi:10.1785/0120120027

Saita H, Nakajima J, Shiina T, Kimura JI (2015) Slab ‐ derived fluids, fore ‐ arc hydration, and sub ‐ arc magmatism beneath Kyushu, Japan. Geophys Res Lett 42, 1685-1693

Sano Y, Takahata N, Kagoshima T, Shibata T, Onoue T, Zhao D (2016) Groundwater helium anomaly reflects strain change during the 2016 Kumamoto earthquake in Southwest Japan. Scientific reports 6, 37939

Schurr B, Asch G, Rietbrock A, Trumbull R, Haberland C (2003) Complex patterns of fluid and melt transport in the central Andean subduction zone revealed by attenuation tomography. Earth Planet Sci Lett 215, 105-119

Sekiguchi H, Aoi S, Honda R, Morikawa N, Kunugi T, Fujiwara H (2006) Rupture process of the 2005 West Off Fukuoka Prefecture earthquake obtained from strong motion data of K-NET and KiK-net. Earth Planets Space 58, 37-43

Setiawan H, Serikawa Y, Nakamura M, Miyajima M, Yoshida M (2017) Structural damage to houses and buildings induced by liquefaction in the 2016 Kumamoto Earthquake, Japan. Geoenvironmental Disasters 4, 13

Shelly DR, Beroza GC, Ide S, Nakamula S (2006) Low-frequency earthquakes in Shikoku, Japan, and their relationship to episodic tremor and slip. Nature 442, 188

Shiradhonkar S, Shrikhande M (2011) Seismic damage detection in a building frame via finite element model updating. Comp Struct 89, 2425-2438

Snieder R, Şafak E (2006) Extracting the building response using seismic interferometry: Theory and application to the Millikan Library in Pasadena, California. Bull Seismol Soc Am 96, 586-598

Suleiman AS, Doser DI (1995) The seismicity, seismotectonics and earthquake hazards of Libya, with detailed analysis of the 1935 April 19, M= 7.1 earthquake sequence. Geophys J Int 120, 312-322

Suyehrio K, Takahashi N, Ariie Y, Yokoi Y (1996) Continental crust, crustal underplating, and low-Q upper mantle beneath an oceanic island arc. Science 272, 390

Suzuki W, Aoi S, Kunugi T, Kubo H, Morikawa N, Nakamura H, Kimura T, Fujiwara H (2017) Strong motions observed by K-NET and KiK-net during the 2016 Kumamoto earthquake sequence. Earth Planets Space 69, 19

Takada Y, Fukushima Y (2013) Volcanic subsidence triggered by the 2011 Tohoku earthquake in Japan. Nat Geosci 6, 637

Takahashi T, Sato H, Nishimura T, Obara K (2007) Strong inhomogeneity beneath Quaternary volcanoes revealed from the peak delay analysis of S-wave seismograms of microearthquakes in northeastern Japan. Geophys J Int 168, 90-99

Takanami T, Sacks IS, Hasegawa A (2000) Attenuation structure beneath the volcanic front in northeastern Japan from broad-band seismograms. Phys Earth Planet Inter 121, 339-357

Tokimatsu K, Kojima H, Kuwayama S, Abe A, Midorikawa S (1994) Liquefaction-induced damage to buildings in 1990 Luzon earthquake. J Geotech Eng 120, 290-307

Tokimatsu K, Mizuno H, Kakurai M (1996) Building damage associated with geotechnical problems. Soils and foundations 36, 219-234

Tsumura N, Matsumoto S, Horiuchi S, Hasegawa A (2000) Three-dimensional attenuation structure beneath the northeastern Japan arc estimated from spectra of small earthquakes. Tectonophysics 319, 241-260

Van Keken PE, Kiefer B, Peacock SM (2002) High‐resolution models of subduction zones: Implications for mineral dehydration reactions and the transport of water into the deep mantle. Geochem Geophys Geosyst 3

Vidales‐Basurto CA, Castro RR, Huerta CI, Sumy DF, Gaherty JB, Collins JA (2014) An attenuation study of body waves in the south‐central region of the Gulf of California, México. Bull Seismol Soc Am 104, 2027-2042

Wada I, Wang K, He J, Hyndman RD (2008) Weakening of the subduction interface and its effects on surface heat flow, slab dehydration, and mantle wedge serpentinization. J Geophys Res 113

Wang Z, Zhao D (2006) Vp and Vs tomography of Kyushu, Japan: New insight into arc magmatism and forearc seismotectonics. Physics Earth Planet Int 157, 269-285

Wang Z, Zhao D, Liu X, Chen C, Li X (2017a) P and S wave attenuation tomography of the Japan subduction zone. Geochem Geophys Geosyst 18, 1688-1710

Wang Z, Zhao D, Liu X, Li X (2017b) Seismic attenuation tomography of the source zone of the 2016 Kumamoto earthquake (M 7.3). J Geophys Res 122, 2988-3007

Whitman D, Isacks B, Kay SM (1996) Lithospheric structure and along-strike segmentation of the Central Andean Plateau: seismic Q, magmatism, flexure, topography and tectonics. Tectonophysics 259, 29-40

Wong V, Rebollar CJ, Munguía L (2001) Attenuation of coda waves at the Tres Vírgenes volcanic area, Baja California Sur, México. Bull Seismol Soc Am 91, 683-693

Wyss M, Shimazaki K, Wiemer S (1997) Mapping active magma chambers by b values beneath the off‐Ito volcano, Japan. J Geophys Res 102, 20413-20422

Xie J, Zimmaro P, Li X, Wen Z (2017) Rupture Directivity Effects on Strong Ground Motion during the 15 April 2016 Mw 7.0 Kumamoto Earthquake in Japan. Bull Seismol Soc Am

Yagi Y, Okuwaki R, Enescu B, Kasahara A, Miyakawa A, Otsubo M (2016) Rupture process of the 2016 Kumamoto earthquake in relation to the thermal structure around Aso volcano. Earth Planets Space 68, 1-6

Yoshida S (2016) Earthquakes in Oita triggered by the 2016 M7. 3 Kumamoto earthquake. Earth Planets Space 68, 176

Yoshimoto K, Wegler U, Korn M (2006) A volcanic front as a boundary of seismic-attenuation structures in northeastern Honshu, Japan. Bull Seismol Soc Am 96, 637-646

Zengin E, Cakti E (2014) Ground motion simulations for the 23 October 2011 Van, Eastern Turkey earthquake using stochastic finite fault approach. Bull Earthq Eng 12, 627-646

Zhao D, 2015. Subduction zone tomography, Multiscale Seismic Tomography. Springer, pp. 55-95.

Zhao D (2017) Big mantle wedge, anisotropy, slabs and earthquakes beneath the Japan Sea. Phys Earth Planet Inter 270, 9-28

Zhao D, Asamori K, Iwamori H (2000) Seismic structure and magmatism of the young Kyushu subduction zone. Geophys Res Lett 27, 2057-2060

Zhao D, Isozaki Y, Maruyama S (2017) Seismic imaging of the Asian orogens and subduction zones. J Asian Earth Sci

Zhao D, Mishra O, Sanda R (2002) Influence of fluids and magma on earthquakes: seismological evidence. Phys Earth Planet Inter 132, 249-267

Zhao D, Wei W, Nishizono Y, Inakura H (2011) Low-frequency earthquakes and tomography in western Japan: insight into fluid and magmatic activity. J Asian Earth Sci 42, 1381-1393.doi:10.1016/j.jseaes.2011.08.003

Zhao D, Yu S, Liu X (2016) Seismic anisotropy tomography: New insight into subduction dynamics. Gondwana Research 33, 24-43

Zhao M, Qiu X, Xia S, Xu H, Wang P, Wang TK, Lee C-S, Xia K (2010) Seismic structure in the northeastern South China Sea: S-wave velocity and Vp/Vs ratios derived from three-component OBS data. Tectonophysics 480, 183-197

Zonno G, Oliveira CS, Ferreira MA, Musacchio G, Meroni F, Mota-de-Sá F, Neves F (2010) Assessing seismic damage through stochastic simulation of ground shaking: the case of the 1998 Faial earthquake (Azores Islands). Surveys in geophysics 31, 361-381

CHAPTER 5

DISCUSSION ABOUT A COMBINATION OF SIMULATED PGA BASED ON DIFFERENT SLIP DISTRIBUTIONS

In earthquake engineering, peak ground acceleration (PGA) is one of the most important intensity measures to evaluate the seismic response to engineering structures and to perform the hazard assessments (Tsai et al. 1993; Cramer et al. 1996; Bracci et al. 1997; Wahlström and Grünthal 2000; Christopoulos et al. 2002; Konstantinidis and Makris 2005; Dueñas-Osorio et al. 2007; Kunnath et al. 2008; Stucchi et al. 2011; Wang 2011). The stochastic finite-fault method is a powerful and simple tool to simulate earthquake ground motions, including the acceleration time series, PGA, Fourier amplitude spectra and the response spectra. When performing the simulations, the source information should be specified. As one of the critical source parameters, the slip distribution field has a significant influence on the simulated ground motions at near field.

The slip distribution field is defined as the relative motions of the hanging wall relative to the footwall of the fault during an earthquake, including the slip amount and motion direction. For example, Figure 5-1 shows the slip distribution field of the 2016 Kumamoto earthquake on the fault plane. Three kinds of major data can be used for the slip distribution inversion, including the strong ground motion (SGM) data (Sekiguchi et al. 1996; Honda et al. 2004; Asano et al. 2005; Ji et al. 2015), teleseismic body-wave (TBW) data (Kikuchi and Kanamori 1996; Antolik and Dreger 2003; Yamanaka and Kikuchi 2003; Shao et al. 2011), and the geodetic data (GPS or InSAR data) (Wright et al. 2003; Schmidt and Bürgmann 2006; Xu et al. 2010; Wu et al. 2016). However, it is not clear which kind of data can provide better results in ground motion simulations.

In this chapter, we discuss the accuracy of the PGA estimated based on the slip distributions inversed from different kinds of data. Further, a combination of simulated PGA for the past earthquakes is proposed to improve the accuracy of simulated PGA based on three or two kinds of PGA.

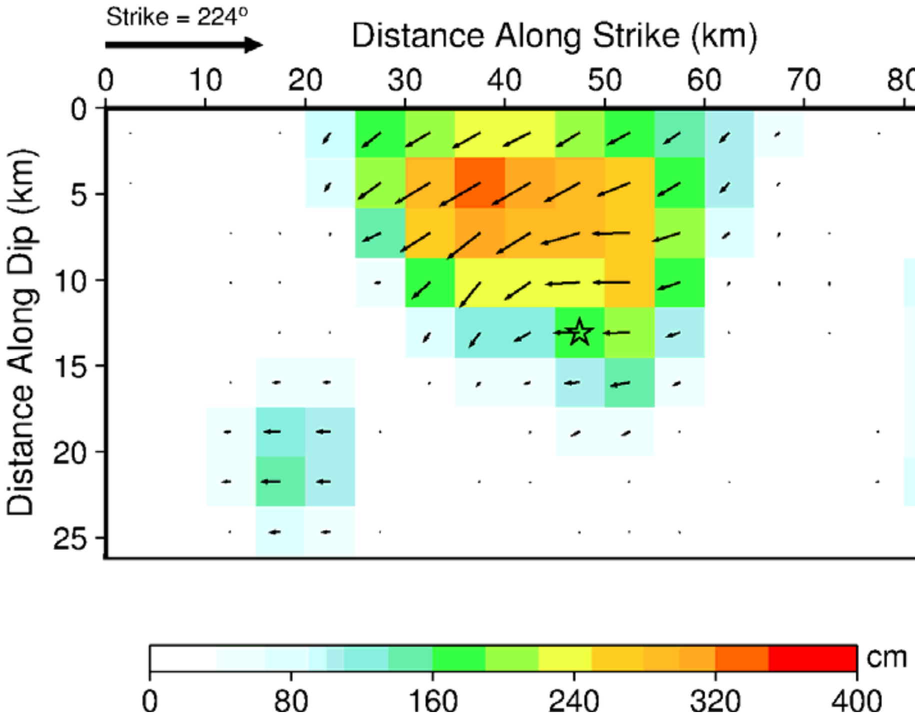

Figure 5-1 Slip distribution field of the 2016 Kumamoto earthquake using the teleseismic body-wave data (reproduced from Hayes (2016a)). The hypocentre location is denoted by a star. The slip amplitude is shown in colour and motion direction of the hanging wall relative to the footwall is denoted by black arrows

5.1 DATA SOURCE FOR ESTIMATING THE SLIP DISTRIBUTION

Many kinds of geophysical data can be used for slip distribution inversion, including the strong ground motion (SGM) data, teleseismic body-wave (TBW) data, and the geodetic data. The most widely-used geodetic data is the Global Positioning System (GPS) data. Besides, the Interferometric Synthetic Aperture Radar (InSAR) data, levelling, trilateration, tsunamic waveform data or other geophysical data are also used sometimes.

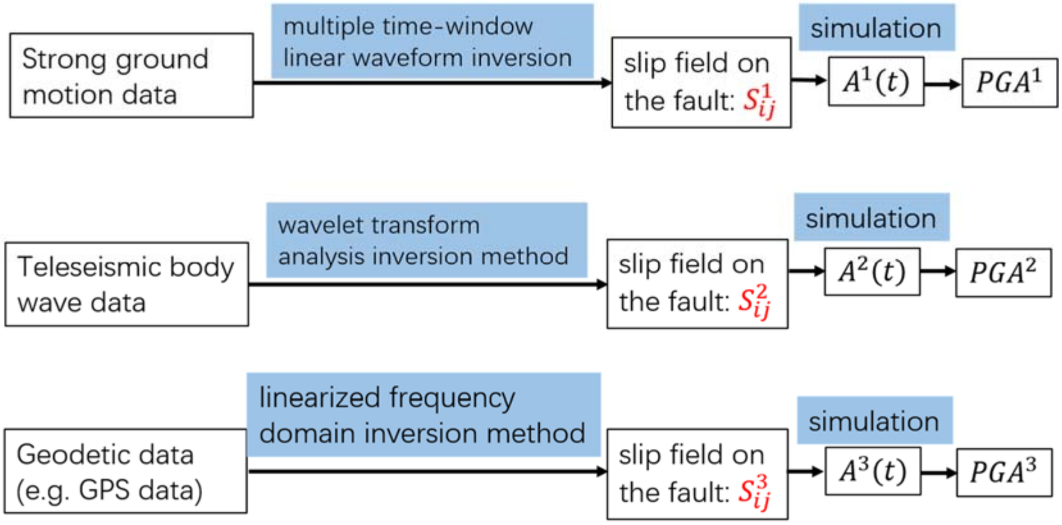

Figure 5-2 Three different slip distribution fields to simulate ground motions

Figure 5-2 shows the commonly used three different slip distribution field to simulate the ground motions using the stochastic finite-fault method. The multiple time-window linear waveform inversion method is usually used for the slip distribution inversion from the SGM data (Asano and Iwata, 2011;2016). Besides, the wavelet transform analysis inversion method can be used for the slip distribution field inversion from the TBW data (Ji et al, 2002). Further, the linearized frequency domain inversion method is developed and applied to the slip distribution inversion of the 2000 Tottori earthquake from the GPS data (Semmane et al, 2005)

Figure 5-3 shows the strong ground-motion stations used for the slip distribution inversion of the 2016 Kumamoto earthquake. Asano and Iwata (2016b) estimated the source processes of the mainshock and foreshock of the 2016 Kumamoto earthquake sequence using the so-called multiple time-window linear waveform inversion method based on the strong ground motions located around the epicentre. Since the inversion accuracy is dependent of the density of the strong ground-motions stations, a relative accurate slip distribution field can be obtained based on a dense observation network. Only some developed countries or regions could support such ground-motion network due to the high cost for operating and maintaining. For example, two strong ground-motion networks, the K-NET and the

KiK-net are installed and covered most of Japan with nearly 1000 and 700 stations respectively. In addition, the California and Taiwan can also provide rich strong ground-motion records for source process inversion.

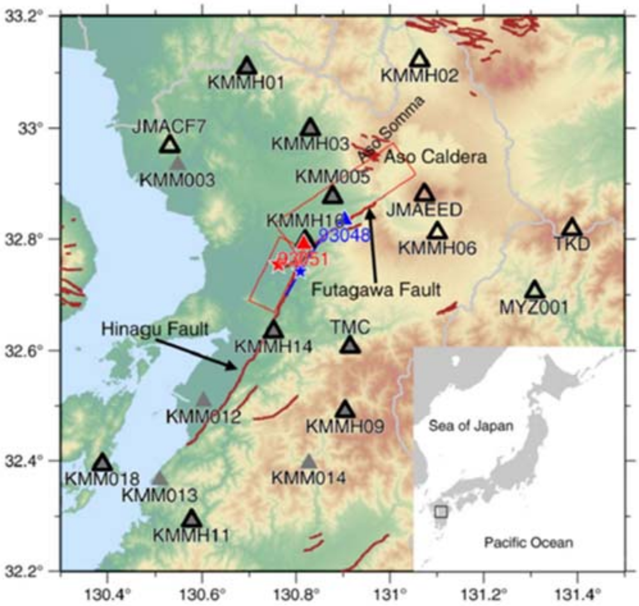

Figure 5-3 Strong motion stations used for the inversion of slip distribution field of 2016 Kumamoto, Japan earthquake (after Asano and Iwata (2016a))

Figure 5-4 shows the teleseismic body-wave stations used for the slip distribution inversion of the 2008 Iwate-Miyagi earthquake. Yagi (2008) inversed the source process of 2008 M6.9 Iwate-Miyagi earthquake using the waveform inversion method based on 48 teleseismic P-wave waveforms. Since the teleseismic data operated by IRIS (Incorporated Research Institutions for Seismology) is the most quickly available ones compare to other data, which are usually received just a few hours after an earthquake occurs, it is usually regarded as the initial data to have a research on the source process.

Figure 5-4 Teleseismic stations used for the inversion of slip distribution field of 2008 Iwate-Miyagi, earthquake, Japan (after Yagi (2008))

Figure 5-5 shows the GPS stations used for the slip distribution inversion of the 1999 Chi-Chi earthquake. Johnson et al. (2001) inverse the source process of the 1999 Chi-Chi, Taiwan earthquake using displacement inversion method based on the 111 GPS stations. The GPS technique is a relatively new one to investigate the displacement of the earth surface, which is generally considered starting from the end of 1980s. As the dislocation theory developed, the slip on the fault plane can be inversed using the displacement on the surface which is observed by GPS stations (Delouis et al. 2004; Gahalaut et al. 2006; Hashimoto et al. 2009; Page et al. 2009; Iinuma et al. 2011; Vigny et al. 2011; Yue and Lay 2011; Crowell et al. 2012; Wright et al. 2012; Jiang et al. 2014). Since the displacement observed by GPS stations is the direct response of the fault motions, they are usually adopted to analyse the co-seismic displacement field and inverse the source process on the fault plane.

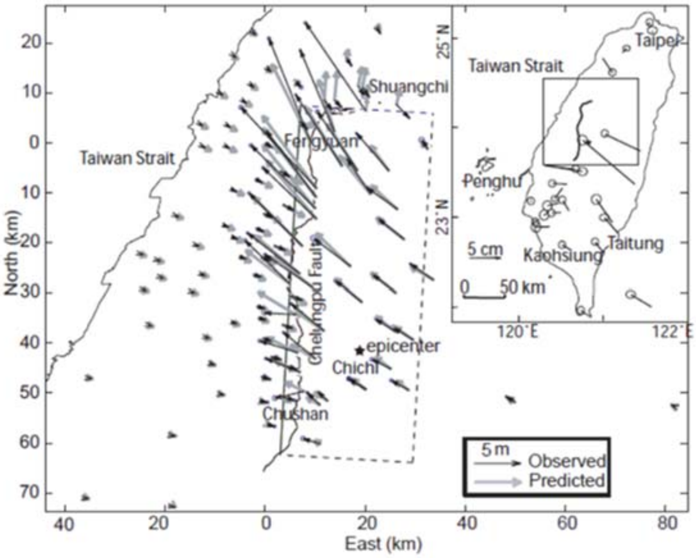

Figure 5-5 GPS stations used for the inversion of slip distribution field of 1999 Chi-Chi, earthquake, Taiwan (after Johnson et al. (2001))

5.2 COMPARISON OF SIMULATED PGA USING DIFFERENT SLIP DISTRIBUTION

For one earthquake, the slip distribution field can be estimated using the strong ground motion data, teleseismic body-wave data, and GPS data. For example, three different slip distributions of the 2008 Iwate-Miyagi earthquake are obtained. Figure 5-6, Figure 5-7 and Figure 5-8 show the source process of this earthquake using the strong ground motion data, teleseismic body-wave data and high-frequency GPS data, respectively. The comparison of them shows that neither the slip amount nor motion direction of fault plane is the same.

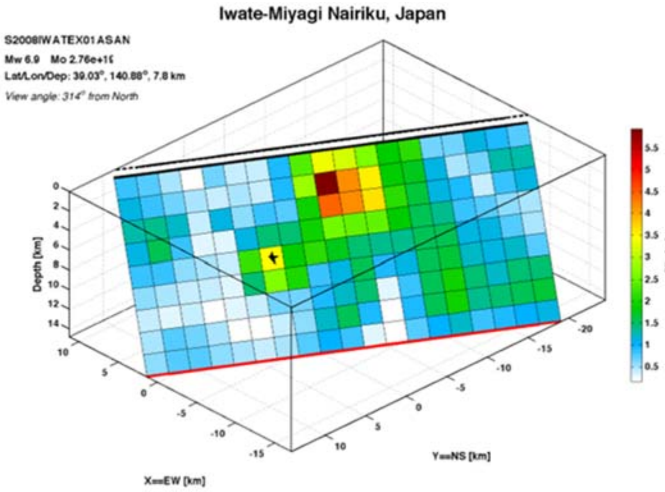

Figure 5-6 The slip distribution field of 2008 Iwate-Miyagi earthquake from the inversion of SGM data (accessed from SRCMOD)

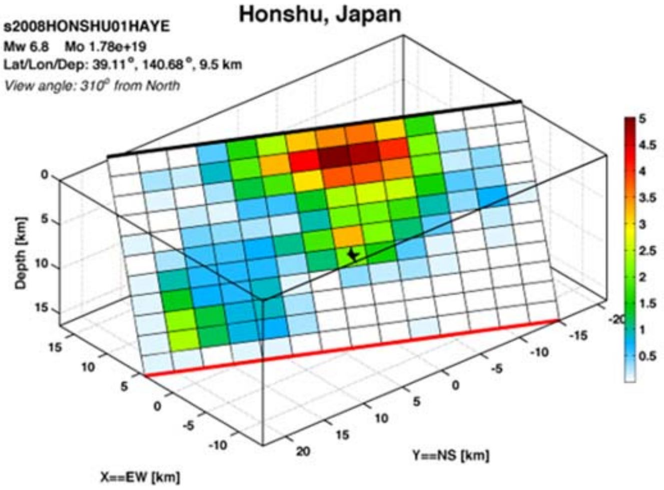

Figure 5-7 The slip distribution field of 2008 Iwate-Miyagi earthquake from the inversion of TBW data (accessed from SRCMOD)

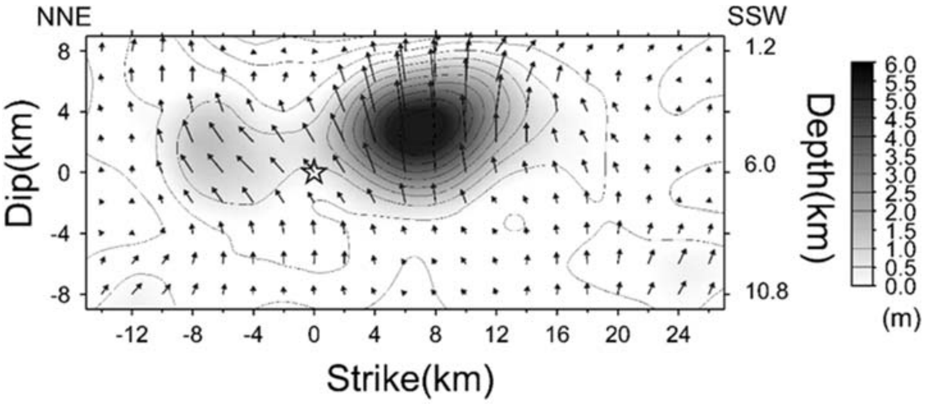

Figure 5-8 The slip distribution field of 2008 Iwate-Miyagi earthquake from the inversion of GPS data (after Yokota et al. (2009))

One of the major purposes in this thesis is to simulate ground motions for the region where the records are unavailable during a past earthquake. When performing the ground motion simulations, the slip distribution field should be input. Then the question is coming. Which slip distribution field inversed from different data performs best? To obtain relatively accurate simulated ground motions, this question mentioned above should be clarified.

The effect of slip distribution on ground motion is investigate and discussed deeply in this chapter. Mai and Thingbaijam (2014) established a rich finite-fault database named as SRCMOD to collect the finite-fault inversion results for global earthquakes. There are more than 300 slip distributions from 146 earthquakes containing in this database. It is convenient to investigate the effect of slip distribution based on this source. In this chapter, most of slip distributions are accessed from it.

To investigate the effect of slip distribution field better, some criteria should be set. Firstly, the event should be inversed using strong ground motion data, teleseismic body-wave data and GPS data separately. That is, at least three slip distributions can be obtianed for one earthquake. Secondly, some near-field strong ground- motion recordings should be available to compare the simluation and observation results. This is because our target to apply the simulation results to landslide hazard assessment. A simulated PGA at middle or far field usually can not attract more attention from engineers due to the small value of PGA. In this study, for the selected earthquakes, only the record with the PGA value larger than 300 cm/s^2 and the epicenter distance less than 100 km is considered.

Table 5-1 The earthquakes and their slip distributions using different data

Earthquake	Refference
1999 Chi-Chi earthquake, Taiwan	Zhang et al. (2004)
	Hayes (2014)
	Johnson et al. (2001)
2000 Tottori earthquake, Japan	Iwata et al. (2000)
	Yagi and Kikuchi (2000)
	Semmane et al. (2005)
2005 Fukuoka earthquake, Japan	Sekiguchi et al. (2006a)
	Yamanaka (2005)
	Kobayashi et al. (2006a)
2007 Noto Hanto earthquake, Japan	Asano and Iwata (2011b)
	Yagi (2007)
	Asano and Iwata (2011b)
2008 Iwate-Miyagi earthquake, Japan	Asano and Iwata (2011a)
	Hayes and Ji (2008)
	Yokota et al. (2009)
2016 Kumamoto earthquake, Japan	Asano and Iwata (2016b)
	Hayes (2016b)
	Fukahata and Hashimoto (2016)

Based on these criteria, 45 records from 6 earthquakes occurred in Japan and Taiwan are selected. The references of slip distribution field of these earthquakes are listed in Table 5-1. The sort of slip distribuitons follows the sequense that strong gorund motion data, teleseismic body-wave data and GPS data. The information of strong ground motion recordings used in this chpater is tabulated in Table 5-2.

Table 5-2 The information of stations used in this study

Earthquake	Station Code	Longtitude ($^{\circ}E$)	Latitude ($^{\circ}N$)	PGA (cm/s^2)
1999 Chi-Chi	C006	120.5520	23.5815	360
	C028	120.6052	23.632	755
	C034	120.5443	23.5212	305
	C041	120.5957	23.4388	650
	C101	120.5622	23.6862	400
	NST	121.0005	24.6312	407
	T045	120.9137	24.5412	525
	T047	120.9387	24.6188	420
	T052	120.7393	24.1980	455
	T065	120.6912	24.0588	800
	T067	120.7200	24.0912	500
	T068	120.7658	24.2772	502
	T071	120.7883	23.9855	650
	T072	120.8488	24.0407	470
	T074	120.9618	23.9622	600
	T075	120.6778	23.9827	330
	T076	120.6757	23.9077	430
	T078	120.8455	23.812	450
	T079	120.8942	23.8395	590
	T088	121.1758	24.2533	525
	T089	120.8565	23.9037	348
	T095	121.0135	24.6917	700
	T102	120.7208	24.2493	300
	T129	120.6843	23.8783	1000
	WGK	120.5622	23.6862	460
	WNT	120.6843	23.8783	940
2000 Tottori	HRSH03	133.137	34.518	361

	HRSH06	132.912	34.914	304
	OKYH08	133.405	34.910	306
	OKYH09	133.677	35.181	337
	OKYH10	133.926	35.283	303
	OKYH14	133.620	34.936	489
	SMNH01	133.260	35.296	849
	SMNH02	133.086	35.224	597
	TTRH02	133.391	35.231	1142
2005 Fukuoka	FKOH03	130.550	33.561	307
2007 Noto Hanto	ISKH01	137.284	37.527	360
	ISKH02	137.041	37.364	380
2008 Iwate-Miyagi	IWTH24	141.012	39.198	538
	IWTH25	140.864	39.009	1450
	IWTH26	141.001	38.969	1372
2016 Kumamoto	KMMH02	131.0629	33.122	687
	KMMH03	130.8301	32.9984	801
	KMMH14	130.7521	32.6345	612
	KMMH16	130.8199	32.7967	1362

In order to disscuss which slip distribution field performs best in ground motion simulations, we use the strochastic finite fault method to investigate it. The input parameters for each earthquake are tabulated in Table S1-6, while the slip distribution fieds are illustrated in Figure S1-18. For each record, we simulate by ten trials and use the average PGA as its simulated one. The simulated PGA and their relative errors using different slip distributions are compared and listed in Table 5-3 and Table 5-4. Here the reletive error is defined as the formula of

$$\text{Relative Error of PGA} = \frac{\left|PGA_{obs} - PGA_{sim}\right|}{PGA_{obs}}, \tag{5.1}$$

where the subscripts of obs and sim indicate the observed and simulated PGA, respectively. Both the average and maximum relative errors of three slip distributions based on the strong ground motion (SGM) data, the teleseismic body-wave (TBW) data and GPS data are all very large, although the one using SGM data performs better than others.

Table 5-3 Simulated PGA using different slip distribution fields

Station code	SGM (in cm/s^2)	TBW (in cm/s^2)	GPS (in cm/s^2)
C006	142	192	143
C028	410	749	485
C034	121	179	131
C041	500	789	510
C101	178	280	203
NST	247	300	409
T045	228	255	543
T047	231	302	425
T052	746	894	2662
T065	485	1461	1125
T067	558	1114	2319
T068	939	580	1854
T071	866	635	926
T072	468	464	625
T074	531	553	622
T075	328	1367	686
T076	374	1774	814
T078	543	574	595
T079	409	474	506
T088	317	270	240
T089	345	417	474
T095	482	591	712
T102	352	374	729
T129	390	1083	867
WGK	289	453	322
WNT	390	1083	867

HRSH03	60	53	53
HRSH06	126	111	94
OKYH08	214	215	182
OKYH09	288	285	280
OKYH10	135	129	112
OKYH14	187	166	173
SMNH01	980	935	903
SMNH02	343	334	285
TTRH02	1924	2096	2283
FKOH03	262	133	243
ISKH01	143	205	180
ISKH02	351	615	488
IWTH24	291	452	395
IWTH25	1488	1065	1821
IWTH26	1311	716	1373
KMMH02	221	165	290
KMMH03	439	477	612
KMMH14	638	590	361
KMMH16	1027	2152	1524

Table 5-4 Comparison of relative errors of simulated PGA using different slip distributions

	SGM	TBW	GPS
Aver. Rel. Err.	36.7%	50.5%	61.8%
Max. Rel. Err	87.0%	314.1%	485.0%

5.3 A COMBINATION ANALYSIS

Though the simulated PGA using three kinds of slip distribution field are all not good enough, is there any possible way to have a composite consideration to improve the simulation accuracy? In this chpater, a combination of three kinds of results is proposed to solve this issue. Since different slip distributions have their own contributions to the real rupture process of one earthquake, their characteristics have been reflected by the simulations. Therefore, the combination of individual results is reasonable which incorparating the composite contributions in the combined results.

5.4.1 THE COMBINATION OF THREE KINDS OF SIMULATED PGA

To have a comprehensive consideration for the contributions of three slip distributions to the simulation results, a linear model containing three kinds of PGA is proposed,

$$PGA = b_0 + b_1 PGA_1 + b_2 PGA_2 + b_3 PGA_3 \tag{5.2}$$

where the subscripts 1, 2, 3 of PGA indicate the simulated PGA using the slip distributions based on the strong ground motion data, the teleseismic body-wave data and the geodetic data, respectively. The coefficient b with the subscripts 0, 1, 2, 3 is the adjustment for individual PGA. To solve this equation, a linear least-squares fit is performed.

The investigation process introduced above is then made as a module and integrated in the practical system for simulating earthquake ground motions. One of the major purposes is to simulate earthquake ground motions during a past earthquake. It is achieved by combining the simulated PGA based on the individual simulation using different slip distributions. The specific process is illustrated in Figure 5-9. The flowchart of the combination of simulated PGA is beginning from the individual simulations. The simulated PGA is then extracted from the acceleration time series. Finally, the combination of simulated PGA is made using the regression coefficients in Table 5-5 and Table 5-9, which is dependent of the kinds of slip distribution field available.

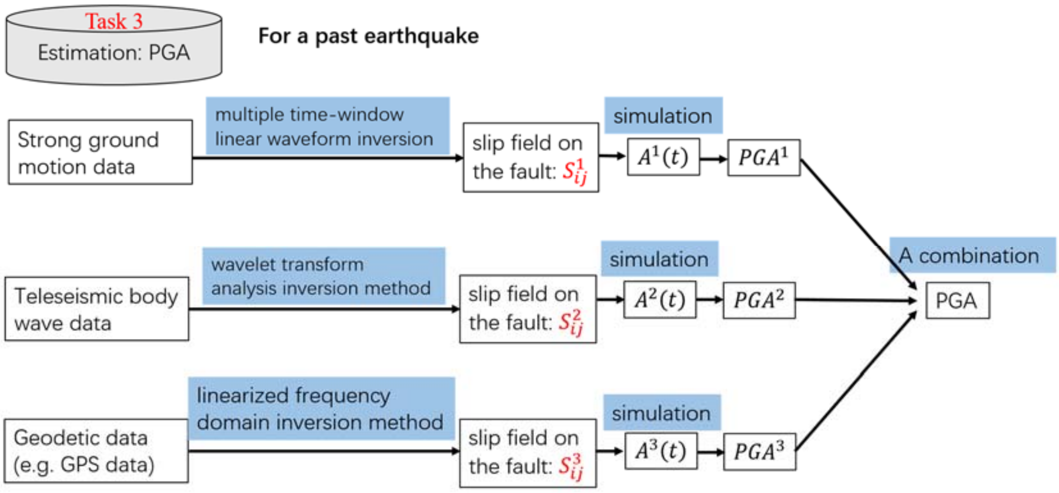

Figure 5-9 The flowchart for the estimation of PGA using the combination of simulated results

To avoid the problem of over validation, that is, all the data used for training and a part of data selected for validation, the 45 records used in this study should be separated into training data and validating data. Under this consideration, nearly 20% of all the 45 records (8) is selected for validation and the rest 80% (37) is for training. The validation data are from the 2007 Noto Hanto earthquake, the 2008 Iwate-Miyagi earthquake, and the 2016 Kumamoto earthquake. Regression coefficient and their 95% confidence intervals of the combined equation using three kinds of PGA are tabulated in Table 5-5.

Table 5-5 Regression coefficients of combined equation using three kinds of PGA

Regression coefficient	Value	95% confidence intervals
b_0	300.1002	(200.6594, 399.5410)
b_1	0.5358	(0.2863, 0.7852)
b_2	0.1428	(-0.0249, 0.3105)
b_3	-0.1178	(-0.2649, 0.0292)

After the regression, the average and maximum relative errors between combined and observed PGA for training and vlidation are also determined and listed in Table 5-6 and Table 5-7 with those of individual PGA. The abbreviation of

Comb in both tables indicates the combined PGA obtianed by equation (5.2). Both the average and maximum relative errors of combined PGA show significant advantages over each of individual simulated PGA.

Table 5-6 Comparison of relative errors of combined PGA of 37 records for training

	Comb.	SGM	TBW	GPS
Aver. Rel. Err.	22.6%	37.6%	52.6%	68.0%
Max. Rel. Err.	78.8%	87.0%	314.1%	485.0%

Table 5-7 Comparison of relative errors of combined PGA of 8 records for validation

	Comb.	SGM	TBW	GPS
Aver. Rel. Err.	24.7%	32.3%	40.7%	33.1%
Max. Rel. Err.	40.6%	67.8%	75.9%	57.8%

The combined PGA in 8 records for validation are specified in Table 5-8. Although some combined PGA are not as good as the individual simulated PGA, the average relative error is less than either of them. For example, in the station ITWH25, the simulated PGA based on the slip distribution field using SGM data matches the obversed PGA better than the combined one. However, it can not represent all the records. In general, the regional PGA should be simulated for a landslide susceptability region. Therefore, the average relative error is a more useful indicator for a region than focusing on the individual site. In short, the accuracy of simulated PGA based on the combination analysis is much improved.

Table 5-8 Comparison of simulated PGA in cm/s^2 using different slip distributions

Station code	Obs.	Comb.	SGM	TBW	GPS
ISKH01	360.3	384.5	142.5	204.5	179.9
ISKH02	380.3	518.4	351.0	615.3	488.4
IWTH24	538.0	473.6	290.6	451.2	395.2
IWTH25	1450.0	1034.7	1487.6	1065.0	1820.5
KMMH02	687.0	408.2	221.2	165.2	290.0
KMMH03	800.5	531.6	439.4	477.0	611.8
KMMH14	612.3	683.7	638.1	590.4	361.1
KMMH16	1362.1	978.1	1027.3	2151.6	1524.3

5.4.2 THE COMBINATION OF TWO KINDS OF SIMULATED PGA

Let's have a deep insight into the regression coefficients of equation (5.2). Besides the constant term b_0, the combined PGA is mostly contributed by the simulated PGA using the slip distribution field from the SGM data due to its largest coefficient, b_1. It is also should be noted that the third coefficient b_3, that is, the contribution from the simulated PGA based on the slip distribution field from GPS data is negative. Therefore, a trial is performed to combined the PGA without using the simulated PGA based on the slip distribution field using GPS data. Another reason to neglect the third term is that its average relative error is the largest one among three kinds of simulated PGA. So, the other combination should be tried only considering the contribution of simulated PGA based on the slip distribution field using the SGM and TBW data. Then, another combined equation is proposed as follows,

$$PGA = b_0 + b_1 PGA_1 + b_2 PGA_2 \tag{5.3}$$

where the subscripts 1 and 2 of PGA indicate the simulated PGA based on the slip distribution using SGM and TBW data, respectively. The regression coefficients of combined equation (5.3) are tabulated in Table 5-9.

Table 5-9 Regression coefficients of combined equation using two slip distributions

Regression coefficient	Value	95% confidence intervals
b_0	299.6273	(197.9080, 401.3466)
b_1	0.4231	(0.2124, 0.6338)
b_2	0.0920	(-0.0669, 0.2508)

The average and maximum relative errors of combined PGA for training and validation are listed in Table 5-10 and Table 5-11, respectively. Such accuracy is also much improved compare to the individual simulated PGA. Similarly, the combined PGA of 8 stations for validation are determined and tabulated in Table 5-12. In short, the combined PGA is much closer to the observed ones due to its lower average relative error, although some exceptions are still existing.

Table 5-10 Comparison of relative errors of combined PGA of 37 records for training

	Comb.	SGM	TBW
Aver. Rel. Err.	24.1%	37.6%	52.6%
Max. Rel. Err.	70.9%	87.0%	314.1%

Table 5-11 Comparison of relative errors of simulated PGA of 8 records for validation

	Comb.	SGM	TBW
Aver. Rel. Err.	23.6%	32.3%	40.7%
Max. Rel. Err.	40.6%	67.8%	75.9%

Table 5-12 Comparison of simulated PGA in cm/s^2 using different slip distributions

Station Code	Obs.	Comb.	SGM	TBW
ISKH01	360.3	379.3	142.5	204.5
ISKH02	380.3	504.9	351.0	615.3
IWTH24	538.0	464.4	290.6	451.2
IWTH25	1450.0	1028.0	1487.6	1065.0
KMMH02	687.0	408.4	221.2	165.2
KMMH03	800.5	529.4	439.4	477.0
KMMH14	612.3	623.9	638.1	590.4
KMMH16	1362.1	932.1	1027.3	2151.6

Two combination models are compared using the average relative errors for training and validation. The differences between two combination models are listed in Table 5-13. The differences between two model are not very significant, although the combination model based on 3 kinds of PGA performs better in most records. It is concluded that when the slip distribution using the geodetic data is unavailable, the combined PGA based on slip distributions using SGM and TBW data are also acceptable.

Table 5-13 Comparison of relative errors of different combination modes

Comb. Model	Aver. Rel. Err. Training	Aver. Rel. Err. Validation
3 kinds of PGA	22.6%	24.7%
2 kinds of PGA	24.1%	23.6%

5.4 CONCLUSIONS

The issue that which slip distribution will result in the most accurate ground motion simulations is clarified in this chapter. A linear combination of PGA simulated using the slip distribution inversion from different data is proposed. The following conclusions can be drawn:

(1) The question of which kind of slip distribution field performs best in the

ground motion simulations is clarified. 45 near-field records from 6 earthquakes are selected to investigate this issue. The ground motion simulations are performed for these records and compared with the observations. The average and maximum relative errors of these records are calculated and compared. It is suggested that neither of them performs well enough although the simulated PGA based on the slip distribution field using the SGM data match the observations better than others.

(2) A linear combination of the simulated PGA is proposed to fix the problem that low-accuracy simulated PGA using individual slip distribution. Two linear combination models are proposed to combine the PGA. The records are separated into two parts, the major part (nearly 80% of records) is used for training the model and the rest part is used for validation. Comparison of the average and maximum relative errors of the combined PGA and the individual simulated PGA shows the accuracy of results is much improved. The difference of accuracy of combined PGA between two combined model is not very significant.

(3) The combination process is made as a module and integrated into the practical system. The PGA in a region without enough observation records can be simulated using the individual slip distribution field and then combined together using this module to improve the accuracy.

REFERENCE

Antolik M, Dreger DS (2003) Rupture process of the 26 January 2001 Mw 7.6 Bhuj, India, earthquake from teleseismic broadband data. Bull Seismol Soc Am 93, 1235-1248

Asano K, Iwata T (2011a) Characterization of stress drops on asperities estimated from the heterogeneous kinematic slip model for strong motion prediction for inland crustal earthquakes in Japan. Pure Appl Geophys 168, 105-116

Asano K, Iwata T (2011b) Source-rupture process of the 2007 Noto Hanto, Japan, earthquake estimated by the joint inversion of strong motion and GPS data. Bull Seismol Soc Am 101, 2467-2480

Asano K, Iwata T (2016) Source rupture processes of the foreshock and mainshock in the 2016 Kumamoto earthquake sequence estimated from the kinematic waveform inversion of strong motion data. Earth Planets Space 68, 147

Asano K, Iwata T, Irikura K (2005) Estimation of source rupture process and strong ground motion simulation of the 2002 Denali, Alaska, earthquake. Bull Seismol Soc Am 95, 1701-1715

Atkinson GM, Assatourians K, Boore DM, Campbell K, Motazedian D (2009) A guide to differences between stochastic point-source and stochastic finite-fault simulations. Bull Seismol Soc Am 99, 3192-3201.doi:10.1785/0120090058

Atkinson GM, Boore DM (1995) Ground-motion relations for eastern North America. Bull Seismol Soc Am 85, 17-30

Atkinson GM, Boore DM (2006) Earthquake ground-motion prediction equations for eastern North America. Bull Seismol Soc Am 96, 2181-2205.doi:10.1785/0120050245

Bracci JM, Kunnath SK, Reinhorn AM (1997) Seismic performance and retrofit evaluation of reinforced concrete structures. J Struct Eng 123, 3-10

Christopoulos C, Filiatrault A, Folz B (2002) Seismic response of self‐centring hysteretic SDOF systems. Earthq Eng Struct Dynam 31, 1131-1150

Cramer CH, Petersen MD, Reichle MS (1996) A Monte Carlo approach in estimating uncertainty for a seismic hazard assessment of Los Angeles, Ventura, and Orange Counties, California. Bull Seismol Soc Am 86, 1681-1691

Crowell BW, Bock Y, Melgar D (2012) Real‐time inversion of GPS data for finite fault modeling and rapid hazard assessment. Geophys Res Lett 39

Delouis B, Vallée M, Meghraoui M, Calais E, Maouche S, Lammali K, Mahsas A, Briole P, Benhamouda F, Yelles K (2004) Slip distribution of the 2003 Boumerdes‐Zemmouri earthquake, Algeria, from teleseismic, GPS, and coastal uplift data. Geophys Res Lett 31

Dueñas‐Osorio L, Craig JI, Goodno BJ (2007) Seismic response of critical interdependent networks. Earthq Eng Struct Dynam 36, 285-306

Fukahata Y, Hashimoto M (2016) Simultaneous estimation of the dip angles and slip distribution on the faults of the 2016 Kumamoto earthquake through a weak nonlinear inversion of InSAR data. Earth Planets Space 68, 1-10.doi:10.1186/s40623-016-0580-4

Gahalaut V, Nagarajan B, Catherine J, Kumar S (2006) Constraints on 2004 Sumatra–Andaman earthquake rupture from GPS measurements in Andaman–Nicobar Islands. Earth Planet Sci Lett 242, 365-374

Hashimoto C, Noda A, Sagiya T, Matsu'Ura M (2009) Interplate seismogenic zones along the Kuril-Japan trench inferred from GPS data inversion. Nature Geoscience 2, 141

Hayes G (2014) Preliminary Finite Fault Results for the Sep 20, 1999 Mw 7.6 23.8340,120.8130 Earthquake (Version 1). Journal Volume, Pages https://earthquake.usgs.gov/earthquakes/eventpage/usp0009eq0#finite-fault

Hayes G (2016) Preliminary finite fault results for the Apr 15, 2016 Mw 7.0 1km WSW of Kumamoto-shi, Japan earthquake (Version 1). http://earthquake.usgs.gov/earthquakes/eventpage/us20005iis#finite-fault Accessed 1 May 2016

Hayes G, Ji C (2008) Preliminary Result of the Jun 13, 2008 Mw 6.8 Honshu Earthquake. Journal Volume, Pages http://earthquake.usgs.gov/earthquakes/eqinthenews/2008/us2008tfdp/finite_fault.php

Honda R, Aoi S, Morikawa N, Sekiguchi H, Kunugi T, Fujiwara H (2004) Ground motion and rupture process of the 2003 Tokachi-oki earthquake obtained from strong motion data of K-NET and KiK-net. Earth Planets Space 56, 317-322

Iinuma T, Ohzono M, Ohta Y, Miura S (2011) Coseismic slip distribution of the 2011 off the Pacific coast of Tohoku Earthquake (M 9.0) estimated based on GPS data—Was the asperity in Miyagi-oki ruptured? Earth Planets Space 63, 24

Iwata T, Sekiguchi H, Matsumoto Y, Miyake H, Irikura K, 2000. Source process of the 2000 western Tottori prefecture earthquake and near-source strong ground motions, Fall meeting of the Seismological Society of Japan.

Ji C, Archuleta RJ, Twardzik C (2015) Rupture history of 2014 Mw 6.0 South Napa earthquake inferred from near-fault strong motion data and its impact to the practice of ground strong motion prediction. Geophys Res Lett 42, 2149-2156

Jiang Z, Wang M, Wang Y, Wu Y, Che S, Shen ZK, Bürgmann R, Sun J, Yang Y, Liao H (2014) GPS constrained coseismic source and slip distribution of the 2013 Mw6. 6 Lushan, China, earthquake and its tectonic implications. Geophys Res Lett 41, 407-413

Johnson KM, Hsu Y-J, Segall P, Yu S-B (2001) Fault geometry and slip distribution of the 1999 Chi-Chi, Taiwan earthquake imaged from inversion of GPS data. Geophys Res Lett 28, 2285-2288

Kikuchi M, Kanamori H (1996) Rupture process of the Kobe, Japan, earthquake of Jan. 17, 1995, determined from teleseismic body waves. J Phys Earth 44, 429-436

Kobayashi R, Miyazaki Si, Koketsu K (2006) Source processes of the 2005 West Off Fukuoka Prefecture earthquake and its largest aftershock inferred from strong motion and 1-Hz GPS data. Earth Planets Space 58, 57-62

Konstantinidis D, Makris N (2005) Seismic response analysis of multidrum classical columns. Earthq Eng Struct Dynam 34, 1243-1270

Kunnath SK, Erduran E, Chai Y, Yashinsky M (2008) Effect of near-fault vertical ground motions on seismic response of highway overcrossings. J Bridge Eng 13, 282-290

Mai PM, Thingbaijam K (2014) SRCMOD: An online database of finite-fault rupture models. Seismol Res Lett 85, 1348-1357

Motazedian D, Atkinson GM (2005) Stochastic finite-fault modeling based on a dynamic corner frequency. Bull Seismol Soc Am 95, 995-1010

Page MT, Custódio S, Archuleta RJ, Carlson J (2009) Constraining earthquake source inversions with GPS data: 1. Resolution-based removal of artifacts. J Geophys Res 114

Schmidt D, Bürgmann R (2006) InSAR constraints on the source parameters of the 2001 Bhuj earthquake. Geophys Res Lett 33

Sekiguchi H, Aoi S, Honda R, Morikawa N, Kunugi T, Fujiwara H (2006) Rupture process of the 2005 West Off Fukuoka Prefecture earthquake obtained from strong motion data of K-NET and KiK-net. Earth Planets Space 58, 37-43

Sekiguchi H, Irikura K, Iwata T, Kakehi Y, Hoshiba M (1996) Minute locating of faulting beneath Kobe and the waveform inversion of the source process during the 1995 Hyogo-ken Nanbu, Japan, earthquake using strong ground motion records. J Phys Earth 44, 473-487

Semmane F, Cotton F, Campillo M (2005) The 2000 Tottori earthquake: A shallow earthquake with no surface rupture and slip properties controlled by depth. J Geophys Res 110.doi:10.1029/2004jb003194

Shao G, Li X, Ji C, Maeda T (2011) Focal mechanism and slip history of the 2011 Mw 9.1 off the Pacific coast of Tohoku Earthquake, constrained with teleseismic body and surface waves. Earth Planets Space 63, 9

Somerville P, Irikura K, Graves R, Sawada S, Wald D, Abrahamson N, Iwasaki Y, Kagawa T, Smith N, Kowada A (1999) Characterizing crustal earthquake slip models for the prediction of strong ground motion. Seismol Res Lett 70, 59-80

Stucchi M, Meletti C, Montaldo V, Crowley H, Calvi GM, Boschi E (2011) Seismic hazard assessment (2003–2009) for the Italian building code. Bull Seismol Soc Am 101, 1885-1911

Tsai K-C, Chen H-W, Hong C-P, Su Y-F (1993) Design of steel triangular plate energy absorbers for seismic-resistant construction. Earthquake spectra 9, 505-528

Vigny C, Socquet A, Peyrat S, Ruegg J-C, Métois M, Madariaga R, Morvan S, Lancieri M, Lacassin R, Campos J (2011) The 2010 Mw 8.8 Maule megathrust earthquake of Central Chile, monitored by GPS. Science 332, 1417-1421

Wahlström R, Grünthal G (2000) Probabilistic seismic hazard assessment (horizontal PGA) for Sweden, Finland and Denmark using different logic tree approaches. Soil Dynam Earthq Eng 20, 45-58

Wang Z (2011) Seismic hazard assessment: issues and alternatives. Pure Appl Geophys 168, 11-25

Wright TJ, Houlié N, Hildyard M, Iwabuchi T (2012) Real‐time, reliable magnitudes for large earthquakes from 1 Hz GPS precise point positioning: The 2011 Tohoku‐Oki (Japan) earthquake. Geophys Res Lett 39

Wright TJ, Lu Z, Wicks C (2003) Source model for the Mw 6.7, 23 October 2002, Nenana Mountain Earthquake (Alaska) from InSAR. Geophys Res Lett 30

Wu Y, Jiang Z, Liang H, Chang L, Chen C, Zhu S, Zhao J, Du J (2016) Coseismic deformations of the 2015 M W 7.8 Gorkha earthquake and interseismic strain accumulation in the Himalayan tectonic belt and Tibetan plateau. Tectonophysics 670, 144-154

Xu C, Liu Y, Wen Y, Wang R (2010) Coseismic slip distribution of the 2008 Mw 7.9 Wenchuan earthquake from joint inversion of GPS and InSAR data. Bull Seismol Soc Am 100, 2736-2749

Yagi Y (2007) March 25, 2007 Noto Hanto earthquake. Journal Volume, Pages www.geol.tsukuba.ac.jp/~yagi-y/EQ/20070325/index.html

Yagi Y (2008) June 14, 2008 Iwate / Miyagi inland earthquake. Journal Volume, Pages http://www.geol.tsukuba.ac.jp/~yaji-y/eng/earthquakes.html

Yagi Y, Kikuchi M (2000) Source Rupture Process of the Tottori-ken Seibu earthquake of Oct. 6, 2000 Journal Volume, Pages https://wwweic.eri.u-tokyo.ac.jp/yuji/tottori

Yamanaka Y (2005) Western Fukuoka-oki earthquake in March 20 (Mj7.0). Journal Volume, Pages http://wwweic.eri.u-tokyo.ac.jp/sanchu/Seismo_Note/2005/EIC163.html

Yamanaka Y, Kikuchi M (2003) Source process of the recurrent Tokachi-oki earthquake on September 26, 2003, inferred from teleseismic body waves. Earth Planets Space 55, e21-e24

Yokota Y, Koketsu K, Hikima K, Miyazaki Si (2009) Ability of 1‐Hz GPS data to infer the source process of a medium‐sized earthquake: The case of the 2008 Iwate‐Miyagi Nairiku, Japan, earthquake. Geophys Res Lett 36

Yue H, Lay T (2011) Inversion of high‐rate (1 sps) GPS data for rupture process of the 11 March 2011 Tohoku earthquake (Mw 9.1). Geophys Res Lett 38

Zengin E, Cakti E (2014) Ground motion simulations for the 23 October 2011 Van, Eastern Turkey earthquake using stochastic finite fault approach. Bull Earthq Eng 12, 627-646

Zhang L, Chen G, Wu Y, Jiang H (2016) Stochastic ground-motion simulations for the 2016 Kumamoto, Japan, earthquake. Earth Planets Space 68, 1-13.doi:10.1186/s40623-016-0565-3

Zhang W, Iwata T, Irikura K, Pitarka A, Sekiguchi H (2004) Dynamic rupture process of the 1999 Chi-Chi, Taiwan, earthquake. Geophys Res Lett 31

CHAPTER 6

IMPROVEMENT OF A PRACTICAL APPROACH OF ESTABLISHING SLIP DISTRIBUTION FIELD FOR A POTENTIAL EARTHQUAKE

6.1 INTRODUCTION

In the ground motion simulations, the source term plays an important role in synthesizing source spectrum (Aki 1967; Brune 1970; Boore 1983; Boore et al. 2003). Among all the source parameters, the slip distribution field decides the weight of seismic moment on each subfault, which controls the radiation energy (Beresnev and Atkinson 1998; Motazedian and Atkinson 2005; Boore 2009; Atkinson and Assatourians 2015). Therefore, it is very important to estimate the source rupture process, not only for the understating of the details of the earthquake rupture on the fault plane, but for applying to the ground motion prediction. For a past earthquake, the process of the fault rupture can be inversed from the observation data mentioned in the last chapter. In the ground motion simulations using the stochastic finite-fault method, the slip distribution field should be specified (Ugurhan and Askan 2010; Zengin and Cakti 2014; Holden and Kaiser 2016; Zhang et al. 2016b; Chen et al. 2017). However, it is difficult to estimate the slip distribution field for a potential earthquake.

In this chapter, an approach of establishing the slip distribution field of a potential earthquake with an assumed magnitude occurs on a specific fault is improved. Specifically, a rectangle-ellipse pattern of the slip distribution field is proposed on the basis of a lot of observations for the slip distribution inversions of past earthquakes. The scaling relations of slip distribution versus seismic moment are established from 17 shallow crustal earthquakes around Japan occurred from 1995 to 2016 with a wider moment magnitude range of M5.8-9.0. A slip distribution field is established by assuming a potential M7 earthquake occurs on the Futagawa fault. Finally, the generated slip distribution field is input into stochastic finite-fault model for the ground motion simulations of 53 KiK-net stations. The simulated PGA and envelopes are compared with the ground-motion recordings from the 2016 Kumamoto earthquake.

6.2 THE PROCEDURE OF ESTABLISHING SLIP DISTRIBUTION

The procedure of establishing the slip distribution field for a potential earthquake occurs on a specific fault is made as a module and incorporated in the practical system for simulating earthquake ground motions. Figure 6-1 shows the flowchart of the module to generating slip distribution field for a potential earthquake.

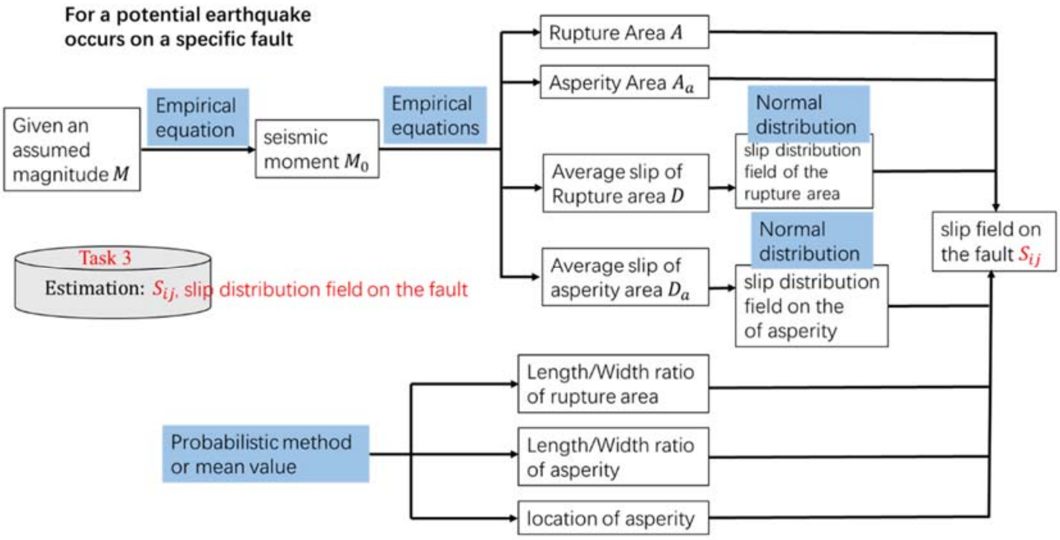

Figure 6-1 The flowchart of generating slip distribution field for a potential earthquake

The procedure is summarized as below:

(1) Calculate the seismic moment M_0 based on the relation between the seismic moment versus the magnitude and the assumed magnitude of an earthquake;

(2) Calculate the rupture areas and average slips of the fault and asperity based on the scaling relations;

(3) Determine the geometries of the rupture and asperity using the average length-to-width ratios;

(4) Generate the slip distribution on the background fault and asperity using the normal probability density function;

(5) Determine the location of asperity using the average normalized distances from the strike and down-dip or the probability method.

It should be noted that the normal distribution of slip on the rupture area and asperity is calculated from a normal probability density function (Figure 6-2). The mean value and the standard deviation of this function is restricted by the maximum, minimum, and the average slip on the asperity.

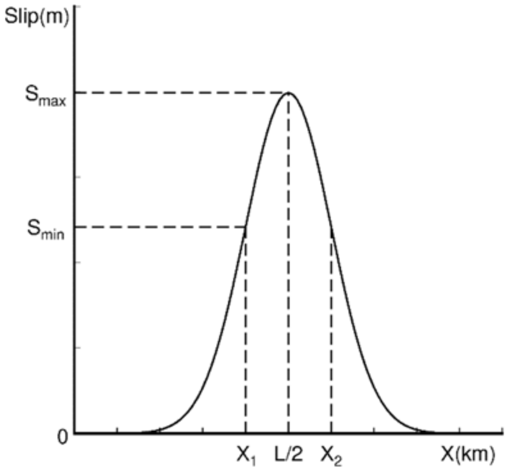

Figure 6-2 The normal probability density function used to determine the slip distribution. The x_1 and x_2 indicate boundary of asperity in the x direction, the L represents the length of the rupture area in km, the S_{max} and S_{min} indicate the maximum and minimum slip on the asperity.

6.3 THE SCALING RELATIONS OF SLIP DISTRIBUTION

The source models reviewed above cannot represent the realistic situations very well. Specifically, an asperity or SMGA is usually defined or determined as a rectangular area (Oth et al. 2007; Maeda et al. 2008; Suzuki and Iwata 2009; Oth

2013; Nozu et al. 2014; Riahi et al. 2015; Adams et al. 2016; Iwaki et al. 2016; Moratto et al. 2017; Walter et al. 2017), which is not consistent with all the slip distribution inversions. Actually, from a lot of observations for the slip distribution results, the region with large slip amount or velocity is an elliptical shape, rather than a normal rectangle. Further discussion will be given in the following section.

This issue has been discussed by some previous studies and some possible ways are provided for approximately estimating the slip distribution field for a future earthquake. For example, Kanamori (1975) define the asperity as the region on the fault rupture surface with large slip amount relative to the average slip on the fault. Somerville et al. (1999) combine the asperity model with the wavenumber spectrum analysis method to quantify the slip heterogeneity on the fault. Irikura and Miyake (2011) develop a recipe for predicting the ground motions from earthquake scenarios based on the empirical Green's function method, which uses outer, inner and extra fault parameters to characterize the source model based on Somerville et al. (1999)'s strategy. Miyake et al. (2003) define the strong motion generation areas (SMGA) as the region with relative large slip velocity on the fault plane and suggest the high-frequency contents of seismic wave are mainly radiated from such areas with high stress drop. They also find the SMGAs coincide with the asperities in size and location. Such representative work suggest to relate the area and stress drop of asperity or SMGA to the seismic moment, which are usually inversed using the empirical Green's function method (Maeda and Sasatani 2009; Bykova et al. 2010; Kurahashi and Irikura 2010; Tanırcan and Savaş 2011; Sadeghi et al. 2013; Sharma et al. 2013; Xia et al. 2015; Sharma et al. 2016; Li et al. 2017; Wang et al. 2017b).

The scaling laws of slip distribution established by Somerville et al. (1999) are based on the onshore earthquakes occurred in western North America mainly, which are not suitable for all the situation, especially for the interplate earthquakes. The reasonability of these scaling laws are still controversial. For example, Suzuki and Iwata (2006, 2007) conclude that the area of SMGA for the interplate earthquake is generally smaller than that of crustal earthquake under the same seismic moment by analysing several M6-7 earthquakes occurred in northeast Japan. Miyake et al. (2006) suggest the predicted area of SMGA for interplate earthquake is larger than that for the crustal earthquakes by investigating the earthquakes with the magnitude range of M6.7-8.4 around Japan. Murotani et al. (2008) establish the scaling relations of source rupture model for interplate earthquakes around Japan which occurred from 1923-2003 with the magnitude range of M6.7-8.4. In their database, some source rupture models are inversed for the same earthquake using different geophysical data. It will restrict the application of the regressed scaling relations due to the narrow seismic moment range. Besides, their suggestion for the identification of asperity without starting from the row- or column-wise operation leads to an irregular asperity, which is not readily to be used for determining the dimension of asperity in the prediction for a potential earthquake. Gonzales et al. (2012) apply the procedure of Somerville et al. (1999) to establish the scaling relations of Mexican subduction zone for the strong ground-motion prediction. However, Rodríguez-Pérez and Ottemöller (2013) determine the scaling relations for the Mexico based on the teleseismic body-wave inversion using the method of Murotani et al. (2008) to identify the irregular asperity. These literatures provide possible solutions to establish slip distribution field for a potential earthquake occurs on a specific fault but with their own limitations.

In geophysics, the fault ruptures on the fault plane start from the shear dislocation of nucleation point or initial rupture point (Dieterich 1992; Rice 1992; Rice and Beltz 1994; Scholz 2002). Then it is considered that the seismic waves radiate from the source by the sphercal propagation (Boore 1972; Sato 1977; Ursin 1983; Jahnke et al. 2008; Ben-Menahem and Singh 2012). As the seimic-wave propagaton, the slip on the fault plane decays from the initial rupture point since the seimic energy transforms to the heat (Lee and Delaney 1987; Mitchell 1995; Nielsen et al. 2000; Goldsby and Tullis 2002; Fialko and Khazan 2005; Mizoguchi et al. 2007). Therefore, a rectangular model is not so much approparate to fit this process. For example, the slip distribution field of the 2008 M6.9 Iwate-Miyagi earthquake inversed from the GPS data shows the significant elliptical distribution of relative large slip area (Figure 6-3). In addtion, the slip amounts of the rectangular asperity model on the four corners are usually significantly less than their nearby region. These small-slip parts of asperity cannot approparately represent the major characteristics of slip on the fault plane. Therefore, in this chapter, an elliptial asperity model is developed as the representative of large slip region on the fault plane.

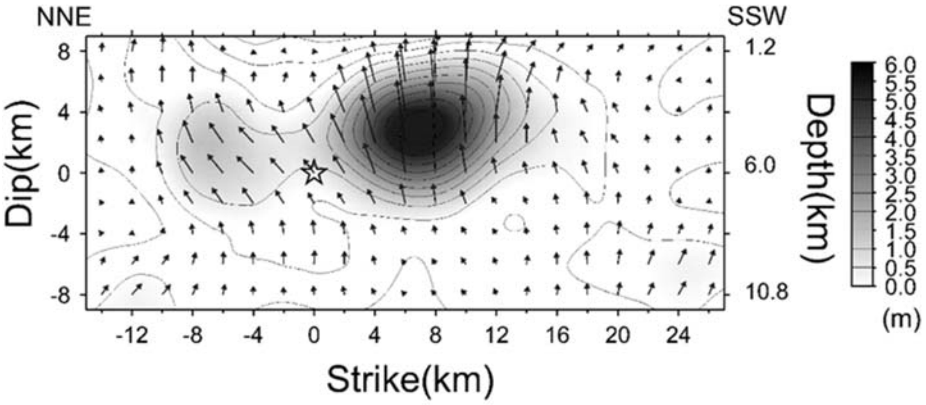

Figure 6-3 The slip distribution field of 2008 Iwate-Miyagi earthquake inversed from the GPS data (after Yokota et al. (2009))

In the slip distribution inversion, the slip distribution field on the fault plane is usually shown as a rectangle. As we know that the ruptures induced by an earthquake cannot spread on the whole fault plane. For example, during the 2008 M7.9 Wenchuan, China earthquake, only the central and western segments of the Longmenshan fault ruptured. Therefore, in this thesis, only the region with obvious slip amount are considered as the so-called rupture area. The specific criterion of the selection of rupture area follows Somerville et al. (1999)'s definition. That is, the average slip of each row or column of the rupture area should be larger than 0.3 times of the average slip of the entire fault plane. If any edge of a region doesn't meet this rule, it will be snipped and excluded.

In this thesis, one pattern of the slip distribution field is proposed to represent the characteristics of the fault slip during an earthquake. This model consists of two parts, a rectangular rupture area and an elliptical asperity. For example, In Figure 6-4, the slip distribution field of the 1997 M6.1 Kagoshima earthquake is represented in this pattern.

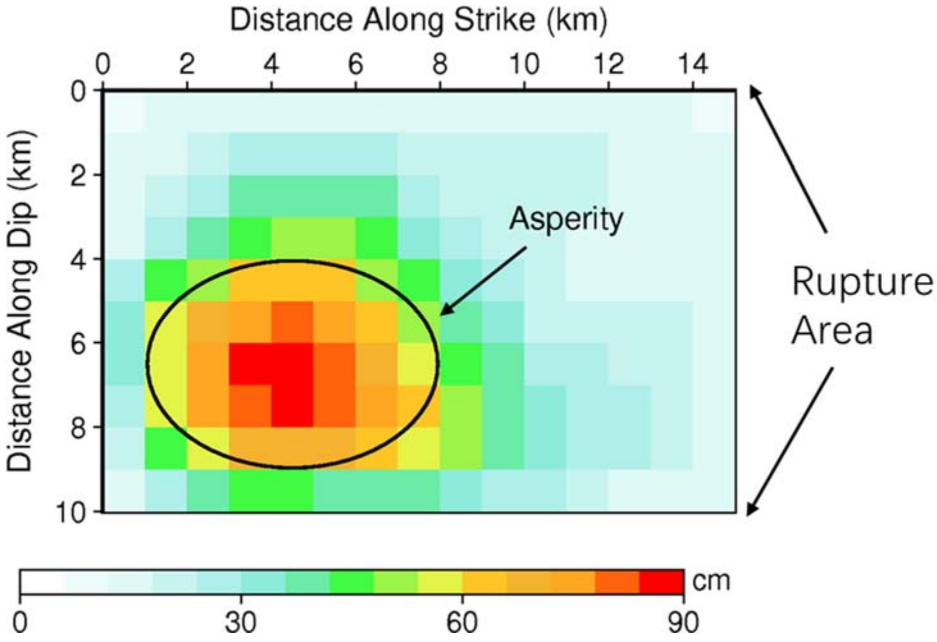

Figure 6-4 The slip distribution field of 1997 M6.1 Kagoshima earthquake (after Horikawa (2001), refigured)

To investigate the characteristics of the rupture area and asperity on the fault plane, 17 earthquakes occurred in Japan are selected. It is not difficult to relate the area and slip of the rupture area and asperity to the seismic moment, because the seismic moment is determined as the multiplication of the shear modulus, the area and average slip of the fault plane. Therefore, the scaling relations of slip distribution field can be established by using the past earthquakes. In this chapter, 17 shallow crustal earthquakes at the depth of 0-25 km and the magnitude of 5.8-9.0 are collected based on the database of Japan from 1995 to 2016. The reason to select the shallow and moderate-to-large earthquakes is the amplitude of seismic wave is generally dependent of the focal depth and the magnitude. A deeper earthquake usually corresponds to smaller amplitudes of the seismic wave comparing with a shallower earthquake. Similarly, an earthquake with a large magnitude usually causes a large PGA values in the observed waveforms at the same condition. One of the major purposes of this thesis is to apply the developed practical system to the landslide hazard assessment. A smaller PGA cannot attract more attention from the engineers. Therefore, only the earthquake meets these two criteria will be used in this study.

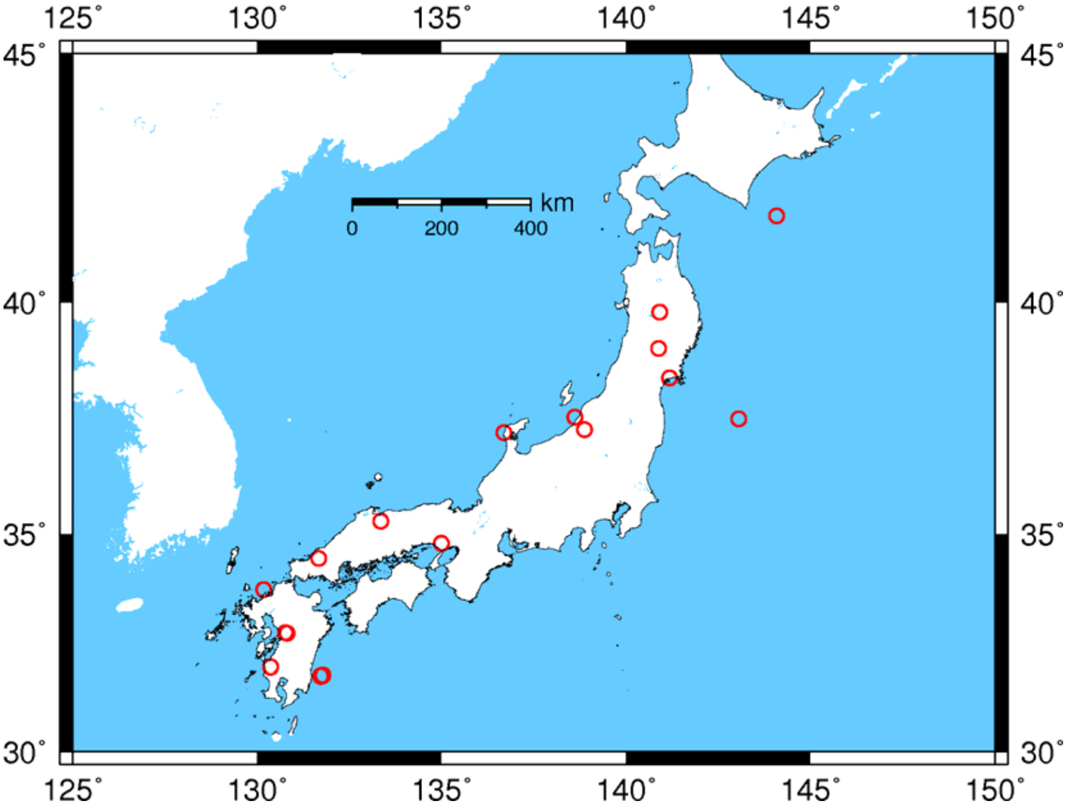

Figure 6-5 The epicentres of earthquakes used in this chapter

Table 6-1 shows the information of earthquakes used in the statistics. In this table, the abbreviation of mech. indicates the focal mechanism of the earthquake, including the strike-slip (shown in SS) and the reverse (RV) earthquakes. To avoid the uncertainty of the slip distributions, only the earthquakes occurred at the inland region are taken into consideration except of the 2005 Fukuoka earthquake, the 2003 Tokachi-oki earthquake, and the megathrust 2011 Tohoku earthquake. The epicentres of the 17 earthquakes are shown in Figure 6-5.

Table 6-1 The information of earthquakes used in the statistics

Earthquake location	Date	Mech.	Mag. (M_w)	Lon./Lat. $(^\circ E/^\circ N)$	Source Reference
Yamaguchi	1997.6.25	SS	5.8	131.66/34.44	F-net
Iwate	1998.9.3	RV	5.9	140.91/39.80	F-net
Kagoshima	1997.3.26	SS	6.1	130.36/31.97	F-net
Miyagi	2003.7.25	RV	6.1	141.17/38.40	F-net
Kumamoto,f*	2016.4.14	SS	6.1	130.81/32.74	F-net
Niigata	2004.10.23	RV	6.6	138.87/37.29	F-net
Fukuoka	2005.3.20	SS	6.6	130.18/33.74	F-net
Tottori	2000.10.6	SS	6.6	133.35/35.28	F-net
Niigata	2007.12.2	RV	6.6	138.61/37.56	F-net
Hyuga-Nata2	1996.12.2	RV	6.7	131.72/31.76	Harvard
Noto Hanto	2007.3.25	RV	6.7	136.69/37.22	F-net
Hyuga-Nada1	1996.10.19	RV	6.7	131.78/31.78	Harvard
Kobe	1995.1.17	SS	6.9	134.99/34.78	Harvard
Iwate-Miyagi	2008.6.13	RV	6.9	140.88/39.03	F-net
Kumamoto	2016.4.15	SS	7.1	130.76/32.75	F-net
Tokachi-oki	2003.9.25	RV	7.9	144.08/41.78	F-net
Tohoku	2011.3.11	RV	9.0	143.05/37.52	Harvard

* means the largest foreshock of Kumamoto earthquake

The information of slip distributions of 17 earthquakes are listed in Table 6-2, Table 6-3, and Table 6-4. The asperities of each earthquake are identified following the procedure of Somerville et al. (1999). The normalized distances of strike and down-dip indicate the distances from centre of asperity to the left and upper sides of the fault plane over the length and width of the fault plane, respectively.

Table 6-2 Slip distributions used for regression

Earthquake location	Focal depth (km)	Data for source process inversion	Reference
Yamaguchi	8	TELE	Ide (1999)
Iwate	5	SGM	Nakahara et al. (2002)
Kagoshima	8	SGM	Horikawa (2001)
Miyagi	5	SGM	Hikima and Koketsu (2004)
Kumamoto,f	11	SGM	Asano and Iwata (2016a)
Niigata	5	SGM	Asano and Iwata (2009)
Fukuoka	11	SGM	Sekiguchi et al. (2006b)
Tottori	11	SGM	Iwata et al. (2000)
Niigata	8	SGM+GPS	Cirella et al. (2008)
Hyuga-Nata2	20.4	SGM+TRIL	Yagi et al. (1999)
Noto Hanto	8	SGM+GPS	Asano and Iwata (2011b)
Hyuga-Nada1	11.6	SGM+TRIL+GPS	Yagi et al. (1999)
Kobe	16.37	SGM	Sekiguchi et al. (2002)
Iwate-Miyagi	5	SGM	Asano and Iwata (2011a)
Kumamoto	11	SGM	Asano and Iwata (2016a)
Tokachi-oki	23	SGM+GPS	Koketsu et al. (2004)
Tohoku	20	SGM	Ide et al. (2011)

Table 6-3 The information of slip distributions of 17 earthquakes used in this chapter

Moment $M_0 \times 10^{25}$ (dyne-cm)	Rupture area in km^2	Aver. Slip of Rupt. in cm	Asperity area in km^2	Aver. Slip of Asp. in cm
0.566	99	20.63	19.6	38.7
0.753	81	47.67	14.1	116.1
1.4	150	33.91	27.5	68.2
1.53	180	31.11	6.3	86.5
2.04	182	35.86	25.9	67.5
7.53	504	66.63	62.8	146.8
7.8	576	71.34	37.7	269.4
8.62	630	90.54	84.82	187
9.3	572	54.29	76.9	157.1
12.3	852	42.18	157.3	83.5
13.6	480	108.64	75.4	227.5
14.3	1032	54.15	133.9	139.7
24.3	1303	79.28	207.9	175.0
27.2	684	120.5	100.5	264.6
44.2	756	186.51	166.5	336.36
821	12000	310.88	1570.8	557.9
53100	94668	1117.84	24976.4	1923.0

Table 6-4 The location information of asperity

Moment $M_0 \times 10^{25}$ (dyne-cm)	Norm. dist. from strike	Norm. dist. from down-dip	L/W of rupture area	L/W of asperity
0.566	0.5	0.5	0.82	1
0.753	0.44	0.17	1	2
1.4	0.3	0.65	1.5	1.4
1.53	0.44	0.1	1.8	2
2.04	0.67	0.54	1.08	0.5
7.53	0.46	0.56	1.56	0.5
7.8	0.81	0.17	1.78	1.3
8.62	0.6	0.36	1.43	1.3
9.3	0.35	0.5	1.55	1.2
12.3	0.5	0.5	1	0.68
13.6	0.53	0.5	1.88	0.67
14.3	0.45	0.41	1	0.8
24.3	0.11	0.35	3.1	1
27.2	0.59	0.28	2.11	1.2
44.2	0.40	0.39	2.33	1
821	0.58	0.45	1.2	0.8
53100	0.39	0.23	1.86	2.88

Scaling relations of slip distribution field are established for Japan, based on the statistical work for these 17 earthquakes. After the 1995 Kobe earthquake, the strong ground-motion networks of Japan, the KiK-net and K-NET, are installed over the entire Japan. The discussion in the last chapter shows that the slip distribution inversion from the strong ground motion is relatively more accurate. That is to say, although some slip distributions can be obtained using other geophysical data before the 1995 Kobe earthquake in Japan, its accuracy may not be good enough. It is meaningful to derive the scaling relations from the slip distribution inversed from the strong ground motion data, besides the situation that it is not calculated or the lower signal-to-noise ratios of the data. In this thesis, the slip distribution field based on the SGM inversion is the first choice.

In this chapter, all the measures or indicators to establish the slip distribution should relate to seismic moment first. For a potential earthquake which will occur on a specific fault, only the given magnitude is known. The magnitude is usually determined based on the relation (Hanks and Kanamori 1979),

$$M = 2/3\,M_0 - 10.7 \tag{6.1}$$

where M is the moment magnitude and M_0 is the seismic moment. Since the seismic moment is a scale of the released energy of an earthquake, the relation between other scales versus the seismic moment is reasonable if they are able to be obtained in a good accuracy.

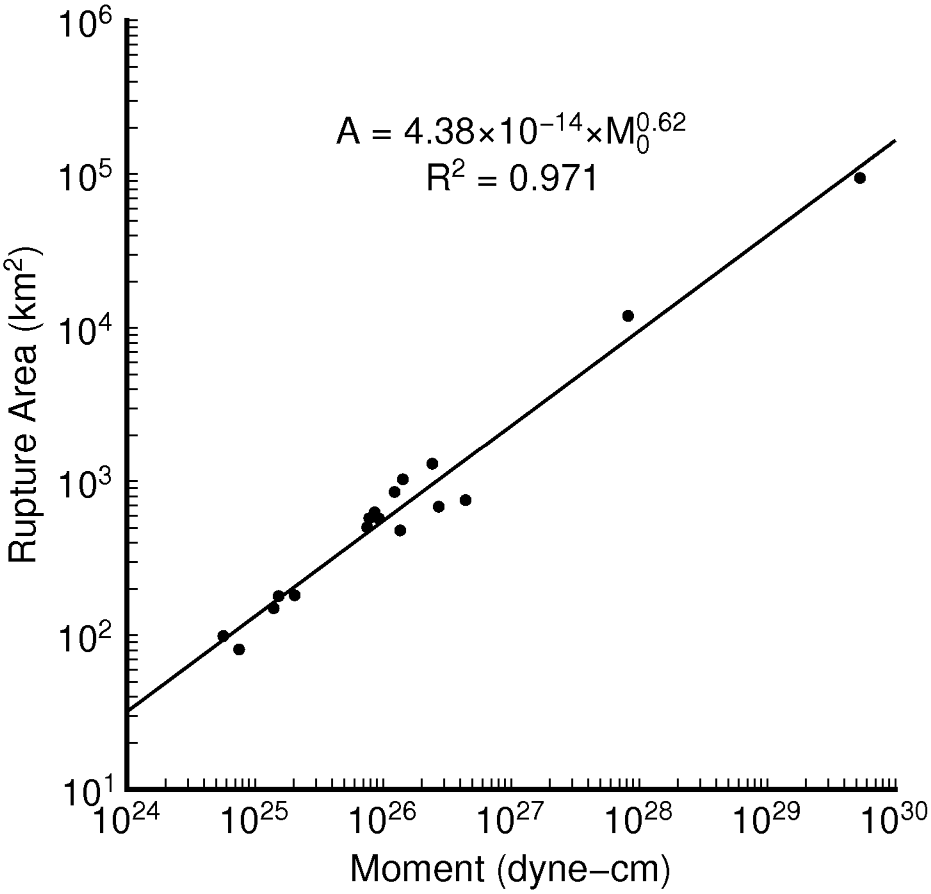

Figure 6-6 The relation of the rupture area versus seismic moment

The relation between the rupture area versus the seismic moment is obtained firstly. The R-squared value of the least-squares regression here is very high, because the seismic moment is directly determined from the rupture area. The relation between the rupture area and the seismic moment shown as

$$A = 4.38 \times 10^{-14} \times M_0^{\ 0.62} \tag{6.2}$$

where A is the rupture area in km^2, and M_0 is the seismic moment in dyne-cm.

And then the relation between the combined area of asperity against the seismic moment is derived. Due to the same reason, the R-squared value of linear least-squares regression is as high as 94.6%. It should be noted that the combined area of asperity indicates the summation of all the asperities of a slip distribution. The specific form of the relation is

$$A_a = 2.11 \times 10^{-16} \times M_0^{\ 0.68} \tag{6.3}$$

where A_a is the combined area of asperity.

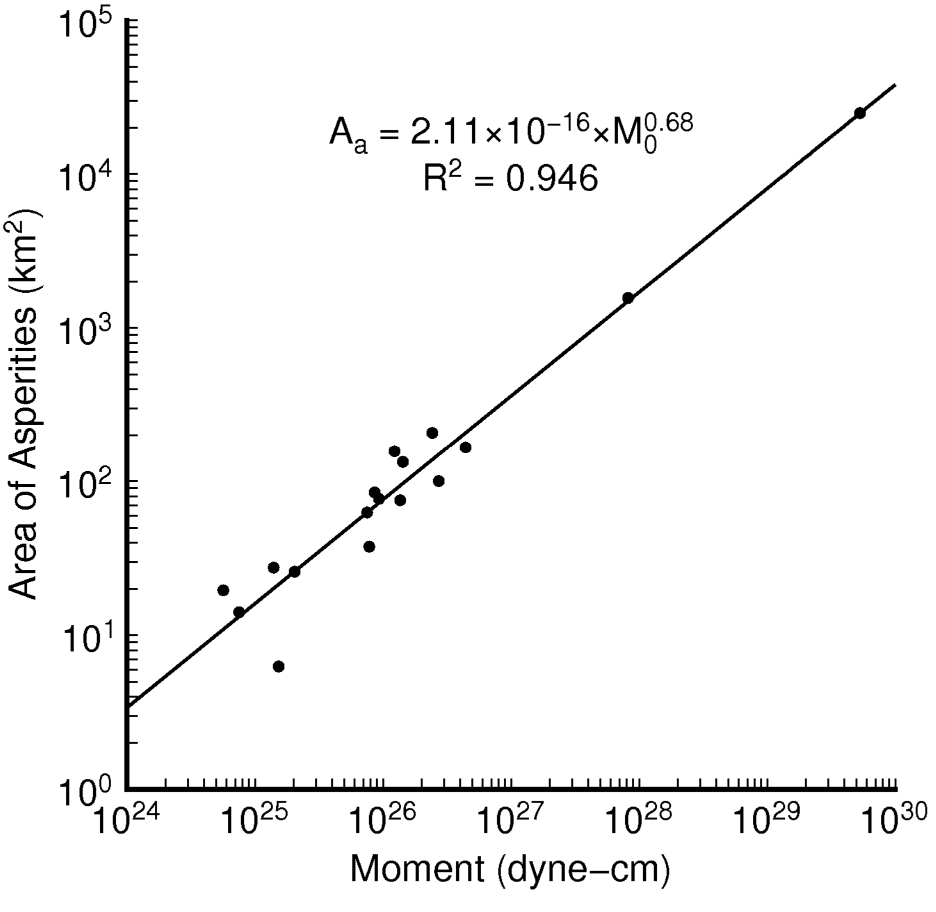

Figure 6-7 The relation of the asperity area versus moment

In addition to the area, the average slip on the rupture area and asperity is equally important since they are also controls the seismic moment. The average slip of rupture area is derived firstly and shown as follows,

$$D = 1.38 \times 10^{-7} \times M_0^{\ 0.33} \tag{6.4}$$

where D is the average slip of the rupture area. The R-squares value of regression is as high as 90%.

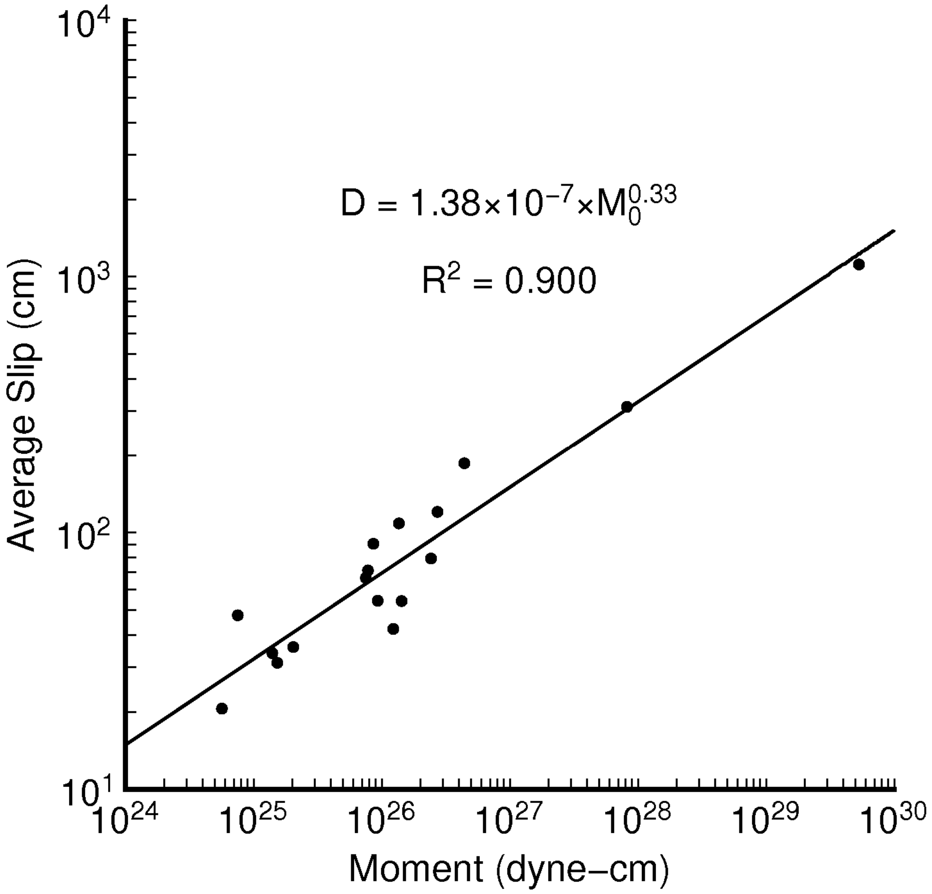

Figure 6-8 The relation of the average slip on the rupture area versus seismic moment

Similarly, the relation between the average slip of asperity versus the seismic moment is also determined. Figure 6-9 shows the average slip of each earthquakes. The relation is formulated as follows,

$$D_a = 1.56 \times 10^{-6} \times M_0^{\ 0.30} \tag{6.5}$$

where D_a is the average slip of the asperity.

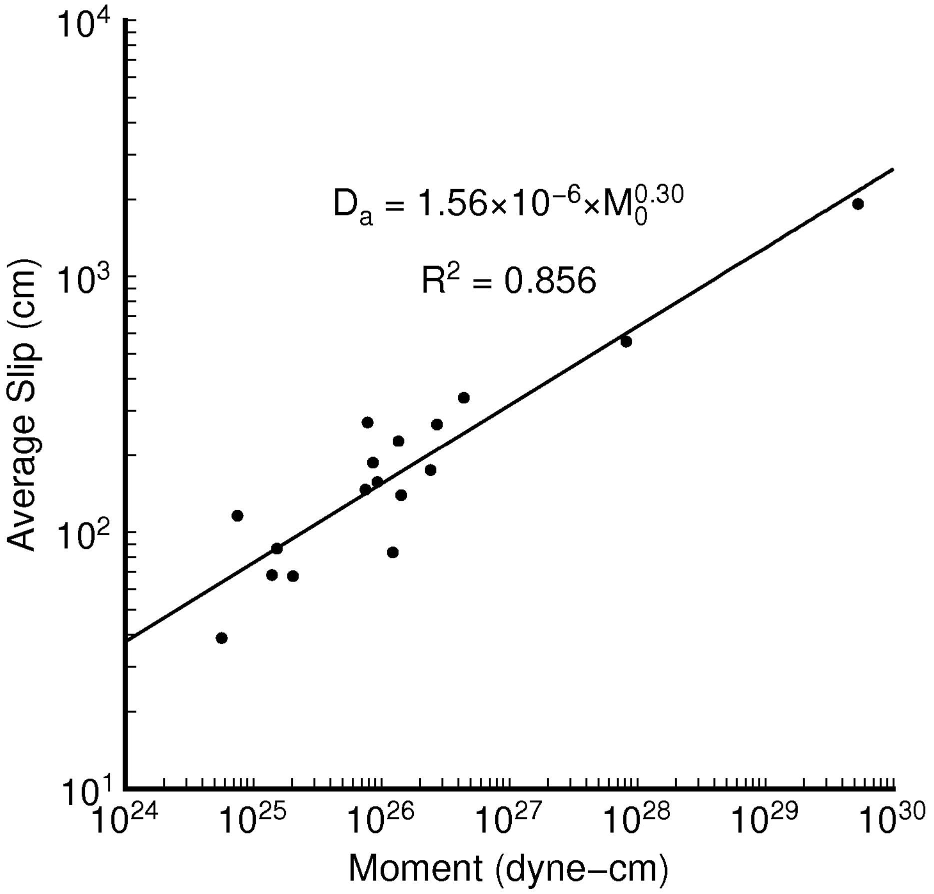

Figure 6-9 The relation of average slip of the asperity versus seismic moment

In addition to the area and average slip, the scaling relations between seismic moment and other variables are also investigated but failed. The length over width ratios of the rupture area and asperity for 17 earthquakes are determined and plotted in Figure 6-10 and Figure 6-11. The average value of them are 1.6 and 1.2. These ratios can be finally used in the geometry determination of the rupture area and asperity.

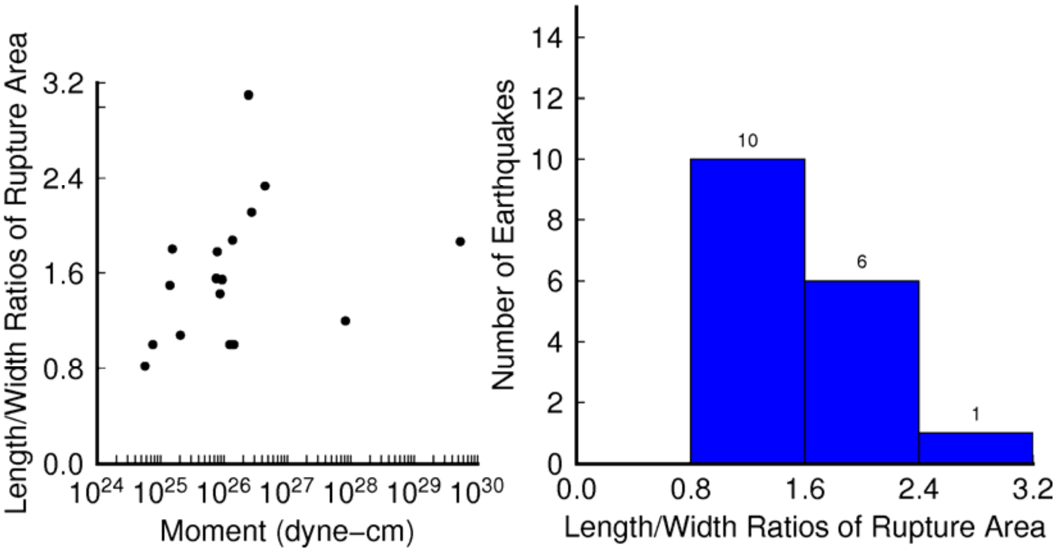

Figure 6-10 The histogram of length over width ratios of the rupture area

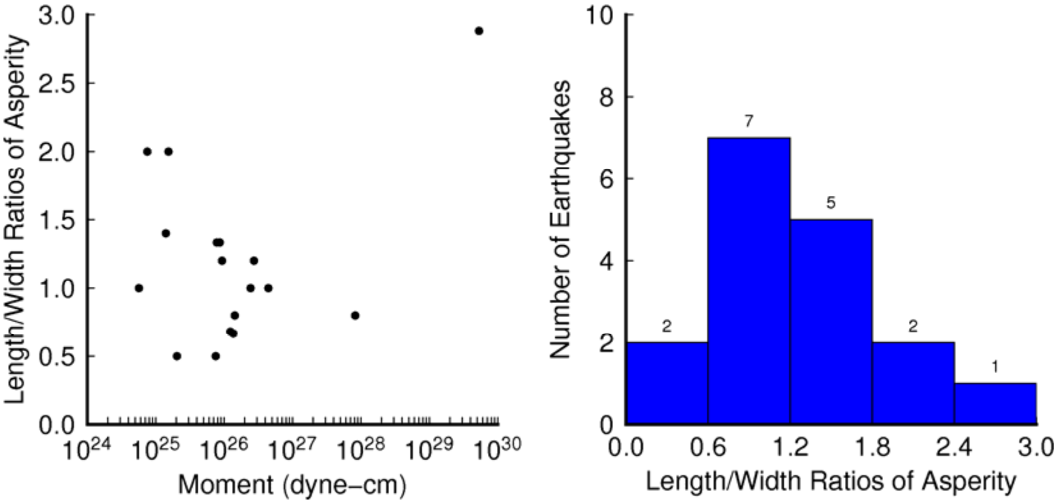

Figure 6-11 The histogram of length over width ratios of asperity

To locate the asperity on a fault plane, the relative coordinates of the asperity centre to the rupture area should be specified. The normalized distance along strike is determined using the ratio of the distance of asperity centre to the left side of rupture area over the length of rupture area. Similarly, the normalized distance along down-dip is calculated using the ratio of the distance of asperity centre to the upper side of rupture area over the width of rupture area. The histograms of them are shown in Figure 6-12 and Figure 6-13. The average values of these two normalized distance are 0.48 and 0.39, respectively. An alternative way to determine the coordinates of asperity centre is the probability method. For example, the normalized distance range of 0.4 to 0.6 has the largest probability in which the asperity locates. Correspondingly, the PGA value determined using the estimated slip distribution field on the basis of the normalized distance in this range also is the most possible value than determined from other normalized distances.

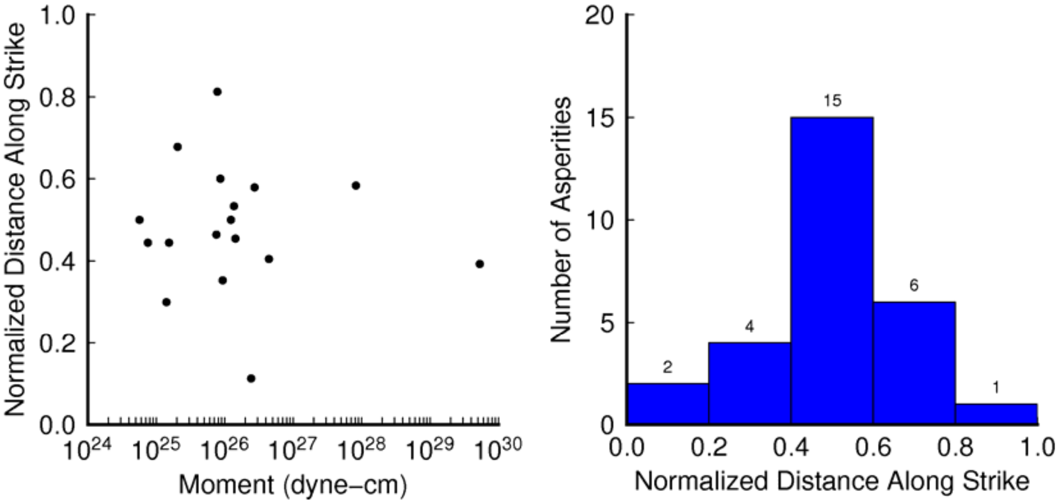

Figure 6-12 The histogram of normal distance of the asperity centre along strike

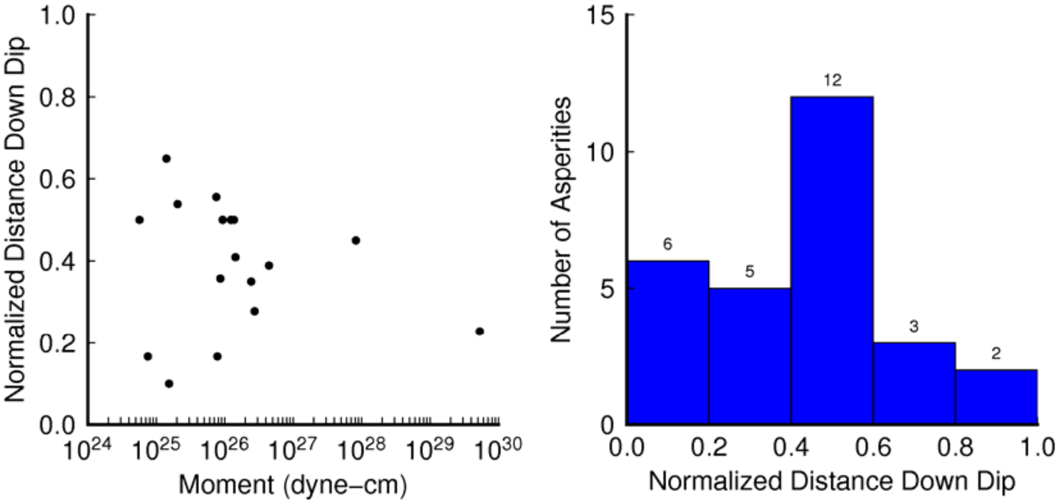

Figure 6-13 The histogram of normal distance of the asperity centre along down-dip

Although some recipes have been proposed to generate slip distribution field for future earthquakes, the approach improved in this thesis is simple and reasonable to operate and apply. Compare to the wavenumber spectrum analysis method (Somerville et al. 1999), a normal distribution is employed in this approach to represent the slip heterogeneity of the source model. Since the stochastic finite-fault method assumes the rupture initially starts from a point dislocation and the seismic wave is radiated as the form of spherical pattern, the assumed normal distribution of slip on the asperity and rupture area is reasonable. That is, the slip amount of subfaults decay from the centre of asperity to the edge. Compare to the recipe proposed by Irikura and Miyake (2011), the extra fault parameters, including the initial rupture point and the rupture pattern, are not required to estimate, which is simpler to apply. In the stochastic finite-fault method, the simulated PGA is less sensitive to the so-called extra fault parameters than other critical parameters. In a word, the approach improved in this thesis is simpler to be applied for simulating ground motions and the results are also acceptable.

6.4 THE CASE OF A M7 EARTHQUAKE OCCURS ON THE FUTAGAWA FAULT

The improved method for generating slip distribution field needs to be validated. The 2016 Kumamoto earthquake is selected to be a target earthquake since its importance to the Kyushu region. Here we assume that a M7.0 earthquake occurs on the Futagawa fault, which is the seismogenic fault of the 2016 M7 Kumamoto earthquake. Figure 6-14 shows the Futagawa fault which induced the M7.0 earthquake.

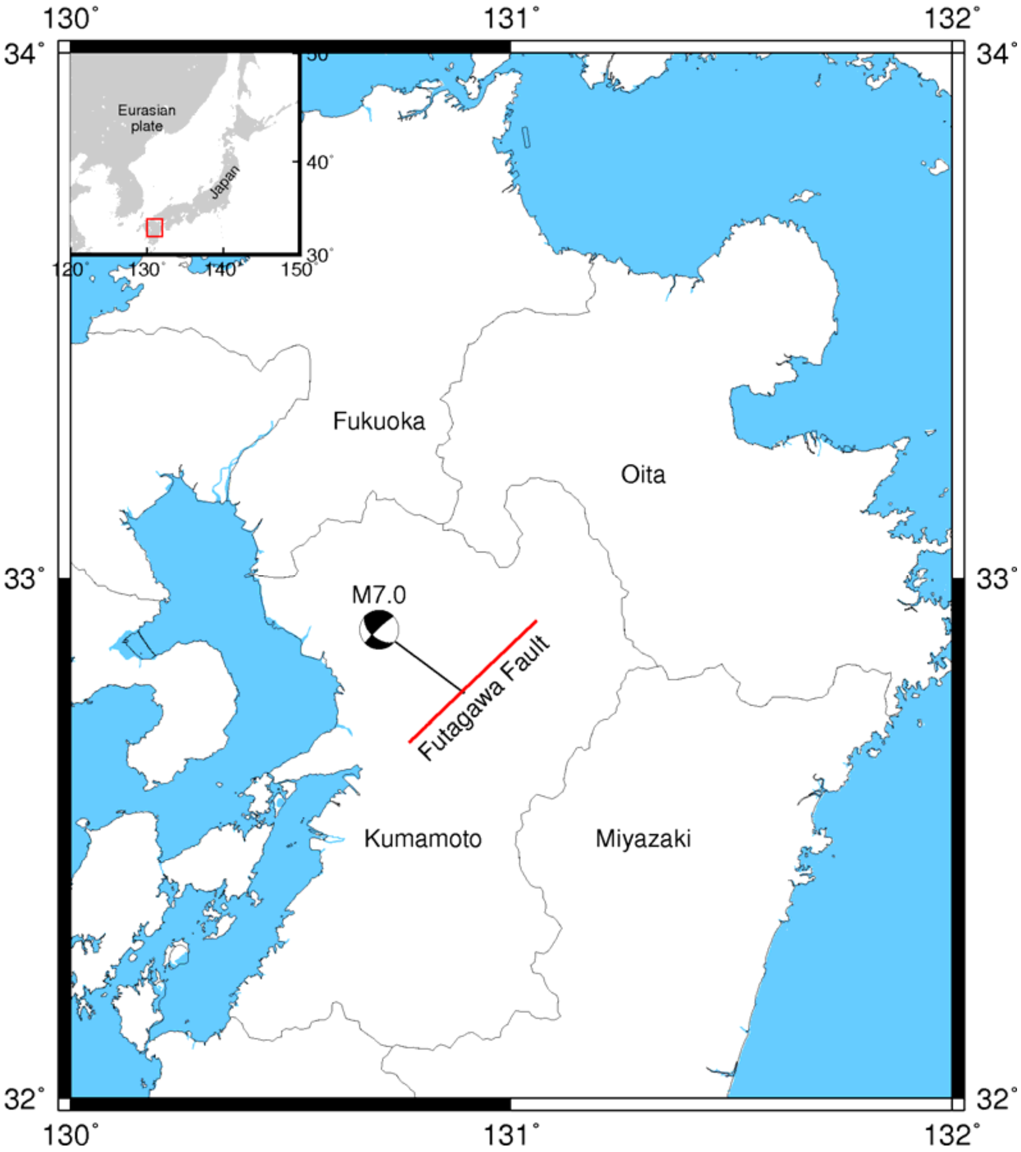

Figure 6-14 The locations of Futagawa fault and a potential earthquake with an assumed magnitude M7.0

6.4.1 THE SPECIFIC PROCEDURES

Then the slip distribution field of the M7.0 earthquake is established using the method we improved in the chapter. The specific procedures are introduced.

(1) The seismic moment of the assumed earthquake can be determined using the equation (6.1). $M_0 = 3.55\times10^{26} dyne\cdot cm$.

(2) The rupture area (A), asperity area (A_a), average slips of the rupture area (D) and asperity (D_a) are determined using equation (6.2-6.5), respectively. $A = 1211.2\ km^2$, $A_a = 178.98\ km^2$, $D = 106.2\ cm$, $D_a = 228.33\ cm$.

(3) The lengths and widths of the rupture area and asperity are determined using the average length-to-width ratios of 17 shallow crustal earthquakes. $L = 44.02\ km$, $W = 27.5\ km$, $L_a = 16.54\ km$, $W_a = 13.78\ km$.

(4) The slip on the asperity and rupture area are generated using the normal distribution. The slip are assigned following the rule that the larger slip is in the central part and then linearly decays to the edge. It should be noted that the slips on the background equal to the whole slip amount on the rupture minuses those of the asperity and are assigned following the same rule as on the asperity (Figure 6-15 and Figure 6-16).

(5) The location of asperity centre is determined using the average normalized distances to the length and width of the 17 earthquakes. $D_1 = 21.13\ km$, $D_2 = 10.73\ km$.

The geometric parameters calculated above should be adjusted further because they are not scalars and hard to be divided in the implementation. Their values before and after the adjustment are tabulated in Table 6-5. The rupture area is divided into 88 (11×8) subfaults, and the size of each one is $4\ km \times 3.5\ km$. Besides, the average slip of the background fault plane is 85 cm, which is determined from the step 4.

Table 6-5 The geometric parameters of asperity and rupture area of a M7 earthquake

Variable	Calculated	Adjusted
A	1211.2 km^2	1232 km^2
Aa	178.98 km^2	176 km^2
L	44.02 km	44 km
W	27.5 km	28 km
La	16.54 km	16 km
Wa	13.78 km	14 km
D_1	21.13 km	20 km
D_2	10.73 km	10.5 km

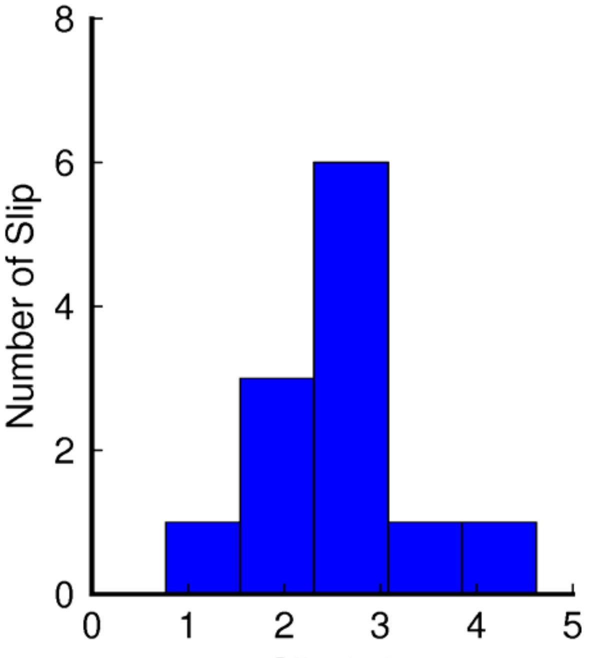

Figure 6-15 The histogram of slip on the asperity

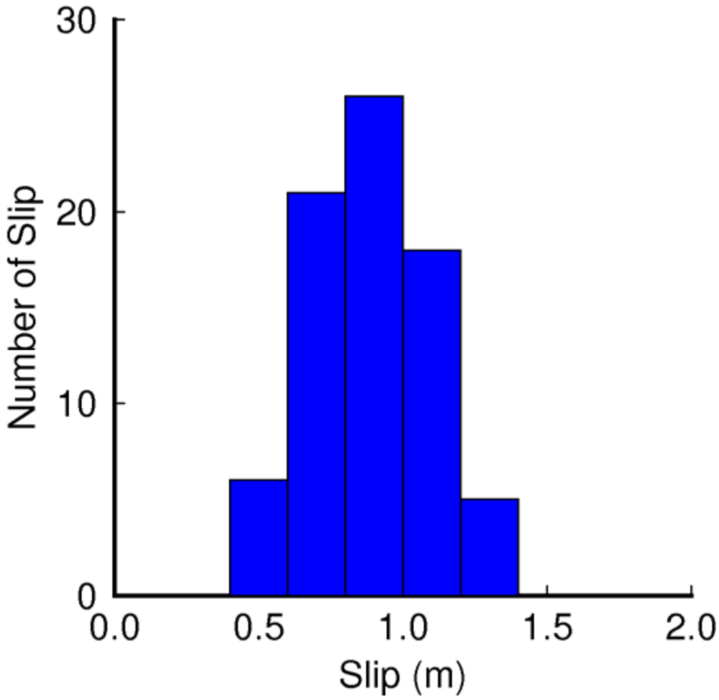

Figure 6-16 The histogram of the slip on the background rupture area

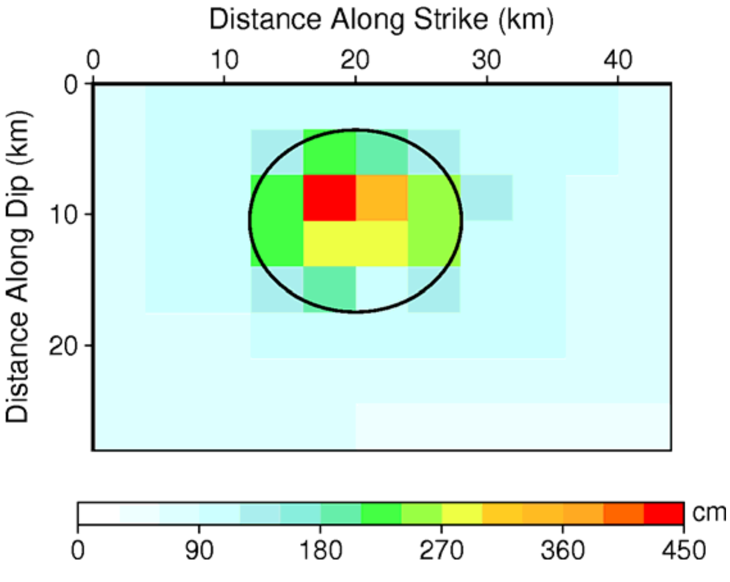

Figure 6-17 The generated slip distribution field of the a M7 earthquake

Then the slip distribution field of a M7 earthquake are established and plotted in Figure 6-17. The asperity is highlighted by an ellipse.

6.4.2 RESULTS AND VALIDATION

To validate the approach for the estimation of slip distribution field of a potential M7 earthquake, 53 KiK-net records from the 2016 Kumamoto earthquake are used. The acceleration time series are simulated using the stochastic finite-fault method with the established slip distribution field and then compared with the observations. The input parameters are tabulated in Table S7. The comparison of observed and simulated PGA are shown in Table 6-6. Figure 6-18 shows the comparison of observed and simulated acceleration time series at one representative station KMMH09. Both the waveform envelops and PGA at the selected station match the observation very well. The average relative error of PGA at the 53 KiK-net station is 35.9%, which is acceptable for a prediction.

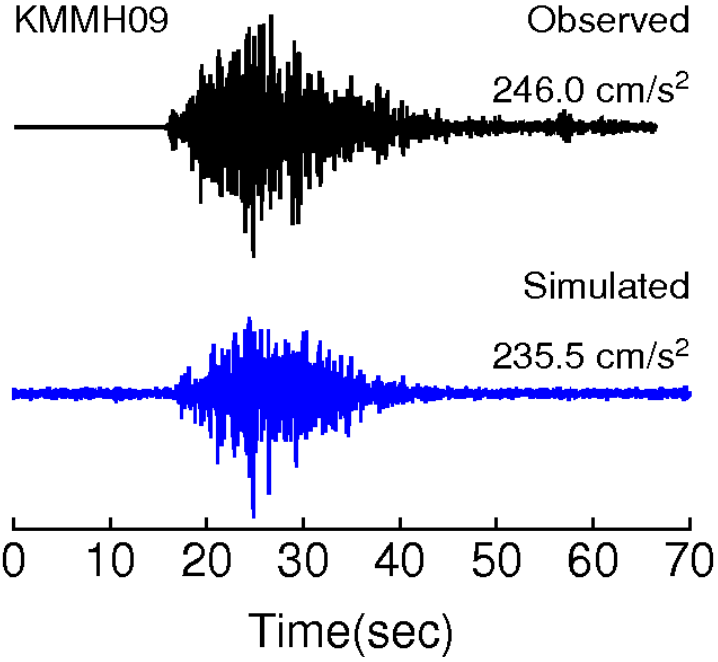

Figure 6-18 The comparison of observed and simulated acceleration time at station KMMH09

Table 6-6 Comparison of observed and simulated PGA using the estimated slip distribution field

Station code	Observed PGA (in cm/s^2)	Simulated PGA (in cm/s^2)
FKOH01	60	43
FKOH03	135	53
FKOH06	75	58

FKOH07	94	89
FKOH08	103	101
FKOH09	43	39
FKOH10	89	88
KGSH01	49	26
KGSH03	37	25
KGSH04	41	18
KGSH05	74	25
KGSH06	30	15
KGSH07	47	17
KGSH08	10	10
KGSH09	13	9
KGSH10	6	6
KGSH12	3	5
KMMH01	252	212
KMMH02	687	266
KMMH03	800	510
KMMH06	180	344
KMMH09	246	235
KMMH10	195	39
KMMH11	88	74
KMMH12	218	62
KMMH13	113	72
KMMH14	612	671
KMMH15	76	42
KMMH16	1362	1231
MYZH04	175	121
MYZH05	142	78
MYZH08	143	39
MYZH09	17	25
MYZH10	98	37

MYZH12	96	25
MYZH13	50	18
MYZH15	118	45
MYZH16	45	41
NGSH01	42	27
NGSH02	23	23
NGSH03	39	25
NGSH04	40	25
NGSH06	30	30
OITH01	70	78
OITH03	25	25
OITH05	89	72
OITH08	86	91
OITH10	49	37
OITH11	598	95
SAGH01	37	35
SAGH02	70	26
SAGH04	149	83
SAGH05	32	48

6.6 CONCLUSIONS

Many earthquake engineering problems need to estimate seismic waves induced by an expected future earthquake. Since the slip distribution field before an earthquake occurs is unknown, the proposed method in the last chapter cannot be applied. For this reason, an approach is improved for establishing the slip distribution field of a potential earthquake with an expected magnitude on a specific fault. Some conclusions can be drawn as follows:

(1) A rectangle-ellipse pattern of the slip distribution field is proposed by a lot of observations. Since the seismic wave is radiated and propagated as the form of spherical wave, the elliptical asperity patter is reasonable.

(2) The scaling relations of the slip distribution field for Japan are established using the rectangle-ellipse pattern based on 17 shallow crustal earthquakes with the magnitude range of 5.8-9.0 from 1995 to 2016. These relations with very high R-squares when performing the linear least-squares regression are reliable.

(3) The procedures of generating the slip distribution field are then proposed. They are made as a module and incorporated in practical system for simulating ground motions.

(4) The improved method, finally, is validated by the case of a potential M7 earthquake occurs on the Futagawa fault. The generated slip distribution field is input into the stochastic finite fault method for simulating the earthquake ground motions. The average error of PGA in 53 records from the 2016 Kumamoto earthquake is 35.9%. The good agreement of the simulated and observed acceleration time series shows the improved approach is reasonable and acceptable.

REFERENCE

Adams M, Twardzik C, Ji C (2016) Exploring the uncertainty range of coseismic stress drop estimations of large earthquakes using finite fault inversions. Geophys J Int 208, 86-100

Aki K (1967) Scaling law of seismic spectrum. J Geophys Res 72, 1217-1231

Asano K, Iwata T (2009) Source rupture process of the 2004 Chuetsu, Mid-Niigata prefecture, Japan, earthquake inferred from waveform inversion with dense strong-motion data. Bull Seismol Soc Am 99, 123-140

Asano K, Iwata T (2011a) Characterization of stress drops on asperities estimated from the heterogeneous kinematic slip model for strong motion prediction for inland crustal earthquakes in Japan. Pure Appl Geophys 168, 105-116

Asano K, Iwata T (2011b) Source-rupture process of the 2007 Noto Hanto, Japan, earthquake estimated by the joint inversion of strong motion and GPS data. Bull Seismol Soc Am 101, 2467-2480

Asano K, Iwata T (2016) Source rupture processes of the foreshock and mainshock in the 2016 Kumamoto earthquake sequence estimated from the kinematic waveform inversion of strong motion data. Earth Planets Space 68, 147

Atkinson GM, Assatourians K (2015) Implementation and validation of EXSIM (a stochastic finite‐fault ground‐motion simulation algorithm) on the SCEC broadband platform. Seismol Res Lett 86, 48-60

Ben-Menahem A, Singh SJ, 2012. Seismic waves and sources. Springer Science & Business Media.

Beresnev IA, Atkinson GM (1998) FINSIM--a FORTRAN program for simulating stochastic acceleration time histories from finite faults. Seismol Res Lett 69, 27-32

Boore DM (1972) Finite difference methods for seismic wave propagation in heterogeneous materials. Methods in computational physics 11, 1-37

Boore DM (1983) Stochastic simulation of high-frequency ground motions based on seismological models of the radiated spectra. Bull Seismol Soc Am 73, 1865-1894

Boore DM (2009) Comparing stochastic point-source and finite-source ground-motion simulations: SMSIM and EXSIM. Bull Seismol Soc Am 99, 3202-3216

Boore DM, Gibbs JF, Joyner WB, Tinsley JC, Ponti DJ (2003) Estimated ground motion from the 1994 Northridge, California, earthquake at the site of the Interstate 10 and La Cienega Boulevard bridge collapse, West Los Angeles, California. Bull Seismol Soc Am 93, 2737-2751

Brune JN (1970) Tectonic stress and the spectra of seismic shear waves from earthquakes. J Geophys Res 75, 4997-5009

Bykova V, Aref'ev S, Rivera L (2010) Simulation of ground motion in the Moscow region using the empirical Green's function. Izvestiya Physics of the Solid Earth 46, 19-33

Chen C-T, Chang S-C, Wen K-L (2017) Stochastic ground motion simulation of the 2016 Meinong, Taiwan earthquake. Earth Planets Space 69, 62.doi:10.1186/s40623-017-0645-z

Cirella A, Piatanesi A, Tinti E, Cocco M (2008) Rupture process of the 2007 Niigata‐ken Chuetsu‐oki earthquake by non‐linear joint inversion of strong motion and GPS data. Geophys Res Lett 35

Dieterich JH (1992) Earthquake nucleation on faults with rate-and state-dependent strength. Tectonophysics 211, 115-134

Fialko Y, Khazan Y (2005) Fusion by earthquake fault friction: Stick or slip? J Geophys Res 110

Goldsby DL, Tullis TE (2002) Low frictional strength of quartz rocks at subseismic slip rates. Geophys Res Lett 29

Gonzales JA, Ramirez-Gaytán A, Huerta-López CI, Rosado-Trillo C, 2012. Seismic Source Characterization for Future Earthquakes, Earthq Res Analysis-New Frontiers in Seismology. InTech.

Hanks TC, Kanamori H (1979) A moment-magnitude scale. J Geophys Res 84, 2348-2350

Hikima K, Koketsu K (2004) Source processes of the foreshock, mainshock and largest aftershock in the 2003 Miyagi-ken Hokubu, Japan, earthquake sequence. Earth Planets Space 56, 87-93

Holden C, Kaiser A (2016) Stochastic ground motion modelling of the largest M w 5.9+ aftershocks of the Canterbury 2010–2011 earthquake sequence. New Zeal J Geol Geophys 59, 187-201.doi:10.1080/00288306.2015.1133664

Horikawa H (2001) Earthquake doublet in Kagoshima, Japan: Rupture of asperities in a stress shadow. Bull Seismol Soc Am 91, 112-127

Ide S (1999) Source process of the 1997 Yamaguchi, Japan, earthquake analyzed in different frequency bands. Geophys Res Lett 26, 1973-1976

Ide S, Baltay A, Beroza GC (2011) Shallow dynamic overshoot and energetic deep rupture in the 2011 Mw 9.0 Tohoku-Oki earthquake. Science 332, 1426-1429

Irikura K, Miyake H (2011) Recipe for predicting strong ground motion from crustal earthquake scenarios. Pure Appl Geophys 168, 85-104

Iwaki A, Maeda T, Morikawa N, Aoi S, Fujiwara H (2016) Kinematic source models for long-period ground motion simulations of megathrust earthquakes: validation against ground motion data for the 2003 Tokachi-oki earthquake.

Earth Planets Space 68, 95

Iwata T, Sekiguchi H, Matsumoto Y, Miyake H, Irikura K, 2000. Source process of the 2000 western Tottori prefecture earthquake and near-source strong ground motions, Fall meeting of the Seismological Society of Japan.

Jahnke G, Thorne MS, Cochard A, Igel H (2008) Global SH-wave propagation using a parallel axisymmetric spherical finite-difference scheme: application to whole mantle scattering. Geophys J Int 173, 815-826

Koketsu K, Hikima K, Miyazaki Si, Ide S (2004) Joint inversion of strong motion and geodetic data for the source process of the 2003 Tokachi-oki, Hokkaido, earthquake. Earth Planets Space 56, 329-334

Kurahashi S, Irikura K (2010) Characterized source model for simulating strong ground motions during the 2008 Wenchuan earthquake. Bull Seismol Soc Am 100, 2450-2475

Lee TC, Delaney PT (1987) Frictional heating and pore pressure rise due to a fault slip. Geophys J Int 88, 569-591

Li Z, Chen X, Gao M, Jiang H, Li T (2017) Simulating and analyzing engineering parameters of Kyushu Earthquake, Japan, 1997, by empirical Green function method. J Seismol 21, 367-384

Maeda T, Ichiyanagi M, Takahashi H, Honda R, Yamaguchi T, Kasahara M, Sasatani T (2008) Source parameters of the 2007 Noto Hanto earthquake sequence derived from strong motion records at temporary and permanent stations. Earth Planets Space 60, 1011-1016

Maeda T, Sasatani T (2009) Strong ground motions from an Mj 6.1 inland crustal earthquake in Hokkaido, Japan: the 2004 Rumoi earthquake. Earth Planets Space 61, 689-701

Mitchell BJ (1995) Anelastic structure and evolution of the continental crust and upper mantle from seismic surface wave attenuation. Reviews of Geophysics 33, 441-462

Miyake H, Iwata T, Irikura K (2003) Source characterization for broadband ground-motion simulation: Kinematic heterogeneous source model and strong motion generation area. Bull Seismol Soc Am 93, 2531-2545

Miyake H, Murotani S, Koketsu K (2006) Scaling of asperity size for plate-boundary earthquakes. Chikyu Monthly ExtraIssue,55, 86-91

Mizoguchi K, Hirose T, Shimamoto T, Fukuyama E (2007) Reconstruction of seismic faulting by high - velocity friction experiments: An example of the 1995 Kobe earthquake. Geophys Res Lett 34

Moratto L, Saraò A, Vuan A, Mucciarelli M, Jiménez M-J, García-Fernández M (2017) The 2011 Mw 5.2 Lorca earthquake as a case study to investigate the ground motion variability related to the source model. Bull Earthq Eng 15, 3463-3482

Motazedian D, Atkinson GM (2005) Stochastic finite-fault modeling based on a dynamic corner frequency. Bull Seismol Soc Am 95, 995-1010

Murotani S, Miyake H, Koketsu K (2008) Scaling of characterized slip models for plate-boundary earthquakes. Earth Planets Space 60, 987-991

Nakahara H, Nishimura T, Sato H, Ohtake M, Kinoshita S, Hamaguchi H (2002) Broadband source process of the 1998 Iwate prefecture, Japan, earthquake as revealed from inversion analyses of seismic waveforms and envelopes. Bull Seismol Soc Am 92, 1708-1720

Nielsen SB, Carlson J, Olsen KB (2000) Influence of friction and fault geometry on earthquake rupture. J Geophys Res 105, 6069-6088

Nozu A, Yamada M, Nagao T, Irikura K (2014) Generation of strong motion pulses during huge subduction earthquakes and scaling of their generation areas. J Japan Associa Earthq Eng 14, 96-117

Oth A (2013) On the characteristics of earthquake stress release variations in Japan. Earth Planet Sci Lett 377, 132-141

Oth A, Wenzel F, Radulian M (2007) Source parameters of intermediate-depth Vrancea (Romania) earthquakes from empirical Green's functions modeling. Tectonophysics 438, 33-56

Riahi A, Sadeghi H, Hosseini SK (2015) Simulation of 2003 Bam (Iran) earthquake using empirical Green's function method via very small and near-fault events. Geophys J Int 201, 1264-1286

Rice JR (1992) Dislocation nucleation from a crack tip: an analysis based on the

Peierls concept. J Mech Phys Solids 40, 239-271

Rice JR, Beltz GE (1994) The activation energy for dislocation nucleation at a crack. J Mech Phys Solids 42, 333-360

Rodríguez-Pérez Q, Ottemöller L (2013) Finite-fault scaling relations in Mexico. Geophys J Int 193, 1570-1588

Sadeghi H, Miyake H, Riahi A (2013) Strong ground motion simulation of the 2003 Bam, Iran, earthquake using the empirical Green's function method. J Seismol 17, 297-312

Sato H (1977) Energy propagation including scattering effects sengle isotropic scattering approximation. J Phys Earth 25, 27-41

Scholz CH, 2002. The mechanics of earthquakes and faulting. Cambridge university press.

Sekiguchi H, Aoi S, Honda R, Morikawa N, Kunugi T, Fujiwara H (2006) Rupture process of the 2005 West Off Fukuoka Prefecture earthquake obtained from strong motion data of K-NET and KiK-net. Earth Planets Space 58, 37-43

Sekiguchi H, Irikura K, Iwata T (2002) Source inversion for estimating the continuous slip distribution on a fault—introduction of Green's functions convolved with a correction function to give moving dislocation effects in subfaults. Geophys J Int 150, 377-391

Sharma B, Chopra S, Kumar V (2016) Simulation of strong ground motion for 1905 Kangra earthquake and a possible megathrust earthquake (Mw 8.5) in western Himalaya (India) using Empirical Green's Function technique. Natural Hazards 80, 487-503

Sharma B, Chopra S, Sutar AK, Bansal B (2013) Estimation of strong ground motion from a great earthquake Mw 8.5 in central seismic gap region, Himalaya (India) using empirical Green's function technique. Pure Appl Geophys 170, 2127-2138

Somerville P, Irikura K, Graves R, Sawada S, Wald D, Abrahamson N, Iwasaki Y, Kagawa T, Smith N, Kowada A (1999) Characterizing crustal earthquake slip models for the prediction of strong ground motion. Seismol Res Lett 70, 59-80

Suzuki W, Iwata T (2006) Source model of the 2005 west off Fukuoka prefecture earthquake estimated from the empirical Green's function simulation of broadband strong motions. Earth Planets Space 58, 99-104

Suzuki W, Iwata T (2007) Source model of the 2005 Miyagi-Oki, Japan, earthquake estimated from broadband strong motions. Earth Planets Space 59, 1155-1171

Suzuki W, Iwata T (2009) Broadband seismic wave radiation process of the 2000 Western Tottori, Japan, earthquake revealed from wavelet domain inversion. J Geophys Res 114

Tanırcan G, Savaş N (2011) Strong ground motion simulation by the Empirical Green's Function method for Bursa-Yalova Region, Turkey. Bull Earthq Eng 9, 1327-1338

Ugurhan B, Askan A (2010) Stochastic strong ground motion simulation of the 12 November 1999 Düzce (Turkey) earthquake using a dynamic corner frequency approach. Bull Seismol Soc Am 100, 1498-1512.doi:10.1785/0120090358

Ursin B (1983) Review of elastic and electromagnetic wave propagation in horizontally layered media. Geophysics 48, 1063-1081

Walter WR, Yoo SH, Mayeda K, Gök R (2017) Earthquake stress via event ratio levels: Application to the 2011 and 2016 Oklahoma seismic sequences. Geophys Res Lett 44, 3147-3155

Wang H, Wen R, Ren Y (2017) Simulating Ground‐Motion Directivity Using Stochastic Empirical Green' s Function Method. Bull Seismol Soc Am 107, 359-371

Xia C, Zhao B, Horike M, Kagawa T (2015) Strong Ground Motion Simulations of the Mw 7.9 Wenchuan Earthquake Using the Empirical Green's Function Method. Bull Seismol Soc Am 105, 1383-1397

Yagi Y, Kikuchi M, Yoshida S, Sagiya T (1999) Comparison of the coseismic rupture with the aftershock distribution in the Hyuga‐nada earthquakes of 1996. Geophys Res Lett 26, 3161-3164

Yokota Y, Koketsu K, Hikima K, Miyazaki Si (2009) Ability of 1‐Hz GPS data to infer the source process of a medium‐sized earthquake: The case of the 2008

Iwate﹣Miyagi Nairiku, Japan, earthquake. Geophys Res Lett 36

Zengin E, Cakti E (2014) Ground motion simulations for the 23 October 2011 Van, Eastern Turkey earthquake using stochastic finite fault approach. Bull Earthq Eng 12, 627-646

Zhang L, Chen G, Wu Y, Jiang H (2016) Stochastic ground-motion simulations for the 2016 Kumamoto, Japan, earthquake. Earth Planets Space 68

CHAPTER 7

A PRACTICAL APPLICATION FOR LANDSLIDE HAZARD ASSESSMENT

7.1 INTRODUCTION

Landslide is one of the most catastrophic geo-hazards causing human injury, fatality and loss of property (Fell 1994; Anbalagan and Singh 1996; Shang et al. 2003; Kanungo et al. 2008). Landslide hazard map using a physically-based approach has been widely used to make decisions for landslide prevention and mitigation (Aleotti and Chowdhury 1999; Ohlmacher and Davis 2003; Lee and Pradhan 2007; Ray and De Smedt 2009). Ground motion intensity measures (e.g. peak ground acceleration (PGA)), are introduced into this approach to identify landslide prone slopes and susceptible areas for the situation that an earthquake occurs (Klein et al. 2001; Capolongo et al. 2002; Nath et al. 2008; Papadopoulou-Vrynioti et al. 2013). To estimate earthquake ground motions so as to carry out practical prediction and landslide prevention measures, the prediction of PGA from a potential earthquake occurs on a specific fault is very important and useful.

Generally, the landslide inventory map can be identified from the pictures taken by satellites or drones after an earthquake (Tantianuparp et al. 2013; Singleton et al. 2014; Turner et al. 2015; Suh and Choi 2017). It is one of the useful data to verify the landslide hazard map by comparing them using GIS (Gupta and Joshi 1990; Carrara et al. 1999; Saha et al. 2002; Ayalew and Yamagishi 2005). The three modules made in the above chapters are combined with the SFFM module to be a practical system for earthquake ground motion simulations. The flowchart of the developed practical system is shown as follows.

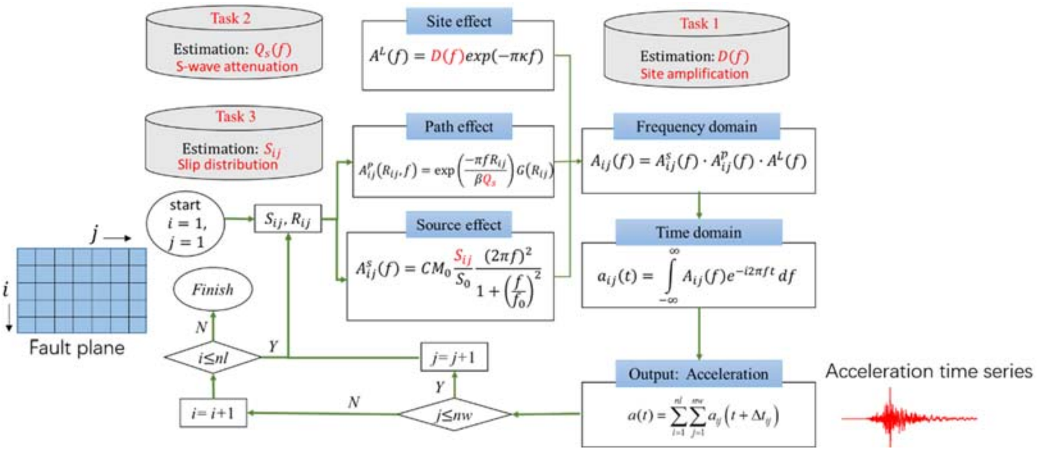

Figure 7-1 The flowchart of the developed practical system for simulating earthquake ground motions paying attention to volcanic zone and asperity on a fault

In this chapter, our practical system is verified by simulating ground motions in the Aso-bridge region, Kumamoto, Japan. The generated slip distribution field is applied to the simulation of acceleration time series. The landslide hazard map based on GIS is produced and compared with the landslides induced by the 2016 Kumamoto earthquake.

7.2 LANDSLIDE HAZARD ASSESSMENT BASED ON THE GIS-BASED MAPPING

One of the most important work of landslide hazard assessment is to evaluate the landslide susceptibility for a region. A large earthquake will induce thousands, even tens of thousands landslides in mountainous region (McPhillips et al. 2014; Xu et al. 2014; Liu et al. 2016). The landslide hazard assessment provides an evaluation for landslide susceptibility regions where landslides are prone to be triggered by a potential earthquake occurs on a specific fault, which is effective to help government make decisions for mitigating landslide hazards. GIS-based landslide hazard mapping technique has been widely-used for identifying landslide susceptibility zones where landslides are prone to happen in a future earthquake

(Chousianitis et al. 2016; Gaprindashvili and Van Westen 2016; Zhou et al. 2016a; Zhou et al. 2016b).

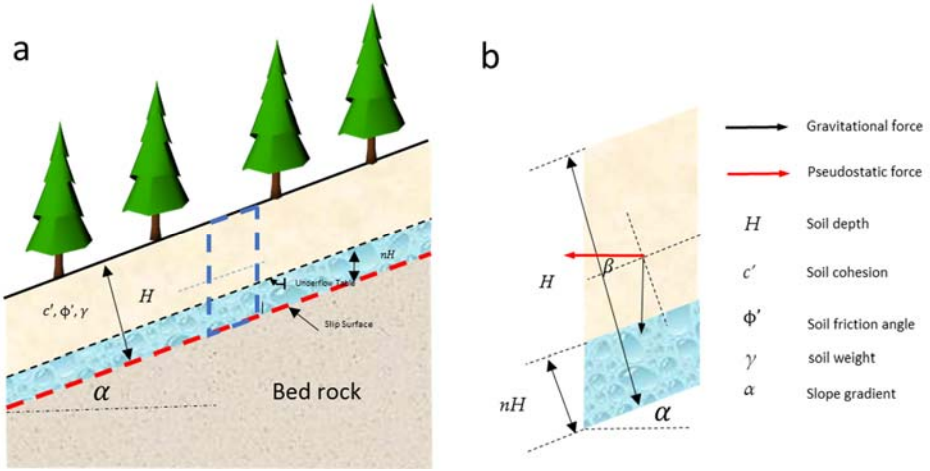

Figure 7-2 (a) Limit equilibrium analysis method for infinite slope considering a seismic force; (b) Force analysis of unit soil slice (dash rectangle in the panel (a)) (after Zhou (2016))

The famous infinite slope model has been widely used for the static slope stability analysis and illustrate in Figure 7-2. In this model, the weight of the sliding mass under its own weight loading is

$$G = \gamma HL \tag{7.1}$$

where G is the weight of the sliding mass, γ is the unit weight of sliding mass, H is the normal thickness of the failure surface, and L is length of the sliding mass. This weight loading can be divided into two orthogonal force, the normal force T_n and the shear force T_s in the form of

$$T_n = G\cos\alpha = \gamma HL\cos\alpha \tag{7.2}$$

$$T_s = G\sin\alpha = \gamma HL\sin\alpha \tag{7.3}$$

where α is the slope gradient. Then the effective normal stress and shear stress are represented in the form of

$$\sigma^{'} = T_n/L - \gamma_w nH\cos\alpha = \left(r - nr_w\right)H\cos\alpha \tag{7.4}$$

$$\tau = T_s/L = \gamma H\sin\alpha \tag{7.5}$$

where r_w is the unit weight of water, n is the percentage of saturated thickness.

The static factor of safety can be expressed in the form of

$$F_s = \frac{c^{'} + \sigma^{'} \tan\varphi^{'}}{\tau} = \frac{c^{'} + \left[\left(r - nr_w \right) H \cos\alpha \right] \tan\varphi^{'}}{\tau} \tag{7.6}$$

For equation (7.6), the numerator represents the resisting force while the denominator is the driving force. It is easy to identify the landslide prone region, of which the F_s is lower than 1, and vice versa.

In this model, when the effect of earthquake is considered into the calculation of F_s under a seismic loading, the equation derived above should be modified. The seismic force can be represented by the product of a seismic coefficient k_s, the PGA value of the seismic wave, and mass weight. In Figure 7-2, the angle between the incident direction of the seismic loading and the surface is β, and this force can be divided into two orthogonal force, the normal force S_n and the shear force S_s in the form of

$$S_n = a\gamma H \sin\beta / g = k_s PGA \gamma H \sin\beta / g \tag{7.7}$$

$$S_s = a\gamma H \cos\beta / g = k_s PGA \gamma H \cos\beta / g \tag{7.8}$$

Considering the seismic loading, equation (7.6) turns to

$$F_s = \frac{c^{'} + \left[\left(\gamma - n\gamma_w \right) H \cos\alpha - k_s PGA \gamma H \sin\beta / g \right] \tan\varphi^{'}}{\gamma H \sin\alpha + k_s PGA \gamma H \cos\beta / g} \tag{7.9}$$

In this chapter, the equation (7.9) is used to assess the regional slope susceptibility.

7.3 PGA SIMULATIONS

The practical system for simulating ground motions is applied to the Aso-bridge region. The location of study area is shown in Figure 7-3. During the 2016 Kumamoto earthquake, the largest landslide is triggered by this devastating earthquake in the Aso-bridge region. For this purpose, this region is selected as our study area.

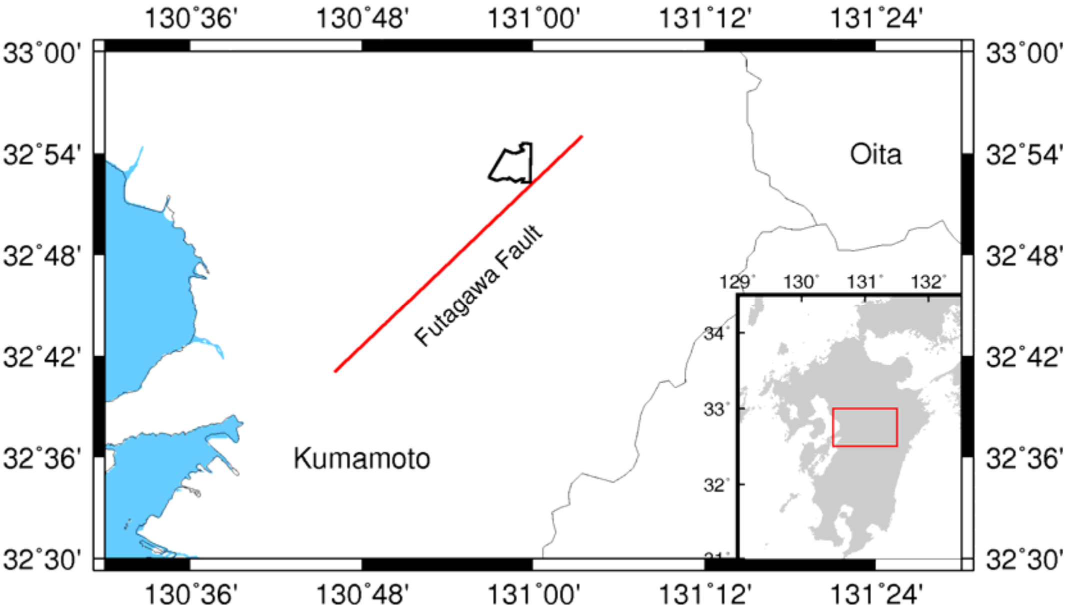

Figure 7-3 The study area of the application

First, the slip distribution field is generated using the module developed in chapter 6. To use this module, an assumed magnitude and a fault should be specified. Here we assume it as the same magnitude as the 2016 Kumamoto earthquake, that is $M = 7.0$. Correspondingly, the seismic moment can be estimated using the equation (6.1) with the value of 3.55e26 dyne-cm. And then the area of rupture region and asperity are also derived from equation (6.2) and (6.3), respectively. The rupture area is 1211.2 km^2 and the asperity area is 178.98 km^2. Further, the average slip on the rupture and asperity is determined with the value of 106.2 cm and 228.33 cm. Next, the slip distributions on the asperity and background of the rupture region are generated using the normal distribution based on the average values. Finally, the location of asperity is fixed on the basis of the averaged normalized distance along strike and down-dip of the 17 shallow crustal earthquake occurred in Japan. The location is also the most possible point due to its largest probability.

The generated slip distribution field is illustrated in Figure 7-4. Compare to the slip distribution inversion from the strong ground motion, it is found that they are very similar. Therefore, it is suggested that the predicted slip distribution field is acceptable.

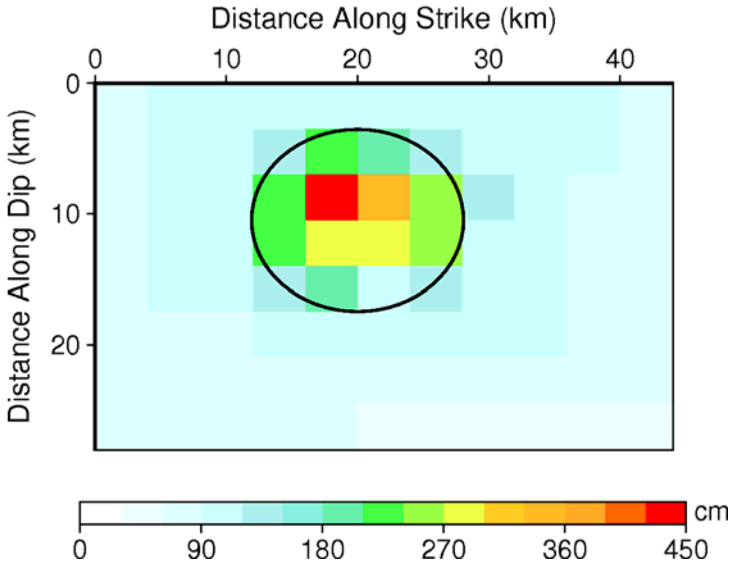

Figure 7-4 The generated slip distribution field of the 2016 Kumamoto earthquake

To furtherly validate the practical system, the earthquake ground motions are simulated based on the meshed grids of this region. The input parameters are listed in Table S7. The site amplification factor used in here are those of the nearby sites KMMH06, KMMH09 and KMMH16 (Figure 3-17). Figure 7-5 shows the simulated PGA distribution of Aso-bridge area by inputting the estimated slip distribution.

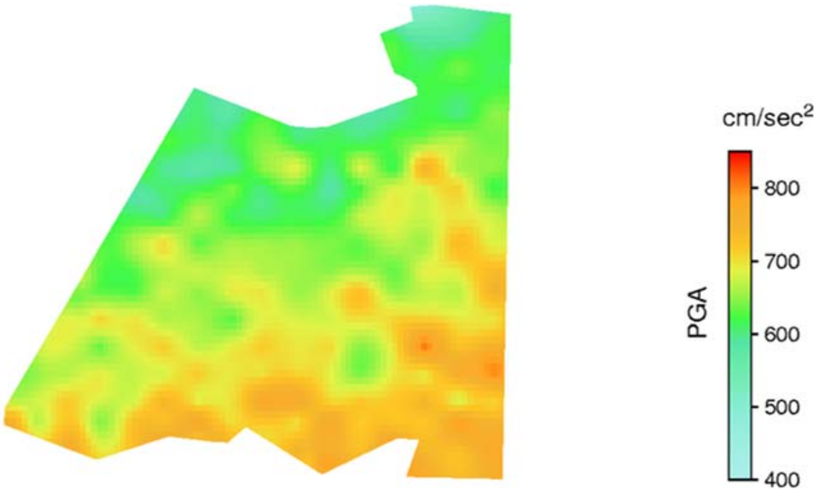

Figure 7-5 The PGA distribution predicted for the Aso-bridge region

7.4 LANDSLIDE HAZARD MAPS

Generally speaking, to forecast the landslide hazard using the physically-based model, one approximate PGA value can be used for a region. For example, the 1995 Kobe earthquake is usually considered as one of the most representative event in Japan. To investigate the effect of a M7 earthquake on the slope susceptibility for a region, some waveforms or PGA from the Kobe earthquake will be used. One of the most widely-used way is to transform the approximate seismic intensity scale to the corresponding PGA values, which is based on the probability of exceedance. For example, the seismic intensity map in Kyushu Island is shown in Figure 7-6. For the study area of this thesis, the approximate intensity scale is 5 upper. In Table 7-1, the corresponding PGA range for each intensity scale is tabulated on the basis of Japan Meteorological Agency and the records from the 2016 Kumamoto earthquake. For this case, the 5 upper corresponds to the PGA value range of 250-600 cm/s^2. Here the median value of this range, 450 cm/s^2, is selected to represent the PGA for the entire study area under an assumption of a M7 earthquake occurs.

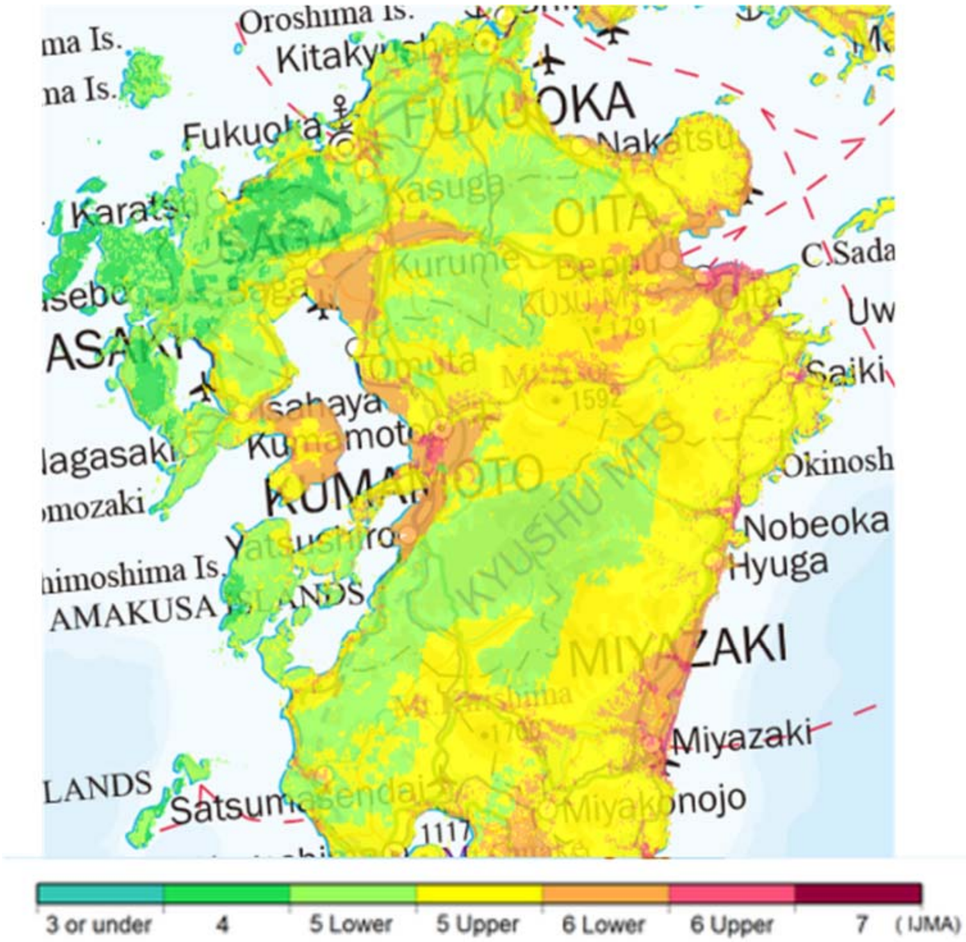

Figure 7-6 Seismic intensity map in Kyushu Island (from Japan Seismic Hazard Information)

Table 7-1 Approximate corresponding PGA range in intensity scale

Intensity	PGA (cm/s^2)
0	< 0.8
1	0.8-2.5
2	2.5-8
3	8-25
4	25-150
5 lower	150-250
5 upper	250-600
6 lower	600-800
6 upper	800-1300
7 upper	>1300

Table 7-2 The geological parameters used in the determination of F_s

Geology Unit	Cohesion (kPa)	Friction angle (°)	Gamma (kN/m^3)	Soil thickness (m)
Deposits and Terrace	5-10	15-25	18	10
Sedimentary	10-15	25-35	19	7
Volcanic	8-15	20-30	20	5

We make the landslide hazard maps for Aso-bridge region using the approximate PGA and the ones we simulated using the practical system. Since the area of the study region is only 12.6 km^2, the general way of using one approximate value to represent the PGA of the entire area is reasonable. Here we use the value of 450 cm/s^2 to make the landslide hazard map for comparison. To calculate the factor of safety, other parameters of equation (7.9) are tabulated in Table 7-2. It should be noted that the cohesion and friction angle are generated by Mente Carlo simulation in 1000 times. Besides, the seismic coefficient in this case is 0.16 , the ground water level is 0.3, the slope angle is extracted from the https://earthexplorer.usgs.gov/.

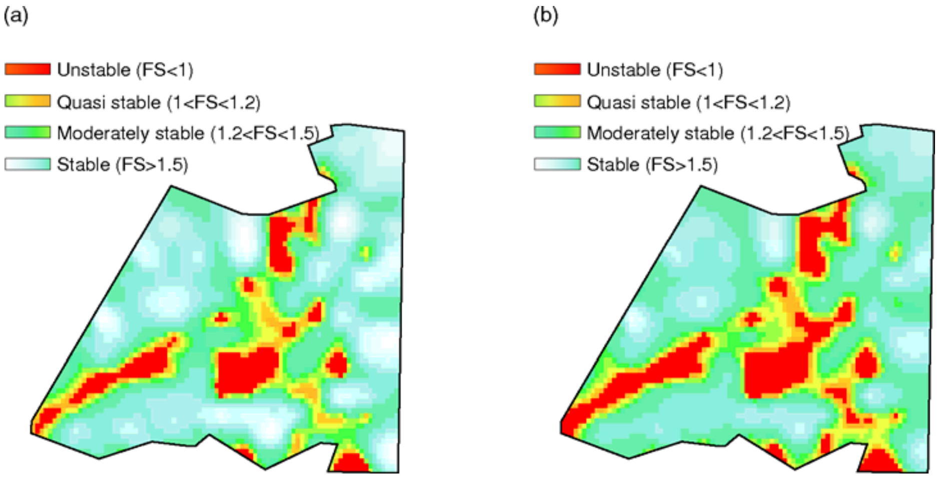

Figure 7-7 Landslide hazard maps (a) based on the approximate PGA (b) based on the PGA simulated in this study

The landslide hazard maps using the approximate value and the PGA we estimated are illustrated in Figure 7-7. From the hazard maps we can visually inspect at the right down corner, some regions are unstable as our prediction whereas is quasi stable predicted by the approximate PGA value. Figure 7-8 shows the comparisons of the inventory maps and landslide hazard maps. It is suggested that our results are in good agreement with the landslides induced by the 2016 Kumamoto earthquake. Besides, the contingency matrix computed for occurred landslides and alerts is determined and tabulated in Table 7-3. The false-alarm is almost the same, whereas the miss-alarm rate drops and the success rate rises when using the proposed method. In general, the miss-alarm rate is more important than other two measures in the landslide hazard assessment, because if a miss-alarmed landslide happens, it would cause a devastate loss of properties and fatalities. The reduced miss-alarm rate proves our simulation results are improved and acceptable for landslide hazard assessment. It is also concluded that the developed system for simulating earthquake ground motions is useful and reliable.

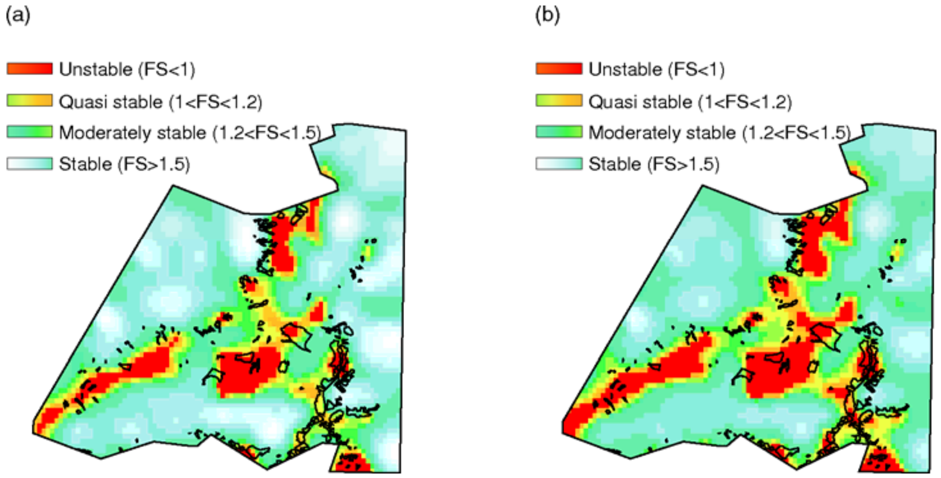

Figure 7-8 Comparison between landslides induced by the 2016 Kumamoto earthquake and the hazard maps (a) based on the approximate PGA (b) based on the PGA simulated in this study

Table 7-3 The contingency matrix of the Aso-bridge area

	Success rate	Miss-Alarm rate	False-Alarm rate
Conventional method	68%	36%	30%
Developed system	72%	18%	31%

7.4 CONCLUSIONS

The three modules made in the above chapters are combined with the SFFM module to be a practical system for earthquake ground motion simulations. The developed practical system is validated by the application to landslide hazard assessment in Aso-bridge region, Kumamoto, Japan. In conventional landslide hazard mapping, an approximate PGA value for an area is used, which makes the accuracy very low. In this study, the PGA for each mesh is calculated based on the generated slip distribution field of the target earthquake on a specific fault by using the developed system. Slope stability analysis is carried out using the PGA of each mesh in landslide hazard mapping. Thus, a landslide hazard map related to a potential earthquake on a specific fault can be made. A landslide hazard map induced by a M7.0 earthquake assumed on the Futagawa fault is made and compared with the landslides induced by the 2016 Kumamoto earthquakes. Compare with the conventional method, the success rate rises from 68% to 72% and the miss alarm rate drops from 36% to 18%. It is suggested that the developed practical system is adaptable and useful in landslide hazard assessment.

REFERENCE

Aleotti P, Chowdhury R (1999) Landslide hazard assessment: summary review and new perspectives. Bull Eng Geology Environm 58, 21-44

Anbalagan R, Singh B (1996) Landslide hazard and risk assessment mapping of mountainous terrains—a case study from Kumaun Himalaya, India. Eng Geology 43, 237-246

Ayalew L, Yamagishi H (2005) The application of GIS-based logistic regression for landslide susceptibility mapping in the Kakuda-Yahiko Mountains, Central Japan. Geomorphology 65, 15-31

Capolongo D, Refice A, Mankelow J (2002) Evaluating earthquake-triggered landslide hazard at the basin scale through GIS in the Upper Sele river valley. Surveys geophys 23, 595-625

Carrara A, Guzzetti F, Cardinali M, Reichenbach P (1999) Use of GIS technology in the prediction and monitoring of landslide hazard. Natural Hazards 20, 117-135

Fell R (1994) Landslide risk assessment and acceptable risk. Canadian Geotech J 31, 261-272

Gupta R, Joshi B (1990) Landslide hazard zoning using the GIS approach—a case study from the Ramganga catchment, Himalayas. Eng Geology 28, 119-131

Kanungo D, Arora M, Gupta R, Sarkar S (2008) Landslide risk assessment using concepts of danger pixels and fuzzy set theory in Darjeeling Himalayas. Landslides 5, 407-416

Klein FW, Frankel AD, Mueller CS, Wesson RL, Okubo PG (2001) Seismic hazard in Hawaii: High rate of large earthquakes and probabilistic ground-motion maps. Bull Seismol Soc Am 91, 479-498

Lee S, Pradhan B (2007) Landslide hazard mapping at Selangor, Malaysia using frequency ratio and logistic regression models. Landslides 4, 33-41

Nath SK, Thingbaijam KKS, Raj A (2008) Earthquake hazard in Northeast India—a seismic microzonation approach with typical case studies from Sikkim Himalaya and Guwahati city. J Earth System Sci 117, 809-831

Ohlmacher GC, Davis JC (2003) Using multiple logistic regression and GIS technology to predict landslide hazard in northeast Kansas, USA. Eng geology 69, 331-343

Papadopoulou-Vrynioti K, Bathrellos GD, Skilodimou HD, Kaviris G, Makropoulos K (2013) Karst collapse susceptibility mapping considering peak ground acceleration in a rapidly growing urban area. Eng Geology 158, 77-88

Ray R, De Smedt F (2009) Slope stability analysis on a regional scale using GIS: a case study from Dhading, Nepal. Environm geology 57, 1603-1611

Saha A, Gupta R, Arora M (2002) GIS-based landslide hazard zonation in the Bhagirathi (Ganga) valley, Himalayas. Int J Remote Sensing 23, 357-369

Shang Y, Yang Z, Li L, Liu Da, Liao Q, Wang Y (2003) A super-large landslide in Tibet in 2000: background, occurrence, disaster, and origin. Geomorphology 54, 225-243

Singleton A, Li Z, Hoey T, Muller J-P (2014) Evaluating sub-pixel offset techniques as an alternative to D-InSAR for monitoring episodic landslide movements in vegetated terrain. Remote Sensing Environm 147, 133-144

Suh J, Choi Y (2017) Mapping hazardous mining-induced sinkhole subsidence using unmanned aerial vehicle (drone) photogrammetry. Environm Earth Sci 76, 144

Tantianuparp P, Shi X, Zhang L, Balz T, Liao M (2013) Characterization of landslide deformations in three gorges area using multiple InSAR data stacks. Remote Sensing 5, 2704-2719

Turner D, Lucieer A, De Jong SM (2015) Time series analysis of landslide dynamics using an unmanned aerial vehicle (UAV). Remote Sensing 7, 1736-1757

CHAPTER 8

CONCLUSIONS AND FUTURE STUDIES

a) CONCLUSIONS

Earthquake ground-motion intensity measures, such as acceleration time series and peak ground acceleration (PGA), are important and necessary data in earthquake engineering. They need to be simulated for the locations where records were not available during a past earthquake or for a future potential earthquake. This thesis provides a possible solution to these target problems and solves some key issues. The following major conclusions can be drawn:

(1) A practical system for simulating earthquake ground motions paying attenuation to volcanic zone and asperity on a fault is established. The developed system is successfully applied to the landslide hazard assessment of the Aso-bridge region based on GIS-based hazard mapping.

(2) A method for estimating site amplification in the region without strong ground motion stations is developed by using the empirical relations between the calculated site amplification and the so-called V_{S30}. The relation in the form of $\log_{10} D(f) = a\left(V_{S30}/V_{ref}\right) + b$ is employed. This method is validated by comparing the calculated and predicted site amplification in five-class sites. This developed method is made as a module for the estimation of site amplification and incorporated in the developed practical system.

(3) A practical Konno-Ohmachi smoothing technique is employed to smooth

the surface and borehole Fourier spectra. Compare to the commonly used triangular smoothing techniques, this technique can provide a good smooth at both low- and high-frequency parts. This smoothing technique is incorporated in the module for the estimation of site amplification.

(4) An analysis method for estimating the S-wave attenuation Q_s considering the volcanic effect is developed and complied as a module. The detailed procedure for determining the Q_s of the region with active volcanoes is specified and integrated in the practical system for simulating earthquake ground motions. The presented method is validated by simulating the ground motions of 9 non-volcanic records from the 2016 Kumamoto earthquake. The accuracy of simulated ground motions is improved using the proposed method.

(5) The question of which kind of slip distribution field performs best in the ground motion simulations is clarified. 45 near-field records from 6 earthquakes are selected to investigate this issue. The ground motion simulations are performed for these records and compared with the observations. The average and maximum relative errors of these records are calculated and compared. It is suggested that neither of them performs well enough although the simulated PGA based on the slip distribution field using the SGM data match the observations better than others.

(6) A combination of the simulated PGA is proposed to solve the problem that low-accuracy simulated PGA using individual slip distribution. Two combination models are proposed to combine the PGA. The records are separated into two parts, the major part (nearly 80% of records) is used for training the model and the rest part is used for validation. Comparison of the average and maximum relative errors of the combined PGA and the individual simulated PGA shows the accuracy of results is much improved. The difference of accuracy of combined PGA between two combined model is not very significant. The combination process is made as a module and integrated in the practical system for the simulation of earthquake ground motions. The PGA in a region without records during a

past earthquake can be simulated using the individual slip distribution field first and then combined together to improve the accuracy.

(7) A method for estimating slip distribution field of a potential earthquake on a specific fault is improved. At first, a rectangle-ellipse pattern based on a lot of observations is proposed to characterize the slip distribution field. Then the scaling relations of slip distribution field are statistically established from the 17 shallow crustal earthquake in Japan from 1995 to 2016. The improved method is made as a module and also incorporated in the practical system. The method is validated by the ground motion simulations of a M7 earthquake occurs on the Futagawa fault. The accuracy of simulated acceleration time series is acceptable.

(8) An application of the developed practical system to the landslide hazard assessment for a potential earthquake on a specific fault is presented. The slip distribution field is established for the Futagawa fault under an assumption that a M7.0 earthquake occurs using the developed system. The ground motion simulations for the Aso-bridge region, Kumamoto, Japan are performed. Slope stability analysis is carried out using the PGA of each mesh in landslide hazard mapping. The results are in good agreement with the landslides induced by the 2016 Kumamoto earthquake. Comparison of the landslide hazard maps using the approximate PGA and the simulated one based on the practical system shows that the developed practical system is useful and adaptable in landslide hazard assessment.

b) FUTURE STUDIES

(1) An effort of separating the synthesizing acceleration time series should be encouraged in the future study. Since the stochastic finite-fault method starts from the shear dislocation of a point and the radiated seismic waves are assumed to propagate as the way of spherical wave, the direction effect has not been considered into the calculation. Some studies report that the so-called direction effect by the observations along and perpendicular to the fault are different at the same epicentre distance.

(2) Since the simulated acceleration time series are the synthesized shear waves, the vertical component of ground motions cannot be simulated. Some relations between the synthesized horizontal and the observed vertical ground motions can be tried to establish. Due to the requirement of vertical component in some engineering problems, these relations is useful for practical applications when considering the effect of vertical component.

(3) The relations proposed in this thesis are almost based on the Japanese database, if other data sources are integrated into the determination of some relationships, such as the relation between site amplification and V_{S30}, the accuracy will higher than those derived in this thesis.

(4) The relations of the site amplification and the V_{S30} is based on the records from the 2016 Kumamoto earthquake. As we know that the site responses for a large earthquake and a small earthquake are usually different. Therefore, the regression coefficients of the relations between the site amplification and the V_{S30} derived in this thesis may not be suitable to evaluate the site amplification for a small earthquake. This issue is very important for evaluating the site response of an engineering site for different assumed earthquakes. It is necessary to investigate the relation between site amplification calculated from some earthquakes and the V_{S30}.

APPENDIX 1

APPENDIX 1

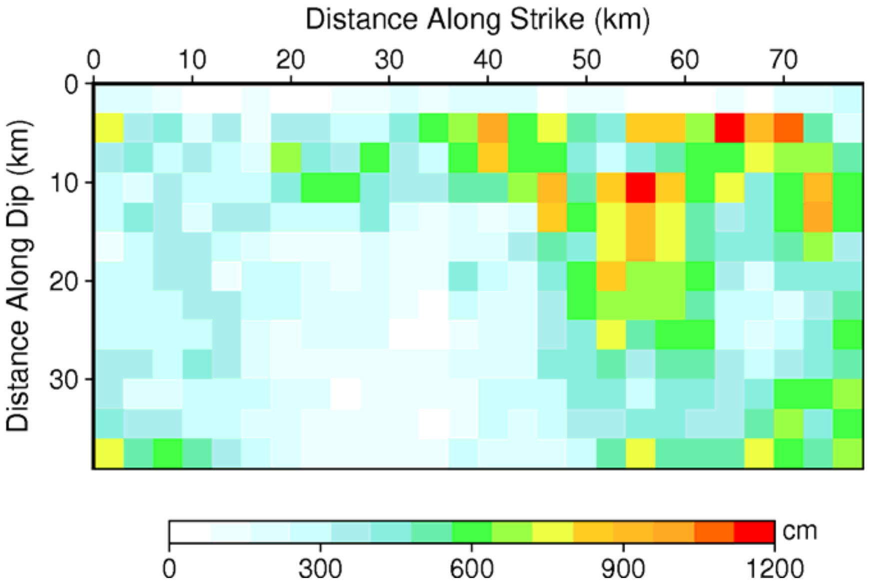

Figure S1 Slip distribution field of 1999 Chi-Chi, Taiwan earthquake inversed by SGM data (refigured from Zhang et al (2004))

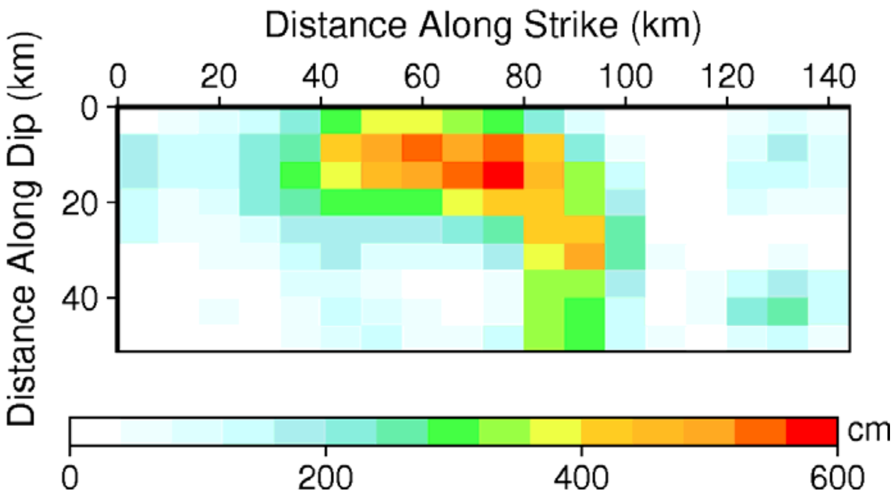

Figure S2 Slip distribution field of 1999 Chi-Chi, Taiwan earthquake inversed by TBW data (refigured from Hayes (2014))

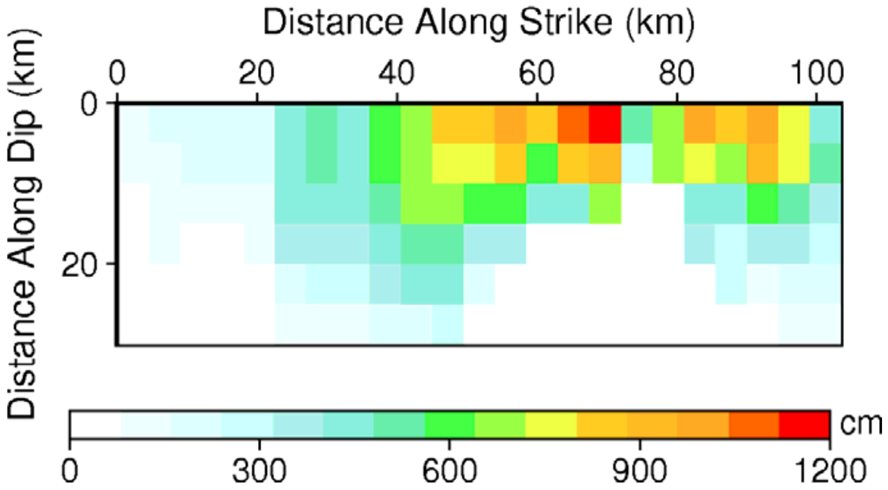

Figure S3 Slip distribution field of 1999 Chi-Chi, Taiwan earthquake inversed by GPS data (refigured from Johnson et al (2001))

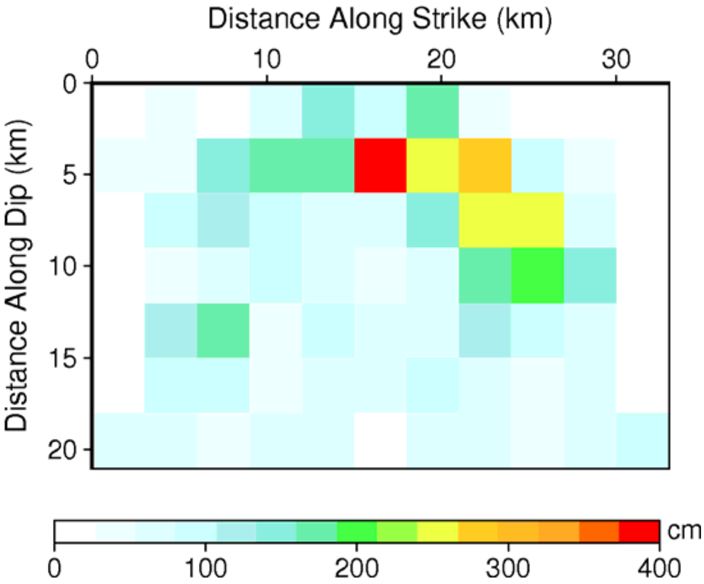

Figure S4 Slip distribution field of 2000 Tottori earthquake inversed by SGM data (refigured from Iwata et al (2000))

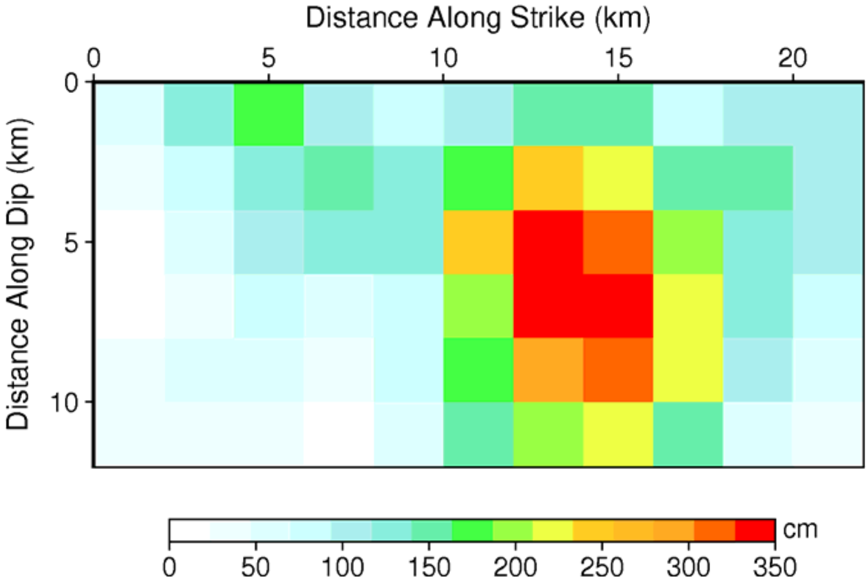

Figure S5 Slip distribution field of 2000 Tottori earthquake inversed by TBW data (refigured from Yagi and Kikuchi (2000))

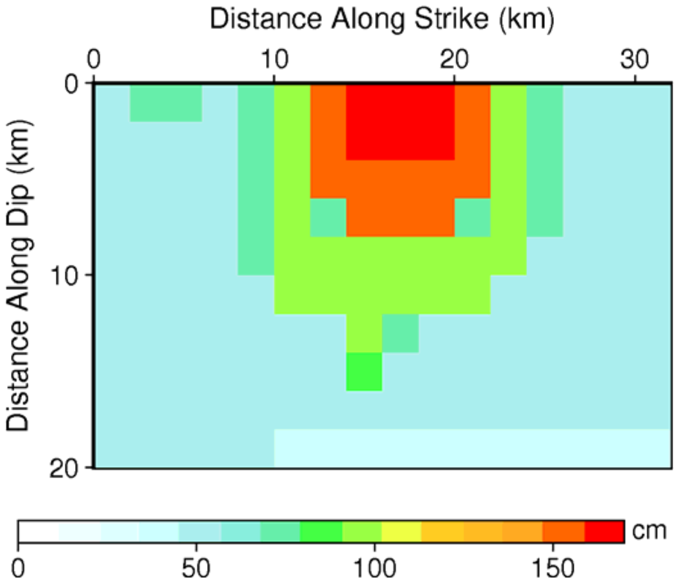

Figure S6 Slip distribution field of 2000 Tottori earthquake inversed by GPS data (refigured from Semmane et al. (2005))

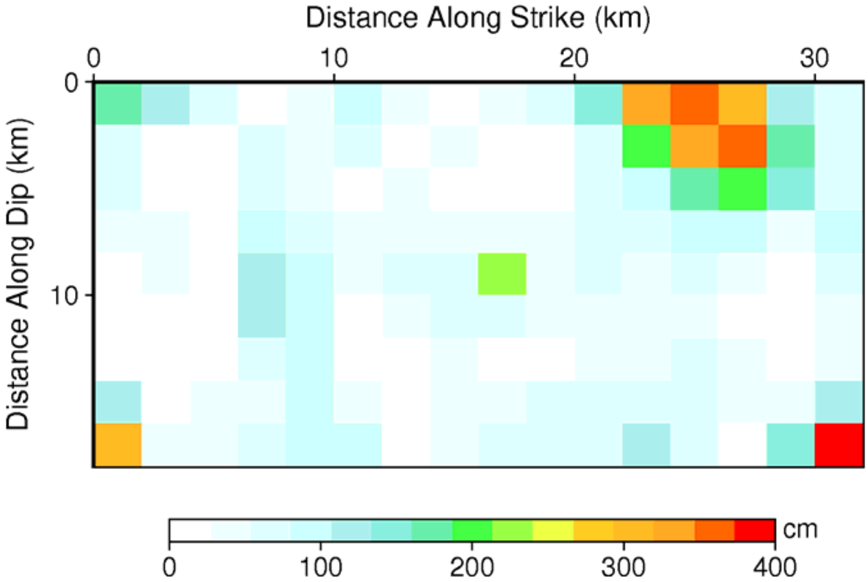

Figure S7 Slip distribution field of 2005 Fukuoka earthquake inversed by SGM data (refigured from Sekiguchi et al. (2006))

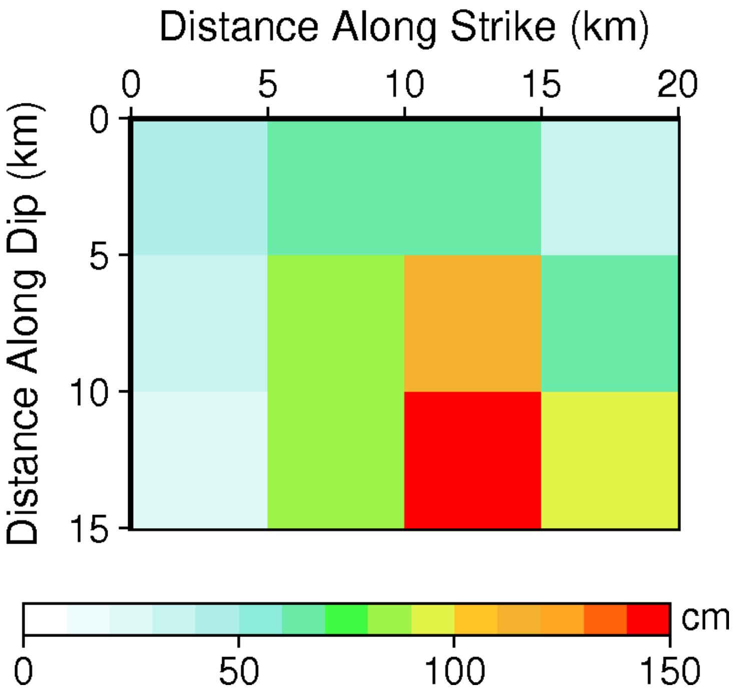

Figure S8 Slip distribution field of 2005 Fukuoka earthquake inversed by TBW data (refigured from Yamanaka (2005))

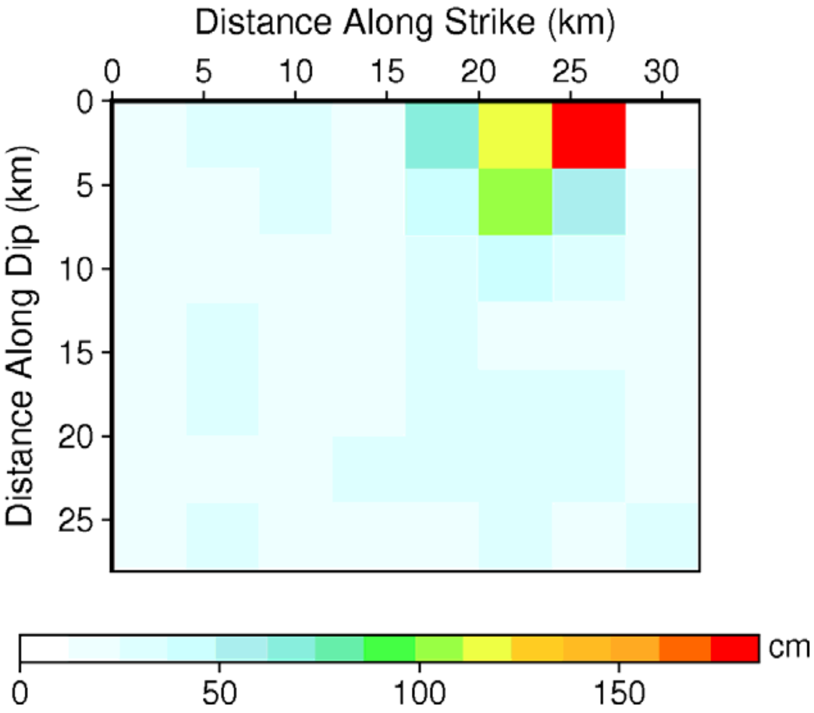

Figure S9 Slip distribution field of 2005 Fukuoka earthquake inversed by GPS data (refigured from Kobayashi et al. (2005))

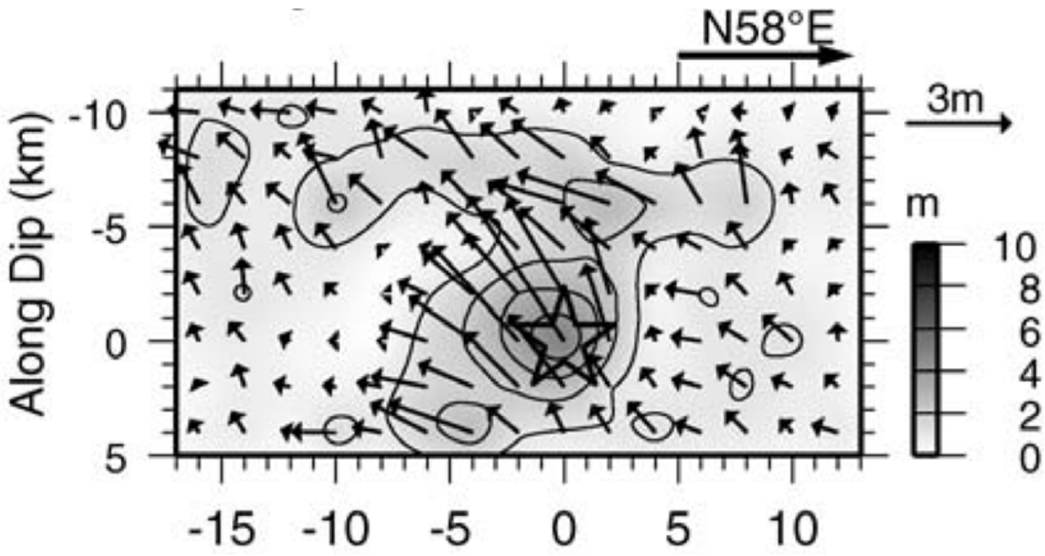

Figure S10 Slip distribution field of 2007 Noto Hanto earthquake inversed by SGM data (after Asano and Iwata (2011b))

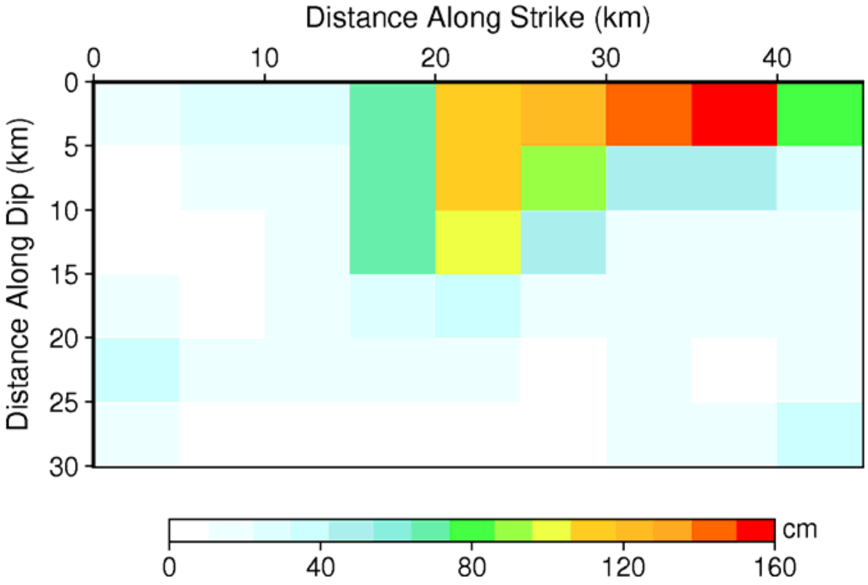

Figure S11 Slip distribution field of 2007 Noto Hanto earthquake inversed by TBW data (refigured from Yagi (2007))

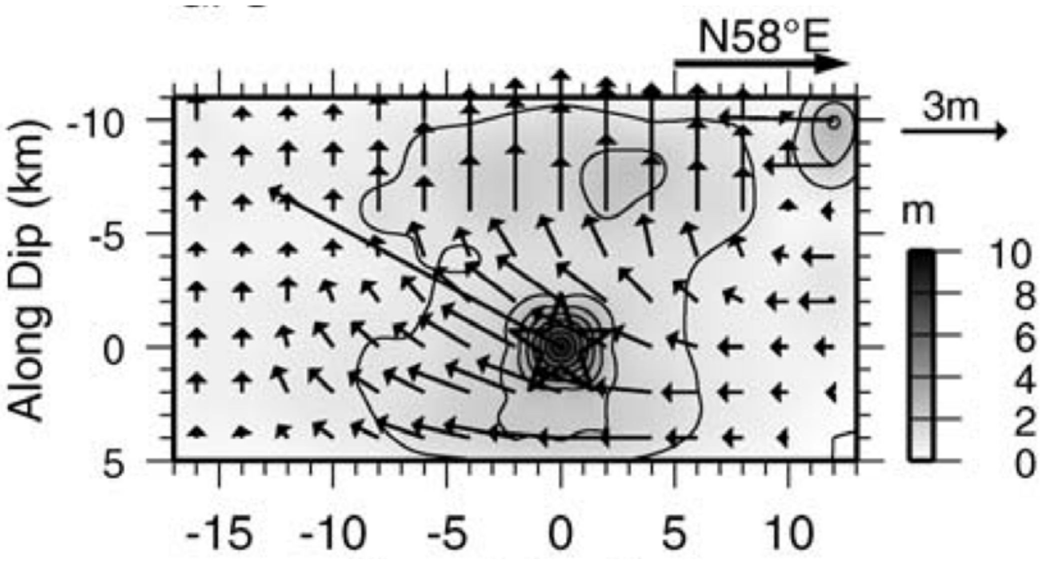

Figure S12 Slip distribution field of 2007 Noto Hanto earthquake inversed by GPS data (after Asano and Iwata (2011b))

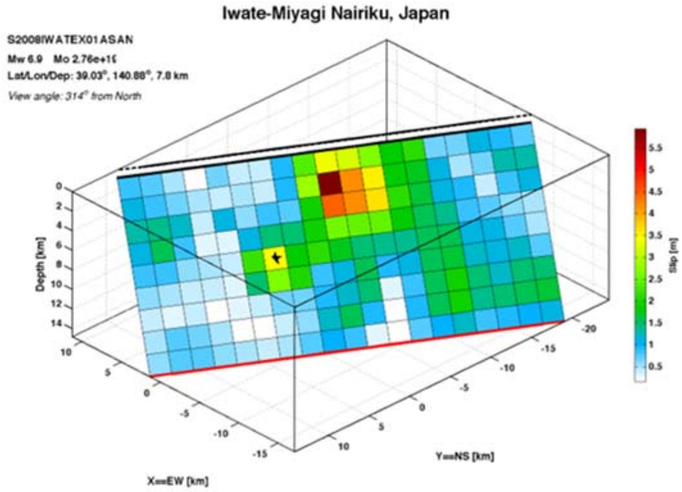

Figure S13 Slip distribution field of 2008 Iwate-Miyagi earthquake inversed by SGM data (accessed from SRCMOD)

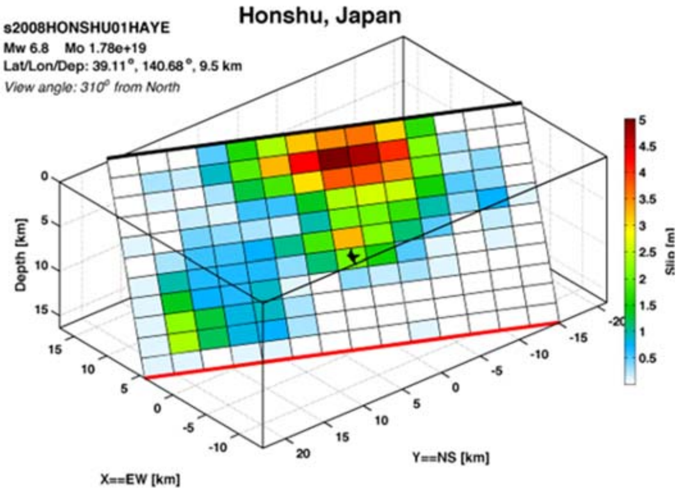

Figure S14 Slip distribution field of 2008 Iwate-Miyagi earthquake inversed by TBW data (accessed from SRCMOD)

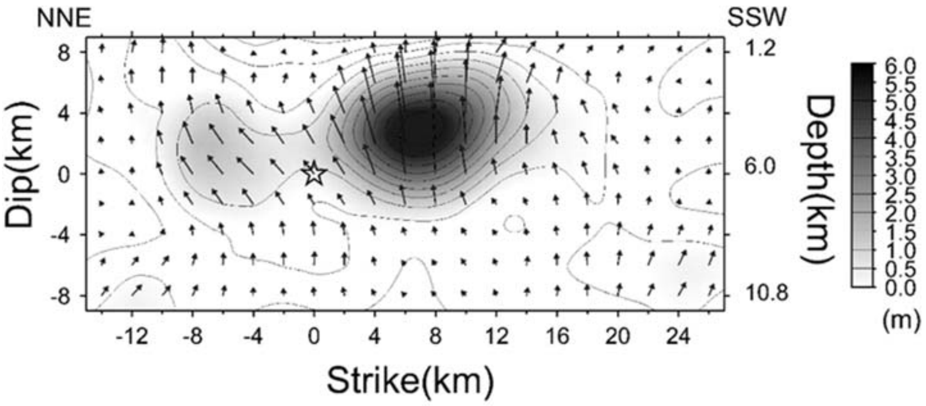

Figure S15 The slip distribution field of 2008 Iwate-Miyagi earthquake inversed by GPS data (after Yokota et al. (2009))

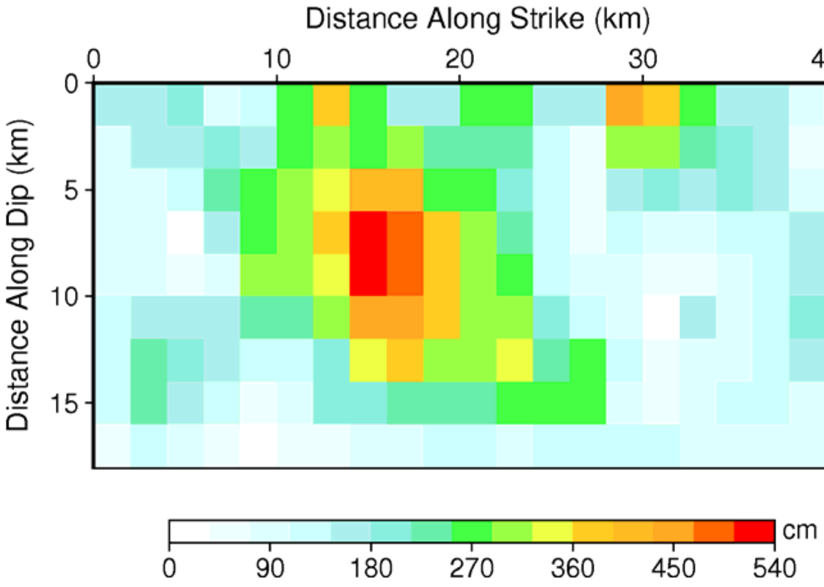

Figure S16 The slip distribution field of 2016 Kumamoto earthquake inversed by SGM data (refigured from Asano and Iwata. (2016))

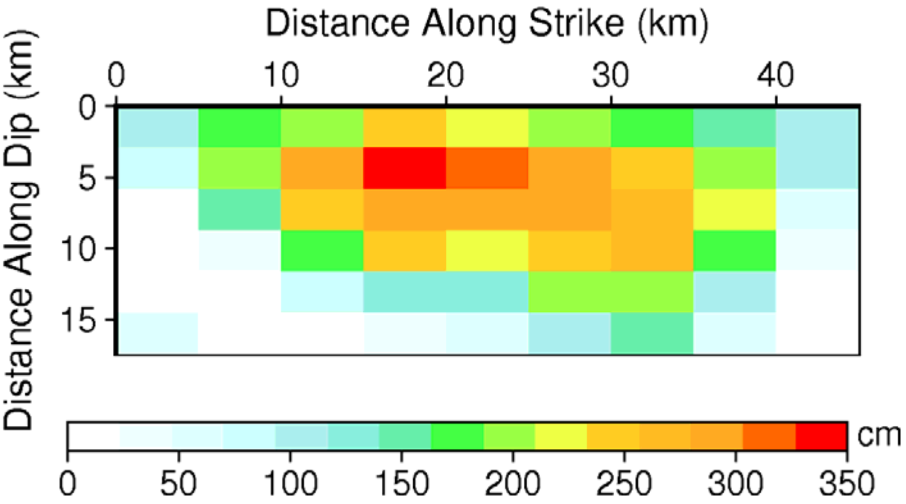

Figure S17 The slip distribution field of 2016 Kumamoto earthquake inversed by TBW data (clipped from Hayes (2016))

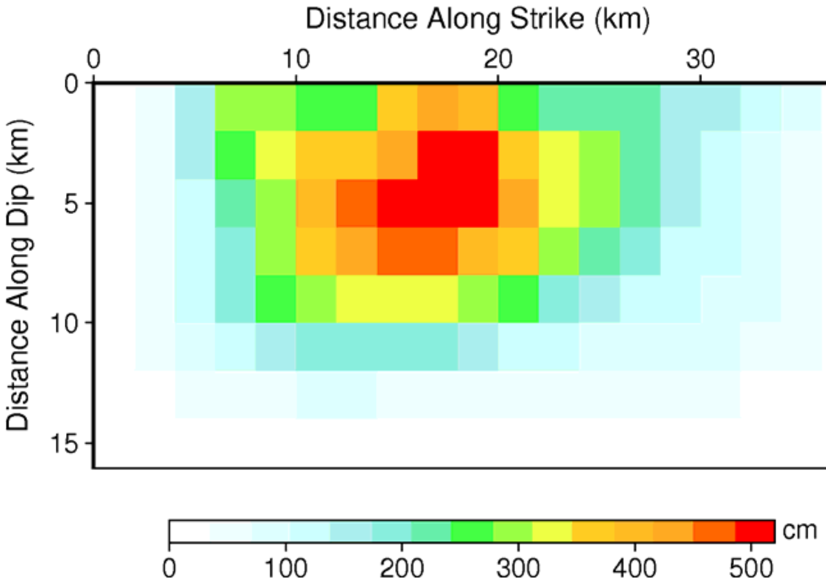

Figure S18 The slip distribution field of 2016 Kumamoto earthquake inversed by GPS data (refigured from Futahata and Hashimoto (2016))

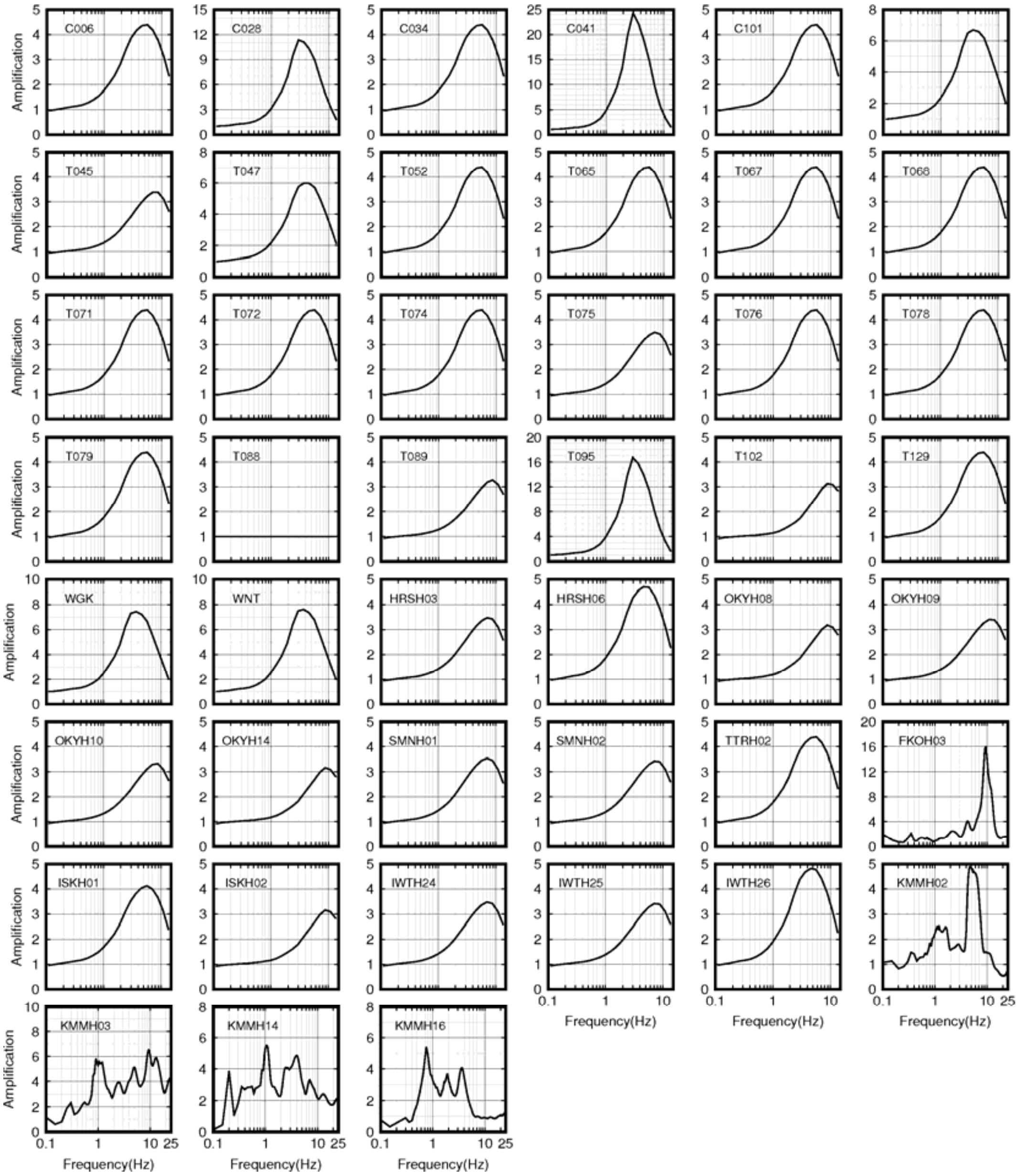

Figure S19 Site amplification used in the combination analysis

APPENDIX 2

APPENDIX 2

Table S1 Input parameters for the stochastic finite-fault model of the 1999 Chi-Chi, Taiwan, earthquake

Parameters	Value	Reference
Source		
Moment magnitude (M_w)	7.6	CWBSN of Taiwan
Hypocenter location	23.87°N, 120.75°E, 7km	CWBSN of Taiwan
Strike and dip angle ($^\circ$)	5 and 34	CWBSN of Taiwan
subfault length and width (km)	3 and 3	Zhang et al. (2004)
	8 and 5.65	Hayes (2014)
	4.5 and 5	Johnson et al. (2001)
Slip distribution	Figure S1	Zhang et al. (2004)
	Figure S2	Hayes (2014)
	Figure S3	Johnson et al. (2001)
Stress drop (bars)	50	This study
S-wave velocity (km/s)	3.7	Roumelioti and Beresnev (2003)
Density (g/cm^3)	2.7	Roumelioti and Beresnev (2003)
Rupture propagation velocity	0.8 β	Atkinson and Boore (2006)

Pulsing area percentage	50%	Atkinson and Boore (2006)
Path		
Geometric spreading, R^b: b=	-1.0 (0-50km) 0 (50-150km) -0.5 (>150km)	Sokolov (2000)
Ground-motion duration, dR, d=	0.0 (0-10km) +0.16 (10-70km) -0.03 (70-130km) +0.04 (>130km)	Atkinson and Boore (1995)
Quality factor	$Q_s = 117 f^{0.77}$	Chen et al. (1989)
Site		
Site amplification	approximate sites	This study
Kappa (s)	0.07	Roumelioti and Beresnev (2003)

CWBSN: Central Weather Bureau Seismological Center

β： S-wave velocity

Table S2 Input parameters for the stochastic finite-fault model of the 2000 Tottori, Japan, earthquake

Parameters	Value	Reference
Source		
Moment magnitude (M_w)	6.6	F-net
Hypocenter location	35.2752°N, 133.3498°E, 11 km	F-net
Strike and dip angle (°)	150 and 85	F-net
subfault length and width (km)	3 and 3	Iwata et al. (2000)
	2 and 2	Yagi and Kikuchi (2000)
	2 and 2	Semmane et al. (2005)
Slip distribution	Figure S4	Iwata et al. (2000)

	Figure S5	Yagi and Kikuchi (2000)
	Figure S6	Semmane et al. (2005)
Stress drop (bars)	71	Pulido and Kubo (2004)
S-wave velocity (km/s)	3.55	Pulido and Kubo (2004)
Density (g/cm^3)	2.8	Atkinson et al. (2009)
Rupture propagation velocity	0.65 β	Pulido and Kubo (2004)
Pulsing area percentage	50%	Atkinson and Boore (2006)
Path		
Geometric spreading, R^b: b=	-1.0 (0-100km) -0.5 (>100km)	Zengin and Cakti (2014)
Ground-motion duration, dR, d=	0.0 (0-10km) +0.16 (10-70km) -0.03 (70-130km) +0.04 (>130km)	Atkinson and Boore (1995)
Quality factor	$Q_s = 146 f^{0.67}$	Pulido and Kubo (2004)
Site		
Site amplification	approximate sites	This study
Kappa (s)	0.05	Zhang et al. (2016)

Table S3 Input parameters for the stochastic finite-fault model of the 2005 Fukuoka, Japan, earthquake

Parameters	Value	Reference
Source		
Moment magnitude (M_w)	6.6	F-net
Hypocenter location	33.74°N, 130.17°E, 9.84 km	F-net
Strike and dip angle (°)	122 and 87	F-net

subfault length and width (km)	2 and 2	Sekiguchi et al. (2006)
	5 and 5	Yamanaka (2005)
	4 and 4	Kobayashi et al. (2006)
Slip distribution	Figure S7	Sekiguchi et al. (2006)
	Figure S8	Yamanaka (2005)
	Figure S9	Kobayashi et al. (2006)
Stress drop (bars)	53	This study
S-wave velocity (km/s)	3.68	Matsumoto et al. (2006)
Density (g/cm^3)	2.6	Matsumoto et al. (2006)
Rupture propagation velocity	0.8 β	Atkinson and Boore (2006)
Pulsing area percentage	50%	Atkinson and Boore (2006)
Path		
Geometric spreading, R^b: b=	-1.0 (0-100km) -0.5 (>100km)	Zengin and Cakti (2014)
Ground-motion duration, dR, d=	0.0 (0-10km) +0.16 (10-70km) -0.03 (70-130km) +0.04 (>130km)	Atkinson and Boore (1995)
Quality factor	$Q_s = 92.5 f^{0.58}$	This study
Site		
Site amplification	Figure S19	This study
Kappa (s)	0.0514	This study

Table S4 Input parameters for the stochastic finite-fault model of the 2007 Noto Hanto, Japan, earthquake

Parameters	Value	Reference
Source		
Moment magnitude (M_w)	6.7	F-net
Hypocenter location	37.2207°N, 136.6860°E, 8 km	F-net
Strike and dip angle (°)	58 and 60	Asano and Iwata (2011b)
subfault length and width (km)	2 and 2 5 and 5 2 and 2	Asano and Iwata (2011b) Yagi (2007) Asano and Iwata (2011b)
Slip distribution	Figure S10 Figure S11 Figure S12	Asano and Iwata (2011b) Yagi (2007) Asano and Iwata (2011b)
Stress drop (bars)	200	This study
S-wave velocity (km/s)	3.7	Maeda et al. (2008)
Density (g/cm^3)	2.8	Maeda et al. (2008)
Rupture propagation velocity	0.8 β	Atkinson and Boore (2006)
Pulsing area percentage	50%	Atkinson and Boore (2006)
Path		
Geometric spreading, R^b: b=	-1.0 (0-100km) -0.5 (>100km)	Zengin and Cakti (2014)
Ground-motion duration, dR, d=	0.0 (0-10km) +0.16 (10-70km) -0.03 (70-130km) +0.04 (>130km)	Atkinson and Boore (1995)
Quality factor	$Q_s = 150 f^{0.7}$	Ghofrani and Atkinson (2011)
Site		
Site amplification	approximate sites	This study
Kappa (s)	0.05	Zhang et al. (2016)

Table S5 Input parameters for the stochastic finite-fault model of the 2008 Iwate-Miyagi, Japan, earthquake

Parameters	Value	Reference
Source		
Moment magnitude (M_w)	6.9	F-net
Hypocenter location	39.0298°N, 140.8807°E, 5 km	F-net
Strike and dip angle ($^\circ$)	209 and 51	F-net
subfault length and width (km)	2 and 2	Asano and Iwata (2011a)
	3 and 2	Hayes and Ji (2008)
	2 and 2	Yokota et al. (2009)
Slip distribution	Figure S13	Asano and Iwata (2011a)
	Figure S14	Hayes and Ji (2008)
	Figure S15	Yokota et al. (2009)
Stress drop (bars)	140	Ghofrani and Atkinson. (2011)
S-wave velocity (km/s)	3.5	Yoshida et al. (2015)
Density (g/cm^3)	2.8	Atkinson et al. (2009)
Rupture propagation velocity	0.8 β	Atkinson and Boore (2006)
Pulsing area percentage	50%	Atkinson and Boore (2006)
Path		
Geometric spreading, R^b: b=	-1.0 (0-100km) -0.5 (>100km)	Zengin and Cakti (2014)
Ground-motion duration, dR, d=	0.0 (0-10km) +0.16 (10-70km) -0.03 (70-130km) +0.04 (>130km)	Atkinson and Boore (1995)
Quality factor	$Q_s = 110 f^{0.69}$	Cultrera et al. (2013)
Site		
Site amplification	approximate sites	This study
Kappa (s)	0.074	Cultrera et al. (2013)

Table S6 Input parameters for the stochastic finite-fault model of the 2016 Kumamoto, Japan, earthquake

Parameters	Value	Reference
Source		
Moment magnitude (M_w)	7.1	F-net
Hypocenter location	32.7545°N, 130.763°E, 11 km	F-net
Strike and dip angle ($^\circ$)	224 and 65	F-net
subfault length and width (km)	2 and 2	Asano and Iwata (2016)
	5 and 2.9	Hayes (2016)
	2 and 2	Fukahata and Hashimoto (2016)
Slip distribution	Figure S16	Asano and Iwata (2016)
	Figure S17	Hayes (2016)
	Figure S18	Fukahata and Hashimoto (2016)
Stress drop (bars)	64	Zhang et al. (2016)
S-wave velocity (km/s)	3.7	Atkinson et al. (2009)
Density (g/cm^3)	2.8	Atkinson et al. (2009)
Rupture propagation velocity	0.8 β	Atkinson and Boore (2006)
Pulsing area percentage	50%	Atkinson and Boore (2006)
Path		
Geometric spreading, R^b: b=	-1.0 (0-100km) -0.5 (>100km)	Zengin and Cakti (2014)
Ground-motion duration, dR, d=	0.0 (0-10km) +0.16 (10-70km) -0.03 (70-130km) +0.04 (>130km)	Atkinson and Boore (1995)
Quality factor	$Q_s = 85.5 f^{0.68}$	Zhang et al. (2016)
Site		
Site amplification	S/B' ratios	Zhang et al. (2016)
Kappa (s)	0.0514	Zhang et al. (2016)

Table S7 Input parameters for the stochastic finite-fault model of a M7 potential earthquake

Parameters	Value	Reference
Source		
Moment magnitude (M_w)	7.0	Assumed
Hypocenter location	32.7545°N, 130.763°E, 11 km	Assumed
Strike and dip angle (°)	224 and 65	F-net
subfault length and width (km)	4 and 3.5	This study
Slip distribution	Figure 6-17	This study
Stress drop (bars)	64	Zhang et al. (2016)
S-wave velocity (km/s)	3.7	Atkinson et al. (2009)
Density (g/cm^3)	2.8	Atkinson et al. (2009)
Rupture propagation velocity	0.8β	Atkinson and Boore (2006)
Pulsing area percentage	50%	Atkinson and Boore (2006)
Path		
Geometric spreading, R^b: b=	-1.0 (0-100km) -0.5 (>100km)	Zengin and Cakti (2014)
Ground-motion duration, dR, d=	0.0 (0-10km) +0.16 (10-70km) -0.03 (70-130km) +0.04 (>130km)	Atkinson and Boore (1995)
Quality factor	$Q_s = 95.7 f^{0.66}$ (volcanic) $Q_s = 122.6 f^{0.74}$ (non-volcanic)	This study
Site		
Site amplification	Figure 3-17	This study
Kappa (s)	0.0514	Zhang et al. (2016)